Apparent polar wandering and its implications for past plate motions

by

Lei Wu

A thesis submitted in partial fulfillment of the requirements for the degree of

Doctor of Philosophy
in
Geophysics

Department of Physics
University of Alberta

Abstract

Paleomagnetism is the study of ancient geomagnetic field vectors recorded by rocks and sediments. With simple spherical geometry, the coordinates of the surface intersections of the paleo(geo-)magnetic dipole can be calculated from remanent magnetization directions. In 1956, Edward Irving reported the first set of paleomagnetic poles of different ages for northwest Europe, and proposed that it is the continents rather than the geomagnetic dipole (i.e., the Earth's spin axis) that have been displaced in the geologic history. The 1960s and 1970s witnessed the glory of paleomagnetism in confirming the plate tectonic theory. Based on the latitudinal and azimuthal constraints from the paleomagnetic inclinations and declinations, many important discoveries about the horizontal movements of continental blocks, such as the accretion of Eurasia and the breakup of Gondwana in the Mesozoic, had been made in this period. More than half a century later, the golden paleomagnetic latitudes and azimuths now have very limited values for most quantitative plate tectonic research because paleomagnetic reconstructions cannot provide rigorous paleolongitude constraints. To address this challenge, this dissertation is targeted at deriving a new method to calculate paleolongitudes from paleomagnetic data.

Contrary to the traditional paleomagnetic reconstructions based on individual paleomagnetic pole positions with respect to a tectonic plate, here we treat paleopoles as an integral sequence and investigate the geometry of paleomagnetic polar wandering trajectory or apparent polar wander path (APWP) for the kinematic implications. Specifically, a studied APWP needs to be divided into different segments, to which circle parameterizations are applied to estimate their stage rotation poles and angles. To correct the errors arising from the fact that all resultant reconstructions are artificially restrained along circle arcs centering at the rotation poles, which renders paleocolatitudes determined from paleomagnetism void, we force the spherical distances between reconstructions and paleo-poles to be the observed paleocolatitudes. To help readers implement this new method, we present a MATLAB-based toolbox PMTec, which can be downloaded from https://sites.google.com/a/ualberta.ca/lei-wu/ and http://www.ualberta.ca/∼vadim/software.htm.

Using our new method, APWP geometric parametrization (APWPGP), we reevaluate the separation history of the East Gondwanaland since 140 Ma. Our reconstructions indicate that the affinity between India and Australia-East Antarctica was broken down around 130-120 Ma, and that Australia and East Antarctica were separated at around 60-40 Ma. We compare our reconstructions against those from other absolute plate motion (APM) models, which reveals tremendous discrepancies among the different APM predictions. There is a trend to dynamically model mantle thermal structures especially those related to sinking slabs, from which they evaluate the quality of various APM models. We argue that this type of research is a round reasoning and it provides little help in the quality discrimination, because the current interpretations of slab-like structures imaged from seismic tomography models were made from plate reconstructions in the first place. The most effective way to prove the quality of our APWPGP method is to reconstruct some collisional tectonic processes and then compare the resultant APM reconstructions with the independent geophysical and geological observations.

Using the APWPGP method, we reconstruct the closing of the Mongol-Okhotsk Ocean (MOO) in the Mesozoic. The APWPs of North China-Amuria (NCA) [Van der Voo et al., 2015], Siberia and Europe for the last 260 Myr [Torsvik et al., 2012] are parameterized for rotation parameters. A new global APM model is constructed in the coordinates of stable Europe, from which APMs of other major continental plates are predicted through the relative plate motion (RPM) models of Torsvik et al. [2012]. Three stages including 260-200 Ma, 200-150 Ma and 150-120 Ma, are discriminated from the temporal variations in the approaching speed of NCA and Siberia and the depth-varying slab volumes. The derived surface kinematics are used to interpret the slab-like high seismic velocity structures related to the subduction of the MOO. The interval of 150-120 Ma witnessed the closing of the remnant paleo-oceanic basin confined between Siberia and NCA. This is supported by a southwestward transition of slabs distributed at the depth of 1800-1300 km, which corresponds to the subduction zones at 140-120 Ma [van der Meer et al., 2010], with an upward reduction in slab volume predicted by the shear-wave velocity model GyPSuM [Simmons et al., 2010]. We find a similarly southwestward trend in the downward geoid undulation in the India-Eurasia geoid low (IEGL). There is a remarkably strong linear correlation of -0.92, with the associated coefficient of determination of 0.84, between the surface geoid height in the IEGL and the underlying slab volume at the depth of 1200-2800 km. Combined with the seismically constrained boundary topographies of the lower mantle, we propose that the mass deficit reflected from the IEGL is mainly caused by the negative

density contrast between the sinking slabs and the ambient lower mantle.

The first principle is that you must not fool yourself and you are the easiest person to fool.
——— *Richard P. Feynman*

Sometimes, some lies that spoken with high confidence could be more receptive than facts that spoken with doubt.
——— *Toba Beta*

In our reasonings concerning matter of fact, there are all imaginable degrees of assurance, from the highest certainty to the lowest species of moral evidence. A wise man, therefore, proportions his belief to the evidence.
——— *David Hume*

Acknowledgements

Learning is a collaborative effort, to which doing thesis projects is the embodiment. I have been fortunate to have had in my life lots of inspiring people who helped me develop strong scientific curiosity and problem-solving skills, and most importantly, a rigourous logic. In this respect, I am particularly indebted to my supervisors, Dr. V.A. Kravchinsky and Dr. D.K. Potter, for their inspiration, encouragement and careful planning of my research projects. Their generous support, invaluable advice and constructive criticisms nurture and uplift me throughout my Ph.D. study.

A special acknowledgement goes to Dr. Y.J. Gu for his patient guidance and enlightening discussion to help me integrate seismic observations with plate reconstructions. Dr. C.A. Currie is appreciated for the helpful suggestions about my research in my annual supervisory meetings. Dr. M. Dumberry and Dr. M. Heimpel are acknowledged for the helpful discussions on my projects. I also want to thank my thesis committee members Dr. K. Muehlenbachs, Dr. M. Freeman and Dr. A. Smirnov for their constructive comments that largely improved this thesis. The Physics administration staff Dr. R. Marchand, Dr. M. Sacchi, Ms. S. Derr, Ms. S. Chan, Ms. S. Hamilton and Ms. C. Steinborn are appreciated for all their help and assistance during my program.

In the paleomagnetic group, I am especially thankful to Dr. M.E. Evans for his great vision and insights, from which I benefit in the run. I owe my sincere gratitude to Mrs. L.P. Koukhar for her technical support in the laboratory. A genuine thank-you goes to my group mates Taslima Anwar, Jiasheng Chen and Dunia Blanco, who made my life and study in Edmonton a lot easier.

I also want to thank my friends at the U of A: Juan Rosas, Benjamin Lee, Daniel Foster, Amanda Kessler, Amr Ibrahim, Yunfeng Chen, Ramin Mohammad Hosseini Dokht, Ruijia Wang, Sohel Bhuiyan, Yaotian Yin, Huilin Wang, Zhenhua Li, Wei Xie, Sibiao Liu and Sohely Pervin. All those joyful moments make the past four years truly memorable.

Last but not the least, I would like to thank my family and friends back home. You make me who I am. Words will not ever be enough to express my gratitude.

Contents

List of Tables

List of Figures

Abbreviations

APMs Absolute plate motions.

APWP apparent polar wander path.

APWPGP apparent polar wander path geometric parameterization.

CCW counterclockwise.

CW clockwise.

EPD expected paleolatitudinal drift.

GAD geocentric axial dipole.

GC great circle.

GCD Great circle distances.

GPS global positioning system.

IEGL India-Eurasia geoid low.

IGRF International Geomagnetic Reference Field.

LIPs large igneous provinces.

LLSVPs large low shear-velocity provinces.

MOO Mongol-Okhotsk Ocean.

NCA North China-Amuria.

NNR no-net-rotation.

PEP paleomagnetic Euler pole.

PTD phase transformation depth.

R2 Coefficient of determination.

RMSE root mean square error.

RPMs Relative plate motions.

SC small circle.

TPW true polar wander.

Nomenclature

D12 The global moving frame of Doubrovine et al. [2012].

GAP-P1 The P-velocity tomography model GAP-P1 of Obayashi et al. [2006].

GyPSuM10p The P-velocity tomography model GyPSuM of Simmons et al. [2010].

LLNL-G3Dv3p The P-velocity tomography model LLNL-G3Dv3p of Simmons et al. [2012].

LLNL_G3D_JPS The S-velocity tomography model LLNL_G3D_JPS of Simmons et al. [2015].

M10 The sinking slab frame of van der Meer et al. [2010].

M12 The paleomagnetically derived true polar wander frame of Mitchell et al. [2012].

M93 The fixed hotspot frame Müller et al. [1993].

MITP08p The P-velocity tomography model MITP08 of Li et al. [2008].

PMTec The Matlab-based toolbox for absolute plate motion reconstructions of Wu et al. [2015].

Q Quality factor to rank paleopoles according the criteria of Van der Voo [1990].

S40RTS The S-velocity tomography model SMEAN of Ritsema et al. [2011].

savani The S-velocity tomography model SMEAN of Auer et al. [2014].

SEMUCB-WM1 The S-velocity tomography model SMEAN of French and Romanowicz [2014].

SMEAN02s The S-velocity tomography model SMEAN of Becker and Boschi [2002].

T12 The global hybrid frame of Torsvik et al. [2012].

T12-TPW The global hybrid frame with true polar wander corrections of Torsvik et al. [2012].

1

Overview: the significance of plate reconstructions

The horizontal motions of the lithosphere on the Earth's surface, i.e., plate tectonics, are one of the biggest discoveries in the twentieth century. Quantifying such kinematic motions of plates is significant for our understanding of the surficial (e.g., mountain building) and internal (e.g., slab descending) evolution of the solid Earth (i.e., lithosphere and mantle), the long-term climate changes, the evolution and extinction of species, energy explorations (e.g., mineral, oil and gas resources) and geohazard predictions (e.g., earthquakes).

Current plate motion vectors can be measured by global positioning system (GPS). To this end, a network of GPS stations with a reasonable spatial coverage needs to be established to derive the motion vectors of the studied plates during a certain time period. Comparable current plate motions are predicted by the model NUVEL-1 (Figure 1.1), which is in the reference frame requiring no-net-rotation (NNR) of the lithosphere with respect to the underlying mantle. This model is determined from seafloor spreading rates, transform fault azimuths (according to magnetic and bathymetric data), earthquake slip vectors (using focal mechanisms) and relative plate motion models (a.k.a., plate circuits) [DeMets et al., 1990].

Different methods are required to investigate past plate motions. The most widely accepted observations include stratigraphic correlations, biogeographic affinities, paleoclimatic proxies, marine magnetic lineations and fracture zones, paleomagnetism, hotspot records and slab distribution. However, quantitative restorations (requiring rotation poles and angles) of past plate motions can only be achieved through paleomagnetic, marine geophysical and hotspot data, all of which to some extent require retrieving records of the ancient geomagnetic field.

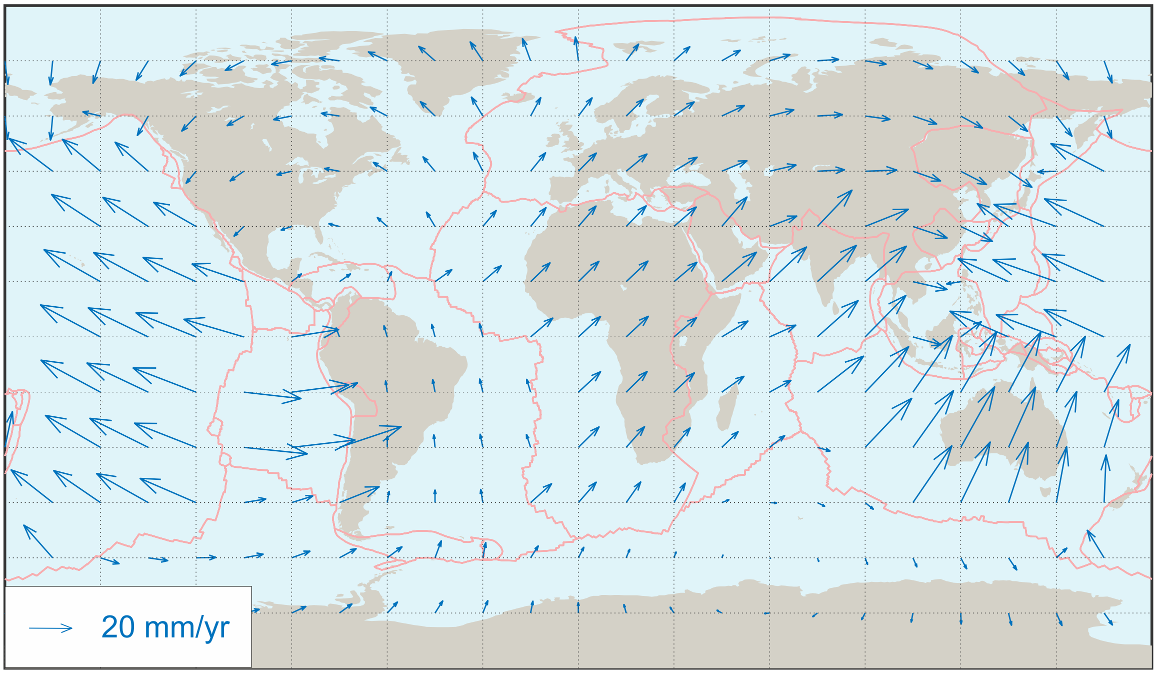

Figure 1.1: The current horizontal plate motion vectors in the no-net-rotation reference frame predicted by the global model NUVEL-1 [DeMets et al., 1990]. Pink lines denote the present-day plate boundaries [Bird, 2003].

1.1 Magnetic field of the Earth

Understanding the basic physics of the present-day geomagnetic field is essential before we jump into the application of paleomagnetic field vectors for plate tectonics. The geomagnetic field is generated by electric currents in the convecting liquid outer core, which is driven by heat flow from the cooling of the inner core. The geomagnetic field vector (H) on the Earth's surface can be decomposed into three components: geographic north (H_N), geographic east (H_E) and vertically downward (H_V) components. Inclination (I) and declination (D) can then be computed from the following equations [e.g., Gubbins and Herrero-Bervera, 2007],

$$I = \arctan \frac{H_V}{\sqrt{H_N^2 + H_E^2 + H_V^2}}, \qquad D = \arctan \frac{H_E}{H_N} \tag{1.1}$$

The geomagnetic field on the Earth's surface is varying with time (t) and location ($90^o - \theta$, ϕ), which can be mathematically described by the spherical harmonic expansion:

$$H(r, \theta, \phi, t) = R_E \sum_{n=1}^{N} \sum_{m=0}^{n} (\frac{R_E}{r})^{n+1} \times [g_n^m(t) \cos(m\phi) + h_n^m(t) \sin(m\phi) P_n^m(\cos\phi)] \tag{1.2}$$

where r is the radial distance from the center of the Earth; R_E is the mean radius of the Earth (6371.2 km); g_n^m and h_n^m are the Gauss coefficients, with n and m being degree and order of the expansion respectively; $P_n^m(\cos\phi)$ is the Schmidt quasi-normalized associated Legendre polynomials. The International Geomagnetic Reference Field (IGRF), updated every five years, is a model to predict the temporal variation of the Gauss coefficients.

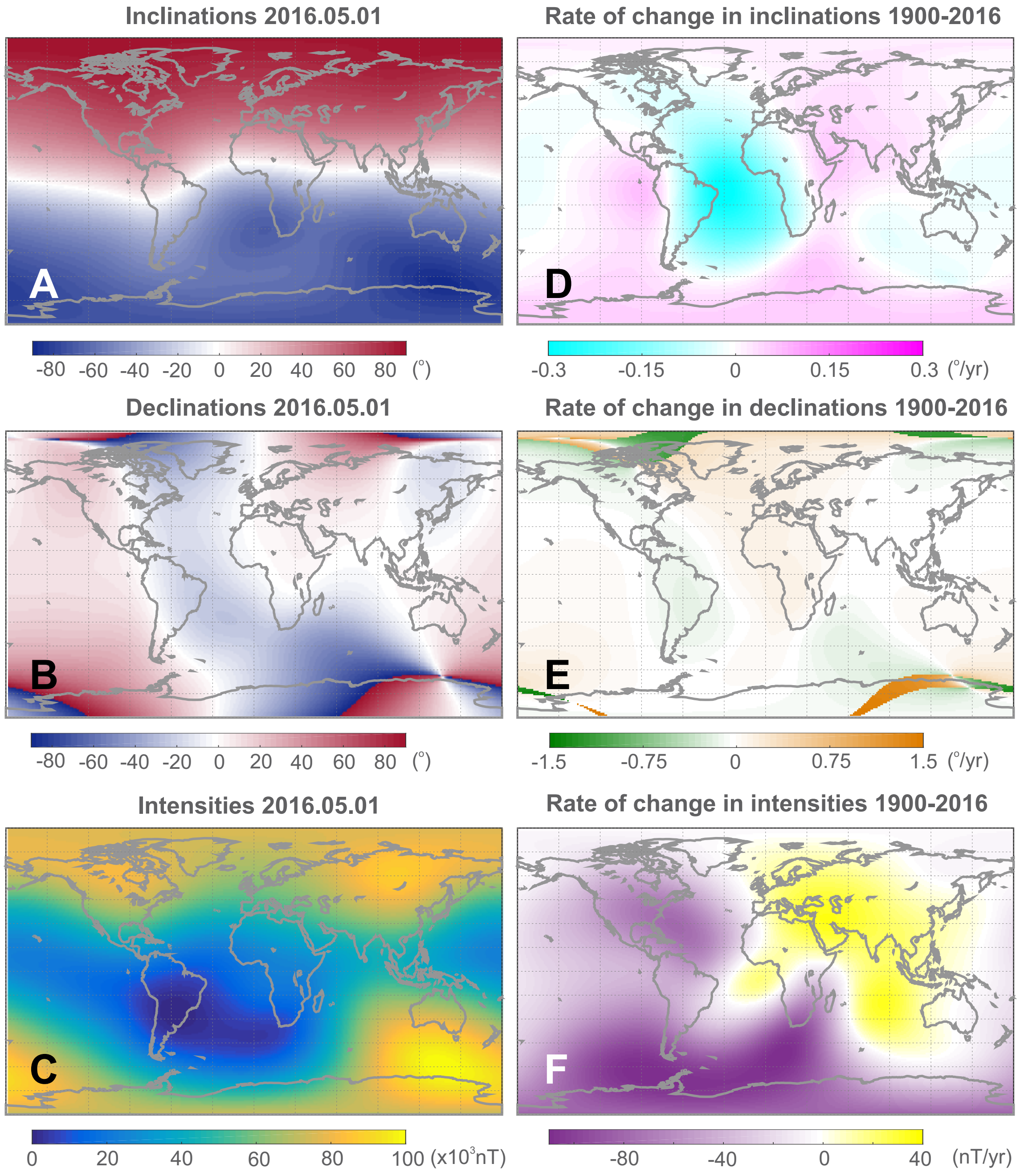

Figure 1.2: Spatial and temporal variations of the geomagnetic field according to the IGRF-12 [Finlay et al., 2015]. (A-C) Contours of global magnetic inclinations, declinations and intensities on the date of 2016.05.01. (D-F) Rate of change in global magnetic inclinations, declinations and intensities between 1900.05.01 and 2016.05.01.

The geomagnetic field on the Earth's surface has been varying with time and location. Figure 1.2 shows the spatial and temporal variations of the geomagetic field predicted by the latest release IGRF-12 [Finlay et al., 2015]. On the date of 2016.05.01, the magnetic equator is largely deformed southward in northern South America with the northern magnetic pole being located in the Canadian Arctic (Figure 1.2A). The global magnetic declinations display a banded appearance with the largest deviations from the meridians around the geomagnetic poles at high latitudes (Figure 1.2B). The most noticeable feature in the global intensity map is the South Atlantic Anomaly where the magnetic intensities are lowest (Figure 1.2C).

The temporal variations of the geomagnetic field are evaluated from the rate of change in the field vectors between 1900.05.01 and 2016.05.01. The fastest changes in inclinations occurred in the South Atlantic ($\sim -0.3^o/yr$) (Figure 1.2D), while declinations varied most speedily around the magnetic poles ($\sim \pm 1.5^o/yr$) (Figure 1.2E). The magnetic intensities have been continuously drifting westward and decreasing since 1900 [Finlay et al., 2015]: except Eurasia, north Africa and the Indian Ocean, most parts of the world exhibit a steady reduction in field intensities since 1900 A.D. (Figure 1.2F).

Such tempo-spatial variations in the geomagnetic field are better illustrated from the evolving geographic coordinates of the geomagnetic north pole (a.k.a., magnetic dip north pole) since 1900 A.D., which are the locations with the magnetic field pointing vertically downwards (Figure 1.3). There has been an accelerating westward drift of the geomagnetic north pole since 1900 A.D. In contrast, there have been relatively steady changes in the locations of the geomagnetic north dipole, which are the intersection points between the tilted axis of a geocentric magnetic dipole and a sphere with the radius of R_E. The differences between the two types of poles reflect the evolving contributions of the non-dipolar components (e.g., quardrupole, octupole). For reconstructing past plate motions, however, we are interested in the relatively stable dipolar component which proves to be even more stable in the geologic time scale.

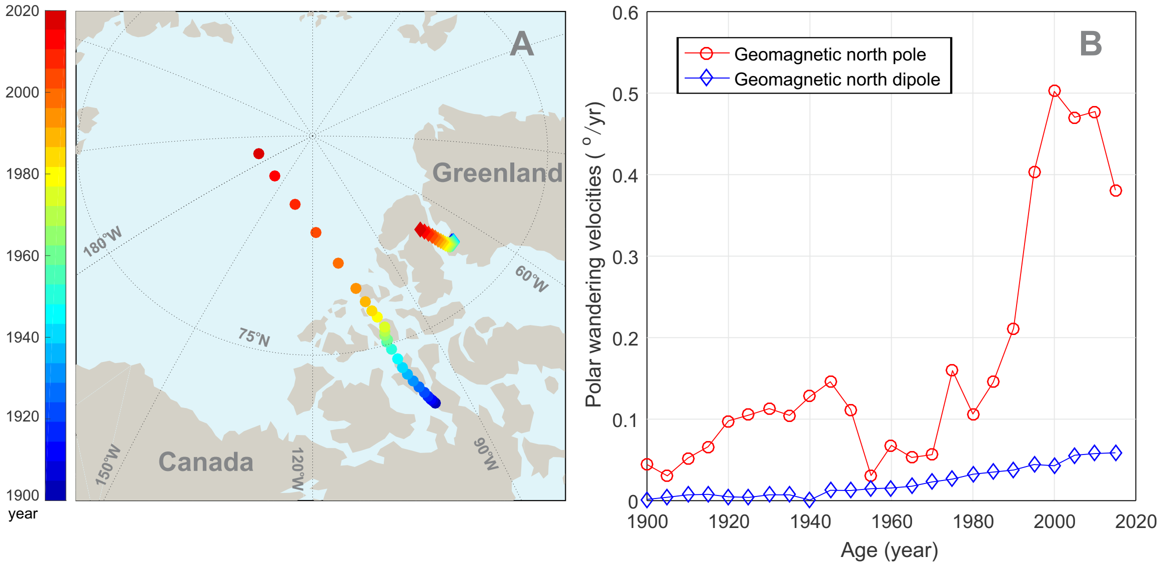

Figure 1.3: Spatial variations (A) and wandering velocities (B) of the geomagnetic north dipole (diamonds) and geomagnetic north pole (circles) since 1900 A.D. according to the IGRF-12 [Finlay et al., 2015].

1.2 Paleomagnetism and continental drift

Irving [1956] reported the first polar wandering data from northwest Europe before the Cenozoic, from which he suggested the physical mechanism for continental drift. The most important assumption for this conclusion is that the geocentric axial dipole (GAD) has been placed at the center of the Earth and aligned with the spin axis [Irving, 1964]. Under this assumption, it is continents rather than the geomagnetic poles, i.e., the Earth's spin axis, that have been moving throughout the geologic history. The paleo-colatitude (θ) for any point of interest can thusly be computed from the recorded ancient inclination (I):

$$\tan I = 2 \cot \theta \tag{1.3}$$

Opdyke and Henry [1969] validated the GAD model for the past 2 Myr by confirming the above relation between the paleo-colatitudes and mean inclinations for the cores collected from the world-wide oceans. Evans [1976] justified the effectiveness of this GAD assumption throughout the Phanerozoic.

Figure 1.4 illustrates the traditional paleomagnetic approach for plate reconstructions. Assuming that the Earth's spin axis has been fixed since 240 Ma, the ancient locations of North America can be restored by rotating the paleo-pole back to the position of the spin axis around an Euler pole, that is centering on a great circle defined by the plane where the paleo-pole and spin axis are located. After rotation, the restored reference site Edmonton at

240 Ma maintains the same colatitude (computed from the paleomagnetic inclination) with the transferred paleo-poles (i.e., the Earth's spin axis), and the reconstructed North America displays the ancient azimuthal orientation with respect to the present-day meridians by unwrapping the recorded paleomagnetic declination. Note, however, that paleolongitudes cannot be constrained from this traditional paleomagnetic reconstruction method, because the recorded paleo-pole at 240 Ma remains the same even if we rotate the restored North America around the spin axis. This 'freedom' to place the studied plates 'anywhere' along the paleo-parallels leads to uncertainties and artifacts in the traditional paleomagnetic reconstructions.

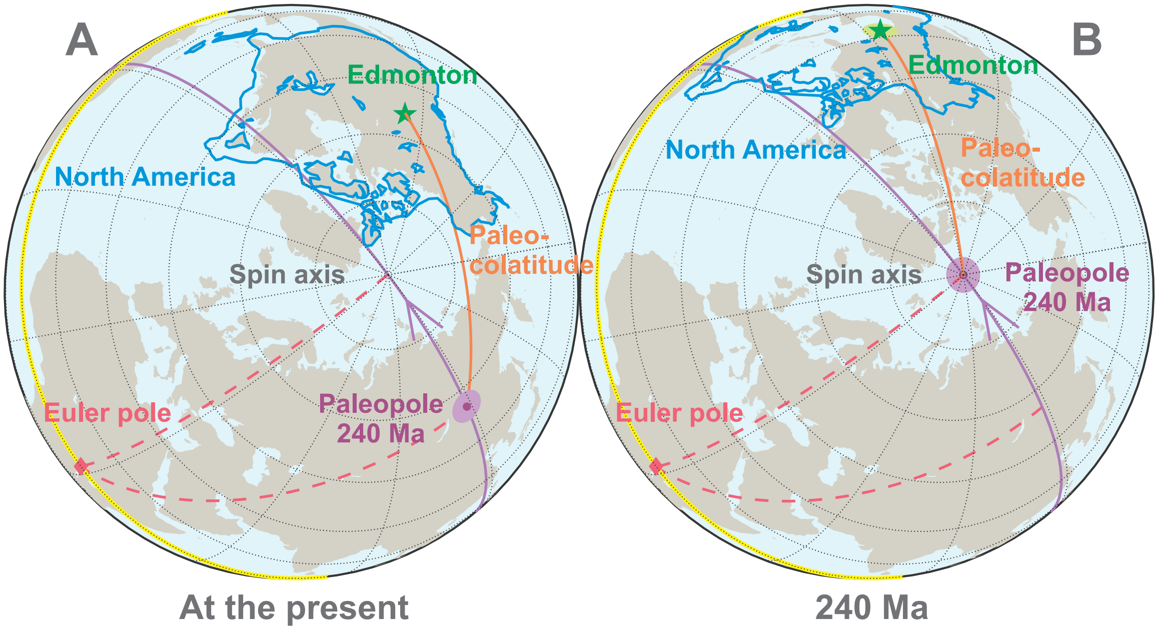

Figure 1.4: Reconstruction of North America back to 240 Ma from paleomagnetic pole of Torsvik et al. [2012]. (A) Blue contours and green star show the present-day geographic locations of North America and Edmonton. Purple dot and circle show the North America paleopole and the corresponding error at 240 Ma. Orange line is the great circle arc (i.e., paleo-colatitude) that connects Edmonton and the paleopole. Purple line highlights the great circle arc connecting the paleopole and the Earth's spin axis, from which the Euler pole (red diamond) is calculated. The angle between the red dashed lines shows the angle to rotating the paleo-pole back to the spin axis (purple arrow marks this rotation direction). Yellow line denotes the geographic equator on which Euler poles derived from this traditional paleomagnetic-based method are unexceptionally located. (B) The reconstructed North America and Edmonton at 240 Ma, by tracing the paleo-pole back to the spin axis based on the GAD model.

1.3 Oceanic survey and seafloor spreading

Evidence from oceanic survey, especially magnetic and bathymetric (i.e., the study of underwater depth) surveying, provides the kinematic mechanism for the motions of the global seafloor. Using the geomagnetic polarity time scale for the last 4 Myr established from paleomagnetic and radiometric dating results obtained from continents, Vine and Matthews [1963] proposed the hypothesis of seafloor spreading from the total magnetic field records over their studied oceanic ridges, whose polarities and intensities were preserved in the oceanic basalts formed at ocean ridges. The resultant estimation of rate of seafloor spreading provided the first evidence to quantify the kinematics of past plate motions.

Figure 1.5 illustrates, in the case of the Juan de Fuca plate, how to constrain motions of seafloor from the magnetic anomaly and fracture identifications. Figure 1.5A shows the total magnetic field anomalies to the west of the North American plate. The motion history of the Juan de Fuca plate can be derived from the central (positive) anomaly associated with the axis of the Juan de Fuca Ridge and the striped pattern of anomalies to its sides, which are offset by fracture zones (describing the flowlines of conjugate plates) disclosed from the bathymetric data (Figure 1.5B). The half spreading rate of the Juan de Fuca Ridge can be computed from the width of the surrounding magnetic lineations and the reversal time scale [Vine, 1966].

To quantitatively restore the temporal evolution of oceanic crust, conjugate isochrons constructed from magnetic crossings of equal ages and associated fracture zone segment intersections need to be rotated back to the central axes of ridges. The derived reconstruction parameters are commonly presented in the form of rotation poles and angles.

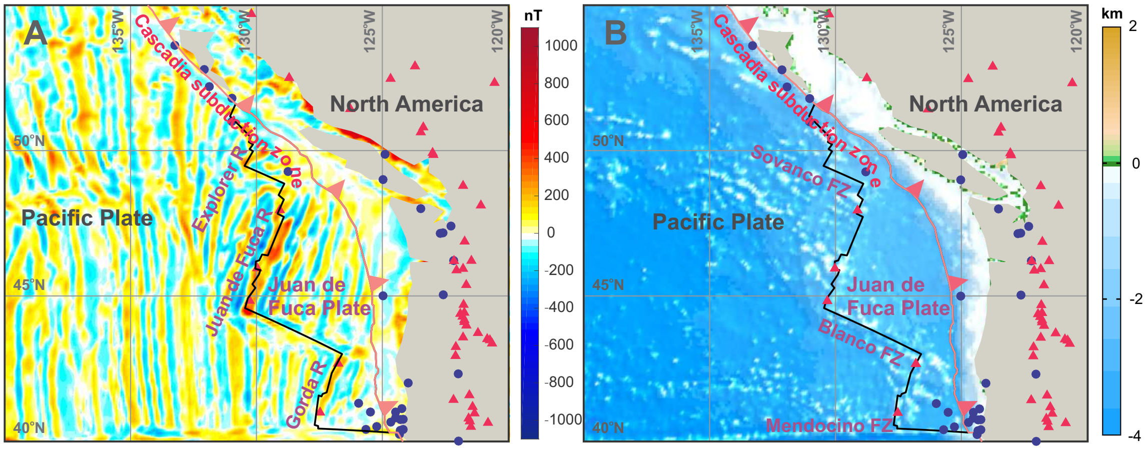

Figure 1.5: Seafloor spreading associated with the Juan de Fuca plate as disclosed from seafloor magnetic and bathymetric surveys. (A) Total intensity anomalies to the west of North America according to the model EMAG2 [Maus et al., 2009]. (B) Bathymetry in the same area determined from ETOPO2 (https://www.ngdc.noaa.gov/mgg/global/etopo2.html). Dark blue dots and red triangles represent the recorded earthquakes and volcanoes since 2150 B.C. (https://www.ngdc.noaa.gov/hazard/). Abbreviations: R - ridge, FZ - fracture zone.

1.4 Plate reconstruction techniques

1.4.1 Relative plate motion reconstruction methods

Relative plate motions (RPMs) are the motions of one lithospheric plate relative to another. They are usually presented in the form of rotation (or Euler) poles and angles. Bullard et al. [1965] derived the first set of rotation parameters for the Atlantic ocean from a least-square fitting of the conjugate continental edges (at 500 fathom = 914.4 metres) bounding the ocean. The limitation of this method is that it cannot determine the process of oceanic spreading during the study period. To overcome the difficulty, Hellinger [1981] developed a technique to find rotation parameters by minimizing the sum of the misfits between the conjugate magnetic crossings and fracture zone intersections. The uncertainties of the best-fit rotations from the least-squares regression are usually represented in the form of 3 × 3 covariance matrices in a coordinate system defined by longitude, latitude and rotation angle [Chang, 1987].

Figure 1.6 demonstrates the derivation of the Euler pole and rotation angle from a rotation group (u_i, v_i), i.e., the conjugate magnetic crossings and fracture zone intersections in the Gulf of Aden, from the spherical regression [Chang, 1987]. Let $\mathbf{R}$ be the true rotation and a 3×3 matrix.

$$v_i = \mathbf{R} u_i \tag{1.4}$$

Let $\tilde{\mathbf{R}}$ be an estimate of $\mathbf{R}$. The best-fit rotation $\tilde{\mathbf{R}}$ can be found by minimizing the sum of the squares of the errors:

$$\sum |v_i - u_i|^2 = \sum (v_i - \tilde{\mathbf{R}} u_i)^t (v_i - \tilde{\mathbf{R}} u_i)] \tag{1.5}$$

The rotation parameters $\mathbf{h} = (h_1, h_2, h_3)^t$ can be derived from the matrix $\mathbf{R}^t \tilde{\mathbf{R}} = \Phi(\mathbf{h})$, such that the direction and magnitude of $\mathbf{h}$ represent the axis and the rotation angle of $\Phi(\mathbf{h})$, respectively [Chang, 1987].

$$\Phi(\mathbf{h}) = \mathbf{I} + \frac{\sin ||\mathbf{h}||}{||\mathbf{h}||} M(\mathbf{h}) + \frac{1 - \cos ||\mathbf{h}||}{||\mathbf{h}||^2} M(\mathbf{h})^2 \tag{1.6}$$

where $||\mathbf{h}||$ is the magnitude of $\mathbf{h}$, $\mathbf{I}$ is the identity matrix and M($\mathbf{h}$) is defined as

$$M(\mathbf{h}) = \begin{pmatrix} 0 & -h_3 & h_2 \\ h_3 & 0 & -h_1 \\ -h_2 & h_1 & 0 \end{pmatrix} \tag{1.7}$$

The error of $\mathbf{h}$ is calculated from

$$cov(\mathbf{h}) = \frac{rH^{-1}_{11\cdot 2}}{N-2s-3} \tag{1.8}$$

where N is the total number of crossings and fracture zone intersections, s is the number of model isochron segments, r is the sum of squared and weighted misfits between the data and the model isochron, $H^{-1}_{11\cdot 2}$ is the upper-left 3×3 submatrix of the matrix $(\mathbf{X}^T\mathbf{X})^{-1}$, and $\mathbf{X}$ is the design matrix of the regression [Chang, 1988].

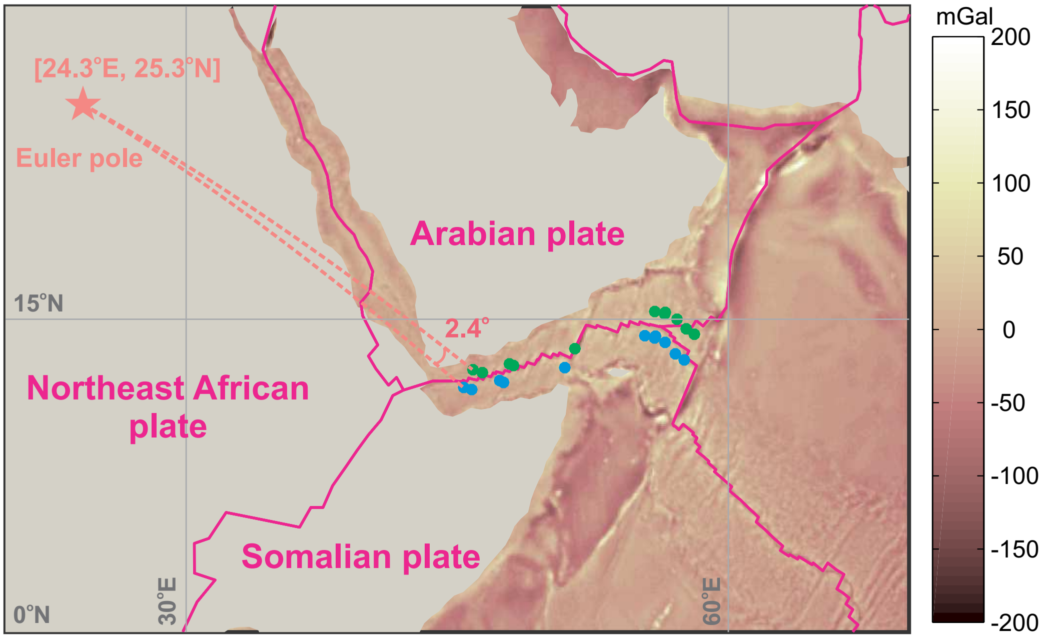

Figure 1.6: Relative plate motions between the Arabian plate and the Somalian plate in the last 20 Myr determined from the spherical regression method. The coordinates of Euler pole and rotation angle are computed from the conjugate crossings and fracture zone intersections ($[u_i, v_i]$, blue and green dots) in the Gulf of Aden [Chang, 1987]. The errors of the Euler parameters are not shown for clarity. The background map shows the free-air anomalies [Balmino et al., 2012] and the present-day plate boundaries [Bird, 2003].

Uncertainty for the reconstructed moving point $\mathbf{m} = (m_1, m_2, m_3)^t$ using the rotation $\tilde{\mathbf{R}}$ is determined from

$$cov(\tilde{\mathbf{R}}\mathbf{m}) = \tilde{\mathbf{R}}M(\mathbf{m})cov(\mathbf{m})M(\mathbf{m})^t\tilde{\mathbf{R}}^t \tag{1.9}$$

According to Chang et al. [1990], rotations can be combined in the following way

$$\tilde{\mathbf{R}}_{1\to n} = \tilde{\mathbf{R}}_{(n-1)\to n}\tilde{\mathbf{R}}_{(n-2)\to(n-1)} \cdots \tilde{\mathbf{R}}_{2\to 3}\tilde{\mathbf{R}}_{1\to 2} \tag{1.10}$$

with the associated uncertainties of

$$cov(\mathbf{h}_{1\to n}) = \tilde{\mathbf{R}}^T_{1\to(n-1)} cov(\mathbf{h}_{(n-1)\to n}) \tilde{\mathbf{R}}_{1\to(n-1)} + cov(\mathbf{h}_{1\to(n-1)}) \tag{1.11}$$

RPM models have broad applications in plate tectonic studies, such as 1) transferring paleo-poles from one plate to another for apparent polar wander path (APWP) constructions [e.g., Besse and Courtillot, 2002; Schettino and Scotese, 2005; Torsvik et al., 2008a], 2) integrating rotation parameters of hotspot tracks from different oceanic plates into a common hotspot reference frame [e.g., Müller et al., 1993; O'Neill et al., 2005; Doubrovine et al., 2012], 3) determining the ages of the world's oceanic lithosphere [e.g., Müller et al., 2008], and 4) providing surface boundary conditions for the time-dependent mantle convection modelling [e.g., Steinberger et al., 2004].

Figure 1.7A shows the restored supercontinent 'Pangea' at 250 Ma, based on the combination of the RPM models and the rotation parameters determined from the 250 Ma paleomagnetic pole of South Africa [Torsvik et al., 2012]. The rotation parameters are organized in a hierarchy such that plates on the designated plate circuits can be reconstructed with respect to the anchored plate(s) without having to use their own rotation parameters (Figure 1.7B). To construct such rotation files, the unique plate IDs need to be identified for the studied plates. In this thesis, most of plate geometries and the associated IDs can be obtained from in the freeware GMAP (http://www.earthdynamics.org/resources.html) and PaleoMac (http://www.ipgp.jussieu.fr/∼cogne/pub/paleomac).

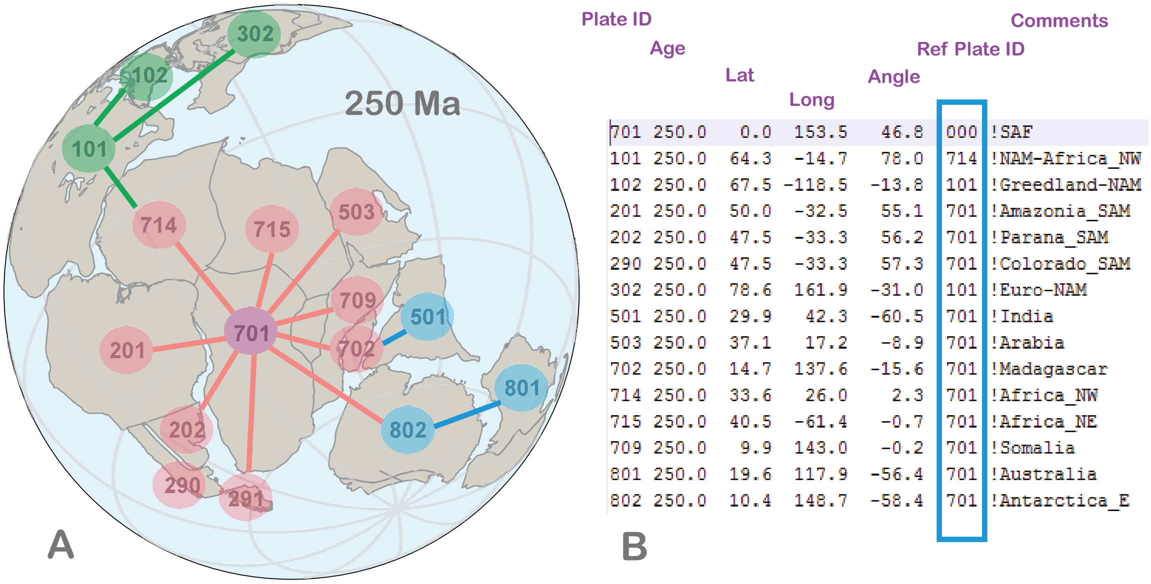

```
701 250.0   0.0  153.5   46.8  000 !SAF
101 250.0  64.3  -14.7   78.0  714 !NAM-Africa_NW
102 250.0  67.5 -118.5  -13.8  101 !Greedland-NAM
201 250.0  50.0  -32.5   55.1  701 !Amazonia_SAM
202 250.0  47.5  -33.3   56.2  701 !Parana_SAM
290 250.0  47.5  -33.3   57.3  701 !Colorado_SAM
302 250.0  78.6  161.9  -31.0  101 !Euro-NAM
501 250.0  29.9   42.3  -60.5  701 !India
503 250.0  37.1   17.2   -8.9  701 !Arabia
702 250.0  14.7  137.6  -15.6  701 !Madagascar
714 250.0  33.6   26.0    2.3  701 !Africa_NW
715 250.0  40.5  -61.4   -0.7  701 !Africa_NE
709 250.0   9.9  143.0   -0.2  701 !Somalia
801 250.0  19.6  117.9  -56.4  701 !Australia
802 250.0  10.4  148.7  -58.4  701 !Antarctica_E
```

Figure 1.7: Topology of plate circuits centering on South Africa. (A) The reconstructions of the major Pangea continents are determined on the combination of the South Africa APWP pole at 250 Ma and the plate circuits of Torsvik et al. [2012]. The major Laurentia, West Gondwana and East Gondwana continents are highlighted in green, red and blue fonts respectively. Plate ID: 101 - North America, 102 - Greenland, 201 - South America, 202 - Parana, 290 - Salado, 291 - Colorado, 320 - Europe, 501 - India, 503 - Arabia, 701 - South Afria, 702 - Madagascar, 709 - Somalia, 714 - Northwest Africa, 715 - Northeast Africa, 801 - Australia, 802 - East Antarctica. (B) Screenshot of the rotation file in the software GPlates (http://www.gplates.org/) to reproduce the plate configuration shown in (A). The plate circuits in effect are highlighted in the sixth column.

1.4.2 Absolute plate motion reconstruction methods

Absolute plate motions (APMs) are motions of a plate relative to some presumably fixed reference points. Hotspots are commonly used as reference points to constrain past plate motions. Müller et al. [1993], for instance, presented one of the widely cited hotspot reference frames by deriving the 'best-fit' rotations of the major plates from the well-dated hotspot tracks in the Atlantic-Indian Ocean. Wessel and Kroenke [1997] proposed a 'hot-spotting' technique to restore the past motions of oceanic plates from seamounts on the seafloor using their geometries. Both methods assume that hotspots have not been moving in the geologic history, which is not supported by 1) the paleomagnetic observation for the formation of the Emperor seamounts associated with the Hawaiian hotspot [e.g., Tarduno and Cottrell, 1997] and 2) the geodynamic modellings for the motions of plume conduits responsible for the hotspot tracks used for constructing APM models [e.g., Steinberger, 2000]. Such non-fixity of hotspots are commonly tackled by correcting their motions using mantle convection modelling [O'Neill et al., 2005; Doubrovine et al., 2012].

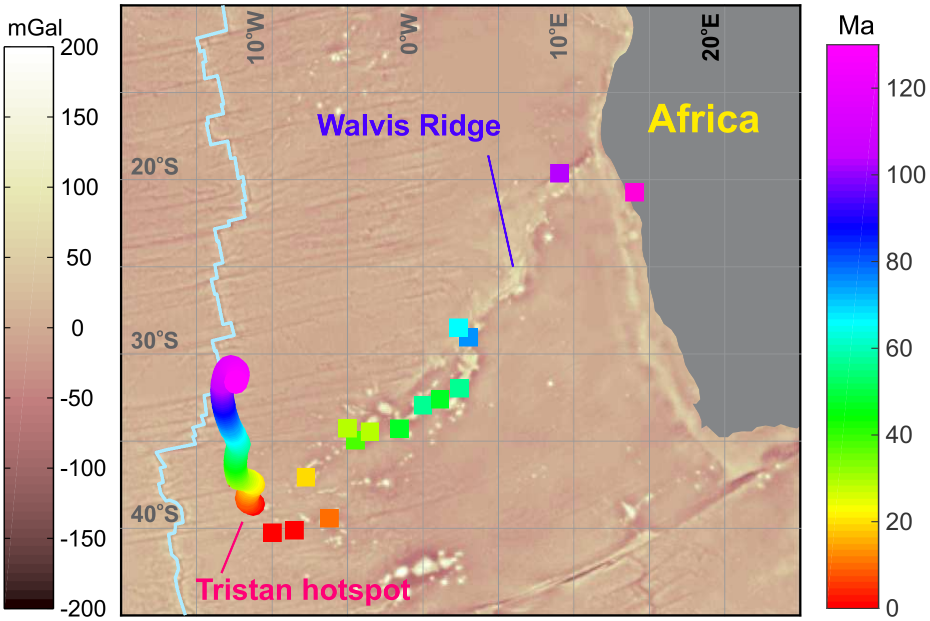

Figure 1.8: Basic elements for constructing a moving hotspot reference frame [Doubrovine et al., 2012]. The color-coded squares mark the locations of dated basalts along the hotspot track (Walvis Seamount Chain) that was sourced from the Tristan hotspot. The color-coded circles are the modeled hotspot motions during the last 130 Myr. The background map shows the free-air anomalies [Balmino et al., 2012] with the present-day plate boundaries [Bird, 2003].

Figure 1.8 uses the data from Doubrovine et al. [2012] to demonstrate the general procedures for deriving moving hotspot frames. Compared with the conjugate data used in RPM studies (i.e., magnetic crossings and fracture zone intersections), here coordinates of hotspots versus those of isochron points (i.e., points along different hotspot tracks with the same ages), and geometry of a single hotspot track versus position of the source hotspot corrected for plume motions are used as the conjugate data sets (u_i, v_i), to which a least-squares regression is applied to derive the best-fit rotation parameters for a studied plate. At least two hotspot tracks from a single plate are needed to derive its 'best-fit' rotations.

As indicated from the ages of the global seafloor [Müller et al., 2008], most of the oceanic crust was formed after 130 Ma, with the exceptions in the west Pacific, north Atlantic and Mediterranean (Figure 1.9). This results in an upper prediction limit for hotspot reference frames because few hotspot tracks older than the Early Cretaceous have been recognized.

Alternative 'fixed references' are proposed to extend the reconstructions of the global lithospheric plates beyond the hotspot records. For instance, Africa is commonly suggested as the reference plate because 1) it experienced the least longitudinal motions and 2) it has been surrounded by spreading ridges after the breakup of Pangea [e.g., Torsvik et al., 2008a]. Another widely used reference is the Earth's spin axis (a.k.a., the axis of the maximum moment of inertia), whose motion trajectory in the geologic history is usually referred as true polar wander (TPW). TPW can be estimated from the ancient mass centers of the global continents (i.e., the axes of the minimum moments of inertia) determined from plate reconstructions [e.g., Steinberger and Torsvik, 2008; Mitchell et al., 2012; Greff-Lefftz and Besse, 2014]. Despite the controversy [e.g., Anderson and King, 2014], deep mantle structures, especially the antipodal large large low shear-velocity provinces (LLSVPs) at the D" layer beneath Africa and Pacific are suggested as a long-term reference to constrain longitudes for the potentially deep-rooted large igneous provinces (LIPs) [e.g., Burke and Torsvik, 2004; Torsvik et al., 2008b]. In addition, there is a recent trend to use descending slabs in the mantle as references to constrain absolute plate motions [e.g., van der Meer et al., 2010]. In this method, the age frame for the sinking slabs at different depths of the mantle needs to be defined and correlated with the past plate motions.

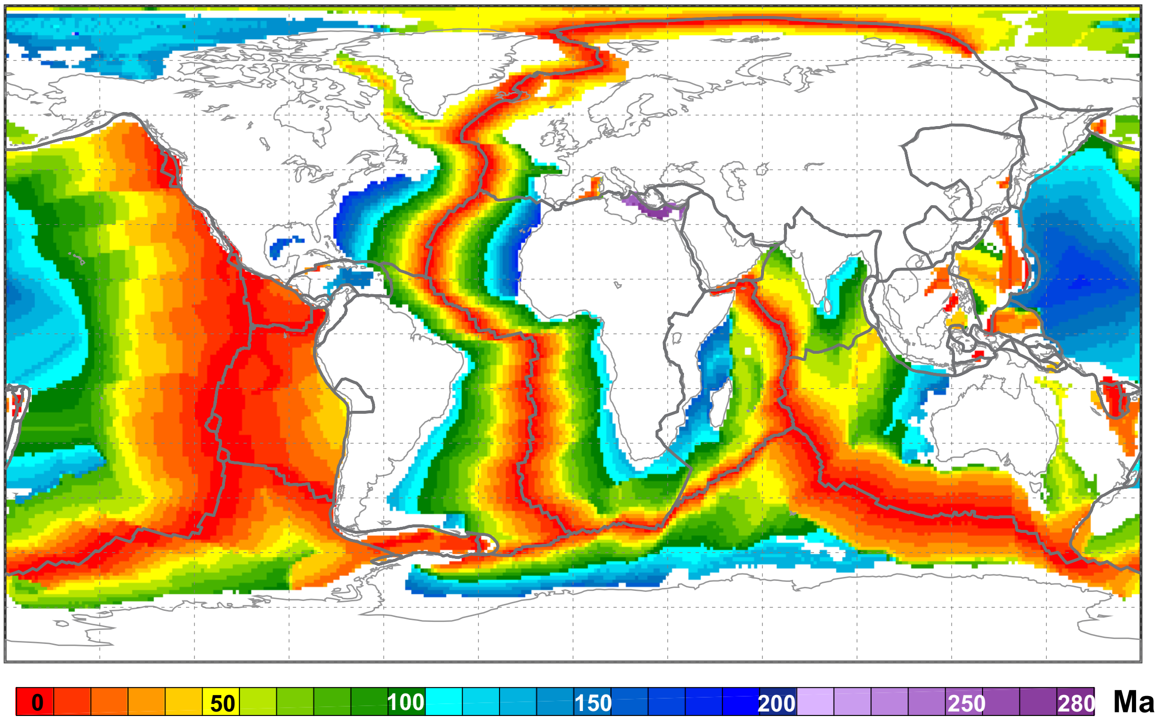

Figure 1.9: Ages of the global oceanic floor [Müller et al., 2008]. Grey lines show the present-day plate boundaries [Bird, 2003].

1.5 Objectives and structure of the thesis

Figure 1.10 shows the reconstructions of a reference point in stable Europe from various APM models that are widely adopted by the geoscience community for plate reconstructions. These models include 1) the fixed hotspot frame in the coordinates of North America (M93:

0-130 Ma, interpolated with an increment of 10 Myr) [Müller et al., 1993], 2) the global moving hotspot frame in the coordinates of stable Europe (D12: 0-120 Ma) [Doubrovine et al., 2012], 3) the sinking slab frame in the coordinates of South Africa (M10: 0-260 Ma) [van der Meer et al., 2010], 4) the paleomagnetically derived true polar wander (TPW) frame in the coordinates of stable Europe (M12: 0-260 Ma) [Mitchell et al., 2012], 5) the global hybrid frame in the coordinates of South Africa (T12: 0-260 Ma) [Torsvik et al., 2012], and 6) the TPW-corrected global hybrid frame in the coordinates of South Africa (T12-TPW: 0-260 Ma) [Torsvik et al., 2012]. For the APM models not presented in the coordinates of stable Europe, (part of) the plate circuit of stable Europe - North America - Northwest Africa - South Africa [Torsvik et al., 2012] is used to transfer the finite rotation parameters.

Overall, all these APM models predict a northeastward motion for the reference point in stable Europe during the last 40 Myr (Figure 1.10). Comparable plate motion directions and velocities are evident for paleomagnetic frames (i.e., T12 and T12-TPW, both in the moving hotspot frame) until 60 Ma (Figures 1.10-1.11). Significant deviations arise among different APM model determinations earlier than 70 Ma when high-quality hotspot traces and age progression determinations become scarce. Similar observations are reported for various APM model determinations in the coordinates of South Africa since 130 Ma (i.e., the lowest limit of the hotspot frame predictions) [Williams et al., 2015]. I deem that the reconstruction discrepancies among the APM models for the last 130 Myr primarily stem from 1) the different references for reconstructions: the 'entire Earth' for the hotspot frames [Doubrovine et al., 2012] and the Earth's spin axis for the paleomagnetic frame [Torsvik et al., 2012], 2) the uncertainties of hotspot frames coming from the different selections of RPM models and the various geodynamic modelled hotspot motions, 3) the errors propagated in transferring rotations using different plate circuits (with varying reliability), 4) the uncertainties in slab characterizations using diverse tomography models and geodynamic modelling methods, 5) the uncertainties in the TPW estimates, and 6) any combinations of the above possibilities.

For the ages earlier than 130 Ma, there are substantial discrepancies between the different APM model predictions (Figures 1.10-1.11). We note that the paleo-longitudes from these models are predicted in the common paleomagnetic frames (without strict longitudinal determinations) [Torsvik et al., 2008a, 2012]. These models are constructed through some anchor points speculated from either slab identifications [van der Meer et al., 2010] or TPW estimates [Mitchell et al., 2012; Torsvik et al., 2012] without proper error propagations for the causes discussed above. For instance, the current estimates of TPW behavior are usually derived from the absolute plate motions of the global plates, for which some poorly-studied plates such as the central-eastern Eurasian plates are assumed to have moved as a unity with stable Europe starting from the Triassic.

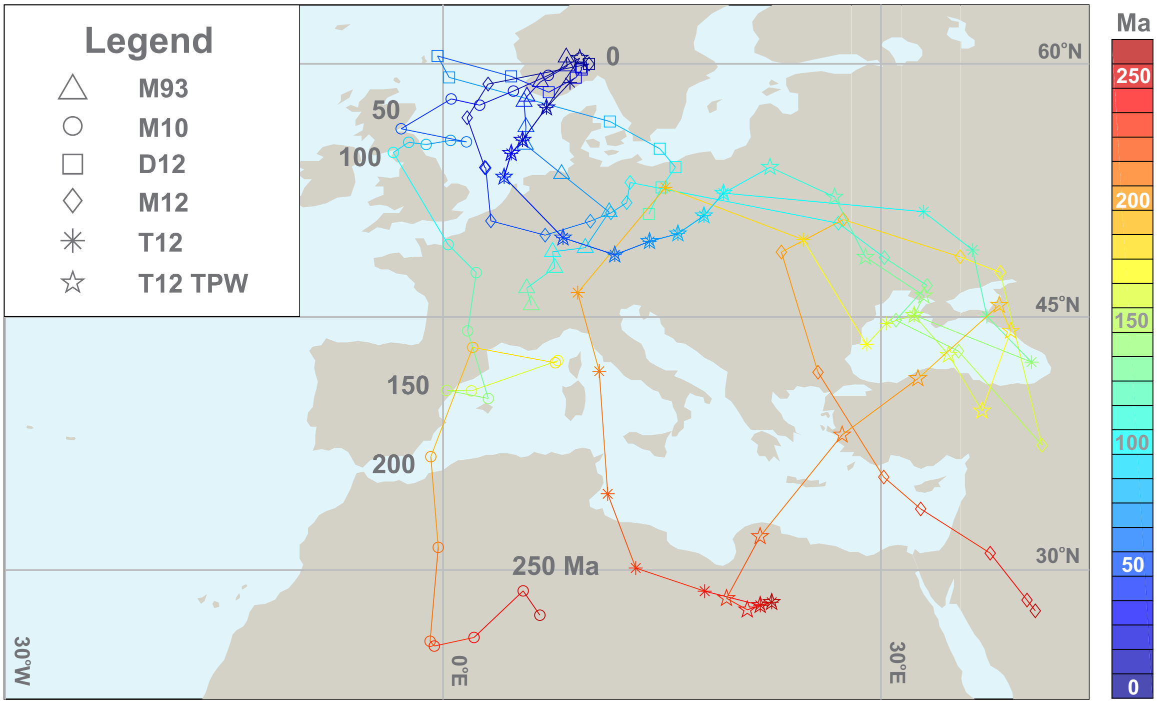

Figure 1.10: Reconstructions of a reference site in Europe for the last 260 Myr predicted from different APM models: M93 [Müller et al., 1993], D12 [Doubrovine et al., 2012], M10 [van der Meer et al., 2010], M12 [Mitchell et al., 2012], T12 [Torsvik et al., 2012], and T12-TPW [Torsvik et al., 2012]. The reconstructions are shown in a color-coded manner to represent paleo-positions different ages. Different symbols represent predictions from different APM models.

The objectives of this thesis are evident from the overview of plate reconstruction methods:

1. To develop a new method to overcome the longstanding challenge of extracting paleolongitudes from paleomagnetic data. The resultant reconstructions should be self-consistent and compatible with independent geologic and geophysical observations.
2. To present this new method in the form of computer application, such that it is accessible both to paleomagnetists and geoscientists without special training in paleomagnetism.
3. To apply the new method to provide new insights to the slab distribution disclosed from seismic studies. To this end, a new and viable approach, primarily based on paleomagnetic and seismic observations, should be formulated to quantitatively link the surface plate tectonics with mantle dynamics.

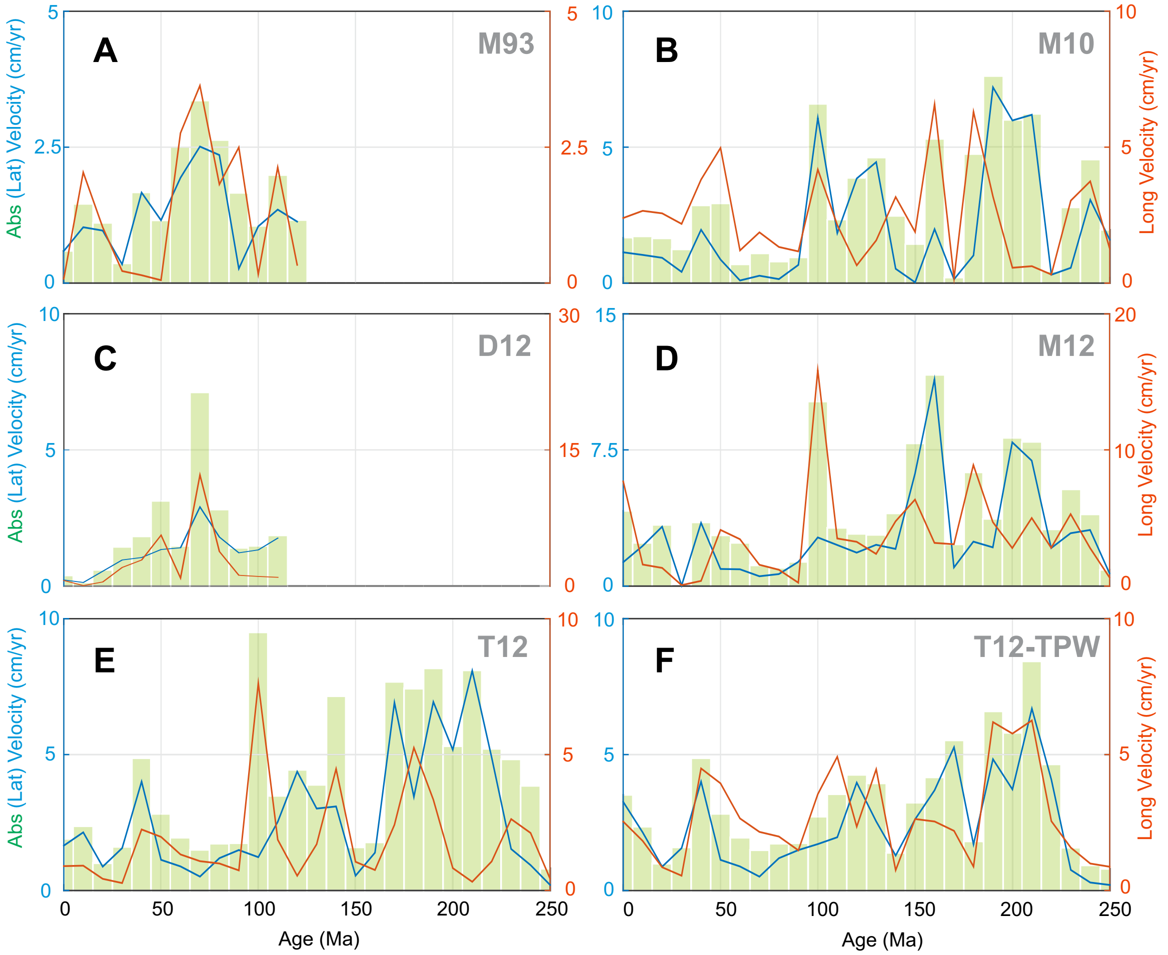

Figure 1.11: Kinematic predictions for the reference site in stable Europe from various APM models. Absolute velocities (green bars) and two orthogonal velocity components (latitudinal and longitudinal components in blue and orange solid lines respectively) are shown here.

To address the above questions, the thesis is organized as follows:

- Chapter 1 explains the significance of plate reconstructions both in theory and applications. The basic concepts and methods associated with plate reconstructions are then reviewed. The motivations and objectives are articulated through the discussion of the discrepancies among the current APM methods.

- Chapter 2 focuses on the formulation of a new algorithm to perform APM reconstructions from paleomagnetic data. The effectiveness of the new technique is attested by restoring the motion history of the east Gondwanaland since the 130 Ma, when the predictions from hotspot reference frames are available for comparison.

- Chapter 3 presents a new Matlab-based toolbox 'PMTec' to implement the reconstruction method proposed in Chapter 2. The data management and potential applications of PMTec are demonstrated with the published data.

- Chapter 4 applies the proposed technique to reconstruct the closing of the Mongol-Okhotsk Ocean in the Mesozoic. The chapter also explores quantitatively the correlations between the past motions of Siberia and North China-Amuria and the slab distribution underneath Eurasia.
- Chapter 5 quantifies the linear dependence between the slab distribution underneath Eurasia and the variations in the surficial geoid height. Based on such correlations, new insights are provided on the genesis of the India-Eurasia geoid low.
- Chapter 6 summarizes the major contributions of this thesis and proposes the future research directions.

2

Geometric parametrization of apparent polar wander path: on constraining paleolongitudes from paleomagnetic data [a]

2.1 Introduction

Quantitatively restoring the absolute motion history of the lithospheric plates has been one of the most long-standing challenges since the advent of plate tectonics. Assuming that hotspots are surficial expressions of plumes rising from the lower mantle [Morgan, 1971], absolute plate motions (APMs) can be derived from hotspot track geometries [e.g., Müller et al., 1993]. With the realization of the instability of hotspot plume [e.g., Tarduno, 2007], recent hotspot reference frames seem to be able to provide more compatible reconstructions with the independent geologic and geophysical observations during 0-130 Ma [e.g., O'Neill et al., 2005; Doubrovine et al., 2012]. For reconstructions earlier than 130 Ma, however, workers still need to use paleomagnetic data despite the complaints about its incapability in providing paleolongitude. Such paleomagnetic-based reference frames are usually constructed under certain assumptions, such the selection of the anchor plate that experienced the least longitudinal motions [Torsvik et al., 2008a].

In recent years, lots of effort has been devoted in quest of extending APM reconstructions beyond hotspot records. For instance, Torsvik et al. [2008a] present a global hybrid reference frame which combines a hotspot reference frame for the last 130 Ma and a paleomagnetic-based frame for the earlier ages. Torsvik et al. [2008b] propose an alternative APM method by correlating large igneous provinces and deep mantle heterogeneities at the core-mantle boundary. In this model, they assume the least longitudinal motions of Africa before 100 Ma which needs justification. van der Meer et al. [2010] established a sinking slab reference

---

[a] A version of this chapter has been published as:
Wu, L., Kravchinsky, V.A., 2014. Derivation of paleo-longitude from the geometric parametrization of apparent polar wander path: implication for absolute plate motion reconstruction. Geophysical Research Letters, 41(13): 4503-4511.

frame where APMs are restored according to the ancient subduction zones deduced from slab remnants in the lower mantle that are imaged from seismic tomography. As a result, up to 18° westward adjustments were proposed to the reconstructions in the global hybrid reference frame [Torsvik et al., 2008a]. Mitchell et al. [2012] present a true polar wander (TPW) reference frame through the mass centers of supercontinents in the geologic history estimated from paleomagnetic poles. Note that all these reference frames were constructed under some assumptions which are still open to debate. New methods independent of those assumptions are in great demand to constrain absolute plate kinematics.

Francheteau and Sclater [1969] make a first attempt to extract rotation poles from geometries of apparent polar wander paths (APWPs). Gordon et al. [1984] apply paleomagnetic Euler pole (PEP) for plate reconstructions by modelling APWP segments with best-fit small circles. The resulting rotation parameters are commonly presented as rotation pole positions and angles. Cox and Hart [1986] predict comparable predictions from hotspot models and PEP analysis, which was expected for APM reconstructions back to Precambrian. However, except for a few trials in constructing APWPs, which were not quite convincing because of the unjustified assumption of constant plate motion velocity over a geologic duration of 10-20 Myr [Van der Voo et al., 1993], applying PEP for APM reconstructions is still an under-developed research topic.

Recently, Smirnov and Tarduno [2010] apply PEP analysis for APM reconstructions using a case of restoring the eruption site of the Siberian traps back to 250 Ma. Using orientation matrices that are constrained from direction cosines of their European APWP, the authors adopt exclusively great circle and small circle fitting to their identified APWP tracks. We argue that such exclusive circle modelling cannot be a sound solution in all cases and that a combined great circle and small circle modelling determined from some optimization procedures should provide a more sensible solution. For instance, such optimal circle fitting can be decided from reliability of the resultant reconstructions, i.e. compatibility with the independent geologic and geophysical observations.

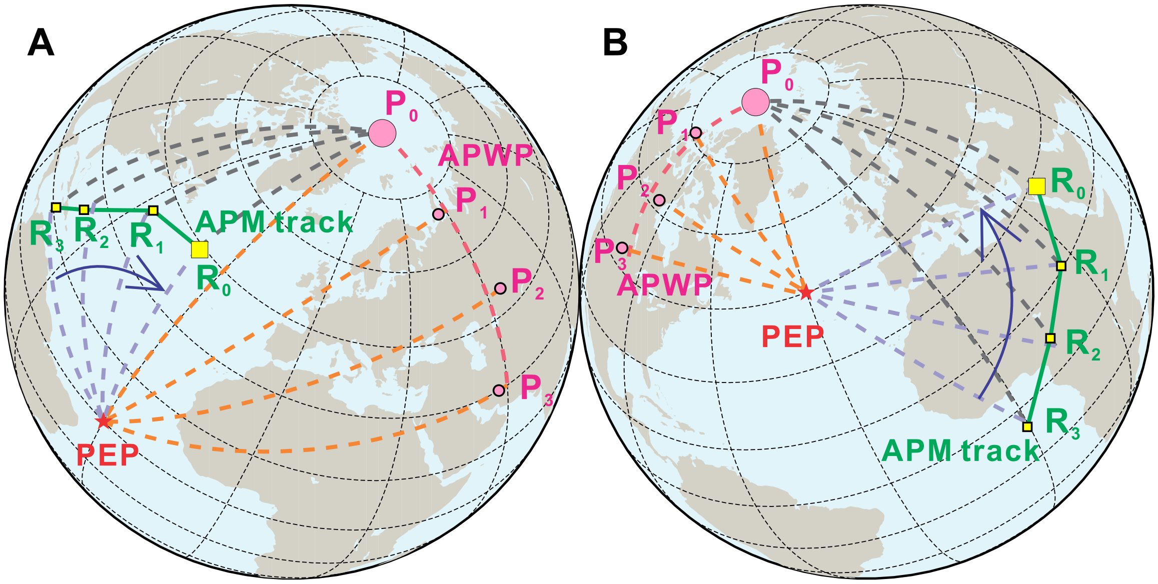

Figure 2.1: Illustration of absolute plate motion (APM) reconstructions from geometric parameterizations of apparent polar wander paths (APWPs). Paleomagnetic Euler pole (PEP, red star) and rotation angle (positive for counterclockwise rotation) can be computed by applying great circle (A) and small circle (B) fitting to a segment of APWP (P_0 to P_3, backward in time with P_3 the oldest pole). The restored APM track (R_0 to R_3, backward in time with R_3 the oldest position) can be computed as a result of Euler rotations and paleolatitude corrections. Such paleolatitude corrections use the paleomagnetic-based paleo-colatitudes as the spherical distances between reconstructions (i.e. R_0 to R_3) and the present-day pole (i.e. P_0).

Another issue associated with APM reconstructions from PEP method is that all reconstructions are restricted to lie along circle arcs centering on paleomagnetic Euler poles. This leads to accumulated errors in the resultant reconstructions in terms of paleo-colatitudes, which are the spherical distances between paleomagnetic poles and a selected point in the present-day geographic reference frame. To provide a solution, we suggest to use paleo-colatitudes as great circle distances between reconstructions and the youngest paleopole (Figure 2.1). The rationale behind such correction is that plates rather than the Earth's rotation axis (represented as trajectory of paleopoles) are considered to have moved throughout the geologic history.

In this chapter, we formulate a new method to extract rotation parameters from APWPs using great circle and small circle modelling. Paleo-colatitude corrections are then applied to the resultant reconstructions to ensure their paleolatitudes are compatible with paleomagnetic predictions. With the new method, we reconstruct the APM history for the East Gondwana continents, including India, Australia and East Antarctica, since 140 Ma. Together with results from the previous relative plate motion studies, our reconstructions shed new light on the separation history among the three continents. Similar predictions from other APM models are shown to quantitatively compare the differences among various methods.

2.2 Methodology

2.2.1 Circle parametrizations of apparent polar wander paths

To parametrize APWP segments for rotation parameters, Gordon et al. [1984] propose a best-fit small circle technique to find rotation centers, which minimize their sums of spherical distances from paleopoles along APWP tracks. This approach is based on a global search with a grid cell of 0.5° × 1°, and as a result it converges on the optimal solutions relatively slowly. To improve computation efficiency, here we apply an iterative algorithm of Fisher et al. [1987], where the optimal circle centers $\widehat{\boldsymbol{\Lambda}}'(x, y, z)$ (row vectors in the Cartesian coordinate system) are derived by minimizing the sums of squares of their angular distances (ψ_i) from the individual paleopoles $\widehat{\boldsymbol{\lambda}_\mathbf{i}}'(l_i, m_i, n_i)$ (direction cosines).

$$(l_i, m_i, n_i)\begin{pmatrix} x \\ y \\ z \end{pmatrix} = \cos\psi_i \tag{2.1}$$

To start the iteration, an initial estimate of circle center needs to be defined. Here we suggest to use Fisherian means $\widehat{\boldsymbol{\Lambda}}_0'(x_0, y_0, z_0)$ of paleopoles along APWP tracks.

$$x_0 = \frac{\sum\limits_{i=1}^{n} l_i}{R}, \quad y_0 = \frac{\sum\limits_{i=1}^{n} m_i}{R}, \quad z_0 = \frac{\sum\limits_{i=1}^{n} n_i}{R}, \tag{2.2}$$

$$R = \sqrt{(\sum_{i=1}^{n} l_i)^2 + \sum_{i=1}^{n}(m_i)^2 + \sum_{i=1}^{n}(n_i)^2} \tag{2.3}$$

where R is magnitude of the resultant vector.

Repeat the following calculations until the difference between the last two iterates $(\widehat{\boldsymbol{\Lambda}}^{(j)}, \psi^{(j)})$ and $(\widehat{\boldsymbol{\Lambda}}^{(j-1)}, \psi^{(j-1)})$ are smaller than 1×10^{-5} degree, :

$$\tan\psi_j = \frac{\sum\limits_{i=1}^{n} \sqrt{[1 - (\lambda_i'\widehat{\boldsymbol{\Lambda}}_{j-1})]}}{\sum\limits_{i=1}^{n} \lambda_i'\widehat{\boldsymbol{\Lambda}}_{j-1}}, \qquad \widehat{\boldsymbol{\Lambda}}_j = \frac{\mathbf{Y}}{\sqrt{\mathbf{Y}'\mathbf{Y}}} \tag{2.4}$$

where i is the *i*th paleopole along tracks (1, 2, ..., n) and j is iteration number. And

$$\mathbf{Y} = \cos\psi_j \sum_{i=1}^{n} \lambda_i - \sin\psi_j \sum_{i=1}^{n} \mathbf{X}_i, \qquad \mathbf{X}_i = \frac{(\widehat{\boldsymbol{\lambda}}_i'\widehat{\boldsymbol{\Lambda}}_{j-1})\widehat{\boldsymbol{\lambda}}_i - \widehat{\boldsymbol{\Lambda}}_{j-1}}{\sqrt{1 - (\widehat{\boldsymbol{\lambda}}_i'\widehat{\boldsymbol{\Lambda}}_{j-1})^2}} \tag{2.5}$$

Note that the circle fitting method described above results in small circles. Great circles are obtained in some special cases when angular distances (ψ_i) between the best-fit circle centers and paleopoles are 90°. Compared with small circle fitting, great circle fitting usually presents a smaller amount of displacement and thusly is a relatively conservative option. Instead of setting (ψ_i) to 90°, we adopt an alternative method of Scheidegger [1965] to calculate great circle centers using orientation matrix T that can be constructed from paleopoles along APWP tracks:

$$\mathbf{T} = \begin{pmatrix} \sum l_i \cdot l_i & \sum l_i \cdot m_i & \sum l_i \cdot n_i \\ \sum m_i \cdot l_i & \sum m_i \cdot m_i & \sum m_i \cdot n_i \\ \sum n_i \cdot l_i & \sum n_i \cdot m_i & \sum n_i \cdot n_i \end{pmatrix} \tag{2.6}$$

Great circle rotation center to an APWP track can be calculated from the eigenvector corresponding to the minimum eigenvalue of the orientation matrix **T**. There is no significant difference in great circle centers calculated from the two methods. Here we choose to use orientation matrix for great circle modelling throughout this work.

Rotation angles Ω_i subtending the fitted APWP tracks are computed from

$$\Omega_i = cos^{-1} \frac{\cos s - \cos p_1 \cos p_2}{\sin p_1 \sin p_2} \tag{2.7}$$

where s, p_1 and p_2 represent angular distance between the starting and ending paleopoles, angular distance between the starting pole and Euler pole, and angular distance between the ending pole and Euler pole. Positive sign is assigned to the counterclockwise rotation backward in time (e.g. from 0 to 40 Ma).

Variance ratio V_r is introduced to help decide the better choice of circle modelling:

$$V_r = (n-3) \frac{r_g - r_s}{r_s} \tag{2.8}$$

where r_g and r_s represent the sums of squares of angular residuals for great circle and small circle fitting respectively. Assuming that r_g and r_s are normally distributed, improvement of small circle over great circle fitting can be tested at 0.05 significance level by comparing V_r with $F_{1,n-3}$ [Gray et al., 1980].

Readers need to treat with caution such a statistical preference (i.e. V_r) to either great circle or small circle modelling. The seemingly better fitting options are highly likely to present questionable APM reconstructions which are incompatible with the independent geologic and/or geophysical data. This is mainly a result of the various quality of input paleopoles and the possible TPW events. Therefore, the optimal circle modelling combinations for the studied APWPs are decided from reasonable APM reconstructions, which in practice requires trials and modifications.

2.2.2 Absolute plate motion reconstructions from paleomagnetic Euler parameters

Rotation matrix R_i can be constructed from paleomagnetic Euler parameters $(\widehat{\mathbf{\Lambda}}_i, -\Omega_i)$, where negative sign before rotation angle signifies counterclockwise rotation during reconstructions [Cox and Hart, 1986].

$$R_i = \begin{pmatrix} x_i x_i(1-\cos\Omega_i)+\cos\Omega_i & x_i y_i(1-\cos\Omega_i)+z_i\sin\Omega_i & x_i z_i(1-\cos\Omega_i)-y_i\sin\Omega_i \\ y_i x_i(1-\cos\Omega_i)-z_i\sin\Omega_i & y_i y_i(1-\cos\Omega_i)+\cos\Omega_i & y_i z_i(1-\cos\Omega_i)+x_i\sin\Omega_i \\ z_i x_i(1-\cos\Omega_i)+y_i\sin\Omega_i & z_i y_i(1-\cos\Omega_i)-x_i\sin\Omega_i & z_i z_i(1-\cos\Omega_i)+\cos\Omega_i \end{pmatrix} \tag{2.9}$$

The reconstructed geographic coordinates of a study point $\widehat{\mathbf{P_J}} = (a_1^j, a_2^j, a_3^j)$ can be calculated using matrix multiplication:

$$\widehat{\mathbf{P_J}}^r = \mathbf{R_i}\widehat{\mathbf{P_J}} \tag{2.10}$$

where $\widehat{\mathbf{P_J}}^r$ represents the restored reference point.

It is common that actual APWPs consist of more than one segment, so stage Euler poles for earlier tracks need to be derived by closing later rotations. This can be achieved by combining rotations using matrix multiplication [Cox and Hart, 1986]:

$$\widehat{\mathbf{\Lambda}}_i^r = \mathbf{R_{i-1}}\mathbf{R_{i-2}}\cdots\mathbf{R_1}\widehat{\mathbf{\Lambda}}_i \tag{2.11}$$

In the same manner, earlier paleopoles can be rotated back to the geographic coordinates of the latest paleopole, further illustrating our basic assumption that plates rather than the Earth's spin axis represented by paleopoles have moved in the geologic history.

$$(\widehat{\lambda_1^j}^c, \widehat{\lambda_2^j}^c, ..., \widehat{\lambda_n^j}^c) = \mathbf{R_{i-1}}\mathbf{R_{i-2}}\cdots\mathbf{R_1}(\widehat{\lambda_1^j}, \widehat{\lambda_2^j}, ..., \widehat{\lambda_n^j}) \tag{2.12}$$

2.2.3 Paleolatitude corrections

Because paleopoles are seldom located along the fitted circle arcs, there will be accumulated errors in the restorations computed from PEPs, leading to incompatible predictions in paleo-colatitudes with paleomagnetic data. Such errors are illustrated in Figure 2.1 where there are deviations between paleopoles and the fitted circle track. Here we propose to use paleo-colatitudes determined from paleopoles to compensate for the errors. Assuming no TPWs during the period of apparent polar wandering, the corrected reconstructions can be obtained by tracing spherical distances along the paleo-meridians defined from the latest paleopole and the original reconstructions.

2.2.4 Error analysis

Errors in circle parameterizations

Errors in the paleomagnetic Euler parameters $(\widehat{\mathbf{\Lambda}}_i, \Omega_i)$ are estimated using a bootstrap procedure similar to that of Smirnov and Tarduno [2010]. Firstly, individual paleopoles along the modelled APWP tracks are treated as discrete Fisherian distributions, from which 100 new paleopoles are resampled using their precision parameters [Fisher et al., 1981]. This results in 100 new APWPs $(\widehat{\boldsymbol{\lambda}}^{(1)}, \widehat{\boldsymbol{\lambda}}^{(2)}, ..., \widehat{\boldsymbol{\lambda}}^{(n)})$, which are named bootstrapped APWPs. We recommend a minimum of 100 bootstrap resamplings for APWPs with 95% confidence ovals no larger than 5°. For APWPs with larger uncertainties, more iterations can be considered. Secondly, both great circle and small circle fittings are implemented to the same segments along the bootstrapped APWPs to calculate the bootstrapped PEPs $((\widehat{\mathbf{\Lambda}}^{(1)}_{GC}, \widehat{\mathbf{\Lambda}}^{(1)}_{SC})$, $(\widehat{\mathbf{\Lambda}}^{(2)}_{GC}, \widehat{\mathbf{\Lambda}}^{(2)}_{SC})$, ..., $(\widehat{\mathbf{\Lambda}}^{(100)}_{GC}, \widehat{\mathbf{\Lambda}}^{(100)}_{SC}))$ and the associated rotation angles. Lastly, confidence ellipses at 0.05 significance in circle fittings are estimated from covariance matrices of the above bootstrapped data sets.

Assuming that the bootstrapped PEPs are Fisherian distributed, $(\widehat{X}_i$ - $\bar{\mathrm{X}})$ is a chi-square distribution with 2 degrees of freedom (i.e., latitude and longitude), where $\widehat{X}_i$ is the ith bootstrapped PEP with the Fisherian mean of $\bar{\mathrm{X}}$. As a result, two-dimensional covariance matrices can be constructed, with the major (minor) semi-axes of the confidence ellipses represented by the maximum (minimum) eigenvectors. Note that PEPs calculated from the main procedure do not necessarily equal to the Fisherian means of the bootstrapped PEPs. The two data sets should converge when bootstrap resampling repetitions are infinitely large. In practice, we consider such discrepancies insignificant when their spherical distances are no larger than 5°. Uncertainties in PEPs are thusly characterized using covariance matrices of the Fisherian means of the bootstrapped PEPs.

Errors in reconstructions

Errors in reconstructions are estimated using the similar chi-square test at the significance level of 0.05, leading to elliptical uncertainty bounds. Error shapes are more complex if plate contours are used for calculations [Smirnov and Tarduno, 2010]. For simplicity, we opt to estimate the true confidence regions using 2D ellipses. Because of error propagations, errors in reconstructions accumulate gradually back to earlier times.

Table 2.1: Apparent polar wander paths for the last 140 Ma in the coordinates of India, Australia and East Antarctica with no true polar wander corrections [Torsvik et al., 2012].

		India		Australia		E.Antarctica	
Age (Ma)	A95 $(^\circ)$	lonP $(^\circ E)$	latP $(^\circ N)$	lonP $(^\circ E)$	latP $(^\circ N)$	lonP $(^\circ E)$	latP $(^\circ N)$
0	1.9	-88.5	353.9	-88.5	353.9	-88.5	353.9
10	1.8	-87.2	60.4	-86.6	119.3	-87.3	319.7
20	2.6	-83.7	74.7	-82.2	113	-85.6	325.9
30	2.6	-79.7	101.7	-77.1	121.4	-84.9	314.9
40	2.9	-74.7	106.8	-72.9	119.5	-84.1	320
50	2.8	-65.1	98.4	-69.6	109.6	-82.9	351.7
60	2.1	-48.5	100.8	-65.5	110.3	-83.6	17.8
70	2.5	-36.4	100.7	-63.1	112.6	-84.1	35.4
80	2.9	-29	103.5	-63.1	118.5	-86.7	34.6
90	2.5	-20.9	111.4	-62.7	130.2	-87.9	209
100	3.3	-19.7	113	-60.8	136.4	-84.9	202
110	3.3	-11.1	115.9	-52.7	140.5	-78.9	172.1
120	2.6	-8.6	116.4	-50.2	146.4	-75.9	183.6
130	2.8	1	117.1	-47.7	146.4	-73.7	178.7
140	6	5.3	117.9	-44.8	147.6	-70.8	176.8

2.3 Paleomagnetic data for the East Gondwana continents

In this work we follow the common definition that APWP describes the rotation of the Earth's spin axis with respect to a studied plate. APM is defined as the rotation of the plate with respect to a 'stationary' free space, and TPW is defined as the rotation of the Earth's spin axis with respect to the same free space. The three terms of rotations can be linked through the multiplication of rotation matrices.

$$R_{APWP} = R_{APM} \times R_{TPW} \tag{2.13}$$

To accurately reconstruct past plate motions, the effect of TPWs on the studied APWPs needs to be corrected before using our proposed apparent polar wander path geometric parameterization (APWPGP) method. Events of TPW later than 130 Ma can be computed by subtracting APMs constrained in hotspot frames from APWPs using the above equation [e.g., Besse and Courtillot, 2002; Doubrovine et al., 2012]. However, such discrepancies could also result from errors in hotspot motions propagated from the adopted APM models and mantle flow models. For earlier ages, episodes of TPW are commonly constrained from paleomagnetic data, from which paleolatitudes and azimuthal orientations shared by 'all' continental plates are used to identify TPW [Steinberger and Torsvik, 2008; Mitchell et al., 2012; Torsvik et al., 2012]. Such estimations are usually based on the selection of certain continents with the least longitudinal motions, which is still open to debate. Therefore, before more accurate TPW can be derived, we choose to use the APWPs of India, Australia and East Antarctica without any TPW corrections [Torsvik et al., 2012] for APM reconstructions.

2.4 Apparent polar wander paths geometric parameterizations

Four APWP tracks are identified for India, Australia and East Antarctica (Table 2.2 & Figure 2.2). Great circle parametrizations prove to be the optimal fitting options from both visual inspection and reliability of reconstructions. Facilitated by our proposed paleolatitude corrections (see section 2.2), there is no need to split the fit of consecutive APWP segments along which paleopoles are not closely located, as long as the circle fit of the longest APWP segment closely resemble the overall fit for all paleopoles (Figure 2.2b, Track Ind-1). Great circle parametrization is preferred for APWP tracks with the short spherical lengths ($< 10°$), (Figure 2.2c, Track E.Ant-2 and Figure 2.2d, Track Aus-2). This is because some small amount of apparent polar wandering could be a result of errors in paleopoles rather than tectonic events. Moreover, some geologically unreasonable translation distances can result using rotation parameters from small circle fitting. For instance, small circle parameterizations to the APWP segments of East Antarctica and Australia during 70-40 Ma (Figures 2.2c-d) would yield to rotations with a spherical displacement of $> 60°$ within 30 Myr, while great circle fittings to the same APWP segments predict more reasonable amount of spherical translations. As discussed in section 2.2, the choice for the optimal circle parametrization methods should be based on reasonable reconstructions. Reconstructions from other APM models such as hotspot frame [Doubrovine et al., 2012] and slab frame [van der Meer et al., 2010], and independent geologic and geophysical observations can be used to assist such inspection.

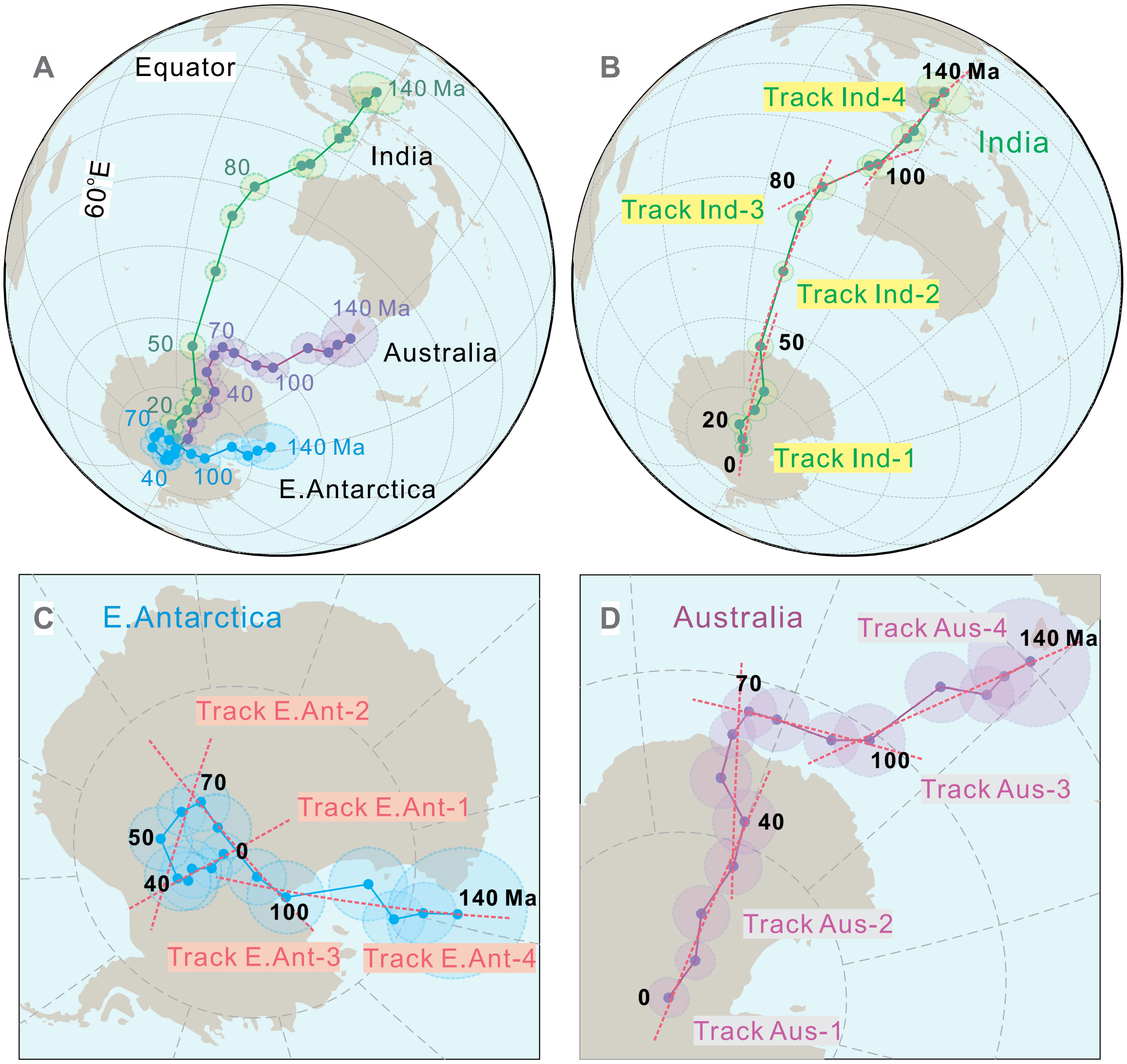

Figure 2.2: Geometric parameterizations of the apparent polar wander paths in the coordinates of India, Australia and East Antarctica (E.Antarctica) for the last 140 Myr. (**A**) Orthographic projection of the APWPs (colored dots) for the three continents without TPW corrections (Table 2.1) [Torsvik et al., 2012]. Also shown are the errors (colored circles) and key ages (black fonts) of the paleopoles. (**B-D**) The fitted APWP tracks are represented as red dash-lines with the resultant Euler parameters shown in Table 2.2.

Table 2.2: The calculated Euler parameters for India, Australia and East Antarctica (Figure 2.2), including paleomagnetic Euler poles (lonE, latE) and the associated rotation angles (Ω, positive for counterclockwise rotation backward in time). Stage Euler poles (lonE', latE') for reconstructions are computed by closing all afterward rotations. Confidence ellipses in rotation poles are defined from the 2 × 2 covariance matrix, where cov(21)=cov(12) (see section 2.2). Great circle distances (GCDs) between the PEPs and the Fisherian means of the bootstrapped PEPs are smaller than 5°, indicating that the estimated confidence ellipses can be used to characterize the errors of the stage rotation poles. The optimal circle parametrization, either in great circle (GC) or small circle (SC), are determined primarily based on reliability of the resulting reconstructions.

		Euler parameters						Errors			
Track	Period (Ma)	lonE ($^\circ E$)	latE ($^\circ N$)	lonE' ($^\circ E$)	latE' ($^\circ N$)	Ω (°)	Fitting code	cov(11) (°)	cov(12) (°)	cov(22) (°)	GCD (°)
India											
Ind-1	0-50	15	1.6	15	1.6	25.3	GC	42.13	5.1	1.4	0.31
Ind-2	50-80	14.2	2.9	14.8	3.1	36.2	GC	26.1	1.5	3.8	0.12
Ind-3	80-100	38.9	37.7	56.3	1.4	12.7	GC	237.4	-2.2	4.0	0.18
Ind-4	100-140	27.2	9.7	26.4	1.4	25.5	GC	140.7	-19.5	309.3	4.61
Australia											
Aus-1	0-40	33.1	0.9	33.1	0.9	18	GC	89.90	10.2	2.0	0.05
Aus-2	40-70	12.1	-4.3	11.5	2.3	10.1	GC	457.7	8.2	5.6	0.19
Aus-3	70-100	112.9	26.8	113.1	-0.9	11.4	GC	254.1	-6.9	5.3	0.15
Aus-4	100-140	72.3	14.2	73.3	0.8	17.3	GC	270.5	7.28	6.6	0.14
East Antarctica											
E.Ant-1	0-40	39.6	0.9	39.6	0.9	-4.7	GC	2505.3	-130.5	7.9	0.80
E.Ant-2	40-70	358.1	5.6	357.9	2.5	7.2	GC	1015.9	-10.6	20.0	0.70
E.Ant-3	70-100	299.8	-0.4	299.3	1.1	-10.9	GC	335.4	27.4	282.9	3.56
E.Ant-4	100-140	80.8	-2.1	80.4	0.8	14.7	GC	551.3	209.2	675.9	2.54

Stage Euler rotations (Table 2.2) and the associated APWP tracks (Table 2.3 & Figures 2.3-2.5) for the studied continents are computed by closing later rotations (see section 2.2). For APM reconstructions, we adopt the present-day contours for the three continents and assume that these contours have remained the same for the last 140 Myr. The reconstructed reference sites after paleo-colatitude corrections do not differ much with those before corrections (Figures 2.3-2.5), further implying the soundness of our circle fittings. For error analysis, we resample with 100 repetitions from the paleopoles along the Indian, Australian and East Antarctic APWPs (Figure 2.6). Both great circle and small circle parameterizations are implemented to the bootstrapped APWP tracks (Figures 2.7-2.9). The confidence areas at the significance level of 0.05 for the stage Euler poles and the resultant restorations are estimated from the bootstrapped PEPs and reconstructions (Tables 2.2 & 2.4, Figures 2.10-2.12).

Table 2.3: Transferred APWP segments for reconstruction purpose by rotating earlier APWP segments into the geographic frame of the first poles (0 Ma).

	India			Australia			E.Antarctica	
Age (Ma)	lonP $(^\circ E)$	latP $(^\circ N)$	Age (Ma)	lonP $(^\circ E)$	latP $(^\circ N)$	Age (Ma)	lonP $(^\circ E)$	latP $(^\circ N)$
0	353.9	-88.5	0	353.9	-88.5	0	353.9	-88.5
10	60.4	-87.2	10	119.3	-86.6	10	319.7	-87.3
20	74.7	-83.7	20	113	-82.2	20	325.9	-85.6
30	101.7	-79.7	30	121.4	-77.1	30	314.9	-84.9
40	106.8	-74.7	40	119.5	-72.9	40	320	-84.1
50	98.4	-65.1						
			40	-7.6	-88.5	40	-5.7	-88.5
50	4.5	-87	50	54.4	-84.9	50	33.1	-85.2
60	94	-73.6	60	80.9	-82	60	61.1	-83.6
70	96.8	-61.5	70	93.4	-80.3	70	75.7	-82.7
80	101.9	-54.2						
			70	352.8	-88.5	70	354.5	-88.4
80	1.8	-87.6	80	234.9	-88.4	80	251.9	-88.2
90	136.2	-81	90	214.9	-83.2	90	221.5	-83.2
100	139.9	-79.2	100	206	-79.9	100	213.9	-80.3
100	-0.9	-87.7	100	0.9	-88.6	100	-2.2	-88.5
110	110.8	-82.1	110	145.8	-82.8	110	144.4	-84.2
120	112.5	-79.5	120	164.4	-79.3	120	172.7	-82.1
130	111.8	-69.9	130	160.2	-77	130	167.4	-79.7
140	112.8	-65.5	140	159.9	-74	140	167.1	-76.7

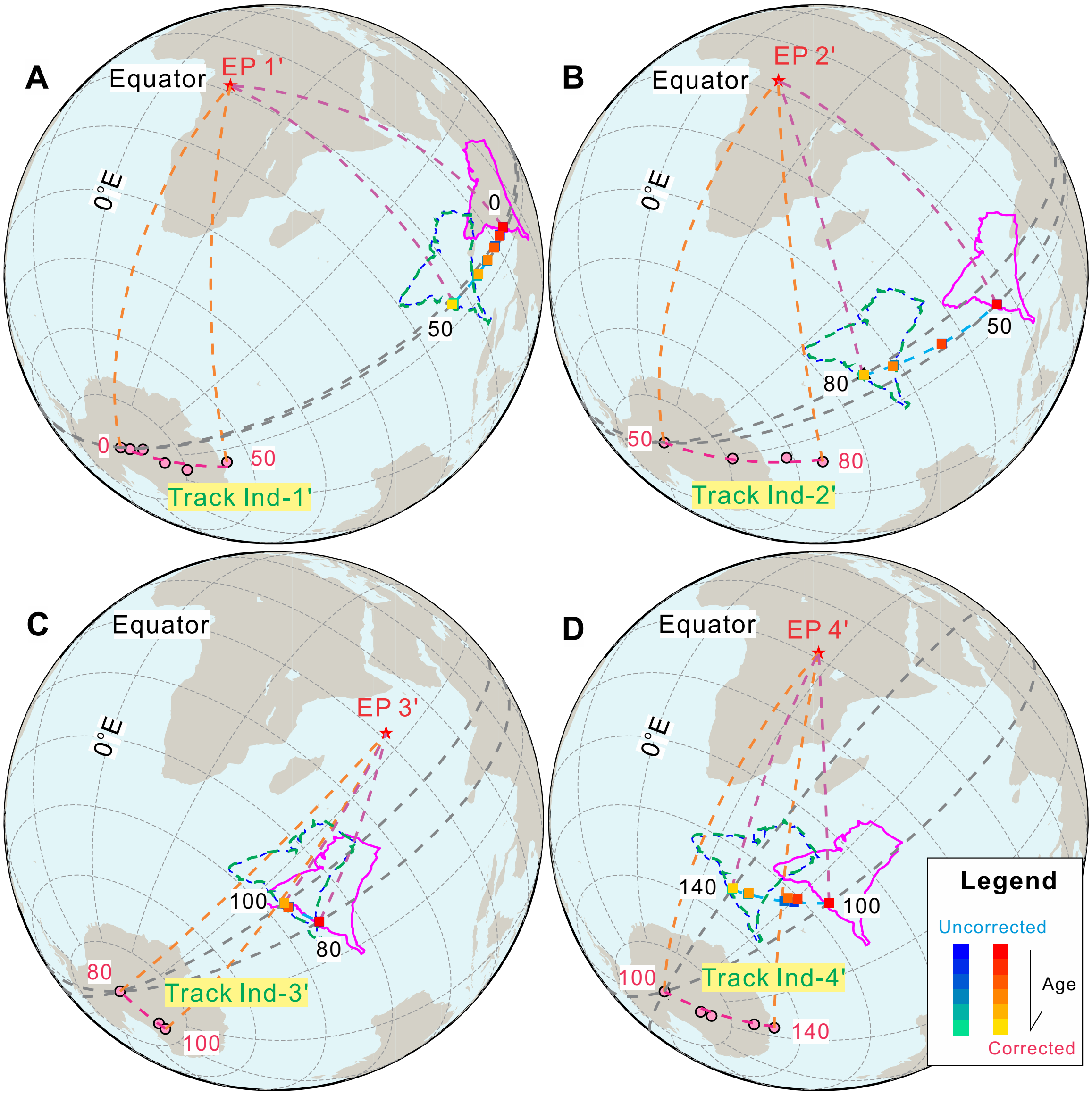

Figure 2.3: Absolute motion reconstructions of India for the last 140 Ma. Blue and green dashed contours indicate the locations of the original and paleolatitudinally corrected reconstructions while magenta contours show the initial locations before each of the four rotation stages. Reconstructions of the reference site [85°E, 20°N] are shown as color-coded squares (Table 2.4), with the cool-colored and warm-colored markers representing the original and paleolatitudinally corrected restorations, respectively. Also shown are the stage rotation poles (EP', red star) (Table 2.2) and the tranferred APWP tracks (Track i', pink dots and dashed lines) (Table 2.3).

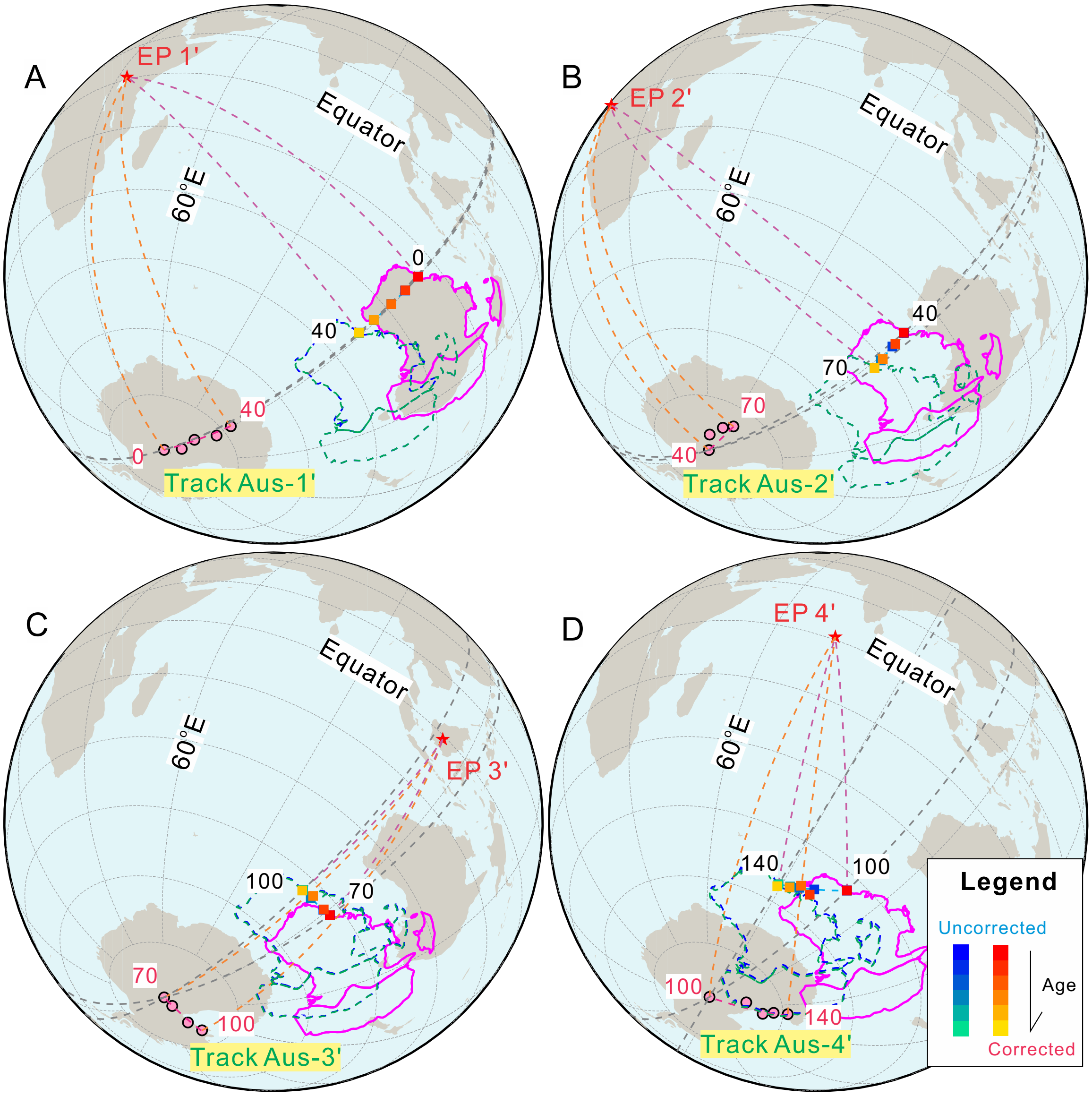

Figure 2.4: Absolute motion reconstructions of Australia for the last 140 Ma using our new APWPGP method. Reconstructions of the reference site [120°E, -20°N] are shown in the color-coded squares (Table 2.4). See the caption of Figure 2.3 for the explanation of other symbols and lines.

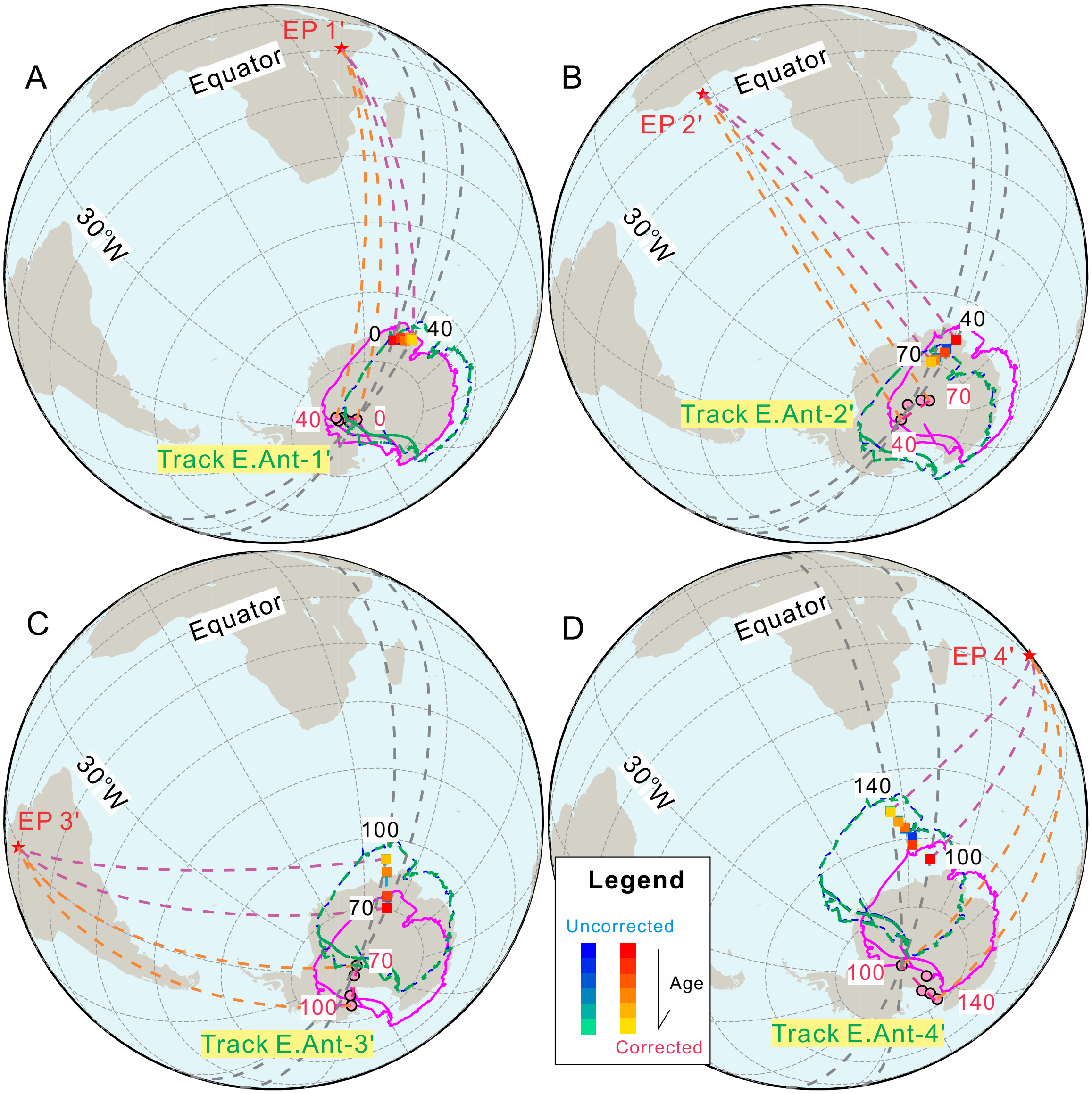

Figure 2.5: Absolute motion reconstructions of East Antarctica for the last 140 Ma using our new APWPGP method. Reconstructions of the reference site [50°E, -70°N] are shown in the color-coded squares (Table 2.4). See the caption of Figure 2.3 for the explanation of the symbols and lines.

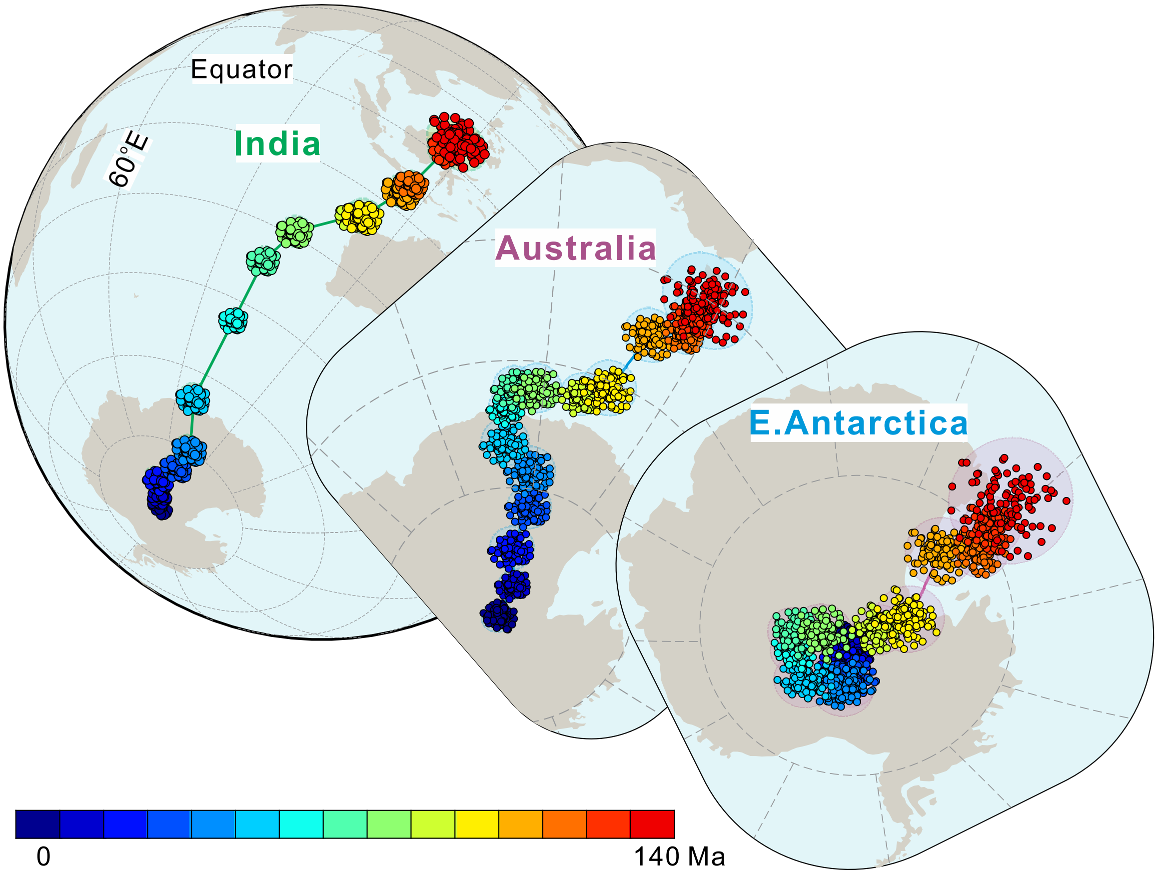

Figure 2.6: Bootstrap resampling with 100 repetitions to the APWPs of India, Australia and East Antarctica.

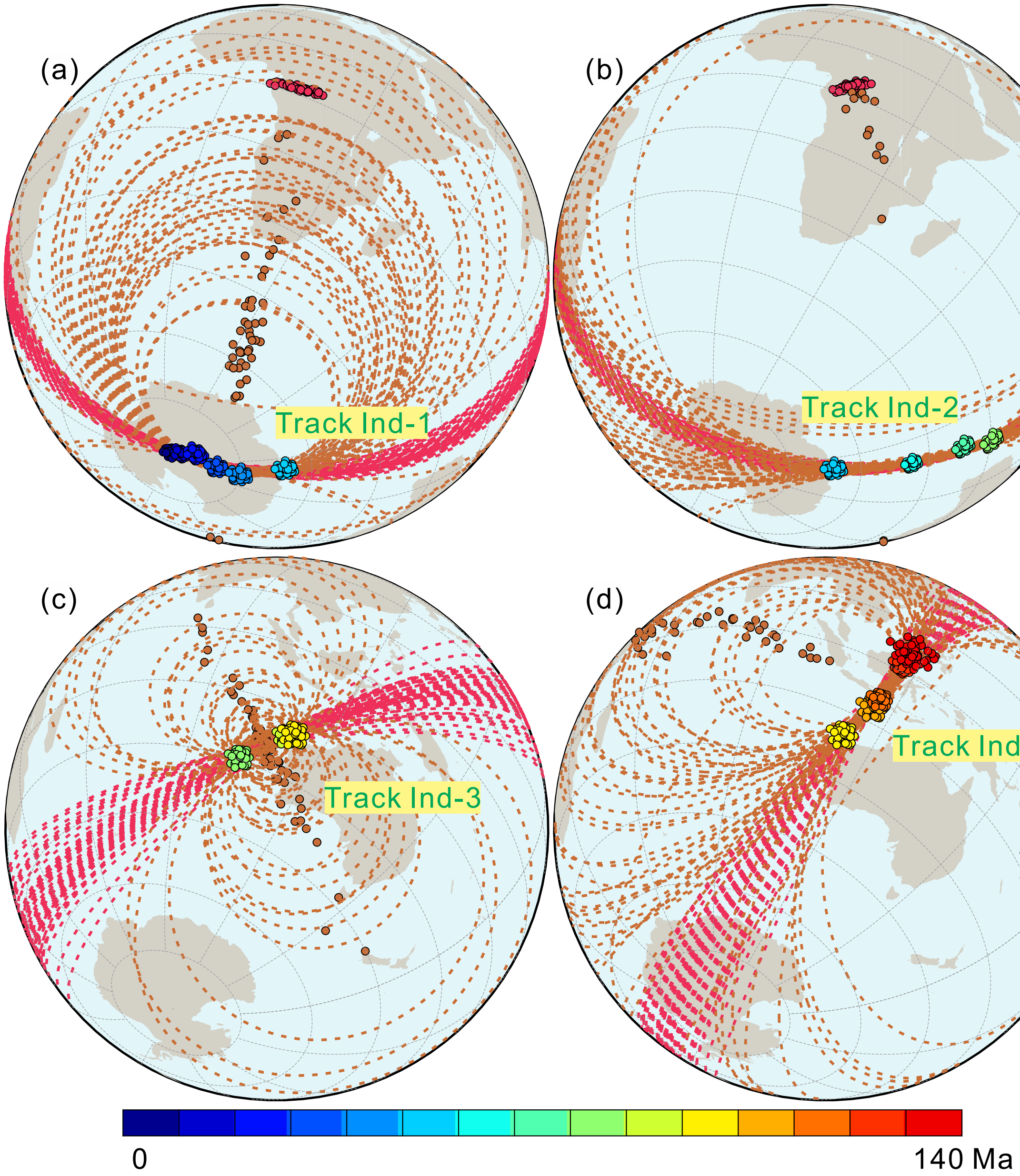

Figure 2.7: Bootstrapped circle parameterizations for the Indian APWP (Table 2.1). The bootstrapped great circle and small circle fittings to the same APWP tracks are shown in red and bronze dashed lines with their bootstrapped PEPs shown in the same colored dots. Bootstrapped paleopoles along each of APWP tracks are marked as color-coded dots.

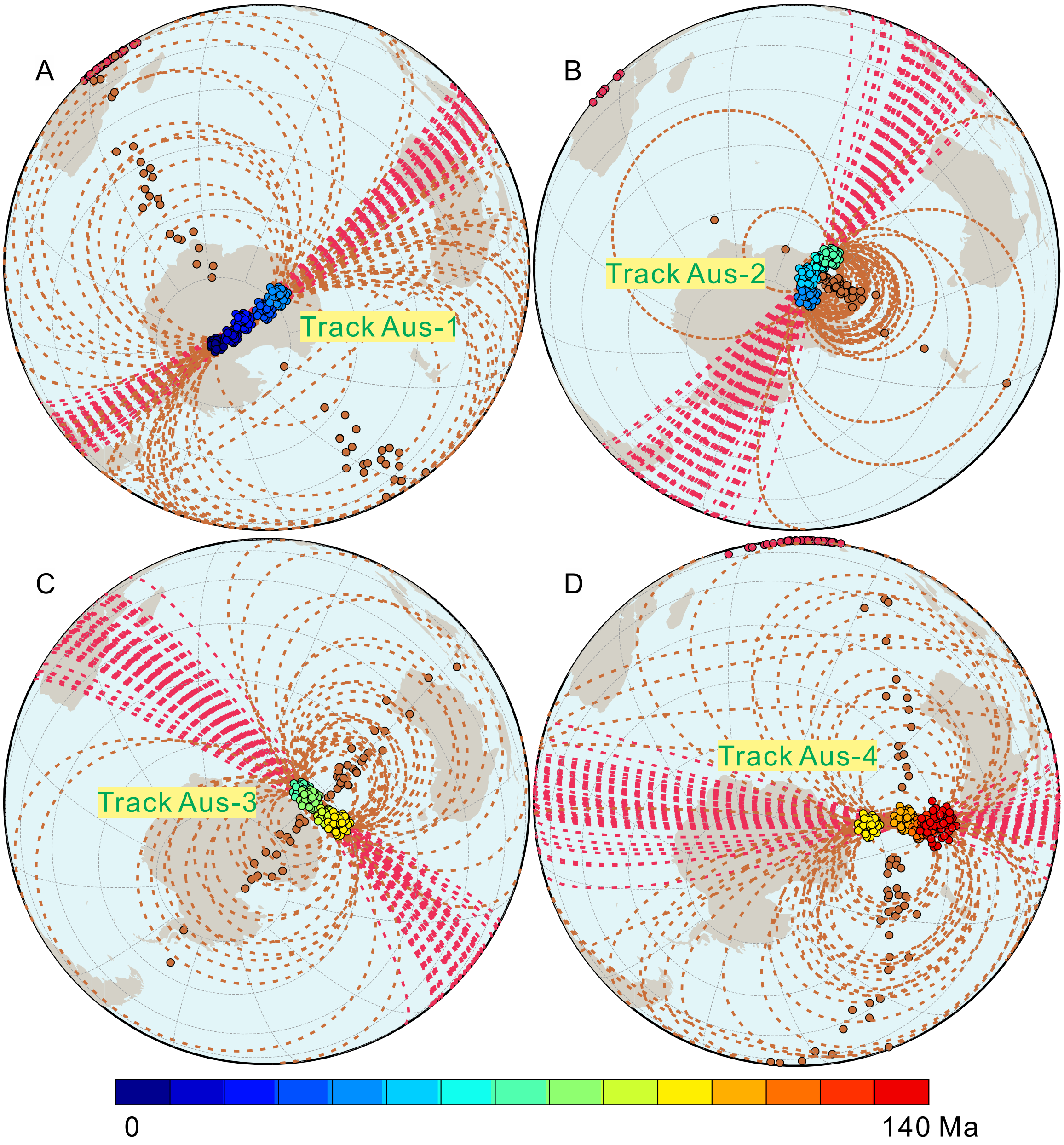

Figure 2.8: Bootstrapped circle parameterizations for the Australian APWP (Table 2.1). Symbols and lines are defined similarly with those in Figure 2.7.

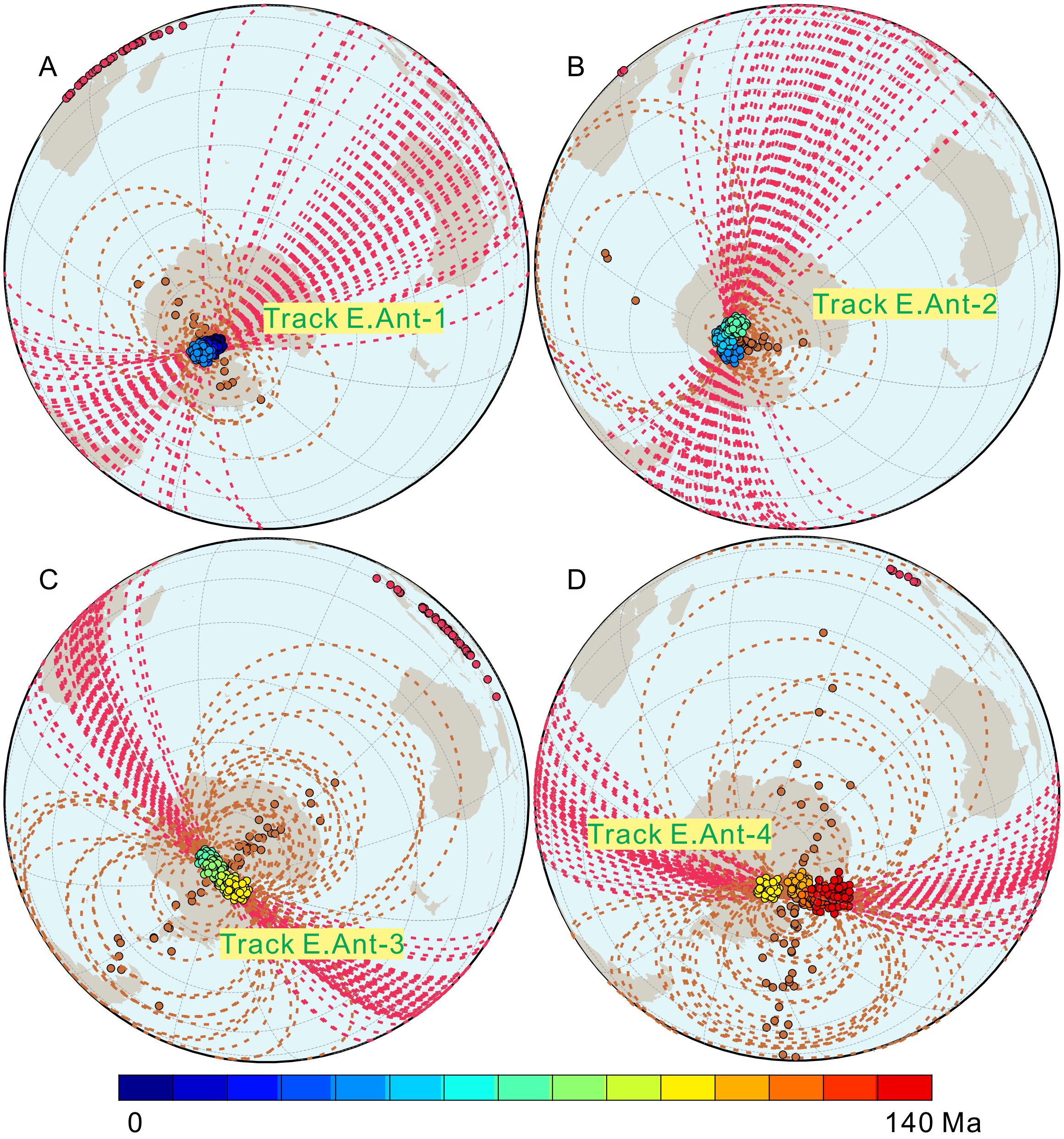

Figure 2.9: Bootstrapped circle parameterizations for the East Antarctic APWP (Table 2.1). Symbols and lines are defined similarly with those in Figure 2.7.

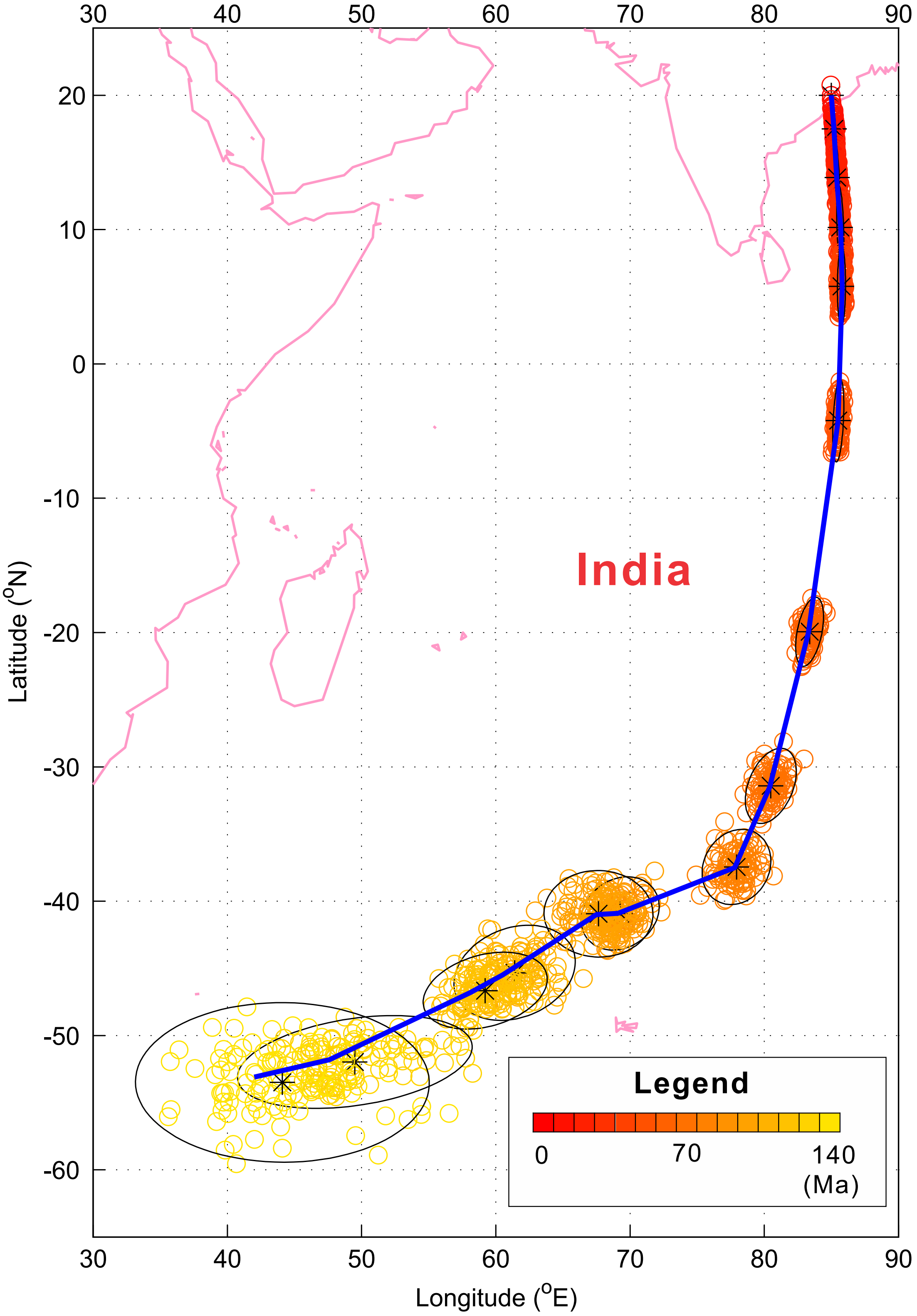

Figure 2.10: Bootstrapped reconstructions of the reference site [85°E, 20°N] in India, from which the error ellipses (black) at the significance level of 0.05 are estimated (Table 2.4). Coastlines are shown in the pink lines. Asterisks mark the Fisherian means of the bootstrapped reconstructions while points connected by the dark-blue solid line represent the original reconstructions.

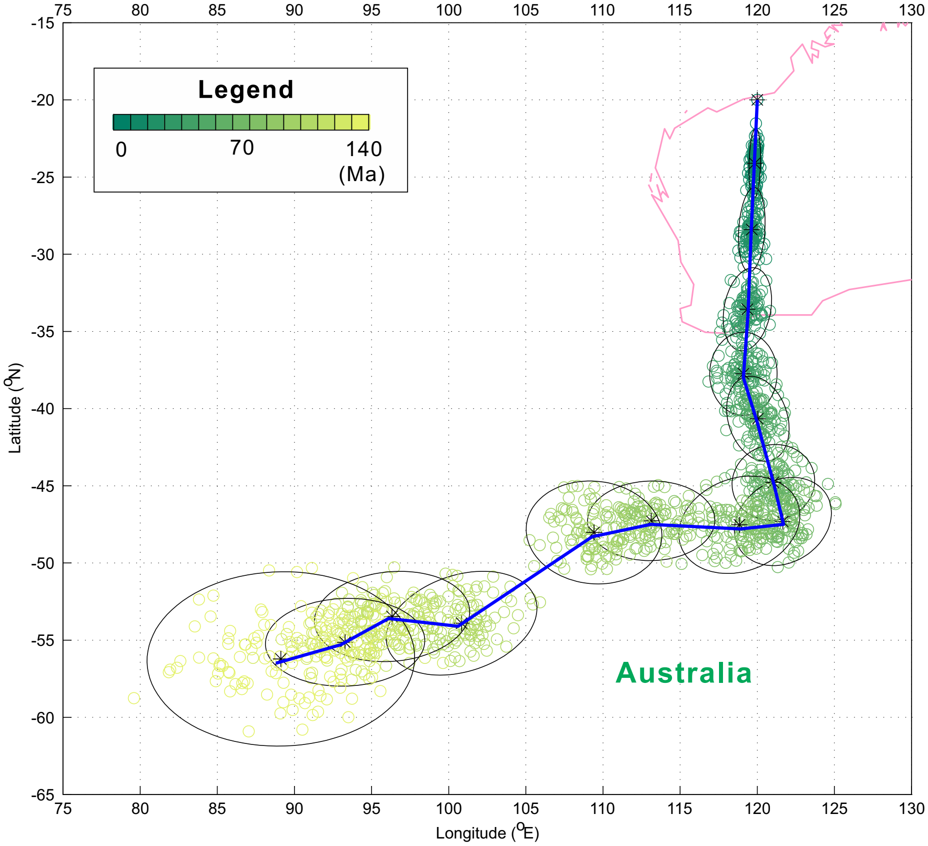

Figure 2.11: Bootstrapped reconstructions of the reference site [120°E, -20°N] in Australia, from which the error ellipses (black) at the significance level of 0.05 are estimated (Table 2.4). See the caption of Figure 2.10 for the descriptions of the symbols and lines.

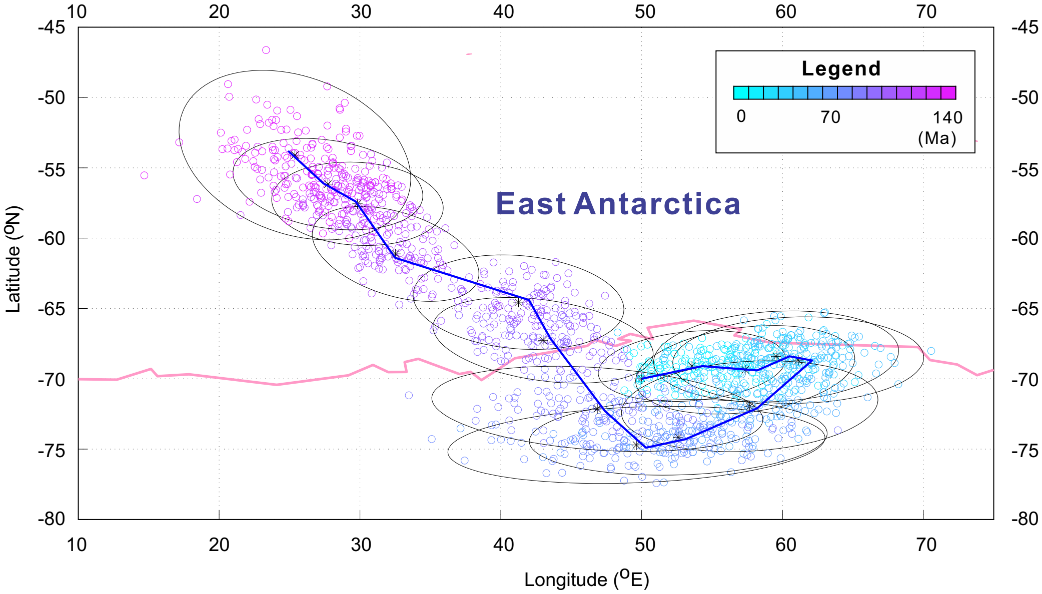

Figure 2.12: Bootstrapped reconstructions of the reference site [50°E, -70°N] in East Antarctica, from which the error ellipses (black) at the significance level of 0.05 are estimated (Table 2.4). See the caption of Figure 2.10 for the descriptions of the symbols and lines.

Table 2.4: The reconstructed paleo-positions and associated errors for the selected reference sites in India, Australia and East Antarctica during 0-140 Ma (Figures 2.10-2.12). 95% confidence ellipses are characterized in the form of 2×2 covariance matrices (cov(21)=cov(12)) that are estimated from the bootstrapped reconstructions (Figures 2.10-2.12). The small GCDs ($< 2^\circ$) between the original reconstructions and the Fisherian means of bootstrapped reconstructions indicates that the estimated confidence ellipses can be used to characterize the reconstruction errors.

	India						East Antarctica					
Age (Ma)	lonR (°*E*)	latR (°*N*)	cov(11) (°)	cov(12) (°)	cov(22) (°)	GCD (°)	lonR (°*E*)	latR (°*N*)	cov(11) (°)	cov(12) (°)	cov(22) (°)	GCD (°)
0	85	20	0	0	0	0	50	-70	0	0	0	0
10	85.2	17.4	0.05	-0.42	5.78	0.1	54.3	-69.1	44.26	3.35	6.34	0.26
20	85.4	13.8	0.05	-0.46	8.27	0.08	58.2	-69.4	60.51	6.28	9.88	0.3
30	85.7	10.1	0.07	-0.3	9.53	0.07	60.5	-68.4	75.72	3.54	10.47	0.35
40	85.8	5.7	0.09	0.04	8.61	0.09	62.1	-68.7	79.39	1.64	9.48	0.36
50	85.5	-4.3	0.17	0.45	9.51	0.09	58.2	-72.1	82.98	4.29	10.44	0.22
60	83.3	-20	1.08	1.16	6.59	0.09	53.1	-74.3	111.87	3.03	7.24	0.19
70	80.4	-31.5	3.6	2.07	7.84	0.11	50.3	-74.9	179.28	6.8	7.52	0.27
80	77.8	-37.5	6.56	1.12	7.83	0.11	47.4	-72.3	138.2	-8.98	9.16	0.23
90	69.1	-40.9	8.45	1.48	7.44	0.13	43.5	-67.1	61.08	-7.5	9.28	0.25
100	67.5	-41	16.45	-0.16	10.37	0.13	42	-64.4	55.99	-3.78	11.29	0.36
110	60.5	-45.5	20.42	3.64	12.56	0.65	32.5	-61.4	35.02	-8.28	11.38	0.28
120	58.1	-46.8	21.36	3.96	8.19	0.77	29.7	-57.4	37.07	-1.79	8.81	0.17
130	47.6	-51.8	76.45	9.93	11.93	1.19	27.4	-56.1	45.42	-5.51	10.57	0.19
140	42	-53.1	119.89	-0.56	35.3	1.31	24.9	-53.8	67.66	-13.92	36.34	0.41
	Australia											
0	120	-20	0	0	0	0						
10	119.8	-24.3	0.14	0.14	5.19	0.19						
20	119.6	-28.6	0.74	0.42	7.43	0.2						
30	119.4	-33.8	2.46	0.96	7.23	0.24						
40	119.1	-38	4.78	0.02	7.25	0.26						
50	120	-40.9	4.09	-1.3	7.59	0.24						
60	121.1	-45	7.17	0.32	6.04	0.22						
70	121.7	-47.5	9.88	1.79	8.17	0.18						
80	118.9	-47.8	15.38	2.4	9.95	0.28						
90	113.1	-47.5	17.03	0.18	6.65	0.23						
100	109.3	-48.3	19.34	-0.9	11.11	0.29						
110	100.6	-54.1	23.86	4.68	11.3	0.24						
120	96.1	-53.6	25.31	1.56	8.56	0.19						
130	93	-55.3	26.68	0.58	8.08	0.23						
140	88.8	-56.5	75.21	1	31.9	0.33						

2.5 Absolute plate motions of the East Gondwanaland continents since 130 Ma

Our reconstructions indicate that India experienced a northeastward translation and a rapid counterclockwise (CCW) rotation (~ 50°) during 140-100 Ma (Figures 2.3D, 2.10 & 2.13). After a mostly eastward drift during 100-80 Ma, there was a much faster climbing in latitudes with an average speed of ~12 cm/yr (the top rate of ~18 cm/yr occurred between 60-70 Ma) and ~ 20° CCW rotation during 80-50 Ma (Figure 2.14C), when the collision between India and Eurasia at ~50 Ma largely decreased its northward motions [Molnar et al., 2010]. Cande and Stegman [2011] suspect that the observed hasty acceleration and deceleration might be related with the upwelling force of the Réunion plume head during 67-52 Ma.

According to our reconstructions, Australia might have experienced a total of ~ 30° CCW rotations with respect to meridians in the past 140 Myr (Figures 2.4, 2.11 & 2.13). There seemed to be a transition from the eastward to northward motions at ~70 Ma for Australia with a strong oscillation in the motion speed during 110-100 Ma (increased to ~8-9 cm/yr) (Figures 2.4 & 2.13-2.15). East Antarctica displayed a similarly eastward drift and CCW rotations during 140-70 Ma before it switched into a slowly northwestward (~2.8 cm/yr) displacement during 70-40 Ma, and then a southwestward (~1.5 cm/yr) drift with clockwise (CW) rotations during 40-0 Ma (Figures 2.5 & 2.13-2.15).

Our reconstructions shed new light on the separation history of the East Gondwanaland since 140 Ma. Firstly, the tectonic affinity between India and East Antarctica might have been broken down by the West Enderby Basin spreading ridge around 130-120 Ma [Gaina et al., 2007] rather than a later ages of 118-90 Ma [Jokat et al., 2010]. Secondly, the breakup between Australia and India might have occurred at 130-120 Ma (Figure 2.13), which could be related with the spreading in the Gascoyne and Cuvier Abyssal Plains initiated at ~132 Ma [Seton et al., 2012, and references therein]. Thirdly, there seems to be closely synchronized (with only a slight deviation) plate motion vectors between Australia and East Antarctica during ~140-80 Ma. After that, Australia progressively drifted northward with an average speed of 4 cm/yr until reaching its present-day location (Figures 2.4 & 2.13B-C). Such observations are consistent with results from the recent relative plate motion (RPM) studies. Ball et al. [2013], for instance, suggest that the tectonic affinity between the two plates was broken up at ~53 Ma after an eastward propagation of rifting at 165-83 Ma and a subsequent seafloor spreading at 83-53 Ma. Whittaker et al. [2013] identify a major change in the relative motion directions between Australia and East Antarctica between 108 and

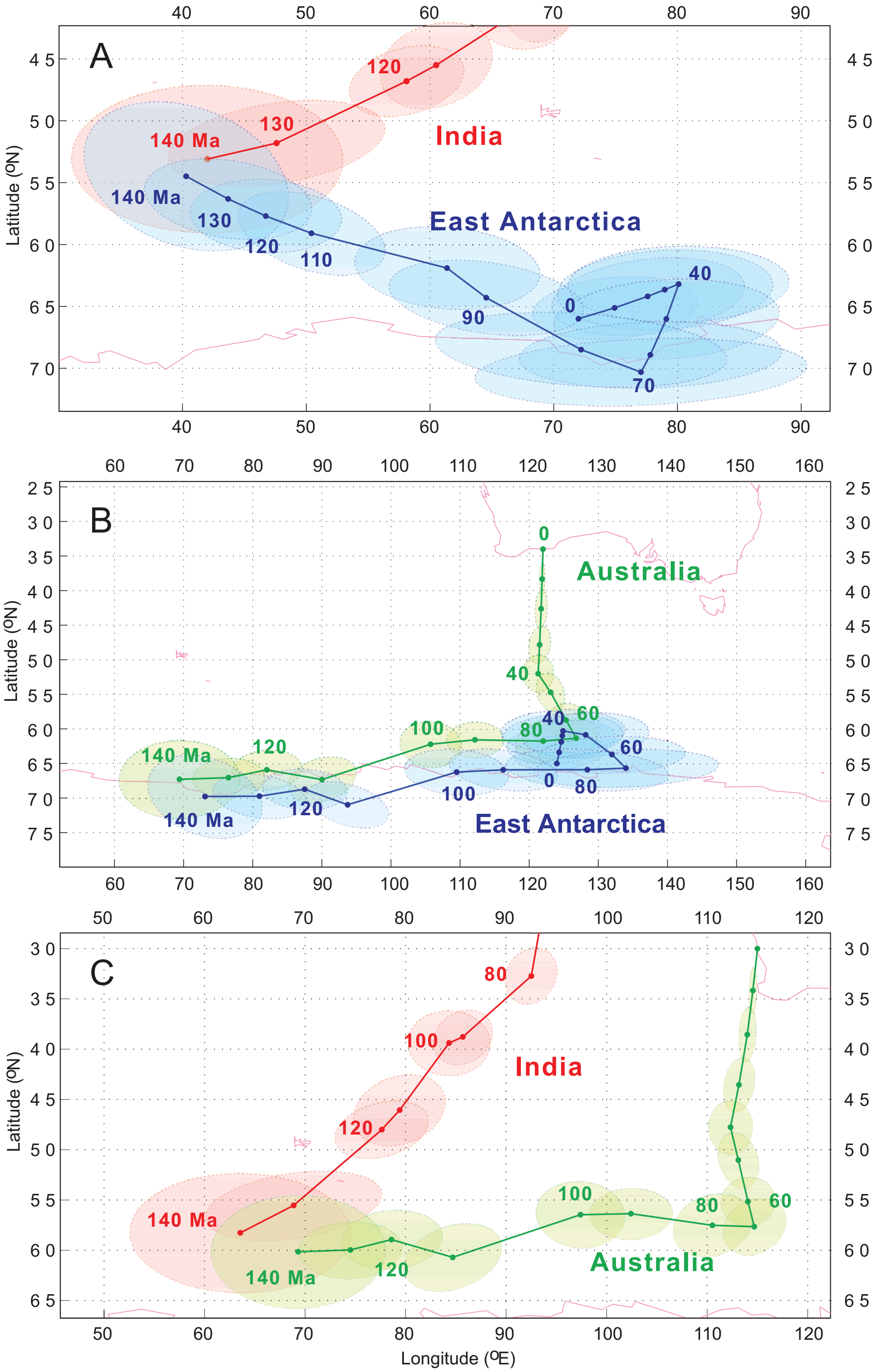

Figure 2.13: Separation history of the East Gondwanaland continents since 140 Ma, as illustrated from the APM reconstructions for the selected reference sites. To better evaluate the dispersion history among the three East Gondwana continents, we calculated the motion trajectories for different reference sites which are restored to be in proximity at the plate polygons at 140 Ma. Reconstructions with uncertainties are shown for (A) India [85°E, 20°N] and East Antarctica [124°E, -65°N], (B) East Antarctica [124°E, -65°N] and Australia [122°E, -34°N], and (C) Australia [115°E, -30°N] and India [96°E, 28°N].

100 Ma, which is slightly later than the 'kink' in their APM paths at 110 Ma (Figure 2.2C-D and Figure 2.13). However, such small discrepancy can be readily reconciliated within errors, considering the reconstruction errors from our proposed APWPGP method and those from the rotation parameters that are derived from the conjugate seafloor magnetic crossings and fracture zone intersections.

To further evaluate the robustness of our APWPGP method, we compare our reconstructions with those from four other APM models derived with different methods: fixed hotspot reference frame (M93) [Müller et al., 1993], global moving hotspot reference frame (D12) [Doubrovine et al., 2012], TPW reference frame (M12) [Mitchell et al., 2012] and global hybrid reference frame (T12) [Torsvik et al., 2012]. Various APM models predict a generally similar form of displacement trajectories but with quite different details (Figure 2.14). To quantify the differences, we calculate expected paleolatitudinal drift (EPD) for the same reference sites using the APWPs without TPW corrections [Torsvik et al., 2012], and then we compare the resultant EPDs with those predicted from different APM models (Figure 2.14D). We find that M93 and D12 significantly deviate from the EPDs during 140-50 Ma, while M12, T12 and our APWPGP model show better resemblance with the EPDs for the last 140 Myr. Simlar discrepancies are seen from the great circle distances (GCDs) of different models with respect to our APWPGP model in the APM reconstructions (Figure 2.14B). The GCDs for M93 and D12 are mostly less than 10° but can reach $\sim 15-25°$ for India and Australia during 50-100 and 130-140 Ma. We urge readers to be cautious to any APM models if their paleolatitudinal predictions do not match those from paleomagnetism. In contrast, the paleomagnetic-based model M12 and T12 show relatively smaller deviations from the EPDs except in such time intervals as 50-30 Ma.

Overall, our APWPGP reconstructions are most close to the predictions from T12 for the last 140 Myr. Reconstructions contradict during 140-130 Ma when our reconstructions do not show a communal southward translation for the three East Gondwana continents. The main reason for this discrepancy is that T12 is based on the assumption of 'quasi-stationary' Africa, which is open to debate. Nonetheless, this discrepancy is within the errors in our reconstructions (Figure 2.14) despite an augment in the GCDs during 140-130 Ma (Figure 2.15B). We find similar but large variations in GCDs between the predictions from APWPGP and M12 (Figure 2.15c), which can be explained by the fact that M12 is constructed by shifting paleo-longitudes of the reconstructions from an earlier version of T12 [Torsvik et al., 2008a] according to their derived episodes of TPW.

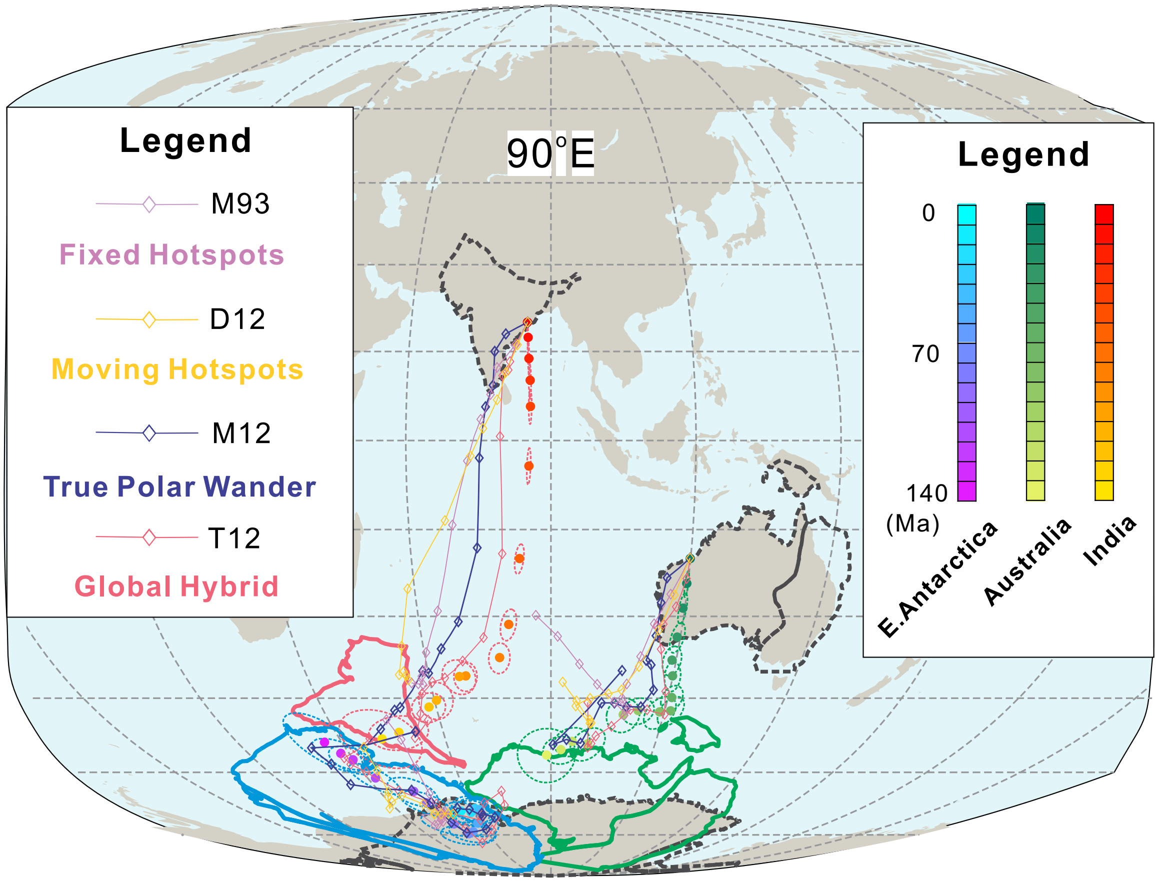

Figure 2.14: Motion history of the East Gondwanalands since 140 Ma predicted from different absolute plate motion models. The reconstructed configuration of the East Gondwanaland continents at 140 Ma from the APWPGP method is shown in the colored contours. The resulting APM trajectories for the references sites and associated error ellipses (Table 2.4) are shown in the color-coded dots. Also shown are the predictions (single-colored symbols and lines) from other APM models for comparison.

2.6 Caveats in the method of apparent polar wander paths geometric parameterizations

Readers need to be cautions when applying the APWPGP method for APM reconstructions. Firstly, there is a high requirement in the accuracy of input APWP(s). Secondly, there could be small errors in the reconstructions after paleolatitude corrections. This is caused by the imperfect restorations of older paleopoles to the geographic coordinates of the youngest paleopole. Thirdly, there could be exhaustive amount of data processing for tracing the somewhat subjectively decided optimal circle fitting options, which are consistent with independent geologic and/or geophysical evidence. Fourthly, there might be some indiscernible plate motions such as purely east-westward translation with respect to the Earth's spin axis (i.e., no APWP). Despite the limitations, the APWPGP method exhibits a good potential to reconstruct APMs back to the deep geologic history as long as there are reliable APWPs.

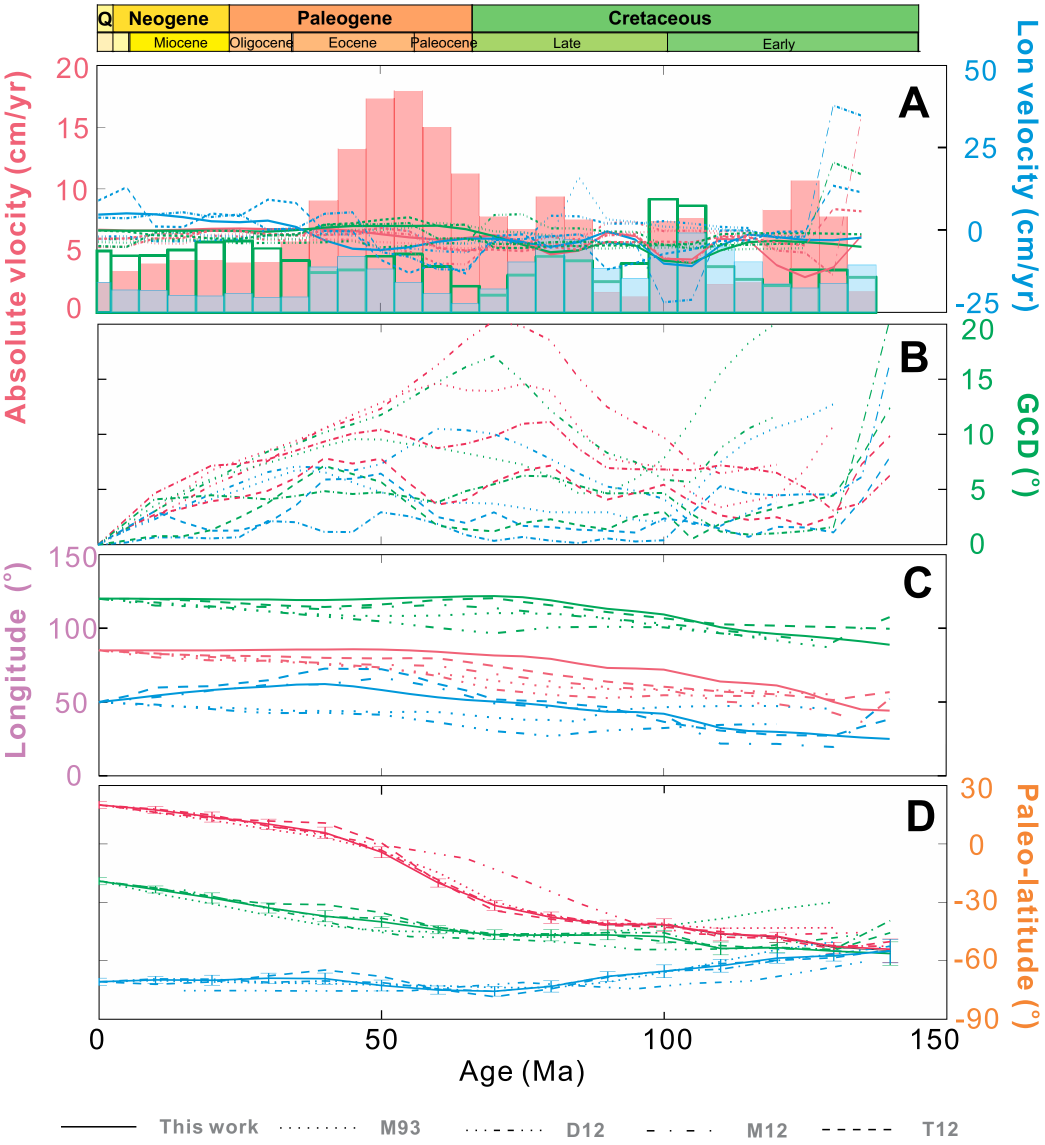

Figure 2.15: Comparison in the kinematic predictions from the various absolute plate motion methods. Red, green and blue colors show the calculations for India, Australia and East Antarctica, respectively. The comparisons are made in terms of (A) absolute motion velocities, (B) GCDs between reconstructions, (C) paleo-longitudinal predictions and (D) paleo-latitudinal predictions.

2.7 Conclusions

Restoring the past absolute plate motions (APMs) is a longstanding challenge in plate tectonic reconstructions. Paleomagnetism has been widely used to reconstruct paleolatitudes and azimuthal orientations but not paleolongitudes. In this chapter, we present a new method to constrain paleolongitudes by geometrically parametrizing apparent polar wander paths. Both great circle and small circle fittings are implemented to the identified APWP tracks to calculate rotation poles and associated angles. From Euler parameters, APMs can be derived for the studied plate geometries. By comparing our technique with other APM methods, we find that various models predict very different APMs. Using our new method, we reevaluate the separation history of the East Gondwanalands since 140 Ma. Our reconstructions indicate that the tectonic affinity between India and Australia-East Antarctica was broken down around 130-120 Ma, and that Australia and East Antarctica were separated at around 60-40 Ma.

3

PMTec: a Matlab-based graphical interface for plate reconstructions from paleomagnetism [a]

3.1 Introduction

Numerical characterization of plate motions on the Earth's surface is one of the longstanding interests and challenges in the geoscience community which underpins the advancement of plate tectonic paradigm. Theoretically, any displacement on the spherical Earth can be represented as a rotation around an Euler pole by a certain amount of angle [e.g. Cox and Hart, 1986; Schettino, 2014]. Using powerful computational facilities, Bullard et al. [1965] first implemented an iterative algorithm to match the conjugate coastlines bounding the Atlantic Ocean. In the studies of relative plate motions, marine geophysical observations including magnetic lineations and fracture zones are widely used to calculate Euler rotations [e.g. Schettino and Turco, 2009]. For absolute plate motions, Euler rotations are usually derived based on the geometric characterization of seamount trails, surface expression of hot spots [Morgan, 1971; Wessel and Kroenke, 1997], or on the combination of relative plate motions models and geometries of hot spots tracks [e.g. Müller et al., 1993]. Note that the formulation of any reliable plate kinematic model should have high-fidelity paleomagnetic constraints. Since the revelation of the compelling evidence that hot spots are not fixed in the mantle [Tarduno, 2007], refined rotation models have been presented mainly through implementing modelling of hot spot motions [e.g. O'Neill et al., 2005; Doubrovine et al., 2012]. By integrating plate motion models and true polar wander estimates, paleomagnetic data can also be used to define Euler rotations [e.g. Steinberger and Torsvik, 2008; Mitchell et al., 2012]. The outcome reconstructions, however, are associated with large uncertainties because of various underlying assumptions such as long-term stability of deep mantle structures [e.g.

---

[a] A version of this chapter has been published as:
Wu, L., Kravchinsky, V.A., Potter, D.K., 2015. PMTec: A new Matlab toolbox for absolute plate motion reconstructions from paleomagnetism. Computers & Geosciences, 82: 139-151.

Torsvik et al., 2014].

Inspired by the reconstruction of the eruption site of ∼250 Ma Siberia Traps using paleomagnetic Euler pole analysis [Smirnov and Tarduno, 2010], Wu and Kravchinsky [2014] formulate and demonstrate the methodology of absolute plate motion reconstructions by geometrically parameterizing apparent polar wander paths (APWP). This approach has the potential to extend absolute plate reconstructions back through deep time using high-quality paleomagnetic data. One primary motivation here is to present a software implementing the methodology of Wu and Kravchinsky [2014] to calculate absolute plate motions from paleomagnetic data. Notably, there is a new reconstruction method gaining popularity in recent years: using sinking slabs and deep mantle structures resolved from global mantle tomography models to correct for existing plate reconstructions primarily defined in the paleomagnetic reference frame [e.g. van der Meer et al., 2010, 2012; Torsvik et al., 2014]. This method usually starts with reconstructions presented in the paleomagnetic frame, and ends with modifying the input finite rotations using ancient subduction zones inferred from users' selected seismic tomography models. Note that reconstruction determinations should not depend on which of the different methodologies is employed, unless one or more of them is constructed on erroneous premises. In practice, we need to find the most sensible reconstructions that can explain as many observations as possible. However, this is not straightforward because of the large uncertainties from various methods. Here we incorporates a whole mantle P-wave tomographic model of Obayashi et al. [2006] with a good resolution of mantle dynamic features so users can fit the seismically derived reconstructions with paleomagnetic observations within uncertainties. The adjustment is usually achieved by rotating the reconstructions around an Euler pole to minimize the fitting discrepancies. In addition, the chapter also aims to promote our APWP construction module for the calculation of APWPs (in the forms of running means and spherical splines) and the correlated kinematic proxy parameters, the standard methods in the community to present and analyze paleomagnetic data for tectonic plate reconstructions.

Lots of software for plate reconstructions have been published in the past decades, such as GMAP [Torsvik and Smethurst, 1999], PaleoMac [Cogné, 2003], PLACA [Matias et al., 2005] and GPlates [Boyden et al., 2011] that can be used for reconstruction data processing and visualization. As a complement to the field, here we present a new MATLAB-based toolbox PMTec to perform absolute plate reconstructions from paleomagnetism. The mounting popularity of MATLAB in academia and industry provides an ideal platform to promote the use of PMTec both for plate tectonic research and educational demonstration purposes.

In this paper, we introduce the theoretical background, the component functioning modules, and data and file management for PMTec. To provide an overview of its usage, the main computation and visualization capabilities of PMTec are demonstrated with published data. The PMTec package together with tutorial document and data can be downloaded from http://www.ualberta.ca/∼vadim/software.htm.

3.2 Methodology

3.2.1 Construction of apparent polar wander paths

High-quality paleomagnetic poles are essential for the construction of reliable APWPs. For users of PMTec, all paleomagnetic data are recommended to be evaluated using the selection criteria proposed by Van der Voo [1990]: 1, adequate demagnetization and remanence components analysis; 2, field test (fold test, conglomerate test and bake test); 3, antipodal reversals; 4, firm statistical results with the number of samples no smaller than 24 and A_{95} no larger than 16°; 5, no large afterward localized rotations; 6, well-constrained age for the host rock; 7, no remagnetizations. For each criterion a given pole passes, it receives one point which will be added up to obtain the quality factor Q ranging from 0 to 7 [Van der Voo, 1990]. The higher the value of Q is, the more reliable the pole would be. For most continental plates, paleomagnetic poles with varying qualities have an unevenly data coverage in ages. Applying up-to-date Euler plate rotation models to transfer coeval poles across continents is one common solution [e.g. Torsvik et al., 2012]. For ages beyond the preservation of marine geophysical data, however, techniques other than using plate circuits are needed to determine the overall patterns of APWPs by averaging out random noises caused by inadequate quality and quantity of available paleomagnetic data. In PMTec, we present two most commonly implemented methods for APWP constructions: running average means and spherical smoothing splines.

Running means are calculated from selected subsets of paleomagnetic data falling within the specified window of time intervals. Elliptical errors of input paleo-poles defined by semi-axes dm and dp need to be converted into circular ones A_{95} using the approximation formula $A_{95} = \sqrt{dm \times dp}$ suggested by Khramov [1987]. Mean pole position with error in each of time windows are computed using the method of McFadden and McElhinny [1995]. Error is not presented if there is only one paleo-pole in a time interval. Practically, there might be some blank intervals (especially for earlier ages before the Middle Paleozoic) when reliable paleo-poles are sparse. Running means paths can be jerky with abrupt cusps and anomalously high migration velocities that can be caused by the combined uncertainties in age progression and paleo-pole positions. In such situation, spherical splines have proved to be able to retrieve the main features of apparent polar trajectory by averaging our random noises [Jupp and Kent, 1987]. However, no errors are estimated from spline calculations.

In PMTec we implement a spherical splines algorithm originally presented by Jupp and Kent [1987] that has been widely used for constructing APWPs. One notable merit of this technique is that spline paths are anchored to the most reliable paleo-poles with higher weights (qualities) [e.g. Jupp and Kent, 1987; Torsvik et al., 2012]. Weighting scheme for the algorithm evolves with time, primarily based on A_{95} [Torsvik and Smethurst, 1999], quality factor Q [e.g. Torsvik et al., 2001] or 7/Q [Torsvik et al., 2012]. In PMTec, we use 7/Q for paleo-poles weighting. Different smoothing parameters S should be tested until visually satisfying paths are obtained. Generally speaking, smaller S produces a less smoothed curve which closely passes input poles, while larger S yields a smoother curve that does not necessarily approach every data point.

3.2.2 Absolute plate motion reconstructions from APWPs

In plate tectonics, Euler rotations, a.k.a. rotation poles and angles, are well-established parameters to describe motion trajectory of the studied plate geometry in a designated reference frame (e.g. spin axis of the Earth) [Cox and Hart, 1986; Schettino, 2014]. Before these parameters, the type of rotations at hands (finite or stage) have to be distinguished: finite rotations (or total rotations) rotate plates to and from their present locations while stage rotations describe plate motions during certain time intervals [Cox and Hart, 1986; Schettino, 2014]. Usually, plate tectonics softwares such as GMAP [Torsvik and Smethurst, 1999] and GPlates [Boyden et al., 2011] use finite rotations which are derived from marine magnetic lineations and sea-floor fracture zones, geometries of hot spot tracks or paleomagnetic data. However, to provide paleo-longitudinal constrains in the paleomagnetic frame, Wu and Kravchinsky [2014] recently formulated the methodology of deriving paleomagnetic Euler rotations (stage rotations) by fitting APWP tracks either with great circle or small circle modelling. In PMTec, we allow the conversion between finite and stage rotations by implementing the formulas summarized by Doubrovine et al. [2012]. Moreover, PMTec also supports the use of finite rotations for plate reconstructions and kinematics calculations. Note that PMTec follows the protocol that positive signs are assigned to rotation angles of counterclockwise rotations for reconstruction purpose. Conversely, performing forward motions would require negative signs for the same rotations.

From stage rotations, PMTec constructs a series of rotation matrices to perform rotations on the spherical Earth. During each rotation stage, paleolatitude corrections need to be applied to the calculations to ensure the paleo-colatitudinal consistency between reconstructions and corresponding paleomagnetic predictions. To this end, Wu and Kravchinsky [2014] suggested the use of paleo-colatitudes defined in the paleomagnetic frame to shift the positions of reconstructions along the great circle arcs (i.e. paleo-meridians) connecting paleo-poles (representing the spin axis) and reconstructions. Errors both for paleomagnetic Euler poles and resulting reconstructions are approximated by covariance matrix ellipses encircling 95% of bootstrapped data points which are assumed to follow Fisherian distribution. Readers are referred to Wu and Kravchinsky [2014] for detailed description of the methodology. The reliability of outcome reconstructions primarily depends on the quality of input APWPs and the rationality of APWP tracks fitting. Note that there might be undetectable plate motions during intervals when no apparent polar wandering is recorded.

3.3 PMTec toolbox presentation

3.3.1 Overview of PMTec

PMTec is developed and optimized on a PC but can also be run on Mac and Linux systems. Table 3.1 lists the major functioning PMTec modules with brief descriptions. The main interface of PMTec is comprised of five panels (Figure 3.1A): logo panel, projection panel, toolbar panel, data visualization panel and utilities panel. The projection panel interactively displays the imported paleomagnetic and geometry data with or without the plotting of background data on the specified map projection. Using the toolbar panel, users can manually adjust viewpoint, add/remove colorbar and save figures as editable *.pdf files. In the utilities panel (Figure 3.1a), eight functioning modules can be called 1) to construct APWPs and derive paleomagnetic Euler rotations (stage rotations) from paleomagnetic data, 2) to perform absolute plate reconstructions using stage rotations or finite rotations, and 3) to visualize and export results in the format of MATLAB structure data. Detailed descriptions about each utility module will be made in the following subsections.

Table 3.1: Summary of the main modules of PMTec.

Module Name	Development Code	Brief description of the primary utilities
PMTec	PMTec	1. Plot paleomagnetic and geometry data with(out) the background of plate boundaries, TOPO2 or whole mantle tomography. 2. Call for the affiliated computation and visualization modules.
Fisher Mean	PMTec_Fish	1. Calculate Fisher statistics for paleomagnetic or directional data.
Bootstrap Resampling	PMTec_BootRes	1. Perform bootstrap resampling for paleomagnetic or directional data.
APWP Construction	PMTec_APWP	1. Construct APWP both in form of running means and spherical spline. 2. Compute the APWP migration velocity, paleolatitude variation and rotation rates for the specified reference site.
Circle Parameterization	PMTec_Euler	1. Fit the specified APWP tracks using both great circle and small circle fitting.
Reconstruction	PMTec_Reconstr	1. Compute absolute plate reconstructions for the specified plate(s) using the APWPGP technique. 2. Uncertainty estimation for the calculated reconstructions of the specified reference site.
Plate Kinematics	PMTec_PtKin	1. Calculate kinematic information (absolute velocity, latitude and longitude velocities and paleolatitude and paleolongitude variations) for the specified reference site 2. Finite and stage rotation poles conversion. 3. Prepare PlateRec.mat file for the animation making.
Plate ID Shape	PMTec_PlateID	1. Make shape file that can be used in GPlates.
Animation Maker	PMTec_AniMaker	1. Make animation from the selected PlateRec.mat file(s) and save the movie in form of *.mov or *.gif.

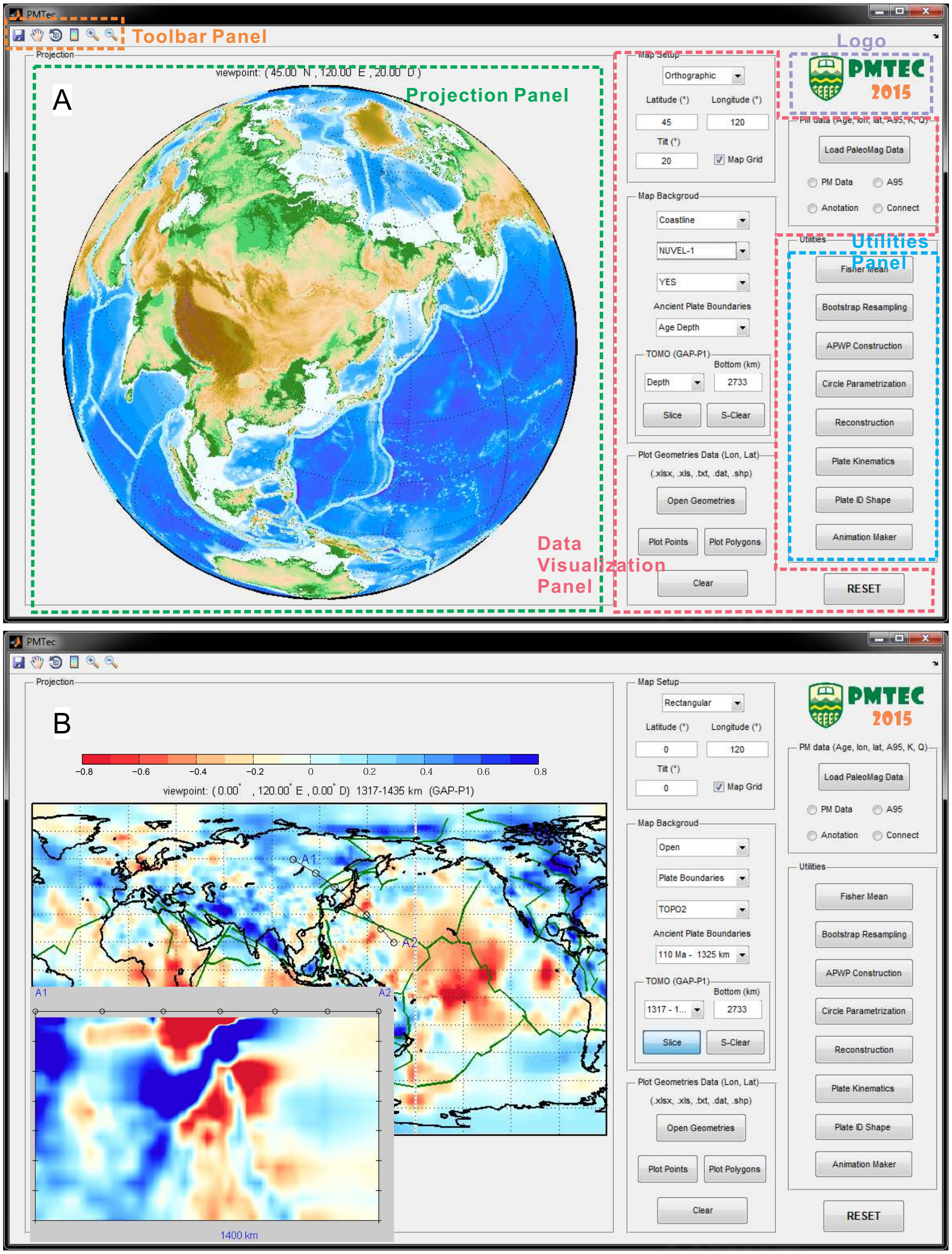

A: viewpoint: (45.00 N , 120.00 E , 20.00 D)
Map Setup: Orthographic; Latitude (°) 45; Longitude (°) 120; Tilt (°) 20; ☑ Map Grid
Map Backgroud: Coastline; NUVEL-1; YES; Ancient Plate Boundaries: Age Depth
TOMO (GAP-P1): Depth; Bottom (km) 2733

B: viewpoint: (0.00 , 120.00 E , 0.00 D) 1317-1435 km (GAP-P1)
Map Setup: Rectangular; Latitude (°) 0; Longitude (°) 120; Tilt (°) 0; ☑ Map Grid
Map Backgroud: Open; Plate Boundaries; TOPO2; Ancient Plate Boundaries: 110 Ma - 1325 km
TOMO (GAP-P1): 1317 - 1...; Bottom (km) 2733

Figure 3.1: Screen shot of the main interface of PMTec, with the colored dashed boxes highlighting the main functionality panels. (A) Orthographic projection of NUVEL-1 plate boundaries [DeMets et al., 1990] (light blue lines) plotted on TOPO2 data grid with a reduction factor of 4 [Hastings et al., 1999]. (B) Rectangular projection of a mid-mantle slice (1317-1435 km) using P-wave tomography model GAP-P1 [Obayashi et al., 2006], where Neo-Tethys and Farallon slabs are clearly resolved underneath present-day southern Eurasia and east coast North America. Also shown in the figure are ancient plate boundaries defined in subduction frame of van der Meer et al. [2010, 2012]. Inset figure shows the vertical cross-section for profile A1-A2 from which the Pacific subduction is distinctly outlined.

In the data visualization panel, users can select a series of popular mapping projections with desired viewpoint: Mollweide, Orthographic, Robinson, Mercator, Sinusoidal and Rectangular. For reference, present-day coastline, plate boundaries [DeMets et al., 1990; Bird, 2003], 2-minute gridded global relief TOPO2 data [Hastings et al., 1999] and a whole mantle P-wave tomography [Obayashi et al., 2006] can be plotted, in addition to input geometry or paleomagnetic data. Given the considerable amount of time to plot all the data from TOPO2, PMTec provides a lower resolution rendering by reducing the original dataset with a factor of four (Figure 3.1A). To facilitate the effort of linking surface plate tectonics with mantle features [e.g. van der Meer et al., 2010, 2012; Torsvik et al., 2014], PMTec includes a set of ancient plate boundaries primarily defined in the subduction frame of van der Meer et al. [2010, 2012] (Figure 3.1B). To allow for adjustments for these boundaries and reconstructions, PMTec also includes a whole mantle P-wave tomography model GAP-P1 [Obayashi et al., 2006] in the form of percentage velocity perturbations with respect to PREM [Dziewonski and Anderson, 1981]. Derived from 7.4 million first arrivals reported to the International Seismological Centre [Obayashi et al., 2006], model GAP-P1 is recommended in PMTec because of its good resolution for large scale mantle features. Figure 3.1B, for instance, shows the tomographic depth slice of 1317-1435 km (mid-mantle) where Neo-Tethys and Farallon slabs are clearly resolved under present-day southern Eurasia and eastern North America. From selected profiles PMTec is able to plot velocity perturbations in vertical cross-sections down to specified depths. (Figure 3.1B). Figure 3.1B inset, for instance, outlines the subduction zone in northwestern Pacific along profile A1-A2.

Table 3.2: Description of the variables and data files used in PMTec.

File type	Data format description	File format	Usage (inpurt) / Source (output)
Input files			
Paleomag (directional) data	(age lat lon A95 K Q)[a]	*.xlsx; *.xls; *.txt; *.dat	PMTec; PMTec_Fish; PMTec_BootRes; PMTec_APWP; PMTec_Euler; PMTec_Reconstr
Geometry data	(lon,lat)	*.xlsx; *.xls; *.txt; *.dat; *.shp	PMTec; PMTec_PtKin; PMTec_Reconstr;PMTec_PlateID
FitCtrl file	(pole1,pole2,GCdirS,SCdirS)	*.xlsx; *.xls; *.txt; *.dat	PMTec_Euler
PEP file	(lonE latE omega npts sign FC)	*.xlsx; *.xls; *.txt; *.dat	PMTec_Reconstr

RecSt file	f1=[APWP,tracks];
	f2=[APWP,tracks_transf];
	f3=[PEP;PEP_transferred];
	f4=[ref ref_cor (ref_adj) (ref_cor)];
	f5=[plate];
	f6=[plate_cor (plate_adj)];
	f7=[(plate_cor)];
	f8=[age Velo LatV LonV];
	f9-f10: backup storage
		*.mat	PMTec_Reconstr; PMTec_PtKin;
			PMTec_AniMaker

APWPboot (DIRCboot)	f1=[bootstrap directions (lon lat)]; f2=[(lonMean latMean A95 K)];	*.mat	PMTec_Reconstr
Finite rotation file	(age lon lat omega)	*.xlsx; *.xls; *.txt; *.dat	PMTec_Reconstr; PMTec_PtKin;
Stage rotation file	(age lon lat omega)	*.xlsx; *.xls; *.txt; *.dat	PMTec_PtKin

PlateRec	f1=[ref];
	f2=[plate];
	f3=[age Velo LatV LonV];
		*.mat	PMTec_PtKin; PMTec_AniMaker

Output files			
Fisher mean	(Dm Im a95 k)	*.txt	PMTec_Fish
APWPboot (DIRCboot)	see above	*.mat	PMTec_BootRes

APWP	f1=Running Mean [age lon lat A95 K npts];
	f2=Spline [age lon lat];
	f3=Running Mean [age Plat V Rot RotV];
	f4=Spline [age Plat V Rot RotV];
		*.mat	PMTec_APWP

Euler Single Fit	Fit=(lonGC latGC omegaGC radiusGC ?? lonSC latSC omegaSC radiusSC ?? npts GCdirS SCdirS Vr Critical Value)	*.txt	PMTec_Euler
Euler Batch Fit	f1=GC fit=(lon lat omega npts dirS FC); f2=SC fit=(lon lat omega npts dirS FC); f3=Fit	*.mat	PMTec_Euler
RecSt file	see above	*.mat	PMTec_Reconstr intermediate calcs
BootAPWP	[bootstrap APWP; bootstrap APWP_transf]	*.mat	PMTec_Reconstr intermediate calcs

---

[a] Q - quality factor for a paleo-pole.

Table 3.2 Continued: Data and files management in PMTec

BootEuGC	f1=GC bootfit=[lon lat omega npts dirS FC]; f2=GC bootfit=[lon lat radius residual]	*.mat	PMTec_Reconstr intermediate calcs
BootEuSC	f1=SC bootfit=[lon lat omega npts dirS FC]; f2=SC bootfit=[lon lat radius residual]	*.mat	PMTec_Reconstr intermediate calcs
StrucEuAPWP	f1=bootfit=[lon lat omega npts dirS FC]; f2=[bootstrap APWP (lon lat)]; f3=[bootEuler para; bootEuler para_transf]	*.mat	PMTec_Reconstr intermediate calcs
BootEuAPWPnew	f1=[Euler para_transf]; f2=[APWP_transf]	*.mat	PMTec_Reconstr intermediate calcs

BootEuNewRG	f1=[bootEuler para];
	f2=[bootEuler para_transf];
	f3=[bootEuler para_transf; bootEulerMean; Cov; GCD];
	f4=Uncertainties[bootEuler bootEuler_transf]
		*.mat	PMTec_Reconstr

BootRec	f1=bootstrap ref; f2=bootstrap ref_transf	*.mat	PMTec_Reconstr intermediate calcs

BootRecRG	f1=[bootstrap ref];
	f2=[bootstrap ref_cor];
	f3=[ref_cor;boot ref_cor Mean;Cov;GCD];
	f4=Uncertainties[boot ref boot ref_cor]
		*.mat	PMTec_Reconstr

Finite rotaion file	(age lon lat omega)	*.txt	PMTec_PtKin
Stage rotaion file	(age lon lat omega)	*.txt	PMTec_PtKin
PlateRec	see above	*.mat	PMTec_PtKin; PMTec_AniMaker
Shape file	(lon lat)	*.shp	PMTec_PlateID
Movie	reconstrcution animation	*.mov; *.gif	PMTec_AniMaker
Figure	saved figures	*.pdf	PMTec
Background data			
Plate boundaries	NUVEL-1 and PB2003 model	StructData140917.mat	PMTec
TOPO2	2-Minute Gridded Global Relief Data	ETOPO2.raw.bin	PMTec
GAP-P1	P-wave whole mantle tomography	StructData140917.mat	PMTec; PMTec_AniMaker

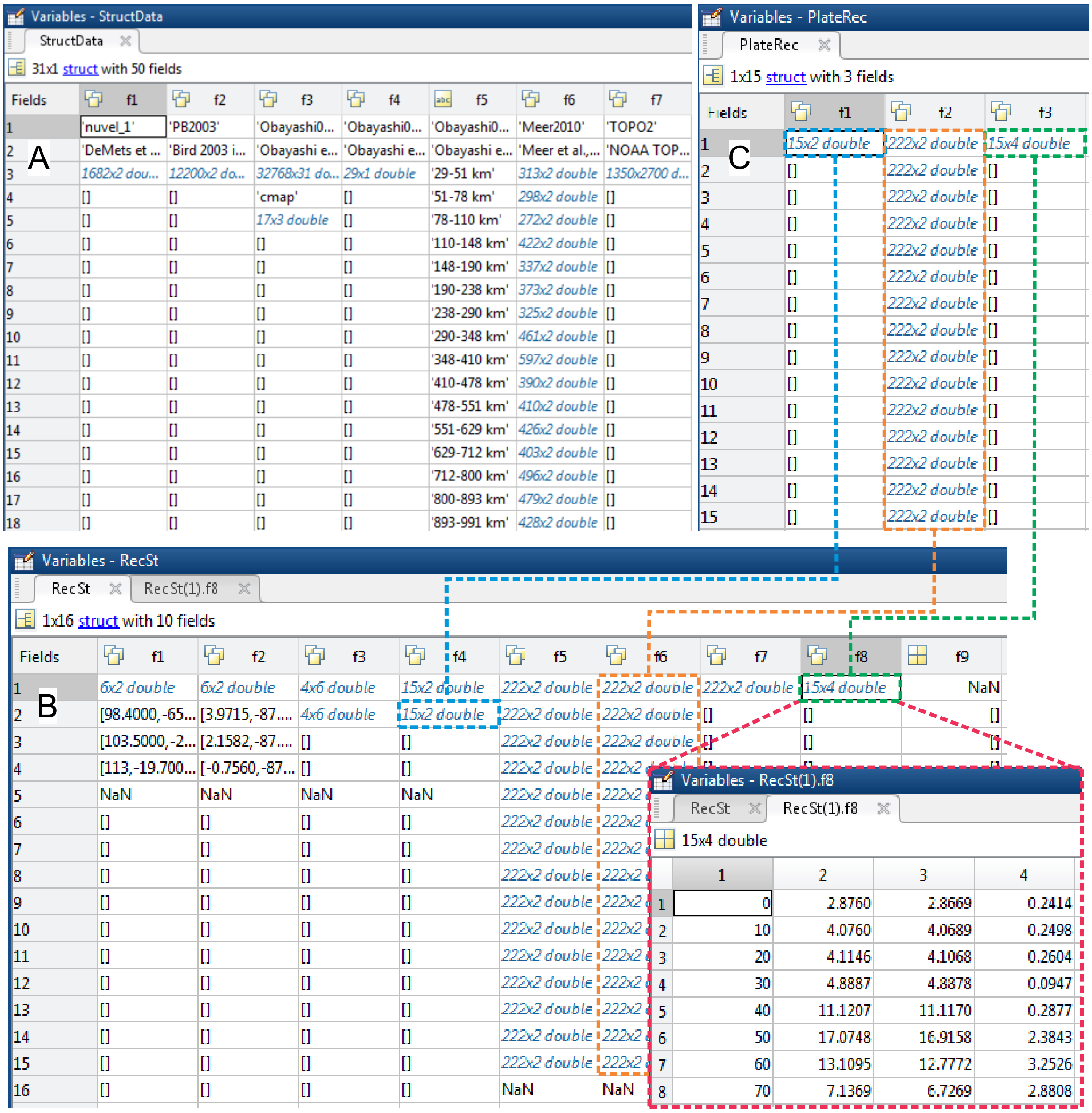

Variables - StructData

StructData

31x1 struct with 50 fields

Fields	f1	f2	f3	f4	f5	f6	f7
1	'nuvel_1'	'PB2003'	'Obayashi0...	'Obayashi0...	'Obayashi0...	'Meer2010'	'TOPO2'
2	'DeMets et ...	'Bird 2003 i...	'Obayashi e...	'Obayashi e...	'Obayashi e...	'Meer et al.,...	'NOAA TOP...
3	1682x2 dou...	12200x2 do...	32768x31 do...	29x1 double	'29-51 km'	313x2 double	1350x2700 d...
4	[]	[]	'cmap'	[]	'51-78 km'	298x2 double	[]
5	[]	[]	17x3 double	[]	'78-110 km'	272x2 double	[]
6	[]	[]	[]	[]	'110-148 km'	422x2 double	[]
7	[]	[]	[]	[]	'148-190 km'	337x2 double	[]
8	[]	[]	[]	[]	'190-238 km'	373x2 double	[]
9	[]	[]	[]	[]	'238-290 km'	325x2 double	[]
10	[]	[]	[]	[]	'290-348 km'	461x2 double	[]
11	[]	[]	[]	[]	'348-410 km'	597x2 double	[]
12	[]	[]	[]	[]	'410-478 km'	390x2 double	[]
13	[]	[]	[]	[]	'478-551 km'	410x2 double	[]
14	[]	[]	[]	[]	'551-629 km'	426x2 double	[]
15	[]	[]	[]	[]	'629-712 km'	403x2 double	[]
16	[]	[]	[]	[]	'712-800 km'	496x2 double	[]
17	[]	[]	[]	[]	'800-893 km'	479x2 double	[]
18	[]	[]	[]	[]	'893-991 km'	428x2 double	[]

Variables - PlateRec

PlateRec

1x15 struct with 3 fields

Fields	f1	f2	f3
1	15x2 double	222x2 double	15x4 double
2	[]	222x2 double	[]
3	[]	222x2 double	[]
4	[]	222x2 double	[]
5	[]	222x2 double	[]
6	[]	222x2 double	[]
7	[]	222x2 double	[]
8	[]	222x2 double	[]
9	[]	222x2 double	[]
10	[]	222x2 double	[]
11	[]	222x2 double	[]
12	[]	222x2 double	[]
13	[]	222x2 double	[]
14	[]	222x2 double	[]
15	[]	222x2 double	[]

Variables - RecSt

RecSt RecSt(1).f8

1x16 struct with 10 fields

Fields	f1	f2	f3	f4	f5	f6	f7	f8	f9
1	6x2 double	6x2 double	4x6 double	15x2 double	222x2 double	222x2 double	222x2 double	15x4 double	NaN
2	[98.4000,-65...	[3.9715,-87....	4x6 double	15x2 double	222x2 double	222x2 double	[]	[]	[]
3	[103.5000,-2...	[2.1582,-87....	[]	[]	222x2 double	222x2 double	[]	[]	[]
4	[113,-19.700...	[-0.7560,-87...	[]	[]	222x2 double	222x2	[]	[]	[]
5	NaN	NaN	NaN	NaN	222x2 double	222x2			
6	[]	[]	[]	[]	222x2 double	222x2			
7	[]	[]	[]	[]	222x2 double	222x2			
8	[]	[]	[]	[]	222x2 double	222x2			
9	[]	[]	[]	[]	222x2 double	222x2			
10	[]	[]	[]	[]	222x2 double	222x2			
11	[]	[]	[]	[]	222x2 double	222x2			
12	[]	[]	[]	[]	222x2 double	222x2			
13	[]	[]	[]	[]	222x2 double	222x2			
14	[]	[]	[]	[]	222x2 double	222x2			
15	[]	[]	[]	[]	222x2 double	222x2			
16	[]	[]	[]	[]	NaN	NaN			

Variables - RecSt(1).f8

RecSt RecSt(1).f8

15x4 double

	1	2	3	4
1	0	2.8760	2.8669	0.2414
2	10	4.0760	4.0689	0.2498
3	20	4.1146	4.1068	0.2604
4	30	4.8887	4.8878	0.0947
5	40	11.1207	11.1170	0.2877
6	50	17.0748	16.9158	2.3843
7	60	13.1095	12.7772	3.2526
8	70	7.1369	6.7269	2.8808

Figure 3.2: Illustration of three cardinal structure variables for PMTec. (A) Data organization of system variable 'StructData'. The first two rows of each fields are string values annotating data names and source publications, with numerical values starting from the third row. Fields after 'f5' are backup storages preserved for future PMTec releases. (B) Structure of variable 'RecSt', which stores APWP tracks, paleomagnetic Euler rotations, reconstructions (reference site and plate geometry) with/without paleolatitude corrections, and plate kinematic parameters. PMTec reads and writes data in file 'RecSt.mat' automatically during calculations. The inset figure shows the way to access structure variables, where 'RecSt(1).f8' is a MATLAB command to extract the first data row in the field 'f8' from variable 'RecSt'. (C) Structure of variable 'PlateRec' for visualizing reconstructions made from stage or finite rotations. The dashed lines and boxes in blue, orange and green show the procedure to construct 'PlateRec' from 'RecSt'. Readers are referred to Table 3.2 for field descriptions of the structure variables used in PMTec. The demonstration data here are the reconstructions of India since 140 Ma [Wu and Kravchinsky, 2014].

For an effective data and file management, a set of variables (system, input and output) are introduced here. Readers are referred to Table 3.2 for detailed descriptions of data organization, file format and usage (as input or output data for different modules) of each variable in PMTec. MATLAB structure array is widely used in PMTec because of 1) its capability of accessing string and numerical values simultaneously and 2) the memory efficiency during computation especially in bootstrap error estimates. In Figure 3.2, the organizations of three most important structure variables in PMTec are illustrated. As the system variable, 'StructData' stores descriptions, references and numerical values of background data, including present-day plate boundaries and GAP-P1 tomography model (Figure 3.2A). Additional fields are created in 'StructData' for potential data inclusions for future PMTec releases. Variable 'RecSt' stores most of numerical values involved in absolute plate motion reconstructions from paleomagnetism, including APWP tracks, Euler rotations, reconstructed plates and corresponding kinematic parameters (Table 3.2). In PMTec, users need to start with building a 'RecSt.mat' file, and proceed to fill in all the designated fields with subsequent computations (Figure 3.2B) before transferring part of results to variable 'PlateRec' for data visualization (Figure 3.2C). Alternatively, 'PlateRec.mat' files can be made from known finite rotations and plate geometries for reconstructions.

3.3.2 From paleomagnetic poles to APWP

Unlike other paleomagnetic softwares such as PaleoMac [Cogné, 2003] and PmagPy [Tauxe et al., 2010] which are designed to process demagnetization and directional data, PMTec focuses on APWP constructions from available paleo-poles. In PMTec, users can calculate both running means and spherical splines from an imported paleo-poles file, which must be prepared in the requested format (Figure 3.3A, Table 3.2). Strict data quality assessment using Voo's scheme [Van der Voo, 1990] beforehand is a must to secure the quality of outcome APWP calculations.

Module PMTec_APWP calculates APWPs and correlated kinematic parameters, including APWP migration velocities, paleolatitude variations and rotation rate for a specified reference site. After loading the data file, users can selectively visualize paleo-poles and their errors (Figure 3.3). For reference, all paleo-poles are automatically annotated with their ages specified in the first column of the imported data file. For running means, various age increments (or steps) and time average windows can be tested for different smoothness of the outcome path. In general, the smaller time windows are, the closer resulting paths are to input data. Similarly, users can specify smoothing parameter and interpolation age to obtain spherical splines with variant smoothness. Larger smoothing parameters tend to smooth outcome curves more. In addition, corresponding time-dependent kinematic proxies can be derived for an arbitrary reference site. All the calculations, i.e. running means, splines and APWP kinematics, are saved and exported as the structure variable ‘APWP’ with four fields (Table 3.2).

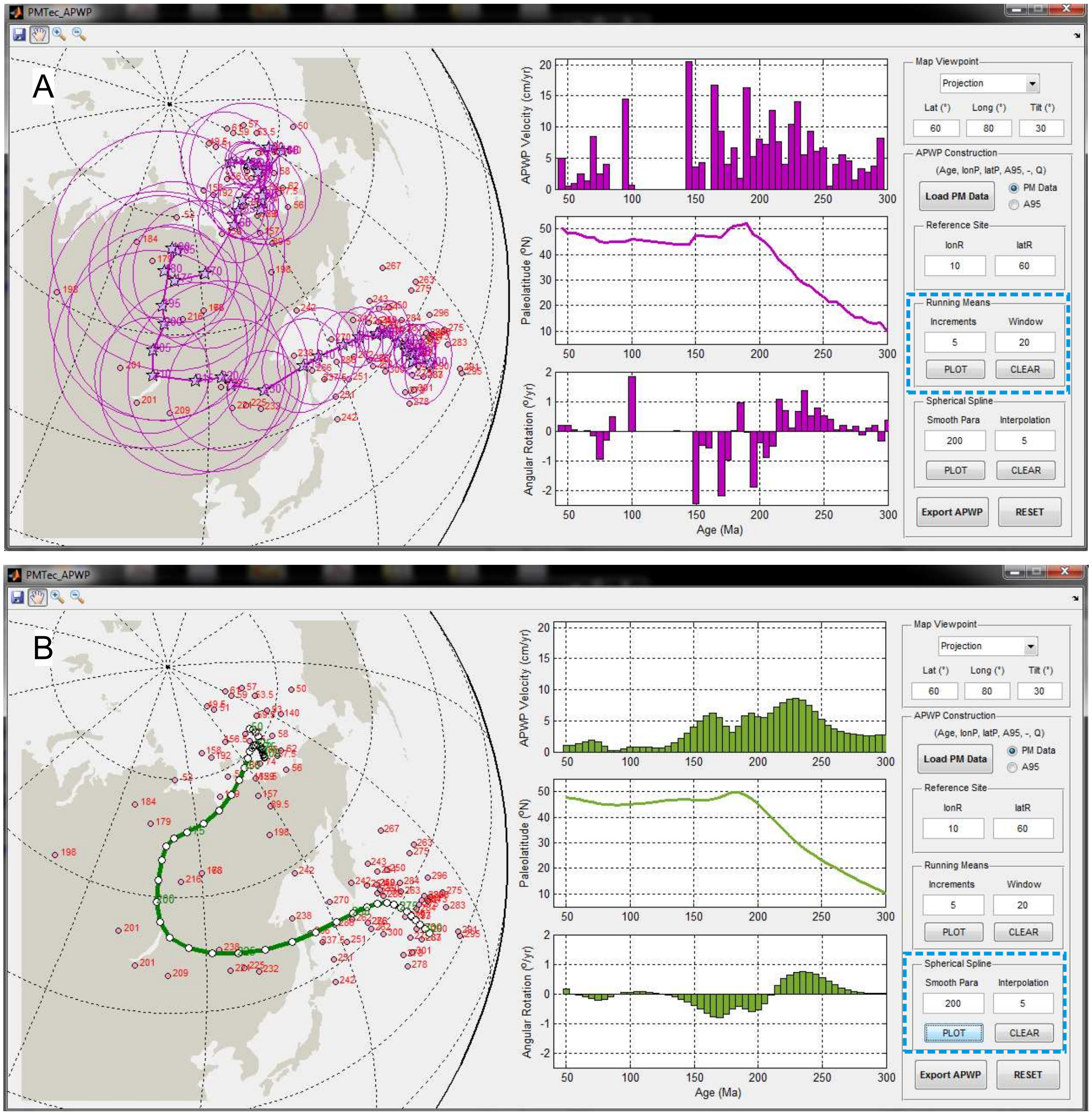

Map Viewpoint: Projection

Lat (°) 60 Long (°) 80 Tilt (°) 30

Reference Site: lonR 10 latR 60

Running Means: Increments 5 Window 20

Spherical Spline: Smooth Para 200 Interpolation 5

Figure 3.3: Illustration of the main utilities of the PMTec_APWP module. Except for running means (A) and spherical splines (B), kinematic proxies including APWP migration velocities, paleolatitudinal and azimuthal variations for an arbitrary reference site can also be computed in the module. European paleomagnetic poles (pink circles) are from Supplementary Table 1b of Torsvik et al. [2001]. Blue dashed boxes mark the governing parameters for APWP calculations.

3.3.3 From APWP to tectonic plate reconstructions

Assuming that no true polar wander occurred during the studied time intervals, paleomagnetic Euler rotations can be derived by fitting APWP tracks using circle modelling. Paleopoles at two ends and rotation directions for circle modelling (great circle and small circle) need to be specified for APWP tracks in the module PMTec_Euler (Figure 3.4A). PMTec_Euler recommends the preferred fitting code by comparing variance ratio (V_r, significant improvement of small circle over great circle modelling) and critical value (C_v, value of F-distribution probability density function $F_{1,n-3}$, where n is the number of poles along the APWP track) at 95% confidence level [Wu and Kravchinsky, 2014]. To accelerate the fitting process, PMTec_Euler allows concurrent circle modelling to several APWP tracks with an input fitting control variable 'FitCtrl' (Figure 3.4B, Table 3.2). The outcomes, i.e. great circle and small circle Euler parameters from batch fittings, are saved and exported in a structure variable (Table 3.2). Note that the fitting code recommended by PMTec is a statistical determination which is not necessarily the optimal fitting option. The optimal fitting code can only be determined when the resulting reconstructions are consistent with geologic and/or geophysical observations [Wu and Kravchinsky, 2014].

PMTec_Reconstr is the core module to perform absolute plate reconstructions from paleomagnetic data. As is discussed in section 3.3.1, PMTec uses structure variable 'RecSt' to manage and manipulate all the data involved in the reconstruction process and error estimation (Figure 3.2B, Table 3.2). Therefore, users need to start with making a 'RecSt.mat' file out of paleomagnetic Euler rotations, APWP and plate geometry files before calculations. PMTec automatically picks the first data point from geometry data file as the reference site; this can be manually changed later. After obtaining reconstructions of all ages, error ellipses both for Euler stage poles and reconstructions can be estimated using an input bootstrap APWP file 'APWPboot.mat' (Table 3.2) generated in the module PMTec_Fish (Table 3.1). Figure 3.5A illustrates the work flow to fill in the designated fields in 'RecSt' step by step. Bootstrapped Euler rotations and reconstructions as well as their uncertainties are saved in separate structure data files 'BootEuNewRG.mat' and 'BootRecRG.mat'. Intermediate calculations during error estimations are saved in variables 'BootAPWP', 'BootEuGC', 'BootEuSC', 'StrucEuAPWP', 'BootEuAPWPnew' and 'BootRec', which if necessary can be exported using the pop-up menu (Figure 3.5B). See Table 3.2 for the detailed descriptions of these variables. In actual plate reconstructions, users may want to modify their reconstructions to produce more 'sensible' ones. This can be achieved by importing separate finite rotation files. The modified reconstructions are saved in field ‘f6’ of ‘RecSt’ with the original calculations being relocated to field ‘f7’ (Table 3.2).

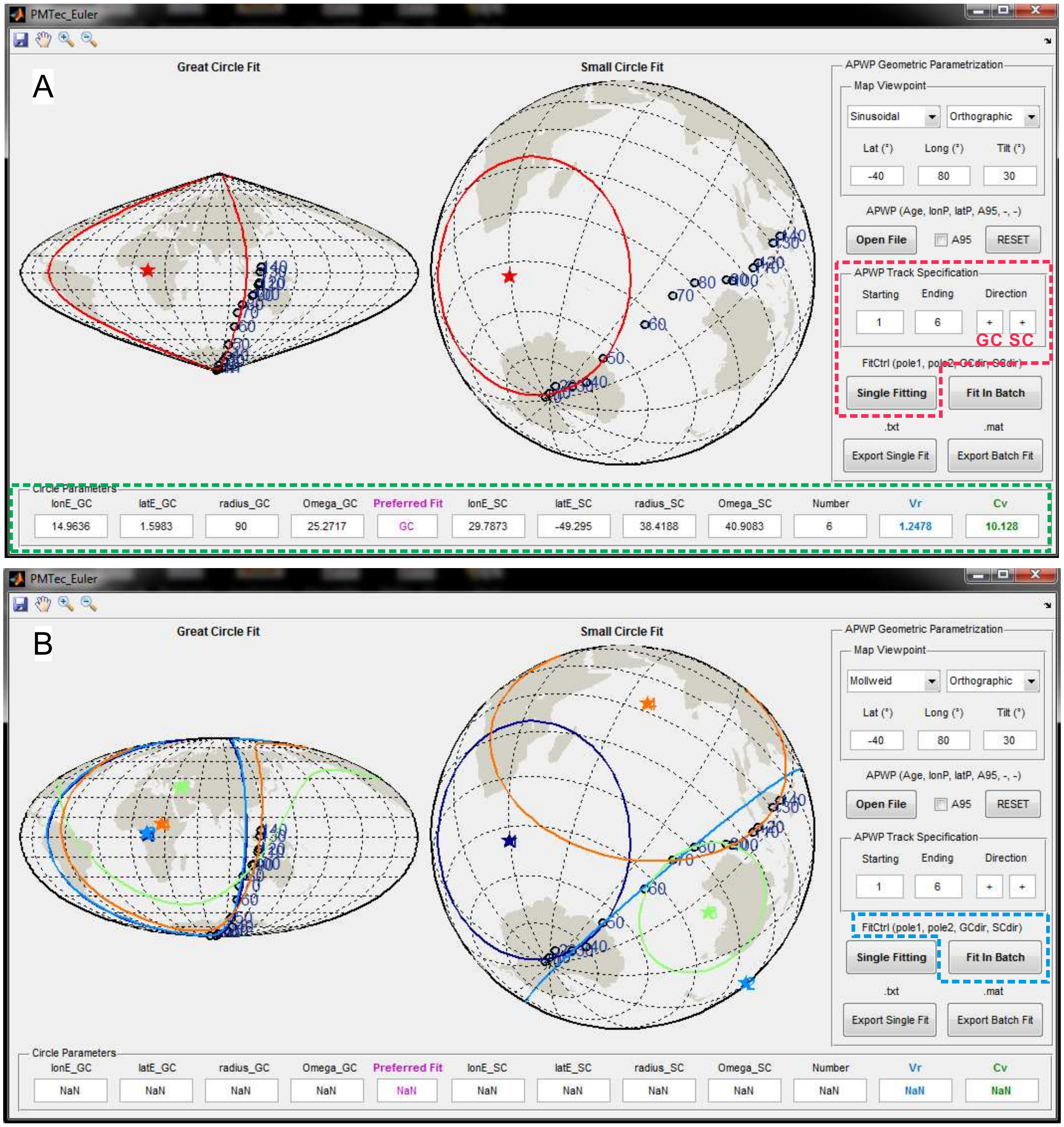

A

Map Viewpoint: Sinusoidal, Orthographic

Lat (°)	Long (°)	Tilt (°)
-40	80	30

APWP (Age, lonP, latP, A95, -, -)

APWP Track Specification

Starting	Ending	Direction	
1	6	+	+

FitCtrl (pole1, pole2, GCdir, SCdir)

Circle Parameters

lonE_GC	latE_GC	radius_GC	Omega_GC	Preferred Fit	lonE_SC	latE_SC	radius_SC	Omega_SC	Number	Vr	Cv
14.9636	1.5983	90	25.2717	GC	29.7873	-49.295	38.4188	40.9083	6	1.2478	10.128

B

Map Viewpoint: Mollweid, Orthographic

Lat (°)	Long (°)	Tilt (°)
-40	80	30

APWP (Age, lonP, latP, A95, -, -)

APWP Track Specification

Starting	Ending	Direction	
1	6	+	+

FitCtrl (pole1, pole2, GCdir, SCdir)

Circle Parameters

lonE_GC	latE_GC	radius_GC	Omega_GC	Preferred Fit	lonE_SC	latE_SC	radius_SC	Omega_SC	Number	Vr	Cv
NaN	NaN	NaN	NaN	NaN	NaN	NaN	NaN	NaN	NaN	NaN	NaN

Figure 3.4: Euler rotations derivation using the module PMTec_Euler. The demonstration data is Indian APWP of 0-140 Ma presented by Torsvik et al. [2012]. (A) Single APWP track fitting by specifying two ending paleo-poles and rotation direction (red dashed box). The text boxes beneath the projection panel (green dashed box) show the calculated circle parameters with the recommended fitting code after comparing variance ratio (V_r) and critical value (C_v) at 95% confidence level [Wu and Kravchinsky, 2014]. (B) Concurrent circle fittings to several APWP tracks by loading control files ‘FitCtrl’ (blue dashed box). Outcome Euler parameters are exported as structure data file (*.mat). See Table 3.2 for the management of data and files involved in the module.

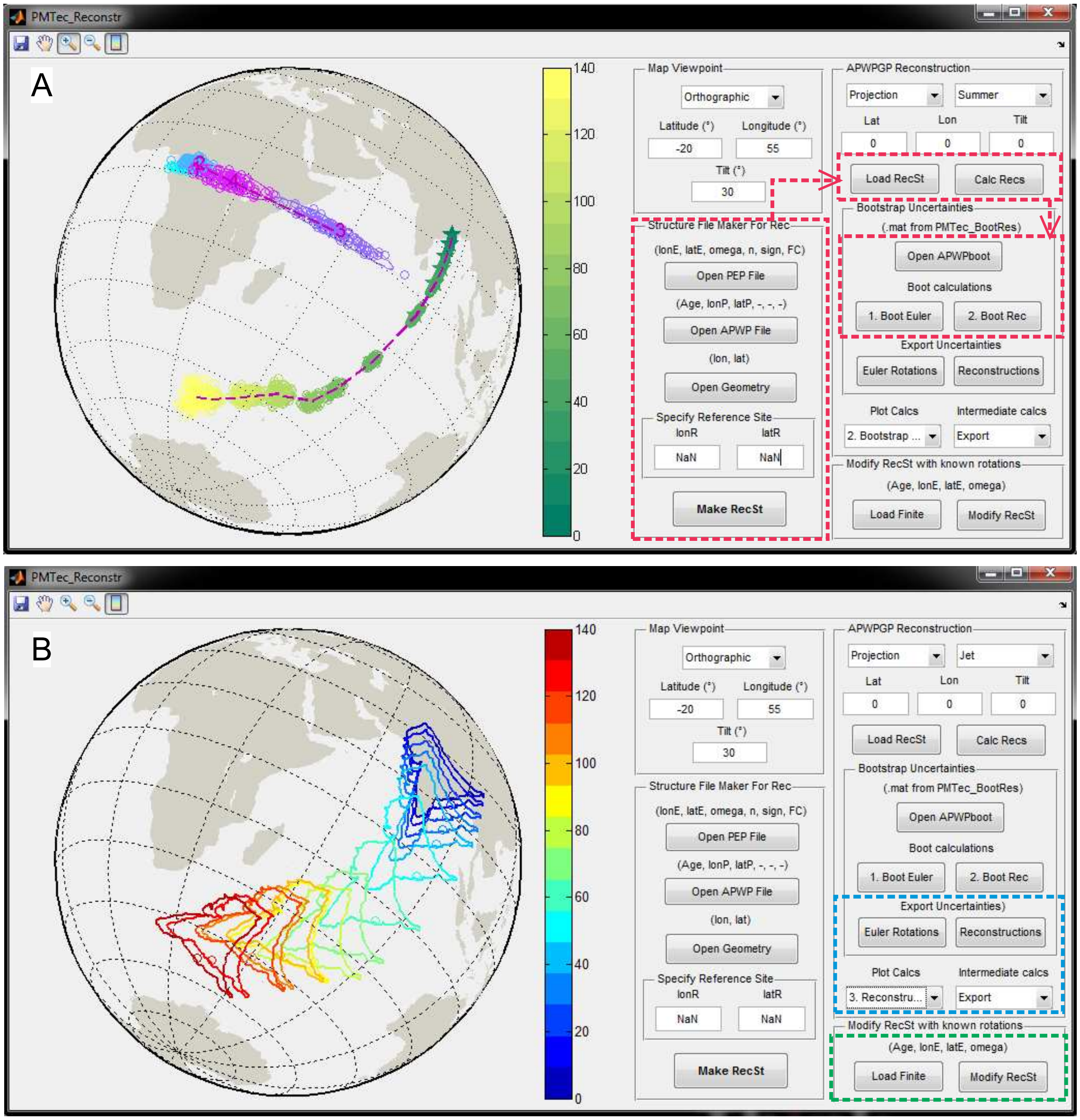

A:

Orthographic
Latitude (°) -20
Longitude (°) 55
Tilt (°) 30
Projection
Summer
Lat 0
Lon 0
Tilt 0
lonR NaN
latR NaN
Plot Calcs 2. Bootstrap ...
Intermediate calcs Export

B:

Orthographic
Latitude (°) -20
Longitude (°) 55
Tilt (°) 30
Projection
Jet
Lat 0
Lon 0
Tilt 0
lonR NaN
latR NaN
Plot Calcs 3. Reconstru...
Intermediate calcs Export

Figure 3.5: Absolute plate motion reconstructions using the module PMTec_Reconstr. Reconstruction file 'RecSt.mat' needs to be prepared from paleomagnetic Euler rotations, APWP and plate geometry files in the required formats (Table 3.2). After loading bootstrap APWP file 'APWPboot.mat' produced in PMTec_BootRes, absolute reconstructions and corresponding errors can be computed (arrows among the red dashed boxes show the operation flow chart), visualized and exported (blue dashed box). Reconstruction file 'RecSt.mat' can be modified afterwards using input finite rotations if necessary (green dashed box). (A) Color-coded Euler poles (pentagrams with colormap 'cool') and reconstructions (pentagrams with colormap 'summer') for a reference site calculated from Indian APWP of Torsvik et al. [2012]. Also shown are their corresponding error ellipses at 95% confidence level. (B) Restored Indian plate motion trajectory since 140 Ma shown with colormap 'jet'. See Wu and Kravchinsky [2014] for the detailed reconstruction procedure.

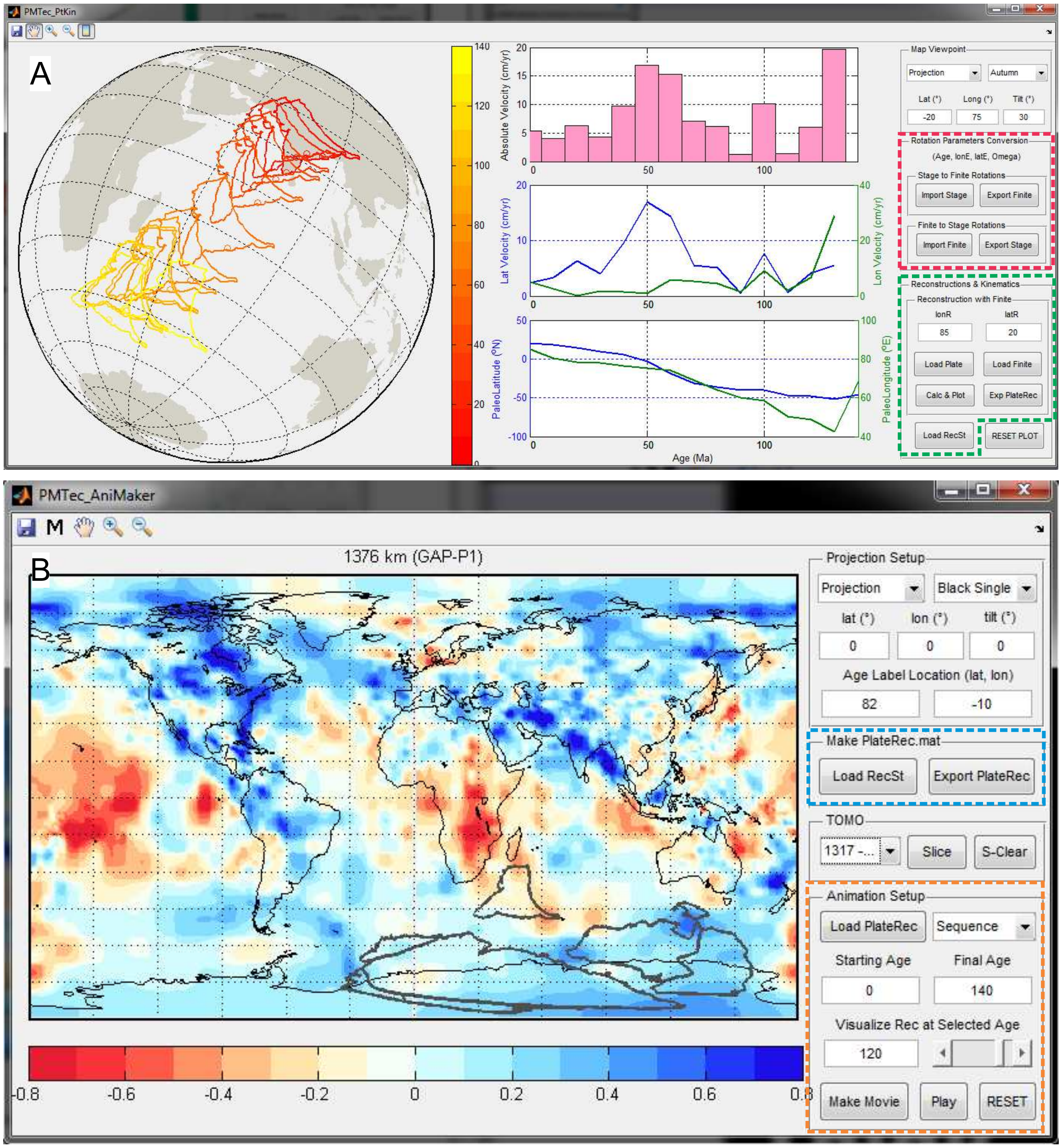

Projection: Autumn

Lat (°): -20 Long (°): 75 Tilt (°): 30

lonR: 85 latR: 20

Projection: Black Single

lat (°): 0 lon (°): 0 tilt (°): 0

Age Label Location (lat, lon): 82 -10

TOMO: 1317 -...

Sequence

Starting Age: 0 Final Age: 140

Visualize Rec at Selected Age: 120

Figure 3.6: Demonstration of kinematic calculations and animation making using module PMTec_PtKin and PMTec_AniMaker, respectively. (A) Functionality of the module PMTec_PtKin. Absolute motion velocity, component velocities (along parallels and meridians), and paleolatitude-paleolongitude variations for a reference site can be computed using reconstruction file 'RecSt.mat' or any known finite rotations for the input plate geometry (green dashed box). The figure shows kinematics of a reference point in India since 140 Ma determined from finite rotations of Mitchell et al. [2012]. PMTec_PtKin allows the mutual conversion between stage rotations and finite rotations (red dashed box). (B) Snapshot of India, Australia and East Antarctica configuration at 120 Ma in the module PMTec_AniMaker. Calculations are made from animation files 'PlateRec.mat' that are produced in PMTec_PtKin using rotations of Mitchell et al. [2012]. Animations, forward motions or backward reconstructions, can be made with (or without) plotting the tomography model of Obayashi et al. [2006] and then exported in the format of *.mov or *.gif (orange dashed box). 'PlateRec.mat' can also be prepared directly out of reconstruction file(s) 'RecSt.mat' here (blue dashed box).

Module PMTec_PtKin performs follow-up calculations to reconstruction files 'RecSt.mat' to obtain the kinematics of a reference site, including absolute motion velocities, velocity components along parallels and meridians, and time variations of its paleolatitude and paleolongitude (Figure 3.6A). The outcome results are saved into field 'f8'. Moreover, PMTec_PtKin allows direct kinematic computation from the loaded plate geometry and finite rotations. To facilitate the comparison between rotations (or reconstructions) obtained from different techniques, we can convert between stage and finite rotations in PMTec_PtKin.

3.3.4 Miscellaneous features

PMTec provides two options to prepare animation files 'PlateRec.mat', one of which is through data export from reconstruction files 'RecSt.mat' in the module PMTec_AniMaker (Figure 3.6B). PMTec_PtKin allows an alternative way to produce animation files during the calculation of kinematic parameters from the input plate geometry and finite rotations (Figure 3.6A). Before visualization, users must ensure the same dimensions for all input animation files (a.k.a. ages of reconstructions) in which calculations during 'blank' ages with no governing rotations must be filled with a row vector [NaN, NaN] in field 'f2'. PlateRec(rowID).f2 = [NaN, NaN], for instance, is a viable MATLAB command to modify field values in animation files. After specifying visualization sequence, i.e. backward reconstructions or forward plate motions, animation can be produced, played and exported in the format of *.gif or *.mov (Figure 3.6B).

To estimate errors in paleomagnetic Euler poles and reconstructions, PMTec_Reconstr needs an input file 'APWPboot.mat' (bootstrapped APWP) which can be generated in the module PMTec_BootRes. Following the methodology proposed by Smirnov and Tarduno [2010] and modified by Wu and Kravchinsky [2014], PMTec represents each paleomagnetic pole (together with errors A_{95}) in terms of discrete Fisherian distributions whose cluttering are determined by precision parameters (kappa). Bootstrap dataset is considered a reasonable representation of the original pole when the confidence ellipse enclosing 99% of the bootstrapped data is approximately tangent to the error of the pole along the maximum axis (Figure 3.7A). Users need to determine sensible precision parameters for each poles before implementing bootstrap resampling for further error estimation (Figure 3.7B).

Two auxiliary modules are provided in PMTec to assist paleomagnetic data processing for plate reconstructions. PMTec_Fish allows a quick computation of Fisherian statistics from paleo-poles or directional data. PMTec_PlateID can be used to produce and modify shape files using desired plate geometry parameters such as plate ID and valid period useful in GPlates.

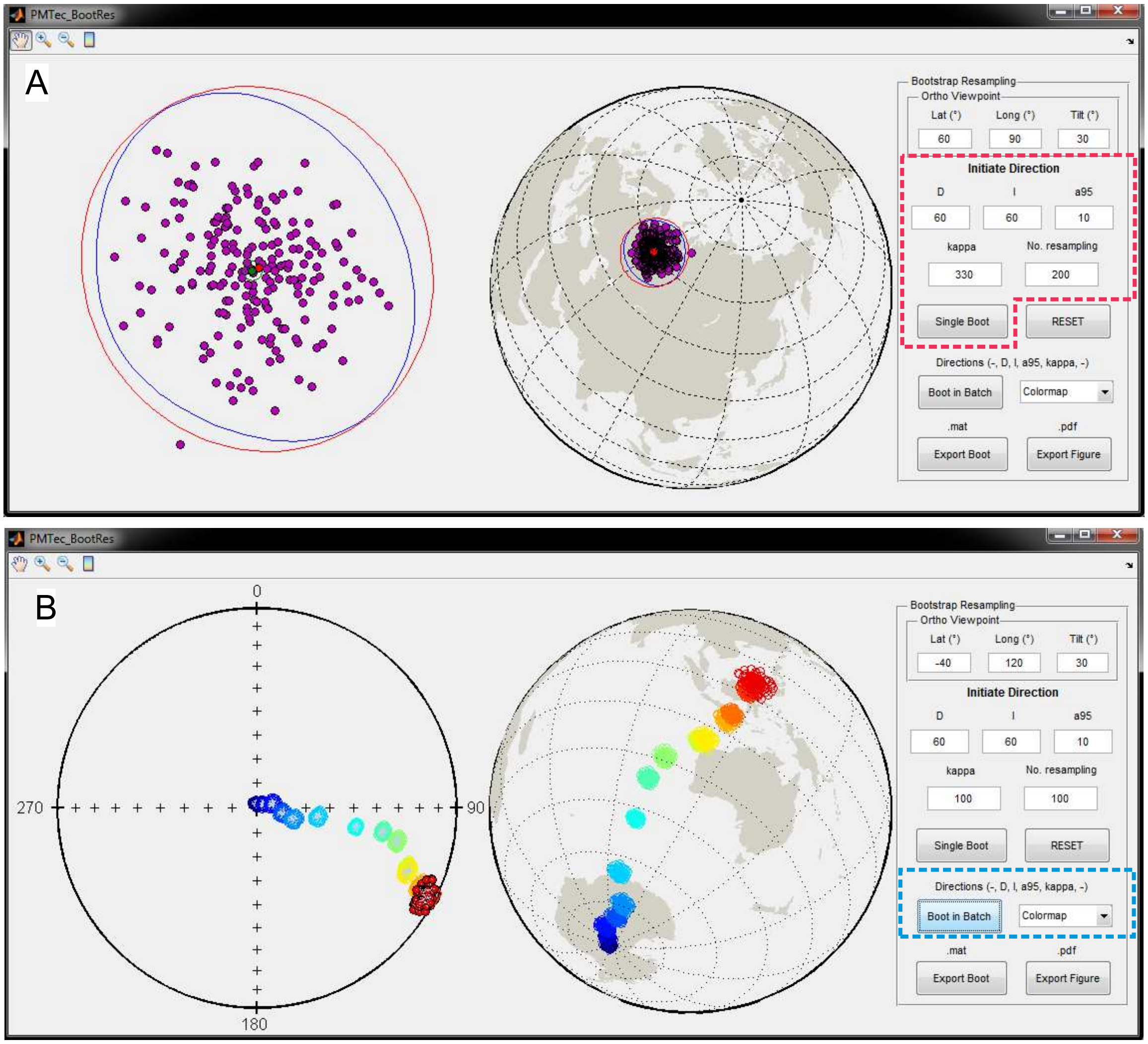

A:

Lat (°)	Long (°)	Tilt (°)
60	90	30

D	I	a95	kappa	No. resampling
60	60	10	330	200

B:

Lat (°)	Long (°)	Tilt (°)
-40	120	30

D	I	a95	kappa	No. resampling
60	60	10	100	100

Figure 3.7: Bootstrap resampling using module PMTec_BootRes. (A) Representation of a single direction as a bootstrap Fisherian distribution (red dashed box). The original direction and its 95% uncertainty cone are shown as red dot and solid circle. The bootstrap directions are marked as magenta dots with the Fisherian mean (green dot) and error (green circle). Blue circle represents a confidence ellipse enclosing 99% of the bootstrap data. Bootstrap representations are considered reasonable when the 95% error boundary of the original direction (red) and the 99% confidence ellipse (blue) visually share the same tangent plane along the maximum ellipse axis. (B) Bootstrap resampling for Indian paleo-poles of 0-140 Ma [Torsvik et al., 2012] (blue dashed box), where kappa(s) in the input direction file are precision parameters estimated using the method illustrated in (A).

3.4 Discussion and conclusions

Here we use published data to demonstrate some essential capabilities of PMTec for data processing and graphical representation. Figure 3.3 illustrates the calculated European APWP in the forms of running means and spherical splines from the paleo-poles compiled by Torsvik et al. [2001] (their Supplementary Table 1b). Figures 3.4-3.5 & 3.7B use the case study of India [Wu and Kravchinsky, 2014] to demonstrate the general procedure to implement the reconstruction technique. To illustrate the flexibility of PMTec in using finite rotations, Figure 3.6 shows reconstructions and corresponding plate kinematics computed from the rotations of Mitchell et al. [2012].

Here we note the potential caveats in interpreting plate reconstructions obtained from PMTec. Firstly, the preferred circle fitting option to a specific APWP track is a statistical recommendation, and does not necessarily lead to the optimal plate reconstructions [Wu and Kravchinsky, 2014]. The sensible fitting code can be decided only when the outcome reconstructions are consistent with geologic, marine geophysical and seismic observations. To assist the correlation between plate reconstructions and mantle structures, a well-resolved whole mantle P-wave tomography model is embedded in PMTec. Secondly, there might be plate motions which cannot be resolved from paleomagnetic Euler poles derived from some APWP tracks [Wu and Kravchinsky, 2014]. Such 'invisible' plate motions were usually made along paleo-parallels with respect to the Earth's spin axis when there is no recorded paleomagnetic polar wandering. As is discussed in section 3.3.3, follow-up corrections can be made in PMTec to the reconstructions using known finite rotations.

To conclude, PMTec is a freeware for plate tectonic research and teaching purposes. The toolbox package, together with the tutorial document and data are available for download from http://www.ualberta.ca/∼vadim/software.htm. Users are allowed to redistribute the software for non-commercial purposes. Please be aware that PMTec is originally developed in MATLAB 2013a and tested only in MATLAB 2014a. Problems might occur with MATLAB releases earlier than 2012b when MathWorks started to update syntaxes for some built-in functions. We choose to follow new syntaxes to facilitate the maintenance and update of PMTec. We encourage and welcome any bug reports, comments and suggestions for PMTec which will be considered for enhancement in future releases.

4

Reconstruction of the closing of the Mongol-Okhotsk Ocean elucidates the genesis of slab geometry underneath Eurasia [a]

Abstract

Understanding the morphology of the lower mantle requires the reconciliation of seismic, geochemical, thermodynamic and mineral physics constraints within a self-consistent tectonic framework. The sinking of subducted oceanic lithosphere preserves the chronological information of penetrative convection in the lower mantle, which can only be understood through the restoration of ancient convergent tectonics. However, there are still no indisputable approaches to effectively constrain absolute plate motions deep into geologic history. Using a new and independent absolute paleomagnetic reconstruction method, we present here the restoration of the closing of the Mongol-Okhotsk Ocean (MOO) which existed between Siberia and North China-Amuria (NCA) during the Mesozoic. Three stages, i.e., 260-200 Ma, 200-150 Ma and 150-120 Ma, are identified from the time-varying approaching speeds of NCA and Siberia and the slab-derived subduction rates within the MOO. The first two stages saw a reduction, mainly through intra-oceanic and then ocean-continent subduction in present-day northern Eurasia, in about 90% ancient oceanic basin confined between Siberia and NCA. The interval of 150-120 Ma witnessed the closing of the remnant paleo-oceanic basin confined between Siberia and NCA, which agrees with a southwestward spatial transition of slabs distributed at the depth of 1300-1800 km and an upward reduction in slab volumes predicted by the shear-wave velocity model GyPSuM. For the first time, our reconstructions quantitatively explain how slabs related to the MOO affect the geometry of the long-wavelength high-velocity discontinuities in the lower mantle.

---

[a] A version of this chapter has been submitted as:
Wu, L., Kravchinsky, V.A., Gu, Y.J., Potter, D.K. Reconstruction of the closing of the Mongol-Okhotsk Ocean in the Mesozoic elucidates the genesis of the slab geometry underneath Eurasia.

4.1 Introduction

Plate tectonic theory predicts the subduction of oceanic lithosphere at convergent plate boundaries. The resultant descending slabs, usually apparent as high-velocity perturbations in tomographic images [van der Hilst and Kárason, 1999], not only contribute to the thermal and density heterogeneities in the mantle, but also shape the Earth's surface elevation [Lithgow-Bertelloni and Silver, 1998], the gravity field [Richards and Hager, 1984; Panet et al., 2014], the topography of the Earth's interior layer boundaries [Hager et al., 1985; Ishii and Tromp, 1999] and the mantle cooling history [Lay et al., 2008]. No simple method, however, is widely accepted to quantitatively relate present-day mantle downwelling structures with time-evolving surface kinematic processes. There are two major difficulties: 1) significant differences in plate reconstructions among various absolute plate motion (APM) models, and 2) significant differences in the inferred mantle structure among various seismic tomography models. To help resolve the issue, we adopt a new paleomagnetic-based absolute reconstruction method, independently of any auxiliary means/data in constraining paleolongitudes, to quantitatively restore the past plate motions of Siberia and North China-Amuria (NCA) bounding the Mongol-Okhotsk Ocean (MOO) in the Mesozoic. The reconstructed closing of the MOO is then integrated with the high-velocity zone beneath Eurasia, often dubbed as a 'slab graveyard' [Van der Voo et al., 1999], which is one of the best resolved structures in global seismic tomography models.

Hotspot reference frames are one of the well-established APM models, but they cannot predict plate motions before 130 Ma because few hotspot tracks older than the Early Cretaceous have been recognized [Müller et al., 1993; Doubrovine et al., 2012]. By establishing anchor points at certain ages to provide longitudinal constraints, through either deep mantle structures [Burke and Torsvik, 2004] or estimates of true polar wandering (TPW) [Steinberger and Torsvik, 2008; Mitchell et al., 2012], paleomagnetism could extend APM reconstructions beyond the hotspot records. Unfortunately, various models have considerable discrepancies in the APM predictions. In recent years, slabs derived from seismic observations have been frequently used to help refine the current APM models [Van der Voo et al., 1999; van der Meer et al., 2010]. However, no consensus has been reached on the standard approach to slab characterizations (e.g., from contours of velocity [van der Meer et al., 2010] or temperature perturbations [Shephard et al., 2012]). It is also unclear how trench migration [Williams et al., 2015], and variations of depth-dependent slab sinking rates in the mantle [Butterworth et al., 2014], would affect the restoration of ancient subduction zones where the polarity determinations are still fairly subjective. Equivocalness occurs when slab remnants are the only auxiliary constraints on ancient plate configurations. Circular reasoning would result if slabs interpreted from mid-lower mantle velocity anomalies (and the current plate reconstructions) are used to refine the current APM models.

To avoid such circular reasoning, here we apply a new paleomagnetism-based APM method, apparent polar wander paths geometric parameterizations (APWPGP) [Wu and Kravchinsky, 2014] (see section 4.2), to independently reconstruct the absolute motions of Siberia and NCA which previously bounded the MOO. Figure 4.1 shows the circle fittings to the identified APWP tracks for Siberia, stable Europe (EU, integrated with Siberia during most of the Mesozoic), and North China (Table 4.2), from which stage (Table 4.3) and finite (Table 4.4) rotation parameters are derived (see section 4.2). The detailed kinematic reconstructions and comparisons with other APM models are presented in section 4.3. Figures 4.2C & 4.2E highlight the crucial interval (260-120 Ma) during the closing of the MOO. This interval is better resolved from our APWPGP method considering the more robust circle fittings to the APWP tracks.

To avoid the uncertainties in deriving ancient subduction zones from tomography models, we adopt the isosurfaces of seismic velocity perturbation contours from the shear-wave velocity model GyPSuM10s [Simmons et al., 2010] to disclose the correlation between the plate motions during the closing of the MOO in 260-120 Ma and the present-day long-wavelength lower mantle structures (i.e., slabs) underneath Eurasia (Figures 4.8A-D) (see section 4.2). In this chapter, such correlation is established based on the depth (time)-varying slab areas, from which we estimate slab production rates (equivalent to subduction rates) during certain time intervals. Then we approximate the slab-pull forces primarily for the subduction of the MOO (Figure 4.8E), whose variations may be reflected from long-wavelength changes in the spherical distances between the suture edges and the average approaching speeds of Siberia and NCA (Figure 4.8F) (see section 4.2).

Table 4.1: The selected high-quality paleomagnetic poles from the North China Block during the Middle Permian - Early Triassic. The numerical ages of the paleo-poles are assigned as midpoints of Period/Epoch in the geologic time scale of Gradstein et al. [2012]. If not presented in the source publications, A_{95} is recalculated using the formula $A_{95} = \sqrt{dm \times dp}$ [Khramov, 1987], where dm and dp are semi-major and semi-minor axes of error ellipses. All the clastic paleo-poles are corrected for the inclination errors (IE) using a factor of 0.6, following the approach of Van der Voo et al. [2015]. The quality of the paleo-poles (Q) is assessed by the widely accepted seven criteria [Van der Voo, 1990]: 1, adequate demagnetization and remanence components analysis; 2, field test (fold test, conglomerate test and bake test); 3, antipodal reversals; 4, firm statistical results with the number of samples no smaller than 24 and A_{95} no larger than 16°; 5, no large afterward localized rotations; 6, well-constrained age for the host rock; 7, no remagnetizations. Paleo-poles get a '1' for passing or a '0' for failing each criterion. A '-' is assigned if a criterion is not mentioned in the source paper. Paleo-poles with comment mark (CM) # are excluded from the calculation of running means (i.e. APWP).

Lithology, location		Age	Sites		Paleo-Poles					Grading	Q	CM	Ref
					(without IE corrections)			(with IE corrections)					
		(Ma)	LonS (°E)	LatS (°N)	LonP (°E)	LatP (°N)	A95 (°)	LonP (°E)	LatP (°N)	1234567			
Early Triassic (T1)													
Redbeds; Shanxi	T1	249.7	111.9	37.6	4.8	50.3	4.8	20.2	55.8	1111-11	6		Shi et al. [2004]
Sediments; Shanxi	T1	249.7	112.0	37.6	4.8	50.3	4.8	20.1	55.8	1111-11	6		Huang et al. [2005]
Redbeds; Shaanxi	T1	249.7	110.2	35.5	348.3	61.9	3.8	8.8	67.8	1-11111	6		Yang et al. [1991]
Redbeds; Shanxi	T1	249.7	110.8	36.3	356.3	64.8	3.0	25.9	69.8	111-1-11	6		Tan et al. [1991]
Sandstone; Shanxi	T1	249.7	110.3	35.5	356.5	57.8	2.8	15.2	63.2	1111-11	6		Ma et al. [1993]
Shale, mudstone; Shanxi	T1	249.7	112.3	37.8	351	50.0	6.0	360	55.1	1-11-11	5		Embleton et al. [1996]
Middle (P2) and Late Permian (P3)													
Sanstone; Hebei and Shanxi	P3	256.0	113.2	38.7	356.9	47.1	15.5	6.3	52.3	1011111	6		Zhao and Coe [1989]
Redbeds; Gansu	P3	256.0	98.0	39.6	358.6	41.0	4.3	11.3	46.8	-1111-1	5		Meng et al. [1989]
Redbeds, andesite; Inner Mongolia	P3	256.0	118.9	42.7	341.7	51.9	6.8	348.7	58.0	1111-11	6	#	Zhao et al. [1990]
Redshale, mudstone; Shanxi	P3	256.0	112.3	37.8	357.4	47.8	4.0	7.5	53.0	1-11-11	5		Embleton et al. [1996]
Mudstone, sandstone; Shaanxi	P2	266.1	110.3	35.5	358.7	49.5	3.4	10.4	54.4	1111-11	6		Ma et al. [1993]
Redbeds; Shanxi	P2	266.1	112.3	37.8	357.8	44.3	5.2	5.6	48.8	1-11111	6		McElhinny et al. [1981]
Sandstone, basalt; Inner Mongolia	P2	266.1	118.4	43.7	3.7	48.7	6.9	16.9	55.7	1111–1	5		Zhao et al. [2013]

4.2 Methods

4.2.1 Paleomagnetic data

The Siberian APWP used for the geometric parameterizations comprises two segments: the stable European running means for 0-240 Ma [Torsvik et al., 2012] and the Siberian running means for 250-260 Ma [Cocks and Torsvik, 2007]. The main segment of the North China APWP (60-230 Ma) is from Van der Voo et al. [2015], with our interpolations at 140, 200 and 230 Ma. The 240-260 Ma segment is calculated in a sliding window of 20 Myr using PMTec [Wu et al., 2015] from the selected high-quality North China paleo-poles (with quality factors no smaller than 5, Table 4.1). For simplification, we assume that the Amuria Block accreted to the North China Block before 260 Ma based on their overlapped paleolatitudes along the suture [Kravchinsky et al., 2002]. In the Cenozoic, significantly low paleomagnetic directions have been reported in East Asian plates with respect to the expected directions from the stable European reference curve [Cogné et al., 2013]. We use the stable European running means of 0-50 Ma [Torsvik et al., 2012] as the first segment of the input North China APWP, mainly to avoid the confusion associated with absolute reconstructions computed from the relatively uncertain North China paleo-poles in the Cenozoic. An error of 16.0° is assigned to the North China APWP poles that are interpolated or averaged from less than two input paleo-poles. Table 4.2 tabulates the input APWPs for the geometric parameterizations. No TPW corrections are made because the current estimates of TPW behavior are usually speculated from the absolute plate motions of global plates [Steinberger and Torsvik, 2008; Torsvik et al., 2010, 2012], on which no consensus has been reached.

Table 4.2: The input APWPs of Siberia, stable Europe and North China for the geometric parameterizations. See Methods for the detailed descriptions.

Siberia APWP					European APWP				North China APWP			
Age	N	A95	Lon	Lat	N	A95	Lon	Lat	N	A95	Lon	Lat
(Ma)		(°)	(°E)	(°N)		(°)	(°E)	(°N)		(°)	(°E)	(°N)
0	24	1.9	173.9	88.5	24	1.9	173.9	88.5	24	1.9	173.9	88.5
10	49	1.8	150	86.7	49	1.8	150	86.7	49	1.8	150	86.7
20	31	2.6	152.1	84.4	31	2.6	152.1	84.4	31	2.6	152.1	84.4
30	24	2.6	146.5	83.1	24	2.6	146.5	83.1	24	2.6	146.5	83.1
40	24	2.9	144.3	81.1	24	2.9	144.3	81.1	24	2.9	144.3	81.1
50	33	2.8	164.7	78.9	33	2.8	164.7	78.9	33	2.8	164.7	78.9
60	44	2.1	172.6	78.2	44	2.1	172.6	78.2	1	16	144.4	76.4
70	32	2.5	175.7	79.2	32	2.5	175.7	79.2	6	8	200	78.6
80	25	2.9	177.9	79.7	25	2.9	177.9	79.7	15	5.7	168.1	79.1
90	28	2.5	167.2	80.4	28	2.5	167.2	80.4	13	5.8	155.5	77.2
100	14	3.3	152.3	80.8	14	3.3	152.3	80.8	3	11.3	164.9	76.2
110	21	3.3	193.1	81.2	21	3.3	193.1	81.2	13	4.6	161.6	75.3
120	28	2.6	190.1	79	28	2.6	190.1	79	20	4.1	162.5	78
130	18	2.8	183.4	75	18	2.8	183.4	75	9	6.6	168	81.1
140	9	6	187.9	72.4	9	6	187.9	72.4	-	16	174.4	76.8
150	15	6.4	154.2	72.9	15	6.4	154.2	72.9	10	5.1	177	72.3
160	19	5.1	143.4	70.5	19	5.1	143.4	70.5	14	4.7	174.3	74.7
170	18	4.6	136.4	67.3	18	4.6	136.4	67.3	5	9.6	160.7	78
180	33	3.4	113.9	68.3	33	3.4	113.9	68.3	2	3.3	106	84.2
190	46	2.9	98.8	64.1	46	2.9	98.8	64.1	2	3.3	106	84.2
200	39	2.8	99.3	57.9	39	2.8	99.3	57.9	-	16	77.7	75.8
210	41	2.2	110.8	56.1	41	2.2	110.8	56.1	2	16	42.1	68.4
220	35	2.3	124.1	52.8	35	2.3	124.1	52.8	2	16	42.1	68.4
230	33	2.5	132.1	50.7	33	2.5	132.1	50.7	-	16	41.8	65.9
240	31	3.6	141.5	52.2	31	3.6	141.5	52.2	6	6.6	14.6	61.5
250	5	5.8	146.2	56.1	34	3.6	149.2	53.4	9	5.5	12.1	57.9
260	4	7.9	156.2	54.2	35	2.6	150.5	53.8	6	3.5	9.6	51.9

4.2.2 Geometric parameterization of apparent polar wander paths

We apply the apparent polar wander paths geometric parameterization (APWPGP) method [Wu and Kravchinsky, 2014] to derive Euler rotation poles and angles for the absolute plate motion reconstructions. Eight tracks (a track connects paleo-poles during a certain interval) are identified from the Siberian (and stable European) APWPs (Figure 4.1A), to which conservative fittings with great circles are implemented to obtain the stage Euler rotation parameters. There are other options for fitting the segment of 60-110 Ma, to which we apply a single great circle fitting considering the statistically insignificant differences between the APWP poles during the interval. Reconstruction errors caused by the imperfect alignment of APWP poles along tracks are reduced by the paleo-latitude corrections [Wu and Kravchinsky, 2014]. This is achieved by using paleo-colatitudes determined from paleomagnetism as the spherical distances between APWP poles and the restored paleo-positions of a reference site, rather than keeping all restorations along circular tracks centering on stage Euler poles [Wu and Kravchinsky, 2014; Wu et al., 2015]. In the same way, the North China APWP segments are fit with great circles (Figures 4.1B-C). Other combinations of track fittings are acceptable (without significantly changing the results) for the APWP poles of 40-150 Ma with heavily overlapped errors (Figure 4.1B).

Error ellipses for rotation poles and reconstructions are characterized by the magnitudes of primary axes (i.e., semi-major and semi-minor) and the angle between the meridian and the right-hand semi-major axis (i.e., azimuth). These parameters are computed from the symmetric uncertainty covariance matrix defined by Wu and Kravchinsky [2014]. The error ellipses for stage and finite Euler rotations are listed in Tables 4.3 and 4.4. Note that the finite rotations here are calculated from the combined stage rotations and paleo-latitude corrections.

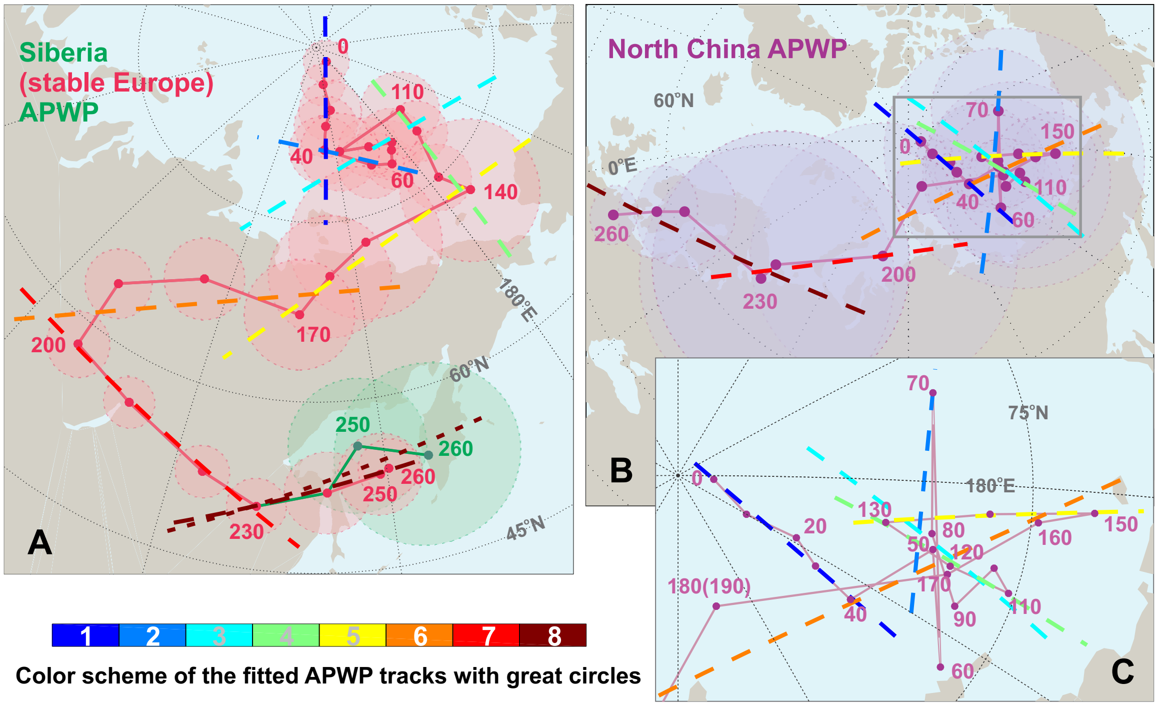

Figure 4.1: Circle fittings (color-coded dashed lines) to the identified APWP tracks. The uncertainties of the APWP poles (Table 4.2) are shown in the single-colored circles. Ages (in Ma) for some of the key poles are labeled. **A**, Circle fittings to the APWPs of stable Europe (EU, red dots and connecting line) and Siberia (green dots and connecting line). The fitted circles for the eighth APWP tracks of EU and Siberia are shown in the regular and short dashed-lines respectively. **B**, Circle fittings to the North China APWP (purple dots and connecting line). **C**, The magnified area that is highlighted in the grey rectangle in **B**. The errors of the APWP poles are not shown for clarity.

Table 4.3: The stage Euler rotation parameters derived from the identified APWP tracks (Figure 4.1). Error ellipses are characterized using semi-major axis (Maj), semi-minor axis (Min) and the angle between meridians and the right-hand semi-major axis (Az).

Euler Rotation Parameters										
		Poles to Tracks		Stage Rotations			Error Ellipses			
Track	Period (Ma)	Lon (°E)	Lat (°N)	Lon (°E)	Lat (°N)	Angle (°)	Maj (°)	Min (°)	Az (°)	Fitting code
Siberia & Stable Europe										
EuSib-1	0-40	49.9	0.8	49.9	0.8	-7.6	22	0.9	-85.2	GC
EuSib-2	40-60	127.6	-8.6	127.8	-1.2	-5.8	31	1.7	-89.2	GC
EuSib-3	60-110	172.1	-9.9	171.7	0.6	-3	380.8	2.1	90	GC
EuSib-4	110-140	270	-1.8	269.2	-0.1	8.9	33.3	3.7	-88.1	GC
EuSib-5	140-170	177	-16.8	176.8	2.8	17.8	405.3	5	89.9	GC
EuSib-6	170-200	145.3	-20.8	146.6	3.7	19.1	13.8	4.8	89.4	GC
EuSib-7	200-230	91.1	-32.1	97.4	0.2	-20.2	6.7	4.3	89.9	GC
Eu-8	230-260	160	-36	153.4	1.1	-11.6	86.5	5.4	-89.9	GC
Sib-8	230-260	164.1	-34.6	157	1.4	-15	13.1	5.1	-86.1	GC
North China										
NCB-1	0-40	49.9	0.8	49.9	0.8	-7.6	22	0.9	-85.2	GC
NCB-2	40-80	174.7	-10.3	174.3	-4	-3.2	399.4	3.3	89.9	GC
NCB-3	80-110	53.4	4.3	52.8	2	-4.1	119.2	4.9	-85.6	GC
NCB-4	110-130	62.1	2.4	61.7	1.7	5.9	73.2	6.9	-86.9	GC
NCB-5	130-150	95.5	-2.7	95.3	-0.9	-9	76.6	8.2	-83.7	GC
NCB-6	150-200	116.6	-8	117	-1.6	24.2	24	9	88	GC
NCB-7	200-230	97.4	-13.2	97.5	-2.9	14.9	74.5	11.3	-88.2	GC
NCB-8	230-260	66.7	-20.8	67.4	0.5	21.4	38.3	14.8	-83.8	GC

Table 4.4: The finite reconstruction parameters for Siberia, stable Europe and North China during the last 260 Myr.

	Siberia						North China					
	Finite Rotations			Error Ellipses			Finite Rotations			Error Ellipses		
Age (Ma)	Lon (°E)	Lat (°N)	Angle (°)	Maj (°)	Min (°)	Az (°)	Lon (°E)	Lat (°N)	Angle (°)	Maj (°)	Min (°)	Az (°)
0	0	0	0	0	0	90	0	0	0	0	0	90
10	48.1	0.9	2.1	2.4	1	-28.8	48.1	0.9	2.1	2.4	1	-28.8
20	51.3	0.7	4.1	2.9	2	-55	51.3	0.7	4.1	2.9	2	-55
30	49.8	0.8	5.6	3.4	2.4	-77.4	49.8	0.8	5.6	3.4	2.4	-77.4
40	49.5	0.8	7.7	4.2	2.7	79.4	49.5	0.8	7.7	4.2	2.7	79.4
50	73.5	-1.3	9.5	4.1	2.5	71.3	62.6	-1.2	7.1	5.4	2.7	87
60	82.9	-2.2	10.5	3.4	2.1	74.6	35.2	2.6	10.4	8.1	3.9	65.6
70	87	-2.5	10.4	3.6	2.5	68.6	118.2	-7.4	7.8	8.6	6.8	81.7
80	89.7	-2.8	10.5	4	2.7	67.1	68	-2	6.9	6.9	4.2	64.4
90	80.8	-2.1	10.3	4.2	2.6	83.9	61.3	0.2	9.5	11.6	4.7	86.7
100	70	-1.3	10.4	7.2	3.1	-88.7	70	-1.2	9	16.5	8.7	81.2
110	103.7	-3.9	11	6.2	3	79.9	66.5	-0.5	10.2	11.3	3.8	88.8
120	96.7	-2.6	13.2	6.1	2.8	87.8	66.3	-1.1	7.7	11.5	3.8	-83.7
130	91.7	-1.3	17.3	6.7	2.8	86.8	71.9	-3.8	4.4	12.1	5.4	-86.2
140	95.8	-1.6	19.8	8.5	5.1	79.7	84.7	-2.9	8.6	21.1	12.3	84.1
150	67	1.9	20.8	9.5	5.5	79.9	87.9	-2.5	13.1	13.6	4.8	89.7
160	57	3.1	22.5	11.2	4.3	83.8	84.6	-2.4	11	13.4	4.2	88.5
170	48.9	3.9	24.7	14.4	3.8	86.9	63.5	-0.1	7.7	18.4	6.9	84.4
180	34.5	6.5	24	17	3.1	88.6	-28.8	7	5.6	12.2	3.4	-75.8
190	16.1	9.4	27.2	22.8	3.3	-86.4	-28.8	7	5.6	12.4	3.3	-75.1
200	14.7	7.4	33.5	24.9	3.8	-84.7	-28.7	5	15	21.8	13.9	-82.6
210	24.1	4.5	34.8	49.9	2.4	-89.5	-59.5	7.6	25.1	18.9	12.9	-61
220	35.6	0.7	37.6	24.9	3.1	83.8	-59.5	7.6	25.1	17.3	12.8	-57.8
230	42.5	-1.7	40.4	12.2	4.1	78.1	-59.4	7.4	26.6	18.8	13.2	-75.5
240	50.9	-4.6	38.4	11.2	4.5	81.5	-77.3	9.3	36	10.3	7.1	-52.5
250	54.6	-5.9	37.3	14.2	6.4	-88.7	-80.2	9.5	38.6	8.7	6.3	-52.1
260	64	-8.9	36.8	13.6	7.1	80.5	-84.1	9.7	43.1	7.6	6.1	-49
			Stable Europe									
240	50.8	-4.6	38.7	9.8	4.4	78.5						
250	57.5	-6.9	37.9	9.1	4.6	74.5						
260	58.6	-7.2	37.8	8.8	3.5	73						

4.2.3 Slab characterization

To characterize slabs in the lower mantle beneath Eurasia (Figures 4.5 & 4.7-4.8), we use the S-velocity model GyPSuM10s constrained from the well-covered (and traced) seismic ray geometries and a joint seismic-geodynamic inversion technique [Simmons et al., 2010]. The model exhibits a positive correlation coefficient (close to one) between S-velocity and thermally derived density in high-velocity zones in the lower mantle [Simmons et al., 2010]. We use isosurfaces of 0.5% velocity perturbations to represent slabs underneath Eurasia (Figures 4.5 & 4.8A-D) to avoid biased visual appearances of mantle structures due to subjective selections of vertical cross-section. Uncertainties are approximated by the areas encompassed in the 0.5±0.1% contours. Such uncertainties, however, do not significantly affect the discontinuous long-wavelength velocity structures caused by slabs. Other widely referred tomography models (GyPSuM10p (0.2±0.1%) [Simmons et al., 2010], LLNL-G3Dv3p (0.4±0.1%) [Simmons et al., 2012], MITP08p (0.3±0.1%) [Li et al., 2008] and SMEAN02s (0.6±0.1%) [Becker and Boschi, 2002]) are used for a comparative presentation (see Figures 4.9-4.10). It should be noted that the values of 0.5±0.1% velocity perturbations for the model GyPSuM10s are adopted by modifying the suggested value of 0.6% of Butterworth et al. [2014] based on our plate reconstructions; the values for other models are selected such that slab locations and volumes are similar among different models. We also note that the suggested contours might include the ambient mantle that is thermally disturbed by sinking slabs.

4.2.4 Linking past plate kinematics with penetrative convection

To disclose the correlation between past plate kinematics and slab distribution, we compute the total areas of high-velocity anomalies with either thermal or compositional origin at different depths in the lower mantle, enclosed in the 0.5±0.1% contours from the S-velocity model GyPSuM10s (Figure 4.8E). Areas encompassed in the X±0.1% contours, where X is the percentage velocity perturbation (given in the previous section), from other models are calculated for comparison (Figure 4.10). We assume that the areas (and the isopachs) approximate the sinking and folded slabs resulting from the downgoing Mongol-Okhotsk (primary) and Tethys (secondary) lithosphere beneath Eurasia, regardless of their respective contributions or subduction polarities of the related paleo-trenches (not critical for the calculations).

The time frame for the horizontal slices of the lower mantle of different depths (Figures 4.8E & 4.10) are established following the suggestions of van der Meer et al. [2010]. This time frame, derived from the average slab sinking rate in the mantle, may not apply to slabs elsewhere when slab stagnation occurs (or occurred) in the transition zone [Simmons et al., 2015]. However, it is robust for the correlation between the plate reconstructions and the depth-varying slab geometries related with the MOO, Farallon and Aegean Tethys slabs, primarily from which the slab sinking rate (and the time frame) in the lower mantle is estimated [van der Meer et al., 2010].

For simplicity, we use slopes of the temporal variations in slab areas (i.e., rates of subduction) to represent slab-pull forces (Figure 4.8E). The time-varying spherical distances at the reference sites along the MOO suture (i.e., Ref-1, Ref-3 and Ref-4 in Figure 4.2), derived from the rotation parameters of Siberia and NCA (Table 4.4), are used as proxies for the size of the downsizing ancient oceanic basin (Figure 4.8F). Accordingly, the average approaching speeds of the continents and the corresponding ranges along the suture are computed as the slopes (Figure 4.8F). Instantaneous velocity vectors for the same reference points are used to illustrate qualitatively the time-varying net forces acting on the suture zone (Figure 4.8F). Note that such net force characterizations are not representative for the whole continents. The actual net torques of forces should be computed from the rate of change in the total angular momentum for the studied continents, which are beyond the focus of this study.

4.3 Reconstructions

4.3.1 Kinematic reconstructions of Siberia and North China-Amuria since 260 Ma

Figure 4.2A shows our restored absolute motions of Siberia and North China-Amuria (NCA) in the coordinates of the reference sites 1) along the Mongol-Okhotsk Suture (Ref-1: [90°E, 45°N]) and 2) at the northwestern corner of the Siberian Traps (Ref-2: [88°E, 69.4°N]). Depending on the distances to the rotation poles, kinematic parameters for different reference points on the same plate can vary significantly. To better investigate the closing process of the Mongol-Okhotsk Ocean (MOO), we use Ref-1 to highlight the absolute motions of the contacting (or suture) boundary of the two continents. Three stages are roughly disclosed (Figures 4.2B-E): 1) 260-200 Ma when the Siberian side of the boundary went north rapidly (∼6 cm/yr) to the near-polar region where it swung eastward (∼140°) after a transition from counterclockwise to clockwise rotation at 220 Ma, while the NCA side drifted as much as ∼30° to approximately the present-day latitude during an overall counterclockwise rotation; 2) 200-150 Ma in which the Siberian edge moved rapidly to the southwest at high latitudes with a predominantly counterclockwise rotation (∼2.5°/Myr), while the NCA edge drifted westward (∼50°) with a counterclockwise rotation at an average rate of ∼1.5°/Myr; 3) 120-0 Ma when both the Siberian and NCA suture boundaries had a mostly eastward translation (∼20°) after their suturing around 150-120 Ma.

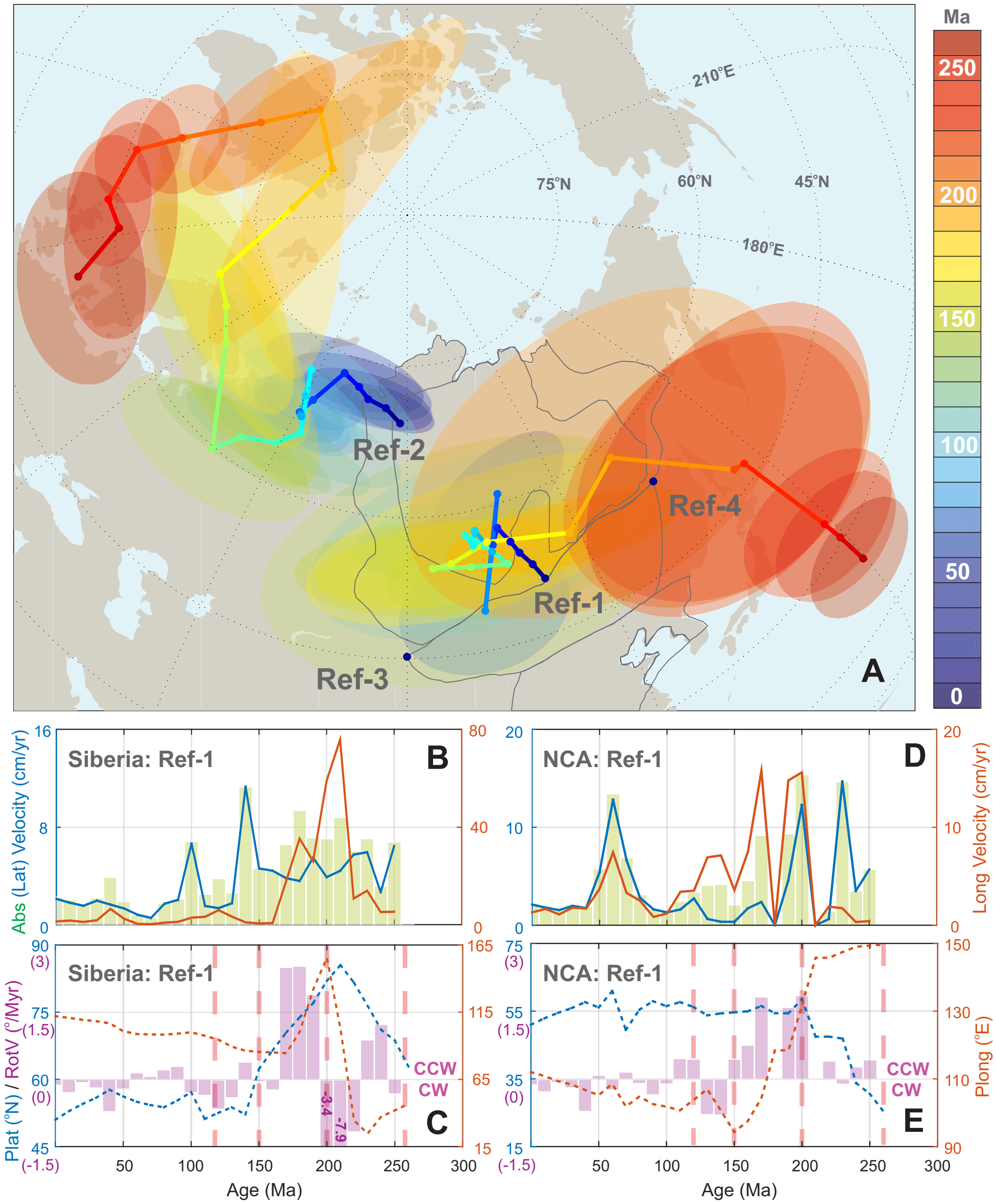

Figure 4.2: Absolute kinematics for the reference sites in Siberia and NCA since 260 Ma, constrained from the APWPGP model (Table 4.4). **A**, Restorations of the reference points Ref-1 ([90°E, 45°N]) and Ref-2 ([88°E, 69.4°N]) to delineate the motion trajectories of NCA and Siberia whose present-day locations are marked by the grey contours. Reconstruction errors are shown in the color-coded ellipses. Ref-3 and Ref-4 are used in Figure 4.8F to illustrate the motions of the whole suture. **B-E**, Kinematic predictions of Ref-1 from the finite rotations of the two continents (Table 4.4). Absolute velocities (green bars) and two orthogonal velocity components (latitudinal and longitudinal components in blue and orange solid lines respectively) are shown in **B** and **C**. Paleo-latitude (Plat) /paleo-longitude (Plong) drift (blue and orange dashed lines) and rotation rates (purple bars) are shown in **D** (the purple fonts indicate the values for the bars that are out of scale) and **E**, where the vertical dashed-lines highlight the crucial intervals during the closing of the MOO.

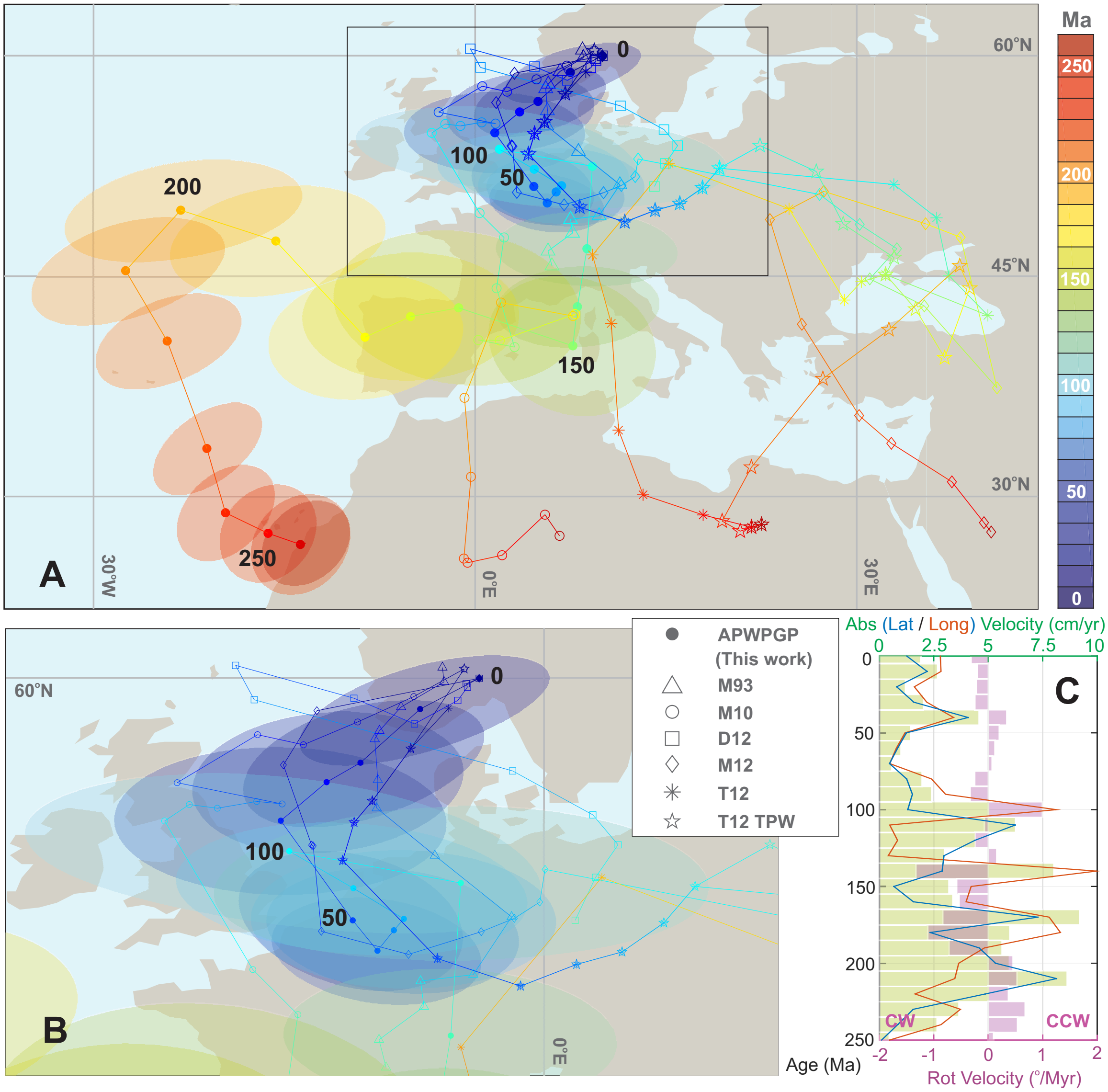

Figure 4.3: Absolute kinematic reconstructions of stable Europe (EU) in the coordinates of a reference site [10°E, 60°N] since 260 Ma. **A**, Comparison of the absolute motion determinations for the reference point from different APM models (Tables 4.5-4.6): M93 [Müller et al., 1993], D12 [Doubrovine et al., 2012], M10 [van der Meer et al., 2010], M12 [Mitchell et al., 2012], T12 [Torsvik et al., 2012], and T12-TPW [Torsvik et al., 2012]. **B**, The magnified area encompassed in the black rectangle in **A**. **C**, The time-varying kinematics of the reference site (averaged in 10 Myr's intervals) predicted from the APWPGP model (this work, Table 4.4). On the top axis are the absolute velocities (green bars) and the two orthogonal velocity components (blue and orange solid lines), while on the bottom axis are the rotational velocities (purple bars). Uncertainties of these kinematic parameters are not illustrated because of the axial asymmetry of the reconstruction errors.

Figures 4.2C & 4.2E highlight the crucial interval (260-120 Ma) during the closing of the MOO. The final closure of the MOO might have occurred at 130-120 Ma based on the following clues. Firstly, there are relatively large uncertainties in the North China paleo-poles and the resultant restorations between 140-130 Ma albeit they overlap with the errors of the Siberian counterparts (Figures 4.1 & 4.7B). Secondly, the slabs (formed during 140-120 Ma) related with the MOO lithosphere display a northeastward migration with an upward pinch-out at the depths of 1800-1300 km (Figure 4.8A), indicating a relocation of subduction zones to the eastern part of the suture zone. Thirdly, Siberia and NCA rotated against each other (Figures 4.2C & 4.2E) with negligible approaching velocities along the suture edges during 130-120 Ma and thereafter (Figure 4.8F). We attribute the reconstruction discrepancies later than 120 Ma, to the limited resolution of the paleo-poles from North China (primary cause) and stable Europe (secondary cause).

4.3.2 Absolute motions of stable Europe predicted from different APM models

A different reference site [10°E, 60°N] in Scandinavia is used to illustrate the absolute motions of stable Europe in the last 260 Myr. Three distinct stages are disclosed (Figure 4.3) according to the finite rotation parameters (Table 4.4) derived from the apparent polar wander paths geometric parameterizations (APWPGP): 1) 260-200 Ma when the (western part of) continent experienced a fast increase in latitude (with a maximum speed of ∼8.5 cm/yr at 210 Ma) and a long-standing counterclockwise rotation (∼0.5°/Myr); 2) 200-150 Ma when it underwent a major eastward translation (∼30°) with a large-scale clockwise rotation (∼0.8°/Myr on average); 3) 150-0 Ma when the continent progressively drifted to its present-day location during a back-and-forth adjustment in the rotation directions. The average absolute and latitudinal velocities were significantly reduced during 160-130 Ma and 70-50 Ma (Figure 4.3C), likely reflecting the increased resistance to the primarily N-S convergence during the demise of the MOO and the Neo-Tethys Ocean (Figure 4.3C).

For comparison, Figure 4.3A shows the reconstructions of the same reference point from other absolute plate motion (APM) models (Table 4.5). These models include 1) the fixed hotspot frame in the coordinates of North America (M93: 0-130 Ma, interpolated with an increment of 10 Myr) [Müller et al., 1993], 2) the global moving hotspot frame in the coordinates of stable Europe (D12: 0-120 Ma) [Doubrovine et al., 2012], 3) the sinking slab frame in the coordinates of South Africa (M10: 0-260 Ma) [van der Meer et al., 2010], 4) the paleomagnetically derived true polar wander (TPW) frame in the coordinates of stable Europe (M12: 0-260 Ma) [Mitchell et al., 2012], 5) the global hybrid frame in the coordinates of South Africa (T12: 0-260 Ma) [Torsvik et al., 2012], and 6) the TPW-corrected global hybrid frame in the coordinates of South Africa (T12-TPW: 0-260 Ma) [Torsvik et al., 2012]. For the APM models not presented in the coordinates of stable Europe, (part of) the plate circuit of stable Europe - North America - Northwest Africa - South Africa [Torsvik et al., 2012] is used to transfer the finite rotation parameters (Table 4.6). Figure 4.4 illustrates the temporal variations of velocities for the same reference site predicted from different APM models.

Table 4.5: Absolute plate motion (APM) models in the coordinates of different continents. See the supplementary text for the description of the models. The M93 model for North America [Müller et al., 1993] is interpolated into 10 Myr steps to facilitate the comparison with other models. Abbreviations: EU - stable Europe, SAF - South Africa, NAM - North America.

Age (Ma)	Lat (°)	Lon (°)	Ang (°)	Lat (°)	Lon (°)	Ang (°)	Lat (°)	Lon (°)	Ang (°)	Lat (°)	Lon (°)	Ang (°)
	M12 - EU			M10 - SAF			T12 - SAF			T12 TPW - SAF		
0	0	0	0	0	0	0	0	83.9	1.5	0	0	0
10	-40.8	30.9	3.8	46.2	-87.9	-1.9	0	80	3.4	0	80	3.4
20	-24.5	46.1	5.4	45.2	-78.6	-4	0	85.6	5.8	0	85.6	5.8
30	-11.1	65.1	7.3	49.7	-70.2	-6.8	0	90.3	7.1	0	90.3	7.1
40	0.5	59.4	7.7	53.1	-55.3	-9.6	0	99	9.5	0	99	9.5
50	6.1	66.3	10.8	51.1	-60.9	-13.1	0	115.6	14.5	0	115.6	14.5
60	13.7	77.1	11.2	43.8	-45.1	-15.9	0	125.3	17.1	0	125.3	17.1
70	20.8	85.2	10.3	44.9	-43.1	-18.2	0	133.3	18.3	0	133.3	18.3
80	27.1	87	10.2	47.3	-41.6	-21.1	0	139.2	19.4	0	139.2	19.4
90	42.1	76.5	12.2	47.2	-39.8	-23.2	0	145.6	20.6	0	145.6	20.6
100	52.1	60.9	15	44	-36.6	-27.2	0	153.2	23	0	153.2	23
110	57.5	117	17.8	35.1	-37.5	-32.7	0	168.7	31.8	0	162.2	24.5
120	58.8	114	22.3	33.1	-33.6	-36.3	0	171.3	36.4	0	166.6	29
130	57.4	118.8	24.7	31.8	-34.4	-39.7	0	170.9	40.7	0	166.9	33.2
140	61.8	72.6	40.9	30.2	-34.9	-44.5	0	172.1	44.2	0	168.8	36.7
150	62.2	79.3	44.1	33.1	-36.7	-44.1	0	167.2	36.9	0	167.2	36.9
160	58.7	94.3	47.4	33.8	-34.1	-43.7	0	165.9	34.6	0	168.4	38.7
170	67.7	62.6	52.7	33.1	-25.2	-45.3	0	163.9	34.1	0	168.7	42.3
180	66.2	52.4	57	31.5	-25	-45.3	0	168.5	27.9	0	175.1	40.7
190	63	37.6	60.7	33	-29.6	-41.1	0	166.6	21.2	0	176.4	40.2
200				29.3	-36.4	-42.3	0	152.2	21	0	171	40.9
210				24	-42.3	-43.7	0	146.3	25.4	0	163	40.1
220	53.5	58.3	64.7	20.3	-46.9	-46.1	0	140.4	31.6	0	153.2	41.4
230	53	68.4	59.3	18.3	-48.8	-44.4	0	140	37	0	147.9	43.2
240	52	85.1	54.1	16	-46.3	-43.9	0	146.1	41.7	0	149.4	44.9
250	49.8	94.1	53.4	14.5	-41.4	-42.1	0	150.7	45.3	0	150.7	45.3
260	49.2	96.3	53.2	12.8	-41.6	-43.3	0	151.8	45.7	0	151.8	45.7
	M93 - NAM			D12 - EU								
0	0	0	0	0	0	0						
10	43.5	119.6	1.3	-71.2	107	0.6						
20	35.4	113.1	3.3	-66.4	156.9	1.5						
30	38.5	107.3	5.3	-60.9	128.1	1.9						
40	47	109.8	7.6	-53.3	88.9	2.8						
50	46.8	112.6	11.2	-35.1	25.8	2.8						
60	46	116.4	15.1	-29.5	-1.3	5.2						
70	46.8	119.6	19.3	-50.3	18.8	5.2						
80	53.3	117.2	24.5	-0.7	115.7	3.5						
90	57.4	104.4	28.2	45.1	101.1	7.1						
100	62.9	89.4	31.7	56.8	77.9	12.3						
110	66.1	77	37.3	55.8	63.4	16.7						
120	66.4	62.1	42.1	53.5	57.2	21						
130	65.9	56.9	45.4									

Table 4.6: Relative plate motion (RPM) models [Torsvik et al., 2012] to transfer different APM models (Table 4.5) into the coordinates of stable Europe. Abbreviations: NWAF - Northwest Africa.

	EU - NAM			NAM - NWAF			NWAF - SAF		
Age	Lat	Lon	Ang	Lat	Lon	Ang	Lat	Lon	Ang
(Ma)	(°)	(°)	(°)	(°)	(°)	(°)	(°)	(°)	(°)
0	66.4	133	-1.2	80.9	22.8	1.3	0	0	0
10	66.4	133	-2.3	80.9	22.9	2.6	0	0	0
20	68.9	132.5	-5.1	80.6	24.4	5.5	0	0	0
30	68.3	131.7	-7	77.4	12.5	8.6	0	0	0
40	66.7	135.6	-9.2	74.5	-1.1	12.6	0	0	0
50	64.4	141	-11.7	75.9	-3.5	16.2	0	0	0
60	55.6	145.8	-14.1	81.6	5.1	19.1	0	0	0
70	55.7	147.1	-16.2	81.6	-6.5	22.4	0	0	0
80	64.1	148	-18.7	78.2	-18.8	27.5	0	0	0
90	66.6	149.9	-20.2	74.3	-22.7	33.9	0	0	0
100	66.8	151.6	-21.1	69.4	-23.5	40.5	0	0	0
110	67.7	153.3	-22.1	67.5	-22.1	47.5	0	0	0
120	69	154.7	-23.1	66	-20.6	54.2	0	0	0
130	69	154.8	-23	66	-19.2	57.7	33.7	26	2
140	69	154.8	-23.1	66.4	-18.2	60.1	33.6	26	2.3
150	69	154.8	-23.1	66.4	-17.8	63.2	33.6	26	2.3
160	69	154.8	-23.3	67.1	-15.1	66.6	33.6	26	2.3
170	69	154.8	-23.5	67.1	-13.9	70.6	33.6	26	2.3
180	69	154.8	-23.6	65.9	-14.5	73.1	33.6	26	2.3
190	69	154.8	-23.6	64.8	-15	75.8	33.6	26	2.3
200	80.6	156.2	-31.5	64.3	-15	77.4	33.6	26	2.3
210	76	159	-28.5	64.3	-14.7	78	33.6	26	2.3
220	78.6	161.9	-31	64.3	-14.7	78	33.6	26	2.3
230	78.6	161.9	-31	64.3	-14.7	78	33.6	26	2.3
240	78.6	161.9	-31	64.3	-14.7	78	33.6	26	2.3
250	78.6	161.9	-31	64.3	-14.7	78	33.6	26	2.3
260	78.6	161.9	-31	64.3	-14.7	78	33.6	26	2.3

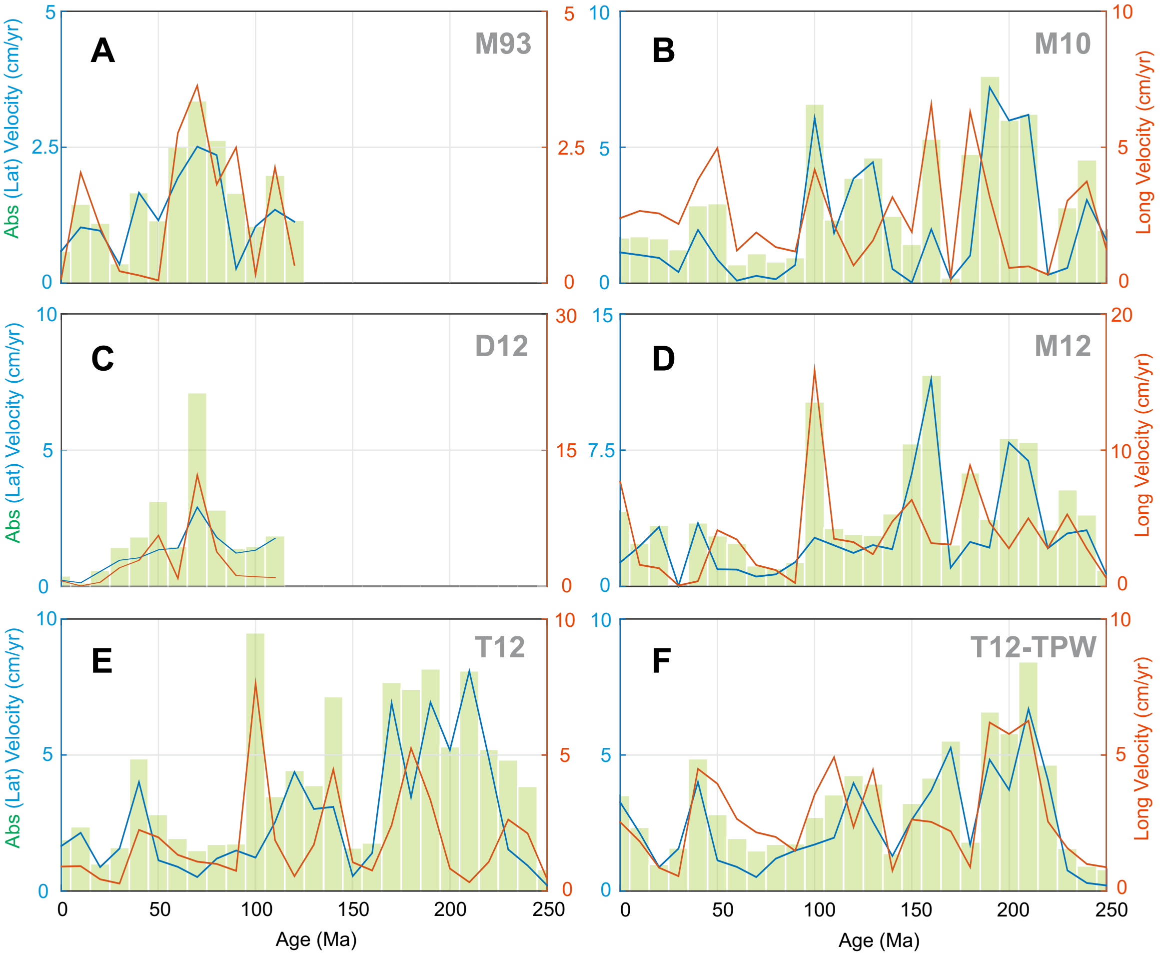

Figure 4.4: Absolute velocity predictions from different APM models (M93 [Müller et al., 1993], D12 [Doubrovine et al., 2012], M10 [van der Meer et al., 2010], M12 [Mitchell et al., 2012], T12 [Torsvik et al., 2012], and T12-TPW [Torsvik et al., 2012]). The axes are organized in the same way as those in Figure 4.3C.

Overall, all the APM models predict a northeastward motion for the reference point in stable Europe during the last 40 Myr (Figure 4.3B). Comparable plate motion directions and velocities are evident among our APWPGP, T12 and T12-TPW (both in the moving hotspot frame) until 60 Ma (Figures 4.3-4.4). Significant deviations arise among different APM model determinations earlier than 70 Ma when high-quality hotspot traces and age progression determinations become scarce. Similar observations are reported for various APM model determinations in the coordinates of South Africa since 130 Ma (i.e., the lowest limit of the hotspot frame predictions) [Williams et al., 2015]. We suggest that the reconstruction discrepancies between the APWPGP and other APM models for the last 130 Myr primarily stem from 1) the different references for reconstructions (i.e., the 'entire Earth' for the hotspot frames [Doubrovine et al., 2012] and the Earth's spin axis for the APWPGP method

[Wu and Kravchinsky, 2014]) 2) the uncertainties of hotspot frames coming from the different selections of relative plate motion (RPM) models and the various geodynamic modelling of hotspot motions, 3) the errors propagated in transferring rotations using different plate circuits (with various reliability), 4) the uncertainties in slab characterizations using diverse tomography models and geodynamic modelling methods, 5) the uncertainties in the TPW estimates, 6) the quality of the input APWPs and the uncertainties in the track fittings from the APWPGP method, and 7) any combinations of the above possibilities.

For the ages earlier than 130 Ma, there are substantial discrepancies between the different APM model predictions (Figure 4.3A). We note that, except for the APWPGP method, the paleo-longitudes from other models are predicted in the common paleomagnetic frames (without strict longitudinal determinations) [Torsvik et al., 2012, 2008a], which are constructed through some anchor points speculated from either slab identifications [van der Meer et al., 2010] or TPW estimates [Mitchell et al., 2012; Torsvik et al., 2012] without proper error propagations for the causes discussed above. For instance, the current estimates of TPW behavior are usually derived from the absolute plate motions of the global plates, which includes speculations on some poorly-studied plates such as the central-eastern Eurasian plates.

As demonstrated above, various APM models predict very different absolute motions of EU since 260 Ma (Figures 4.3-4.4). To a large degree, such differences accentuate the need for reliable plate reconstructions. The high quality of our reconstruction parameters is evident from the predicted absolute motions of the continents, anchored to EU through plate circuits, which bound the Atlantic Ocean (Figure 4.5 and Table 4.6). The restored locations of EU and the Americas are compatible with the spatial distribution of Aegean Tethys, Farallon and Venezuela slabs, all of which are consistently revealed from seismic studies [van der Meer et al., 2010; Sigloch and Mihalynuk, 2013]. The robustness of our reconstruction parameters is strengthened during our correlation between the past plate motions associated with the closing of the MOO and the present-day slab geometries underneath Eurasia. The present-day contour locations of the continental plates involved in this study are shown in Figure 4.6 as a reference.

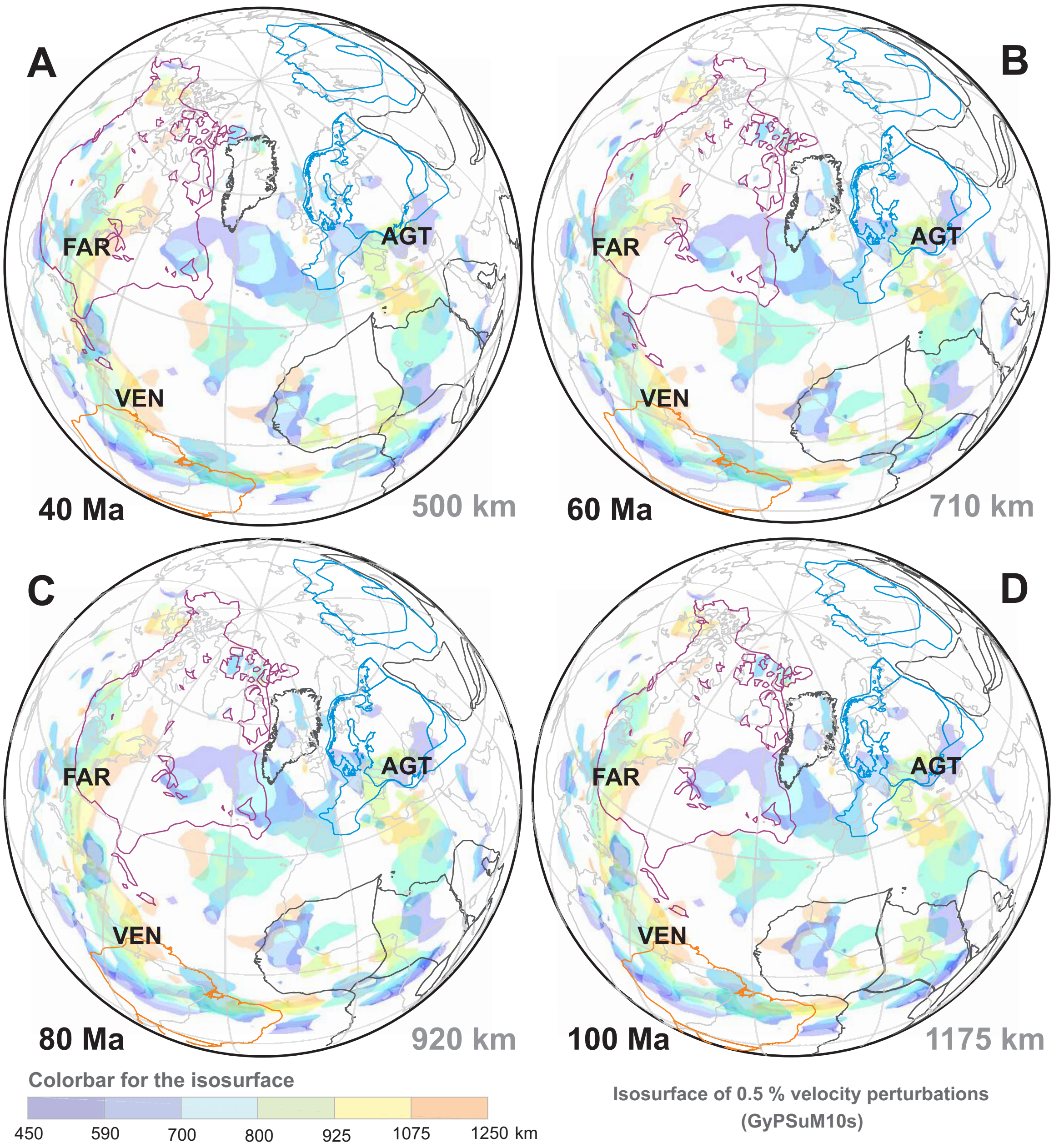

Figure 4.5: Snapshots of the predicted absolute motions of the continents bounding the Atlantic Ocean in the last 100 Myr. The isosurfaces of 0.5% velocity perturbations (color-coded to different depths) from the S-velocity model GyPSuM10s are shown as a reference. The edges of the isosurfaces are visually distorted because of the viewpoint of the three-dimensional spherical projection. The correlation between depths and reconstruction ages is established following van der Meer et al. [2010]. The locations of the Aegean Tethys (AGT), Farallon (FAR) and Venezuela (VEN) slabs are marked in the isopachs.

Figure 4.6: Contours of the continental plates predicted by the APWPGP reconstruction parameters through plate circuits. Continents highlighted in colors are matched with some well-studied slabs shown in Figures 4.5 & 4.7.

4.4 Implications on the genesis of the slab morphology

4.4.1 The closing of the Mongol-Okhotsk Ocean in the Mesozoic

The first stage of the 260-120 Ma interval featured the subduction of at least one third of the ancient oceanic lithosphere between Siberia and NCA in 260-200 Ma (Figure 4.8E), when the spherical distances between the two suture edges were reduced by ∼65% (Figure 4.8F). This massive subduction, most likely through an intra-oceanic convergence, concentrated on paleo-trenches that were close to the present-day western Siberia and mid-western Amuria (Figures 4.7D & 4.8E). The amount of slab formation in the stage, a proxy for subduction speed, decreased at a near-constant rate. This suggests persistent slab-pull forces from the downgoing oceanic lithosphere being applied to Siberia and NCA (Figure 4.8E), which likely drew them toward each other at an average speed of ∼8.8±0.6 cm/yr (Figure 4.8F). Depending on the net forces after integrating the inferred slab-pull with other forces on the continents (e.g., ridge push, continental resistance and transform resistance), Siberia and NCA exhibited constantly changing motion directions and speeds (Figures 4.2B, 4.2D & 4.8F). We assume that net forces aligned plate motions averaged in our smallest reconstruction duration of 10 Myr.

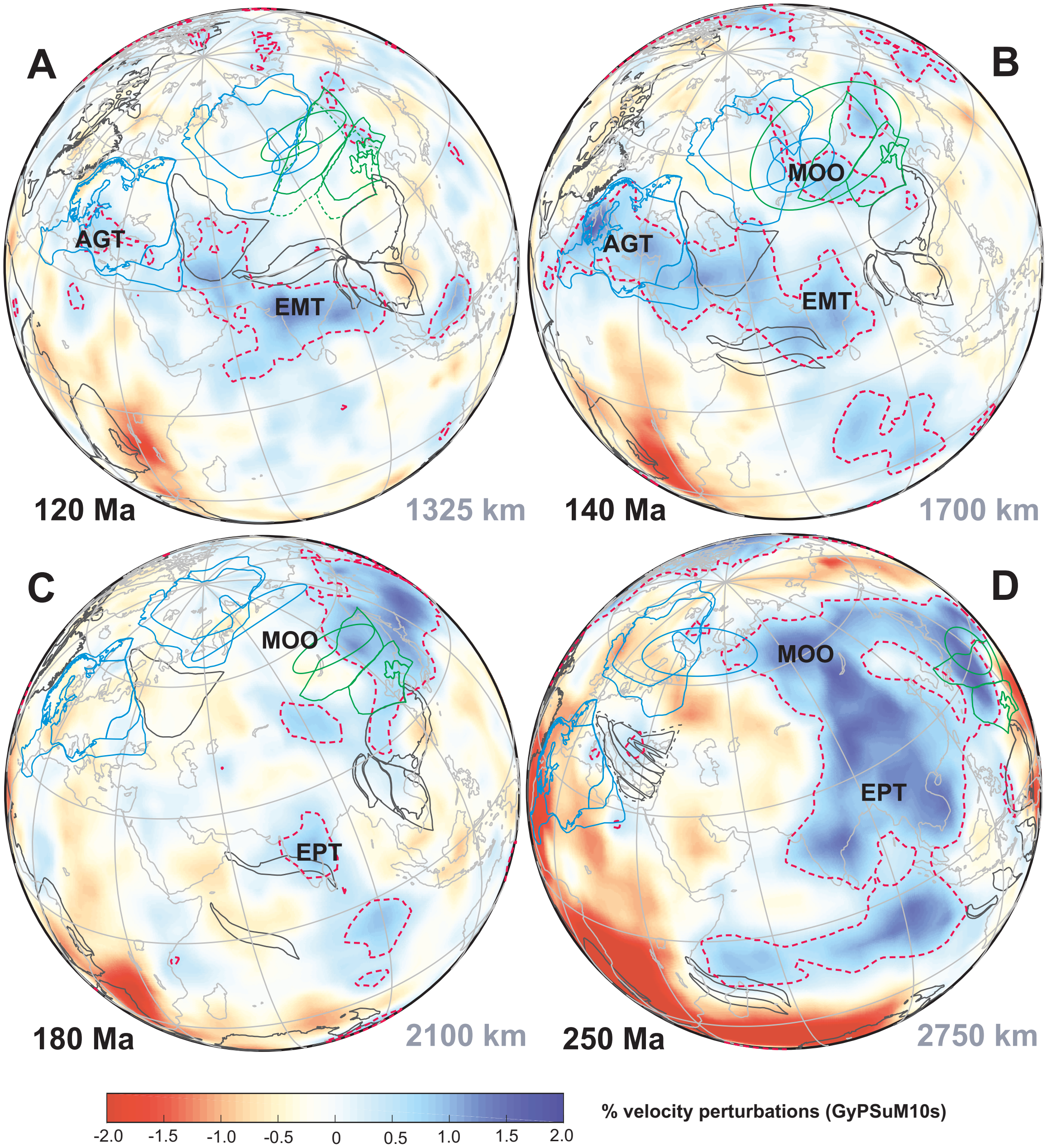

Figure 4.7: Reconstructions of the East Eurasian plates at the key ages during the closing of the MOO. Error ellipses of the restored Ref-1 are shown both on the Siberian and NCA side of the suture. The Southeast Asian plates are placed following the suggestions of Metcalfe [2013]. The ancient Kazakhstan collage system with the present-day contour (dark grey dashed contour) at 250 Ma in **D** is illustrated according to Xiao et al. [2015]. The dashed plate contours (green) in **A** show the adjusted position of NCA within uncertainties. Red dashed contours are the horizontal slices of the isopachs of the 0.5% velocity perturbations.

The second stage in 200-150 Ma is a transitional period when ∼25% of the original oceanic basin was subducted, predominantly in the vicinity of NCA (Figures 4.8B & 4.8E-F). In this stage, the average approaching speed of the suture edges dropped substantially to

∼3.6±0.3 cm/yr (Figure 4.8F). There was an overall rise in the subduction rate, with a downward discontinuity at ∼180 Ma induced by either a drop in the slab-pull forces or an increase in the opposing forces (Figure 4.8E). At 180 Ma, the net forces acting on Siberia seemed to be shifted by ∼90° counterclockwise (Figure 4.8F), while relatively smaller changes in the net forces occurred to NCA during its predominantly westward translation (Figure 4.8F & Figure 4.2E). We attribute the deceleration in the amount of slab production at 180 Ma to an excess resisting force, as indicated from the stronger convergence to the (north)east of NCA, accumulated on the western part of the paleo-oceanic basin confined between the two continents (Figure 4.8B). This adjustment of the plate motions could accommodate the accelerated subduction rates to the west of NCA (Figure 4.8E). This is supported by the westward displacement of slabs formed between 180 Ma (∼2100 km, green contour) and 150 Ma (∼1800 km, cyan patch) (Figure 4.8A).

Based on the insignificant approaching speeds (∼0.4-0.6 cm/yr) (Figure 4.8F), the interval of 150-120 Ma might be the last stage in closing the remnant paleo-oceanic basin confined between Siberia and NCA. This process was accompanied by the opposite senses of rotations for the two continents and a southwestward migration of slabs (i.e., subduction zones) at a depth of 1800-1300 km (between 140-120 Ma) with an upward reduction in volume (Figure 4.8C-D). The passage between the MOO and the Meso-Tethys might be shut down during 140-130 Ma (Figures 4.7A-B), as reflected from 1) the upward pinch-out of slabs to the west of NCA (around [80-100°E, 40-50°N] in the present-day coordinates) above the depth of 1400 km (corresponding to ∼130 Ma) (Figure 4.8C), 2) the transition in the rate of slab formation at ∼1600 km (Figure 4.8E), and 3) the restricted subduction zone(s) to the east of NCA and to the south of Eurasia at 120 Ma (Figure 4.8D). Our inferred closing interval of the MOO is consistent with the geologic estimation based on the subduction-induced magmatism along the suture [Tomurtogoo et al., 2005, and references therein].

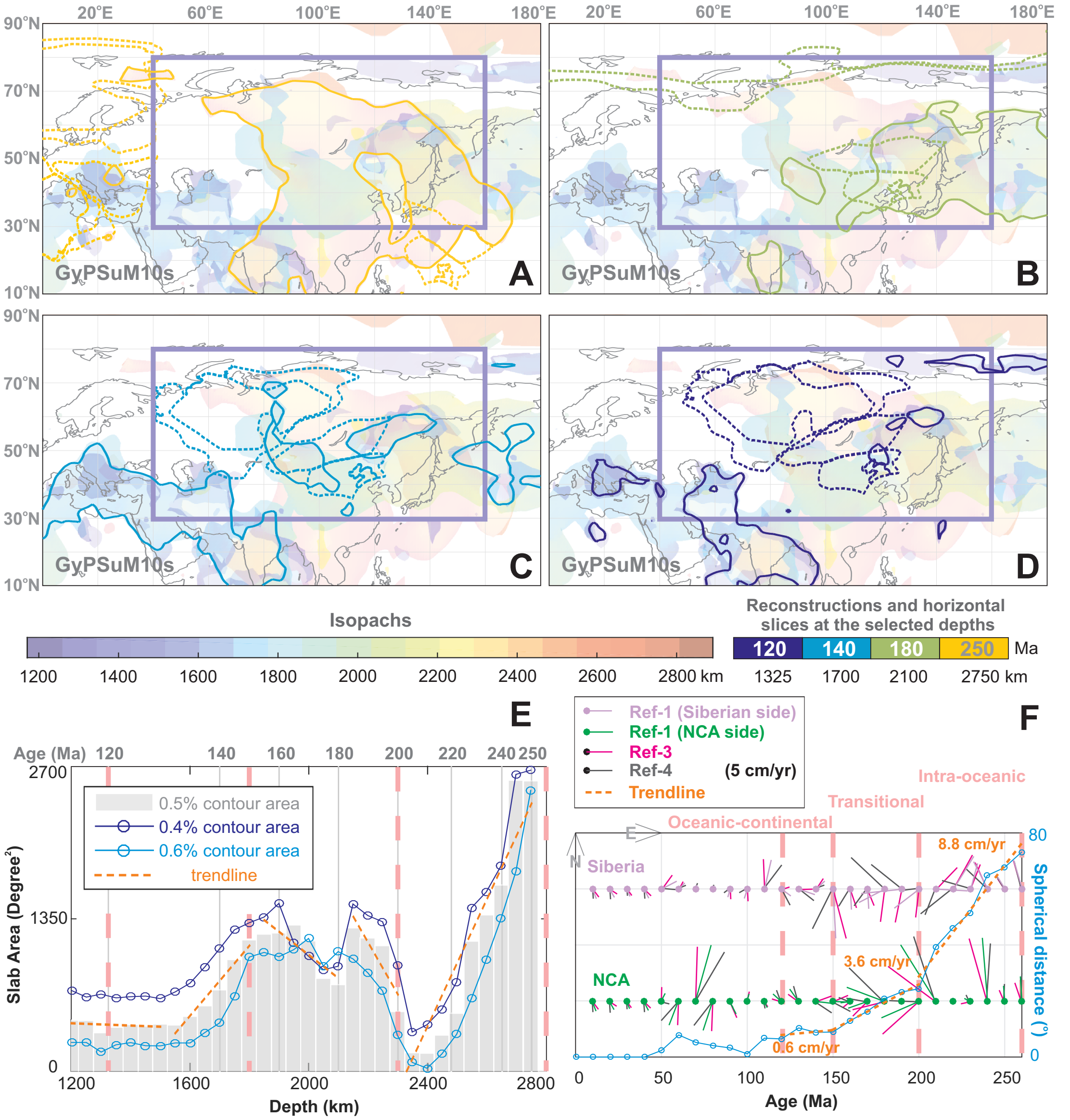

Figure 4.8: Linking plate reconstructions with slab geometries. **A-D**, Isopach characterization of slabs (color-coded to different depths), which are enclosed in the 0.5% contours from the S-velocity model GyPSuM10s [Simmons et al., 2010], in the lower mantle beneath Eurasia. The shading of an orange-yellow color (an overlap of several colors representing different depths) delineate the distribution of high-velocity zones in the lowermost mantle. The color-coded solid lines mark the horizontal slab slices at the selected depths (Figure 4.7). The plate reconstructions (of the same ages) are shown in the dashed-lines using the same color conventions. The reconstructed contours of EU and Kazakhstan are shown only at 250 Ma for clarity. The correlation between depths and reconstruction ages is established according to van der Meer et al. [2010]. **E**, Depth-varying slab areas enclosed in the purple rectangle ([40-160°E, 30-80°N]) in **A-D**. Trendlines for the 0.5% contour areas in five intervals whose slopes (rates of subduction) are used to represent the slab-pull forces. **F**, Time-varying absolute velocity vectors for the reference sites (Ref-1 in colors and Ref-3 and Ref-4 in greys) along the suture. The variations in the velocity vectors reflect the instantaneous impacts of the acting net forces. Also shown are the temporal variations of the spherical distances (SD) (light blue dots and connecting line, scaled to the gridlines) for Ref-1, as predicted from the finite rotations of Siberia and NCA (Table 4.4). Average approaching speeds of the suture boundaries (Ref-1,3,4) are estimated from the slopes of the best-fit trendlines (dark blue dashed-lines), which disclose three stages foremost during the closing of the MOO. Ranges for the slopes are determined from the SD calculations for Ref-3 and Ref-4 (Figure 4.2A). The average approaching speeds and associated ranges are 8.8 [8.2, 9.3] cm/yr in 260-200 Ma, 3.6 [3.4, 3.9] cm/yr in 200-150 Ma and 0.6 [0.4, 0.6] cm/yr in 150-120 Ma.

4.4.2 Comparison of the various seismic tomography models

There appears to be the best consistency between our APWPGP reconstructions and the S-velocty model GyPSuM10 [Simmons et al., 2010], as reflected from our correlation between the past plate motions and the present-day descending mantle structures associated with the closing of MOO. In comparison, other tomography models are quite distinct in predicting locations and areas of slabs in the lower mantle beneath Eurasia (Figures 4.8A-E & 4.9-4.10). The first main discrepancy occurs below ∼2600 km (Figures 4.9-4.10), the phase transition layer D" where the phase change from perovskite to post-perovskite could cause a ∼2% increase in S-velocity, and a small decrease or increase in P-velocity [Garnero and McNamara, 2008]. Nonetheless, different models are generally consistent in revealing the long-wavelength high-velocity discontinuities beneath Eurasia. Another main discrepancy with a larger magnitude exists at the depths of 1800-2300 km (highlighted in the magenta rectangles in Figures 4.8A-E & 4.10) where most P-velocity models exhibit a strong anti-correlation with S-velocity models [Ishii and Tromp, 1999; Trampert et al., 2004; Simmons et al., 2010]. Here we suggest that the complex correlations between seismic parameters (i.e., S-velocity, P-velocity and density) must be considered in future tomographic applications, such as identification of ancient subduction zones and geodynamic modelling of the mantle thermal structure (e.g., for constraining the motions of hot spots). We also notice a trace of slab (around [80-90°E, 65-70°N]) at ∼1700 km underneath the restored Siberia at ∼140 Ma. These low-velocity anomalies are revealed only in the model GyPSuM10 (Figure 4.9).

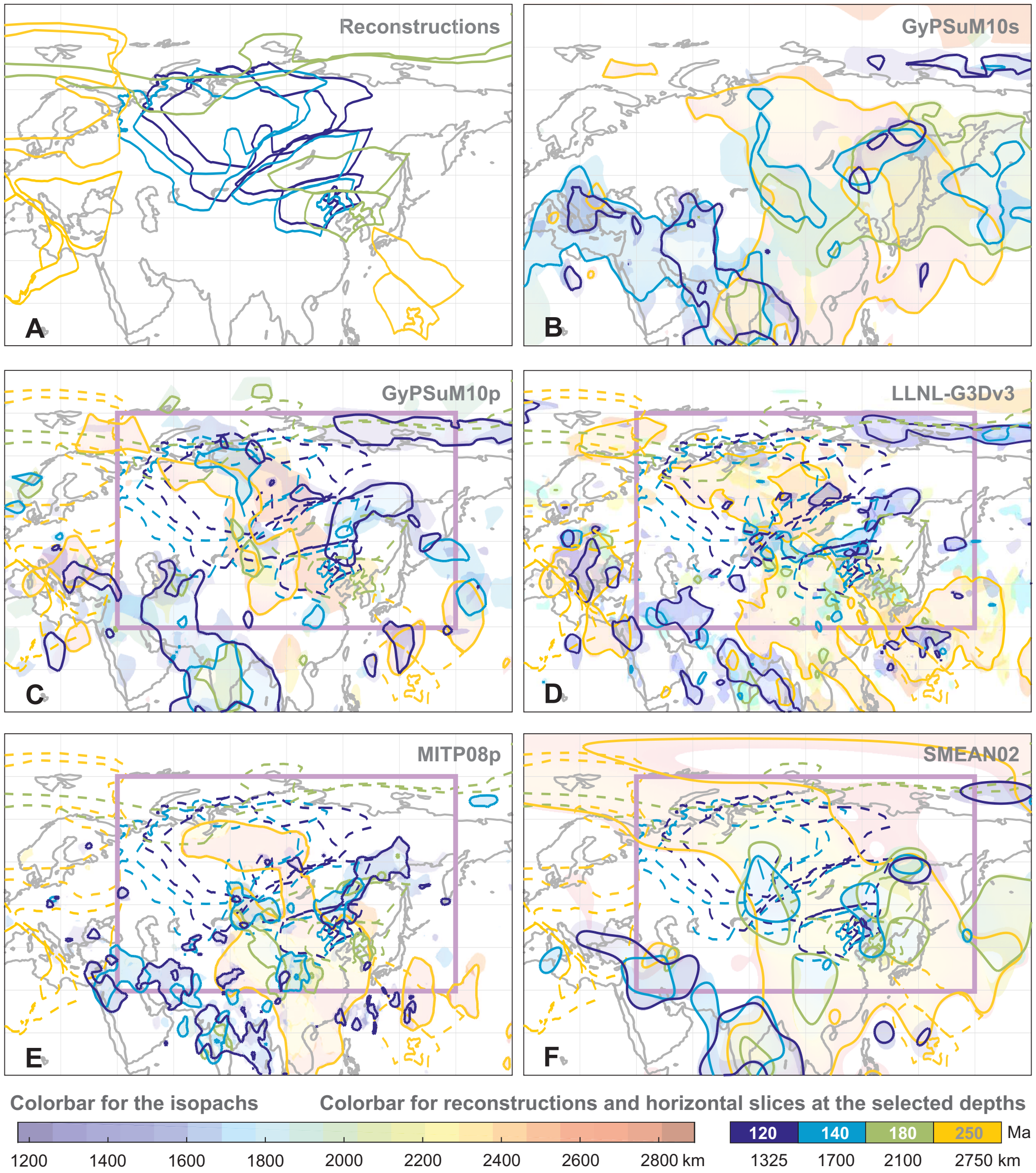

Figure 4.9: Isopach characterization of slabs in the lower mantle beneath Eurasia using different tomography models. **A-B**, Separations of the reconstructions (A) and the slab delineation (B) shown in Figure 4.8A-d. The restored Siberian contour at 180 Ma (lime green) is distorted because of the map projection. **C-F**, Slab characterizations using GyPSuM10p [Simmons et al., 2010], LLNL-G3Dv3p [Simmons et al., 2012], MITP08p [Li et al., 2008] and SMEAN02 [Becker and Boschi, 2002], where 0.2%, 0.4%, 0.3% and 0.6% of velocity perturbations are used (see section 4.2). The reconstructions (dashed lines) and the horizontal slices of slabs (solid lines) are marked in the same color scheme. Purple rectangles highlight the region for the inspection of the depth-varying slab areas (Figure 4.10).

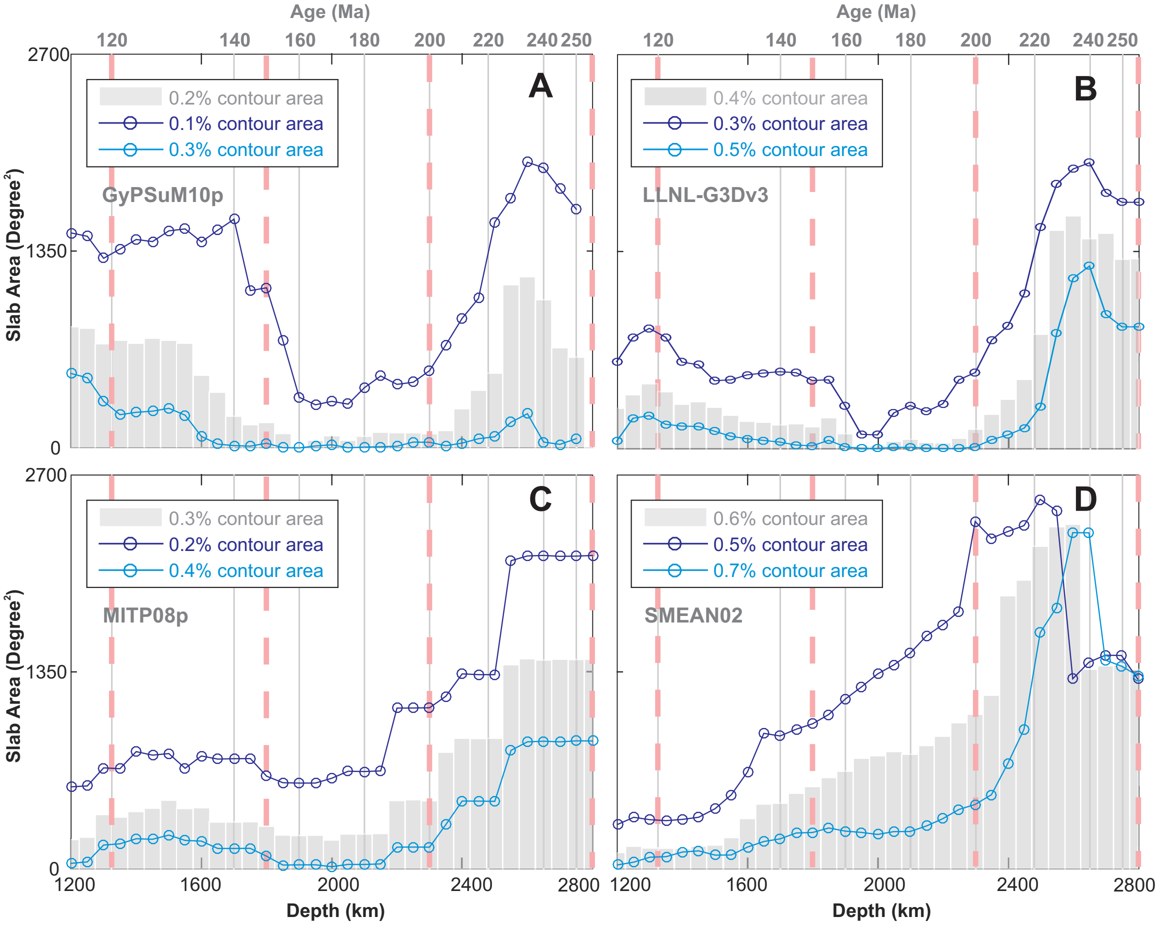

Figure 4.10: Depth-varying slab areas (in the purple rectangles in Figure 4.9) predicted from the different tomography models. Errors are approximated by the areas enclosed in the X±0.1% contours, where X is the percentage velocity perturbation (see section 4.2). The correlation between depths and reconstruction ages is established following van der Meer et al. [2010].

4.5 Conclusions

Understanding present-day mantle convection requires an accurate reconstruction of past plate motions, especially those associated with convergent tectonics. However, existing absolute plate motion reconstructions generally require paleo-positional constraints (especially for paleolongitudes) from poorly understood mantle structures, which results in circular reasoning since their interpretations as subducted oceanic lithospheres (or slabs) were based on plate reconstructions in the first place. In this study, we adopt a new APM reconstruction method to independently restore the plate motions of Siberia and North China-Amuria (NCA), which had bounded the Mongol-Okhotsk Ocean (MOO) in the Mesozoic, for the last 260 Myr. We find that the closing of the remnant paleo-oceanic basin confined between Siberia and NCA could have been accomplished at 150-120 Ma. This observation agrees with a southwestward transition of slabs distributed at the depth of 1300-1800 km and an upward reduction in slab volumes predicted by the shear-wave velocity model GyPSuM. Our reconstructions quantitatively explain how slabs related to the MOO affect the geometry of the long-wavelength high-velocity discontinuities in the lower mantle. With the published relative plate motion models, we also present a new paleomagnetic-based absolute plate motion reference frame in the coordinates of stable Europe for the last 260 Myr.

5

Anti-correlation between slab volume in the lower mantle and the geoid height in the India-Eurasia geoid low [a]

Abstract

Descending slabs in the mantle, usually represented as high-velocity perturbations in tomographic images, provide an important driving mechanism for mantle circulation by inducing thermal and density heterogeneities. Such mantle downwelling shapes the Earth's gravity field by introducing mass anomalies associated with the sinking slabs and the deformed internal layer boundaries within the Earth. Geodynamic studies suggest a negative correlation between slab locations and geoid height, which could be explained by the dynamic model of density(temperature)-driven mantle flow. However, it is still unclear how the spatial distribution of sinking slabs is correlated with the variations of geoid height. Also, work has been scarce to compare the seismically observed and the geodynamically predicted deformation of the main density/viscosity interface of the mantle. Here we correlate the geoid height in the India-Eurasia geoid low (IEGL) with the high-velocity zone beneath Eurasia, which is one of the best resolved slab structures in seismic tomography models. We find a remarkably strong linear correlation of -0.92, with the associated coefficient of determination of 0.84, between the surface geoid height and the slab volume at the depth of 1200-2800 km underneath Eurasia. Together with the seismically constrained boundary topographies of the lower mantle, we propose that the mass deficit reflected from the IEGL is mainly caused by the lower density of the sinking slabs with respect to the ambient lower mantle. Such density unequilibrium between slabs and the ambient lower mantle could provide a new driving mechanism for mantle convection.

---

[a] A version of this chapter will be submitted as:
Wu, L., Kravchinsky, V.A., Gu, Y.J., Potter, D.K. Could descending slabs be less dense than the ambient lower mantle?

5.1 Introduction

The geoid is an equipotential surface of the Earth's gravity corresponding to mean sea level. The geoid height or undulation (in metres), which is the displacement between the geoid and the reference ellipsoid, reflects the mass distribution of the Earth. Understanding mass heterogeneity in the mantle is important because it dominates the moments of inertia of the Earth and, therefore, the location of the spin axis [Anderson, 2007]. The global geoid is characterized by alternating geoid highs and lows. Geographically, there are two antipodal geoid highs centered on the central Pacific and Africa in the equatorial region, between which there is a continuous geoid low extending from Siberia through the Indian Ocean, Antarctica, Hudson's Bay to South Atlantic Ocean.

Descending slabs in the mantle, usually represented as high-velocity perturbations in tomographic images, provide an important driving mechanism for mantle circulation induced by the associated thermal and density heterogeneities. Such mantle downwellings shape the Earth's gravity field by introducing internal mass anomalies related to slabs and deformation of the Earth's interior boundaries [Hager, 1984; Richards and Hager, 1984; Hager and Richards, 1989]. There is a similar proposal to use thermal anomalies in the mantle to account for long-wavelength geoid anomalies and the associated boundary deformation [Parsons and Daly, 1983]. As illustrated in Figure 5.1, density (or temperature) heterogeneities in the mantle drive convection in the viscous mantle on geologic time scales: a denser (or cooler) downgoing mass anomaly can push down the lower boundary and at the same time pull down the upper boundary. The situation is reversed for a less dense (or hotter) upwelling mass anomaly. Accordingly, the geoid can be dynamically modelled with the constraints primarily from surface boundary conditions (e.g., free slip, current plate motions), seismic tomography models, viscosity profiles, and depth-varying scaling factors relating seismic velocity anomalies to purely thermally originated density anomalies [Hager and O'Connell, 1981]. Such geodynamic models relating subduction history, slab distribution and seismic velocity anomalies suggest that slabs in the upper mantle are related to long-wavelength geoid highs, while slabs in the lower mantle are associated with long-wavelength geoid lows [Hager and Richards, 1989; Ricard et al., 1993; Steinberger, 2000]. These geodynamic models also show that the geoid can be affected by 1) postglacial rebound [Simons and Hager, 1997], 2) lateral variations in viscosity owing to different depths of the internal boundaries such as the bottom of lithosphere [Spasojevic et al., 2010], and 3) nonthermal density heterogeneity especially the chemically distinct antipodal large low shear-velocity provinces in the lowermost mantle beneath Africa and Pacific [Steinberger and Holme, 2008; Davies et al., 2014]. A recent model further suggests that mantle upwellings above slab graveyards can cause discrete geoid lows within a larger trough [Spasojevic et al., 2010].

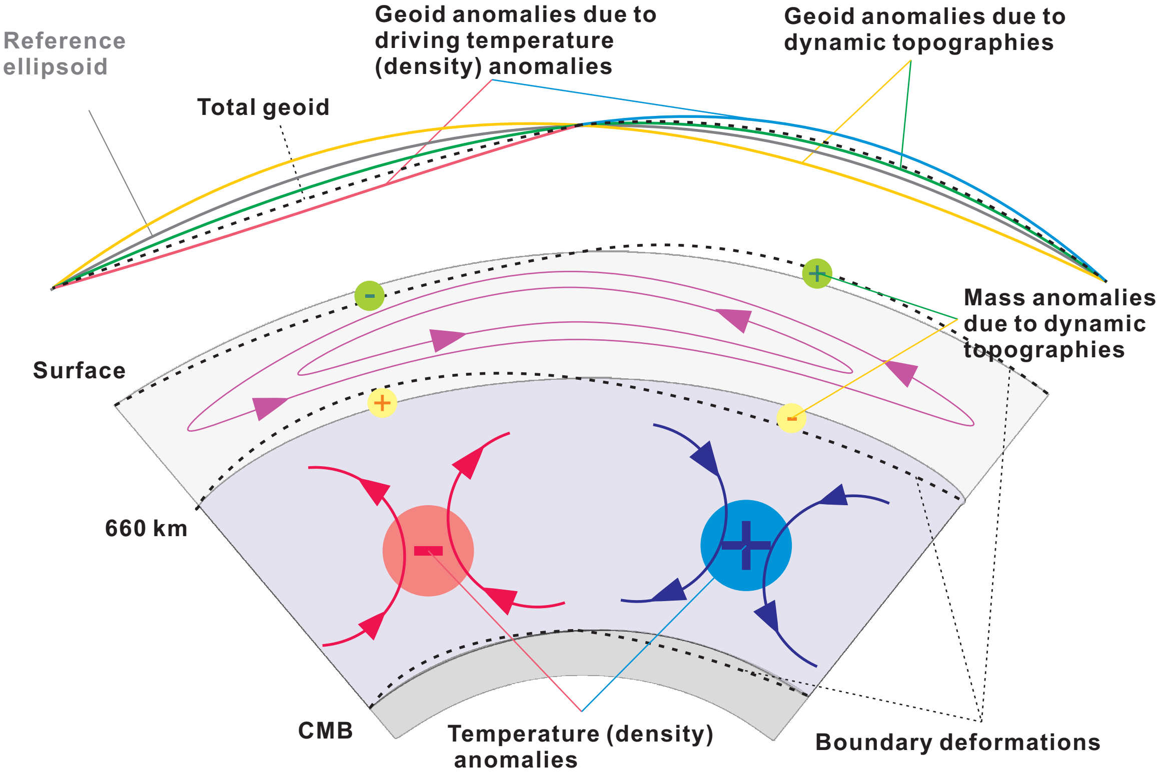

Figure 5.1: Schematic illustration, after Richards and Hager [1984], of the geoid undulation caused by the density (or temperature) contrasts which drive a two-layered mantle convection. Plus and minus signs mark positive (blue) and negative (red) density (or temperature) contrasts. The solid lines in the cross-section indicate the main density/viscosity interfaces and the dashed lines show their displaced topography due to convection. The total geoid anomalies result due to the mass anomalies from the flow-induced boundary deformation and the driving density (or temperature) contrasts.

The robustness of these density-driven flow circulation models is commonly evaluated from global correlation coefficients between observed geoid and that predicted with spherical harmonic expansion of degree 2-15. However, global-scale correlations are not sensitive to local geoid variations such as those within the India-Eurasia geoid low (IEGL), i.e., the largest trough of the geoid, as seen from easterly deviated trough of the modeled IEGL [e.g., Zhang and Christensen, 1993; Steinberger, 2000] and misfit in the geoid amplitudes [Spasojevic et al., 2010]. One might therefore question the estimated mantle viscosity variations and dynamic topographies primarily derived from these dynamic models. Also, work has been scarce to compare the seismically observed and the geodynamically predicted deformation of the main density/viscosity interface of the mantle. To provide new insights on these issues, here we quantitatively explore the relationships between the long-intermediate wavelength geoid undulations inside the IEGL, the slab distribution (i.e., driving mass anomalies) and the boundary deformation of the main density/viscosity interfaces in the mantle. The IEGL is investigated here because it is suggested to bear a spatial relationship with the sinking slabs in the lower mantle which are characterized as high-velocity discontinuities from seismic imaging [Anderson, 1982; Chase and Sprowl, 1983; Richards and Engebretson, 1992]. With the recent advances in seismic tomography, here we are able to compare the observed boundary undulations with those predicted from the dynamic models.

5.2 Methods

5.2.1 Slab characterization

To characterize slabs in the lower mantle beneath Eurasia, we use the S-velocity model GyPSuM10s constrained from the well-covered and traced seismic ray geometries and a joint seismic-geodynamic inversion technique [Simmons et al., 2010]. The model exhibits a positive correlation coefficient (close to one) between S-velocity and thermally derived density in high-velocity zones in the lower mantle [Simmons et al., 2010]. We use isosurfaces of 0.5% velocity perturbations to represent slabs underneath Eurasia to avoid biased visual appearances of mantle structures due to subjective selections of vertical cross-section. We assume that the isopachs approximate the sinking and folded slabs related to the downgoing Mongol-Okhotsk and Paleo-Tethys lithosphere in Eurasia [van der Meer et al., 2010; Van der Voo et al., 2015], regardless of their respective contributions or subduction polarities of the related paleo-trenches (not critical for the calculations). Note that the suggested contours might include the ambient mantle that is thermally disturbed by sinking slabs which, however, do not significantly affect the discontinuous long-wavelength velocity structures caused by slabs. Other widely referred S-velocity tomography models S40RTS (0.5%) [Ritsema et al., 2011], SEMUCB-WM1 (0.45%) [French and Romanowicz, 2014], savani (0.6%) [Auer et al., 2014] and LLNL_G3D_JPS (0.25%) [Simmons et al., 2015] are used for a comparison.

The time frame for the horizontal slices of the lower mantle of different depths (Figures 5.2 & 5.3) are established following the suggestions of van der Meer et al. [2010]. This time frame, derived from the average slab sinking rate in the mantle, may not apply to slabs elsewhere when slab stagnation occurs (or occurred) in the transition zone [Simmons et al., 2015]. However, it is robust for the correlation between the plate reconstructions and the depth-varying slab geometries related with the Mongol-Okhotsk Ocean (MOO), Farallon and Aegean Tethys slabs, primarily from which the slab sinking rate (and the time frame) in the lower mantle is estimated [van der Meer et al., 2010].

5.2.2 Correlating slab distribution and geoid height

To quantify the linear correlation between the slab geometry and the geoid height variations inside the India-Eurasia geoid low (IEGL), we estimate the degree of slab overlap on a grid cell of 1° × 1° for the studied map area along the vertical direction in a 50 km increment between the depths of 1200 km and 2800 km. Each grid cell is awarded one point if its percentage velocity perturbation at each depth is no smaller than 0.5% in the S-velocity model GyPSuM10s [Simmons et al., 2010]; a zero is assigned otherwise. The resulting cumulative slab overlap along the vertical direction for each grid cell, which ranges from 0 to 28 in total (i.e., 1200:50:2800 km) and can be seen as 'slab volume' in the depth range of the lower mantle (Figure 5.2B), is then subjected to a low-pass filter with a moving window of 25° to ensure comparable lateral length scales with those in the IEGL (Figure 5.3). The Pearson linear correlation coefficient (ρ) between the geoid height (H) and the 'smoothed' cumulative slab overlap (S) after the filtering is calculated for the grid cells in the area encompassed in the 0 m isoline of the IEGL (Figure 5.5).

$$\rho(H,S) = \frac{\sum(H_i - \bar{H})(S_i - \bar{S})}{\sqrt{\sum(H_i - \bar{H})^2}\sqrt{\sum(S_i - \bar{S})^2}} \tag{5.1}$$

where $\bar{H}$ and $\bar{S}$ are the means of the datasets ($H_{i=1\to n}$) and ($S_{i=1\to n}$), respectively. The associated confidence intervals at the significance level of 0.05 are estimated using the frequently applied Fisher transformation [Fisher, 1958]. Coefficient of determination (R2) and the associated root mean square error (RMSE) are calculated to measure the strength of such linear dependence between H and S.

$$R^2 = 1 - \frac{\sum(H_i - m_r \times S_i)^2}{\sum(H_i - \bar{H})^2}, \qquad RMSE = \sqrt{\frac{\sum(H_i - m_r \times S_i)^2}{n}} \tag{5.2}$$

where m_r is the slope determined from simple linear regression. To evaluate the robustness of the linear relationship between H and S from the selected region, we compute the spatial variations of ρ and R^2. A good linear relationship is confirmed when the absolute value of correlation coefficient ($|\rho|$) and R^2 are close to 1 with small RMSE. The computations are performed to the 1° × 1° grid cells which are enclosed in a sliding 'square' with the side length of 11°. This 'square', centering on each of the grid cells, moves from the lower left to the upper right of the area [0-180°E, 0-90°N] (Figure 5.4).

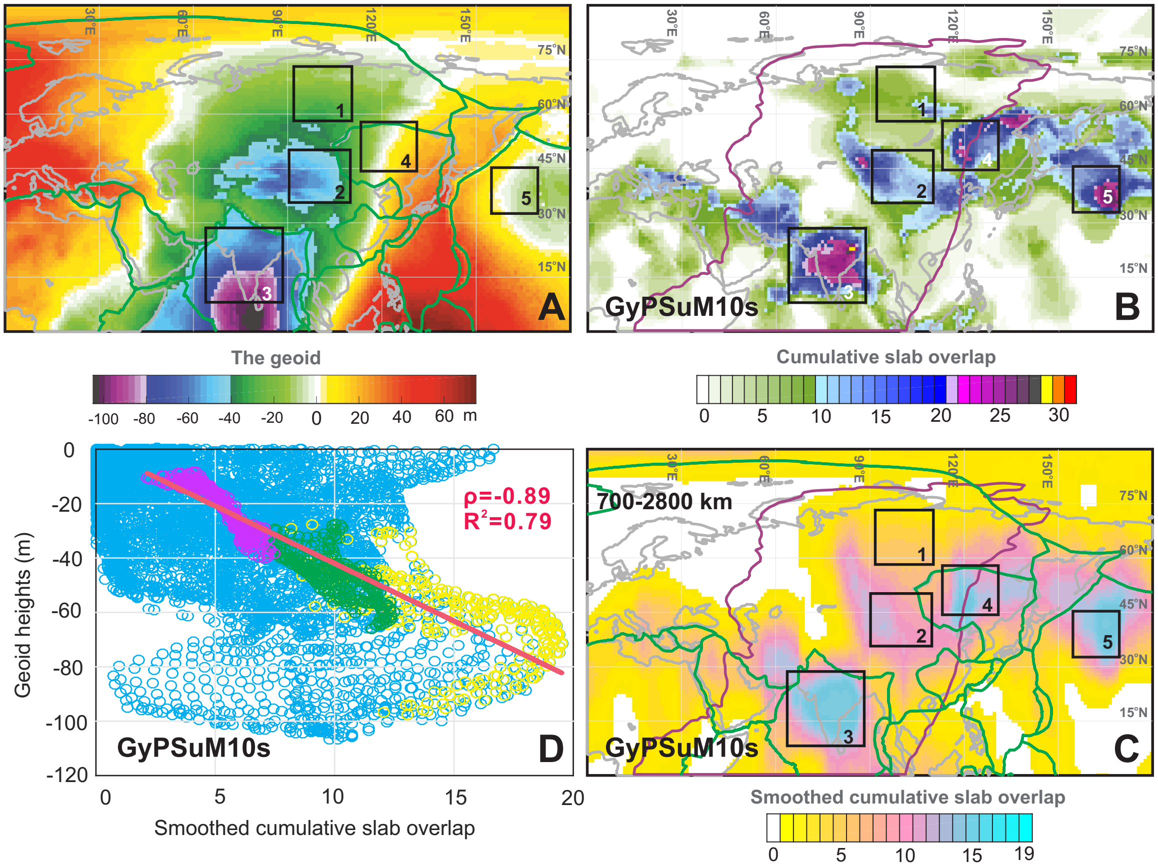

Figure 5.2: Correlation between the geoid height and the slab distribution inside the India-Eurasia geoid low. (A) Morphology of the geoid height according to the model EGM2008 [Pavlis et al., 2012]. The green lines delineate the present-day plate boundaries [Bird, 2003]. (B) The cumulative slab overlap in the lower mantle according to the shear-velocity model GyPSuM10s [Simmons et al., 2010]. The horizontal slices of slabs at four depths are shown to indicate the spatial transition of subduction zones before and after the closure of the MOO. The numbered black rectangles highlight the areas with heavy overlap of slabs between 700-2800 km (see the main text for the discussion). The purple line shows the 0 m isoline encompassing the India-Eurasia geoid low (IEGL). (C) The 'smoothed' cumulative slab overlap after applying a low-pass filter with a moving window of 25° (see section 4.2). (D) Scatter plot of the geoid height (H) and the 'smoothed' cumulative slab overlap (S) between 700-2800 km for the grid cells encompassed in the polygonal regions inside the IEGL. The purple, green and yellow markers represent the datasets (S, H) covering the Rectangle 1, 2 and the Indian continental region in 3, from which the Pearson linear correlation coefficient (ρ) of -0.89 and the coefficient of determination (R^2) for a simple linear regression are computed. The blue markers show the dataset covering the region inside the 0 m isoline of the IEGL.

To accentuate the reducing effect of slab overlap on the geoid height inside the IEGL, we calculate the Pearson correlation coefficients between H and S for the grid cells enclosed in the black rectangles 1-3, which display an increasing degree of slab overlap (Figures 5.2-5.3) and the robust linear relationship between H and S ($R^2 \geq 0.5$) (Figure 5.4). To avoid geoid displacement caused by the lateral variations in the surface topography and crustal/lithospheric thickness from ocean to continent [Turcotte and McAdoo, 1979; Anderson, 2007], we limit the calculations to the Indian continental region in rectangle 3 (Figure 5.5). Finally, we perform the same calculations to the slabs between the depths of 700-1200 km and 700-2800 km to explore their potential relationships with the geoid height (Figures 5.2-5.4). The same calculations are performed using other shear-velocity models listed in section 5.2.1, to evaluate if any detected correlation between the surface geoid height and the underlying slab distribution in Eurasia stands (Figures 5.6-5.13).

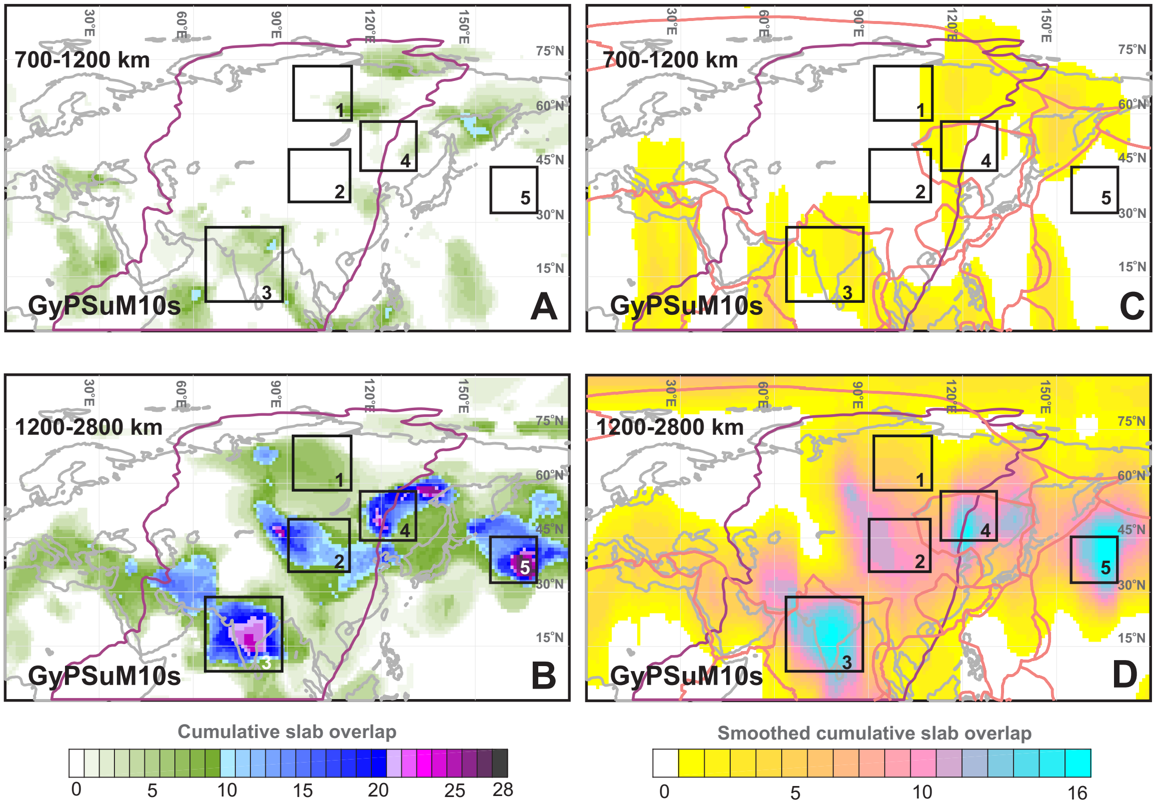

Figure 5.3: (A-B) Slab overlap in the lower mantle according to the shear-velocity model GyPSuM10s [Simmons et al., 2010] and (C-D) the long-wavelength features revealed from a low-pass filtration using a moving window of 25°. The purple lines represent the 0 m isoline encompassing the IEGL, in which the linear correlation coefficients are -0.15 and -0.55 between the geoid height and the 'smoothed' cumulative of slab overlap for the depths of 700-1200 km and 1200-2800 km, respectively (Table 5.1). The correlation coefficient for the areas within the black rectangles 1-3 is -0.76 ($R^2 = -0.58$) for the depths of 1200-2800 km; the same correlation is improved to be -0.92 ($R^2 = -0.84$) after excluding the oceanic region from the rectangle 3 (Table 5.1, see section 4.2). The pink lines in (C-D) delineate the present-day plate boundaries [Bird, 2003].

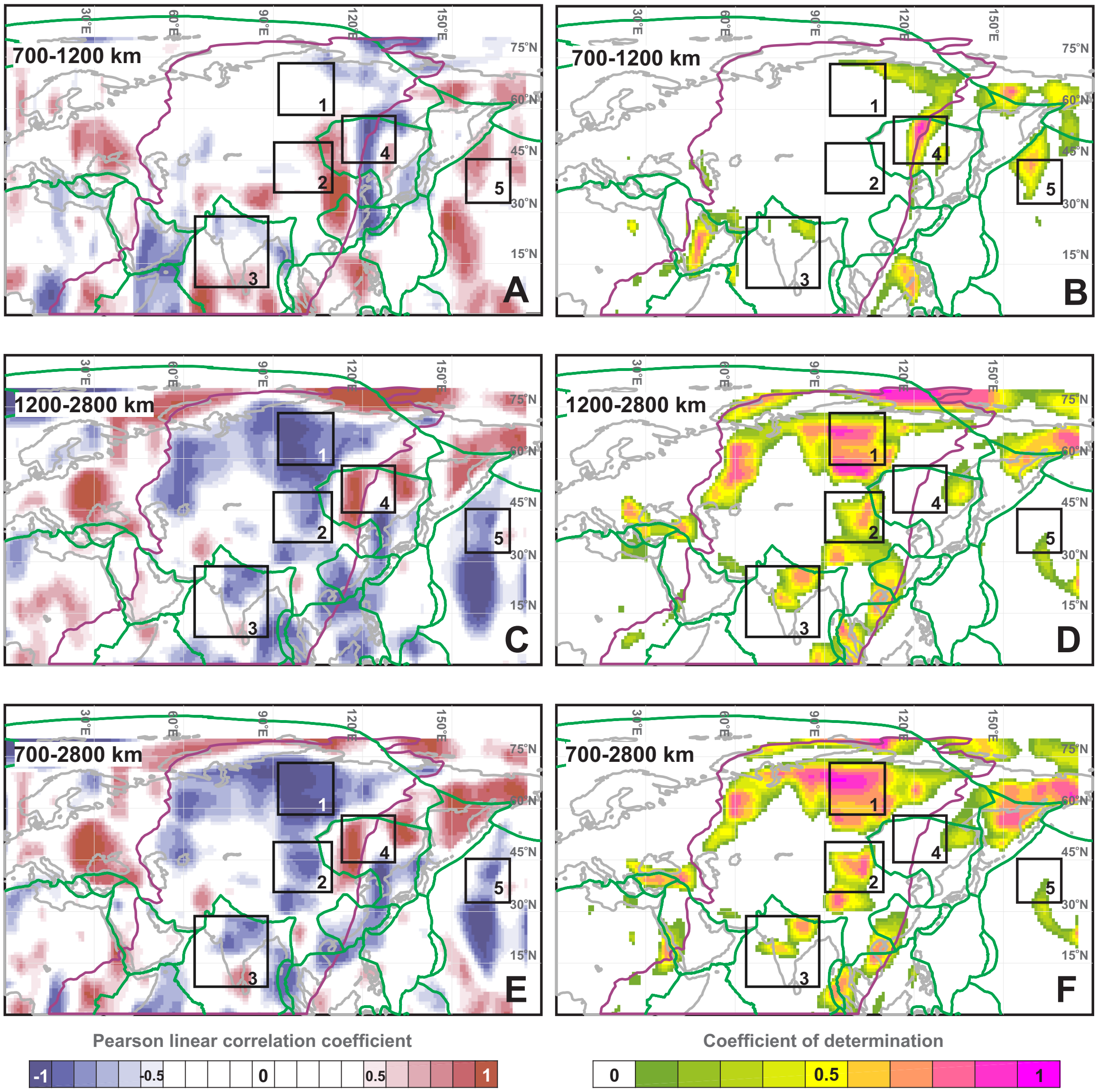

Figure 5.4: Spatial variations in the Pearson linear correlation coefficients (ρ) between the geoid height (H) and the 'smoothed' cumulative slab overlap (S) of different depths, and the variations in the associated coefficients of determination (R^2) from simple linear regression for assessing the robustness of such linear relations. The linear relations are considered robust when R^2 is larger than 0.5. The computations are performed to the 1° × 1° grid cells which are enclosed in a sliding 'square' with the side length of 11°. This 'square', centering on each of the grid cells, moves from the lower left to the upper right of the area [0-180°E, 0-90°N]. The green lines delineate the present-day plate boundaries [Bird, 2003]. The purple line shows the 0 m isoline encompassing the IEGL. The computations are based on the shear-velocity model GyPSuM10s [Simmons et al., 2010].

5.3 Results

There is no simple correlation between the cumulative slab volume in the lower mantle and the geoid height inside the 0 m isoline of the IEGL (Figure 5.2). This is seen from the correlation of -0.53 with the associated R^2 of 0.00 and RMSE of 39.78 for the slabs at the depth of 700-2800 km (Table 5.1). This poor linear relationship could result from small-scale lateral variations in crustal thickness, surface topography, collisional tectonics in central Asia, lateral variations in the slab volume, and boundary deformation in the mantle. To focus on the impact of the slab volume on the surface geoid height, we select the regions enclosed in the rectangles 1-3 in Figure 5.2. These regions show a strong linear correlation ($|\rho| > 0.5$) with acceptable robustness ($R^2 > 0.5$) between the slab volume and the geoid height (Figure 5.4). We exclude the datasets covering the Indian ocean from the rectangle 3, considering the geoid undulation induced during such lateral variations as the surface topography and crustal/lithospheric thickness from ocean to continent. The potential mass anomalies in the crust and lithosphere with wavelength larger than a few hundred kilometers are suggested to be mostly compensated through isostasy [e.g., Anderson, 2007; Turcotte and Schubert, 2014].

As predicted, the mass excess associated with the ongoing trench subduction elevates the geoid height [Chase, 1979]. The banded appearance of the IEGL (i.e., the alternating occurrences of geoid highs and lows) is therefore caused by the subduction of oceanic plates to both its sides in the Mediterranean and the circum-Pacific (Figure 5.2A). By correlating the slab distribution and the geoid height, there appears to be a strong linear relationship between the surface geoid height and the cumulative slab overlap in the lower mantle. Specifically, the slabs in the lowermost mantle can lower the geoid height by $\sim$40 m (e.g., Rectangle 1 in Figures 5.2A-B) while overlap of slabs at different depths is able to reduce the geoid height by another 40-70 m (e.g., Rectangles 2 & 3 in Figures 5.2A-B). The datasets (H, S) from the continental regions in the Rectangles 1-3 exhibit a strong linear correlation of -0.89 with the associated R^2 of 0.79 and RMSE of 8.99 (Figure 5.2C-D), robustly indicating a strong anti-correlation between the geoid height and the slab volume at the depth of 700-2800 km. This is consistent with the southeastward strengthening in the downward geoid undulation from visual inspection, together with an increasing cumulative slab overlap in the lower mantle (Figures 5.2-5.3). This reducing effect on the surface geoid height inside the IEGL is primarily caused by the slabs at the depths of 1200-2800 km, as indicated from their improved anti-correlation of -0.92 with the associated R^2 of 0.84 and RMSE of 7.72 (Table 5.1 & Figure 5.5). The same conclusion can be drawn from the equally robust linear correlation between the geoid height and the cumulative slab overlap at the depths of 1200-2800 km and 700-2800 km, and the not good correlation for the slabs at the depth of 700-1200 km (Figures 5.6-5.13).

Table 5.1: Pearson correlation coefficients (ρ) between the geoid height (H) and the 'smoothed' cumulative slab overlap (S) for the polygonal regions (Figure 5.2) inside the India-Eurasia geoid low (Figure 5.5). The negative sign before correlation coefficient indicates the anti-correlation between H and S. The lower (ρ_L) and upper (ρ_U) bounds for the correlation coefficients are calculated at the significance level of 0.05. The strength of the linear relationship between H and S, whose slope (m_r) is estimated from linear regression, is examined from the coefficient of determination (R^2) with the associated root mean squared error (RMSE). The calculations are performed using the shear-velocity model GyPSuM10s [Simmons et al., 2010].

Polygonal region	ρ(H,S)	ρ_L	ρ_U	m_r	R^2	RMSE
700-1200 km:						
Geoid 0 m isoline	-0.15	-0.17	-0.12	-15.88	0.00	24.11
Rectangle 3	0.16	0.08	0.24	-32.45	0.00	34.06
Rectangle 3 (Indian subcontinent)	-0.08	-0.20	0.05	-27.52	0.00	24.85
Rectangles 1-3	-0.48	-0.52	-0.43	-31.30	0.00	35.22
Rectangles 1-3 (Indian subcontinent)	-0.44	-0.49	-0.39	-26.37	0.00	32.89
1200-2800 km:						
Geoid 0 m isoline	-0.55	-0.56	-0.53	-5.00	0.00	39.02
Rectangle 1	-0.87	-0.89	-0.84	-4.78	0.74	4.32
Rectangle 2	-0.75	-0.77	-0.74	-4.88	0.54	5.77
Rectangle 3	-0.07	-0.16	0.01	-5.76	0.00	21.02
Rectangle 3 (Indian subcontinent)	-0.62	-0.69	-0.53	-4.88	0.38	11.78
Rectangles 1-3	-0.76	-0.79	-0.74	-5.47	0.58	15.38
Rectangles 1-3 (Indian subcontinent)	-0.92	-0.93	-0.91	-4.87	0.84	7.72
700-2800 km:						
Geoid 0 m isoline	-0.53	-0.54	-0.51	-4.40	0.00	39.78
Rectangle 1	-0.92	-0.94	-0.91	-4.30	0.72	4.50
Rectangle 2	-0.73	-0.78	-0.67	-4.61	0.53	5.84
Rectangle 3	0.03	-0.06	0.11	-4.80	0.00	23.35
Rectangle 3 (Indian subcontinent)	-0.52	-0.60	-0.42	-4.01	0.21	13.32
Rectangles 1-3	-0.73	-0.76	-0.70	-4.73	0.52	16.44
Rectangles 1-3 (Indian subcontinent)	-0.89	-0.90	-0.88	-4.22	0.79	8.99

The reducing effect of slab overlap on the geoid height shed lights on the cause of the southwestward reinforcement of the IEGL minima, in accordance with the independent geologic and geophysical observations that ancient subduction zones (and the resultant slab locations) were restrained along the Tethys after the closure of the MOO [van der Meer et al., 2010; Van der Voo et al., 2015] (Figures 5.2-5.3). However, the damping influence of slab overlap on the geoid height can be cancelled by other factors, such as the variations in topography and lithospheric thickness from ocean to continent (e.g., Rectangle 3 in Figures 5.2 & 5.5), the mass addition from stagnant slabs at the 660 km discontinuity [Fukao et al., 2009] (e.g., Rectangle 4 in Figure 5.2) and upwellings in the upper mantle [French and Romanowicz, 2015] (e.g., Rectangle 5 in Figure 5.2).

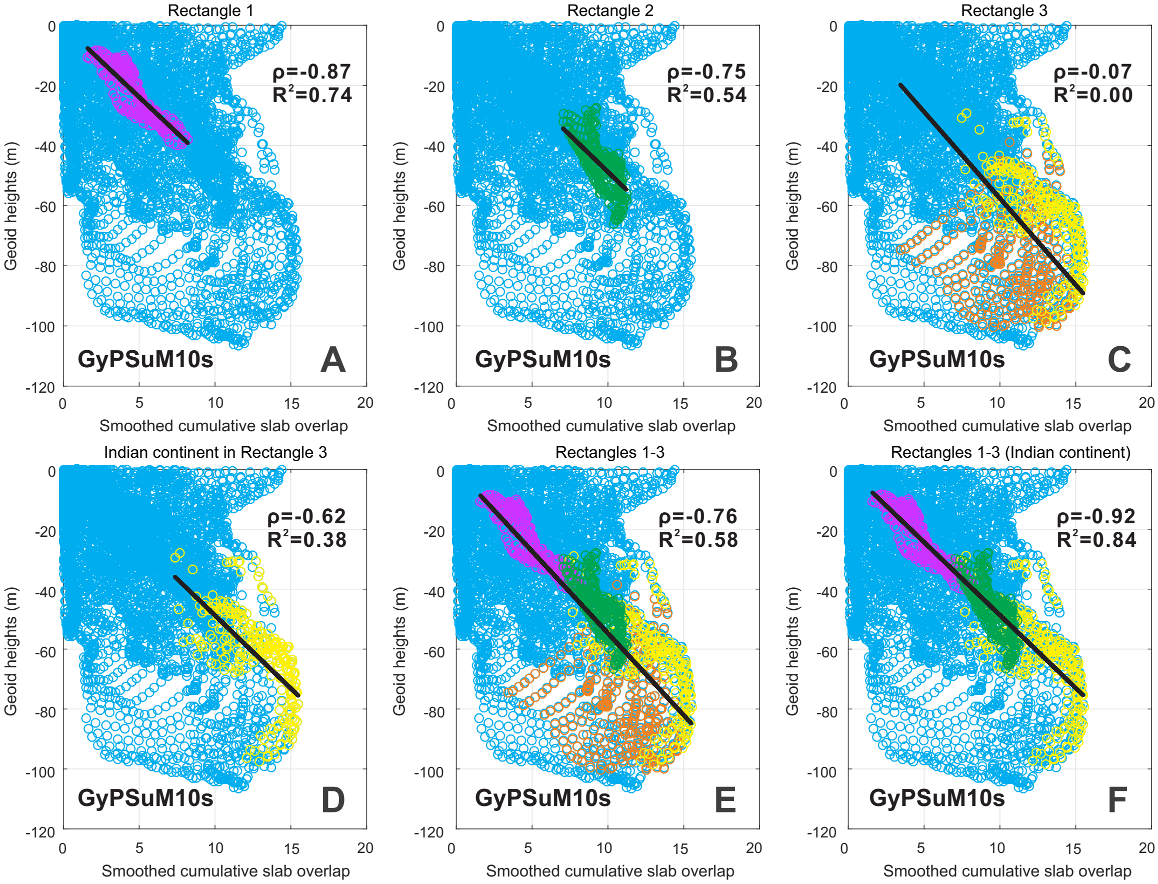

Figure 5.5: Scatter plots of the geoid height (H) and the 'smoothed' cumulative slab overlap (S) between 1200-2800 km for the selected polygonal regions inside the India-Eurasia geoid low (Figure 5.2). The regression line (black) are calculated from the datasets H and S enclosed in different regions, as represented by the markers of various colors: purple - rectangle 1; green - rectangle 2; orange - Indian Ocean in the rectangle 3; yellow - Indian subcontinent in the rectangle 3; blue - the polygonal region inside the 0 m isoline of IEGL. The associated coefficient of determination (R^2) measures the strength of the Pearson linear relationship (ρ, correlation coefficient) between H and S. Parameters regarding Pearson correlations and linear regressions are listed in Table 5.1. The calculations are performed using the shear-velocity model GyPSuM10s [Simmons et al., 2010].

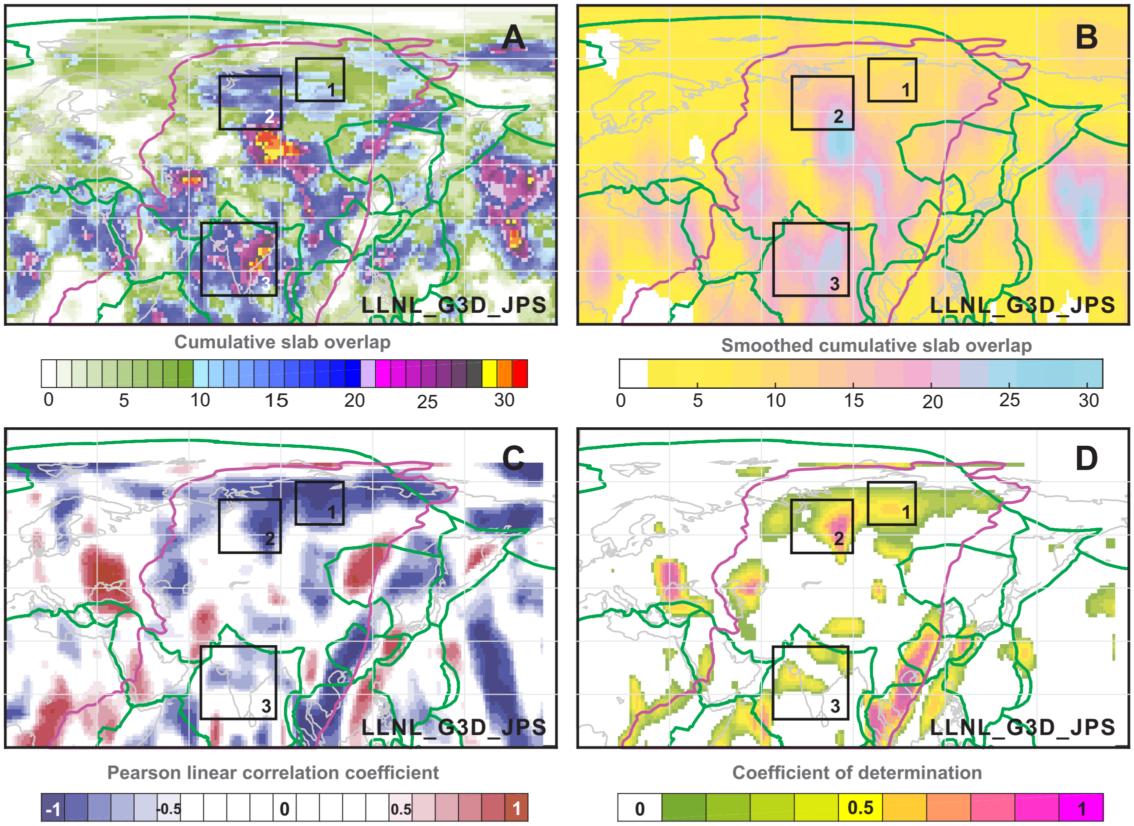

Figure 5.6: Slab distribution at the depth of 1200-2800 km, predicted by the shear-velocity model LLNL_G3D_JPS [Simmons et al., 2015], and the associated spatial correlation with surface geoid height. (A) Cumulative slab overlap at the depth of 1200-2800 km. (B) Smoothed cumulative slab overlap. (C-D) Spatial variations in the correlation coefficients between the geoid height and the 'smoothed' cumulative slab overlap, and the variations in the associated coefficients of determination from simple linear regression.

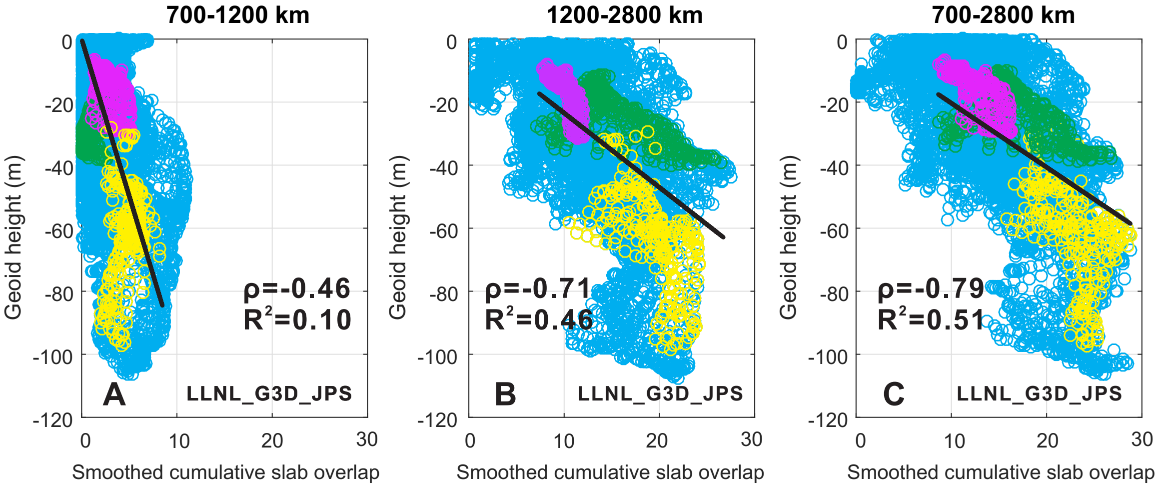

Figure 5.7: Scatter plots of the geoid height (H) and the 'smoothed' cumulative slab overlap (S) at different depth intervals for the selected rectangular regions inside the India-Eurasia geoid low (Figure 5.6). The computations are based on the shear-velocity model LLNL_G3D_JPS [Simmons et al., 2015]. See Figure 5.5 for the explanations of the markers of various colors.

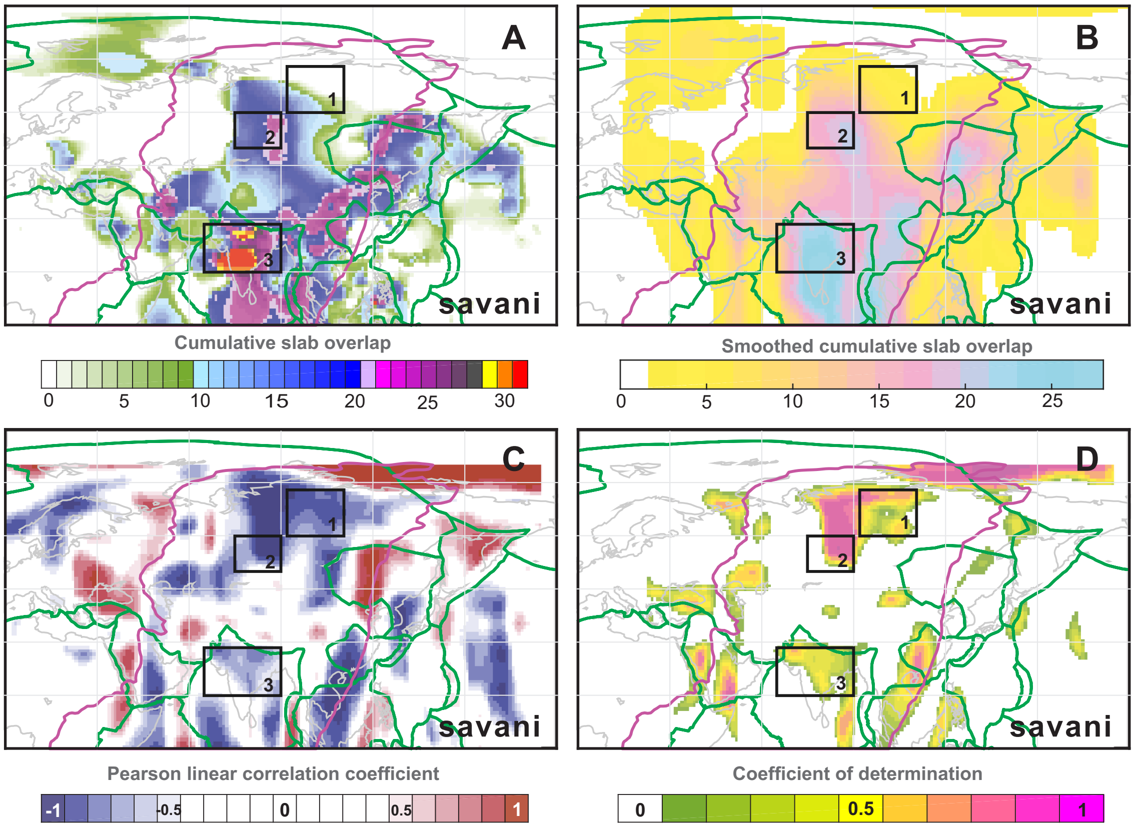

Figure 5.8: Slab distribution at the depth of 1200-2800 km, predicted by the shear-velocity model savani [Auer et al., 2014], and the associated spatial correlation with surface geoid height. (A) Cumulative slab overlap at the depth of 1200-2800 km. (B) Smoothed cumulative slab overlap. (C-D) Spatial variations in the correlation coefficients between the geoid height and the 'smoothed' cumulative slab overlap, and the variations in the associated coefficients of determination from simple linear regression.

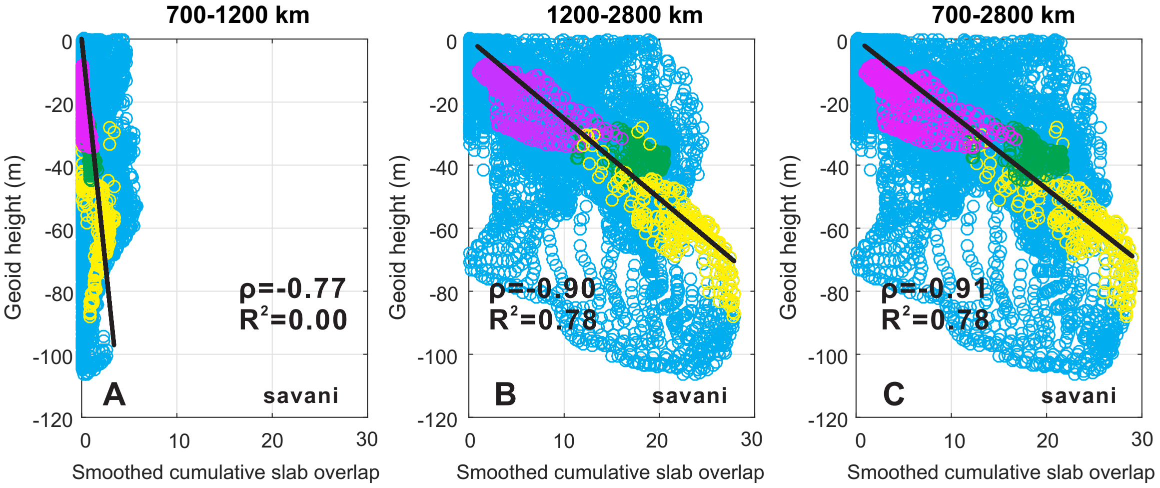

Figure 5.9: Scatter plots of the geoid height (H) and the 'smoothed' cumulative slab overlap (S) at different depth intervals for the selected rectangular regions inside the India-Eurasia geoid low (Figure 5.8). The computations are based on the shear-velocity model savani [Auer et al., 2014]. See Figure 5.5 for the explanations of the markers of various colors.

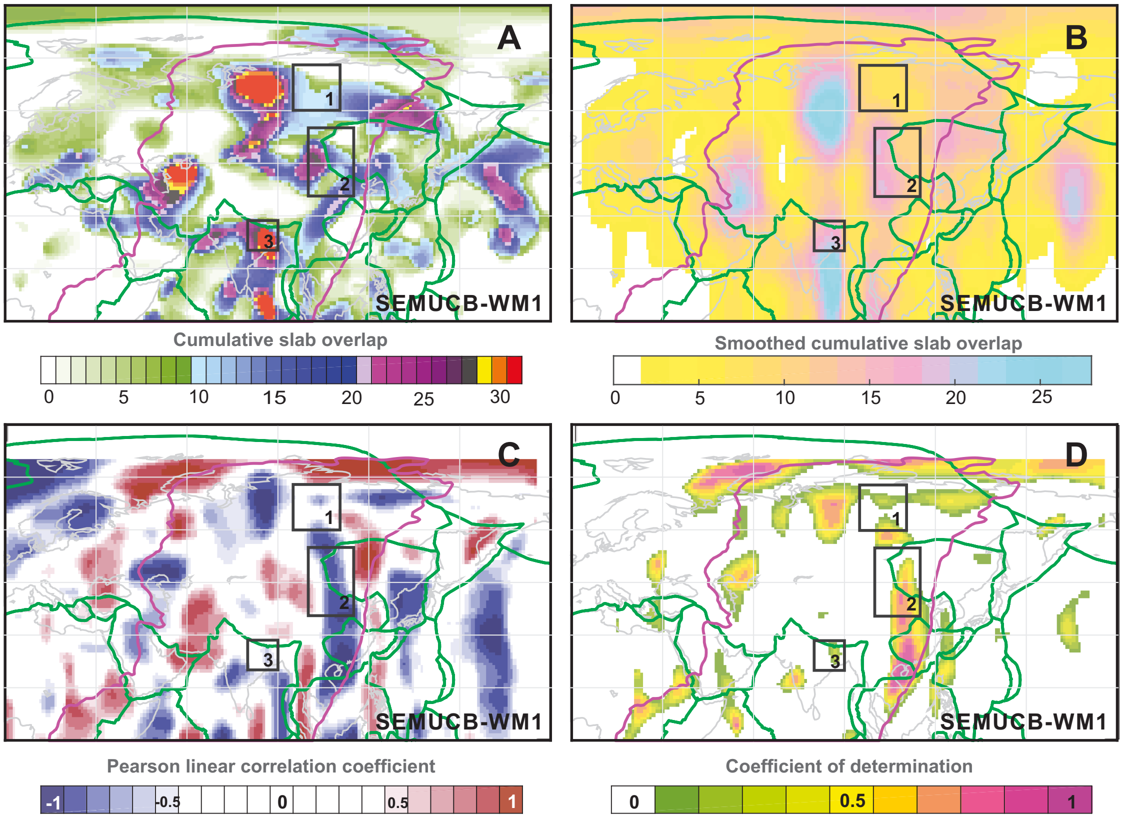

Figure 5.10: Slab distribution at the depth of 1200-2800 km, predicted by the shear-velocity model SEMUCB-WM1 [French and Romanowicz, 2014], and the associated spatial correlation with surface geoid height. (A) Cumulative slab overlap at the depth of 1200-2800 km. (B) Smoothed cumulative slab overlap. (C-D) Spatial variations in the correlation coefficients between the geoid height and the 'smoothed' cumulative slab overlap, and the variations in the associated coefficients of determination from simple linear regression.

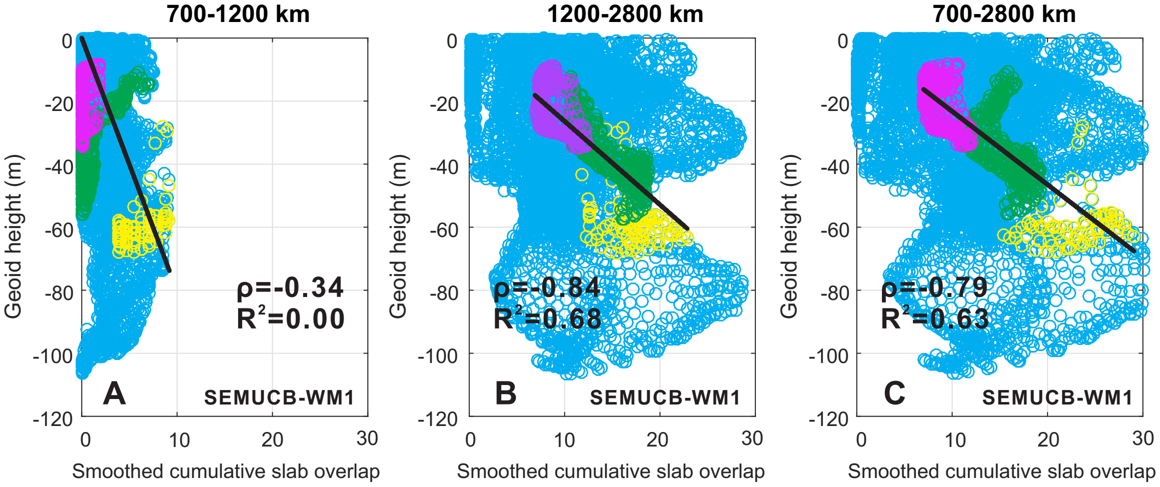

Figure 5.11: Scatter plots of the geoid height (H) and the 'smoothed' cumulative slab overlap (S) at different depth intervals for the selected rectangular regions inside the India-Eurasia geoid low (Figure 5.10). The computations are based on the shear-velocity model SEMUCB-WM1 [French and Romanowicz, 2014]. See Figure 5.5 for the explanations of the markers of various colors.

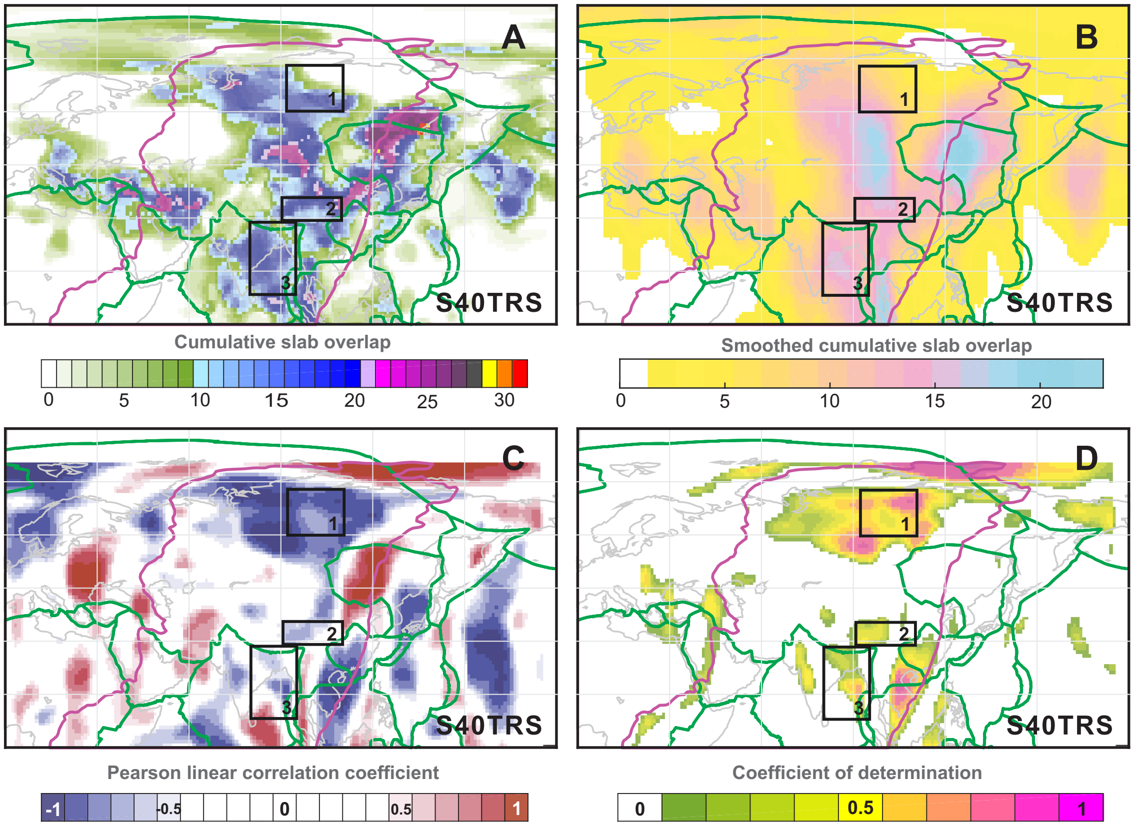

Figure 5.12: Slab distribution at the depth of 1200-2800 km, predicted by the shear-velocity model S40TRS [Ritsema et al., 2011], and the associated spatial correlation with surface geoid height. (A) Cumulative slab overlap at the depth of 1200-2800 km. (B) Smoothed cumulative slab overlap. (C-D) Spatial variations in the correlation coefficients between the geoid height and the 'smoothed' cumulative slab overlap, and the variations in the associated coefficients of determination from simple linear regression.

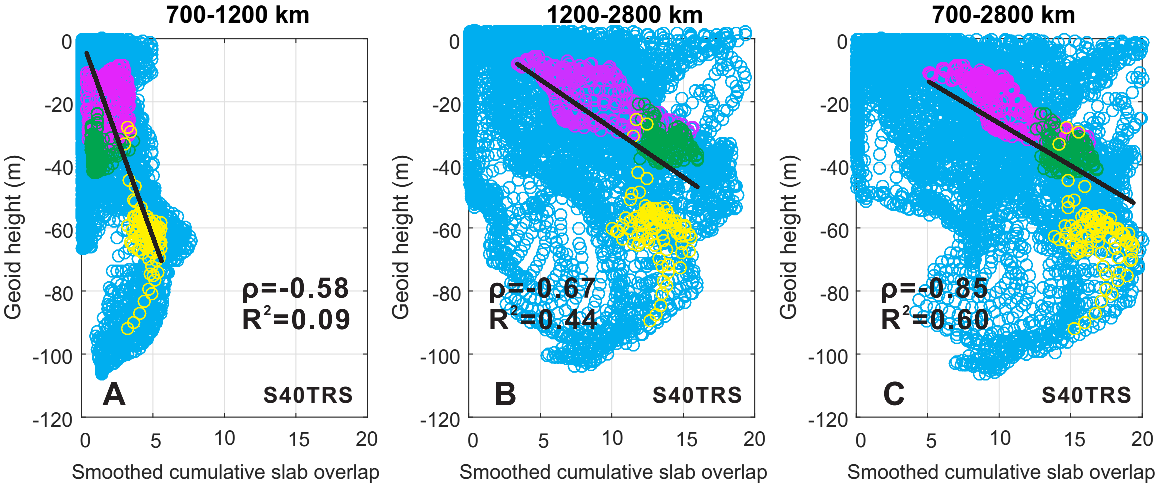

Figure 5.13: Scatter plots of the geoid height (H) and the 'smoothed' cumulative slab overlap (S) at different depth intervals for the selected rectangular regions inside the India-Eurasia geoid low (Figure 5.12). The computations are based on the shear-velocity model S40TRS [Ritsema et al., 2011]. See Figure 5.5 for the explanations of the markers of various colors.

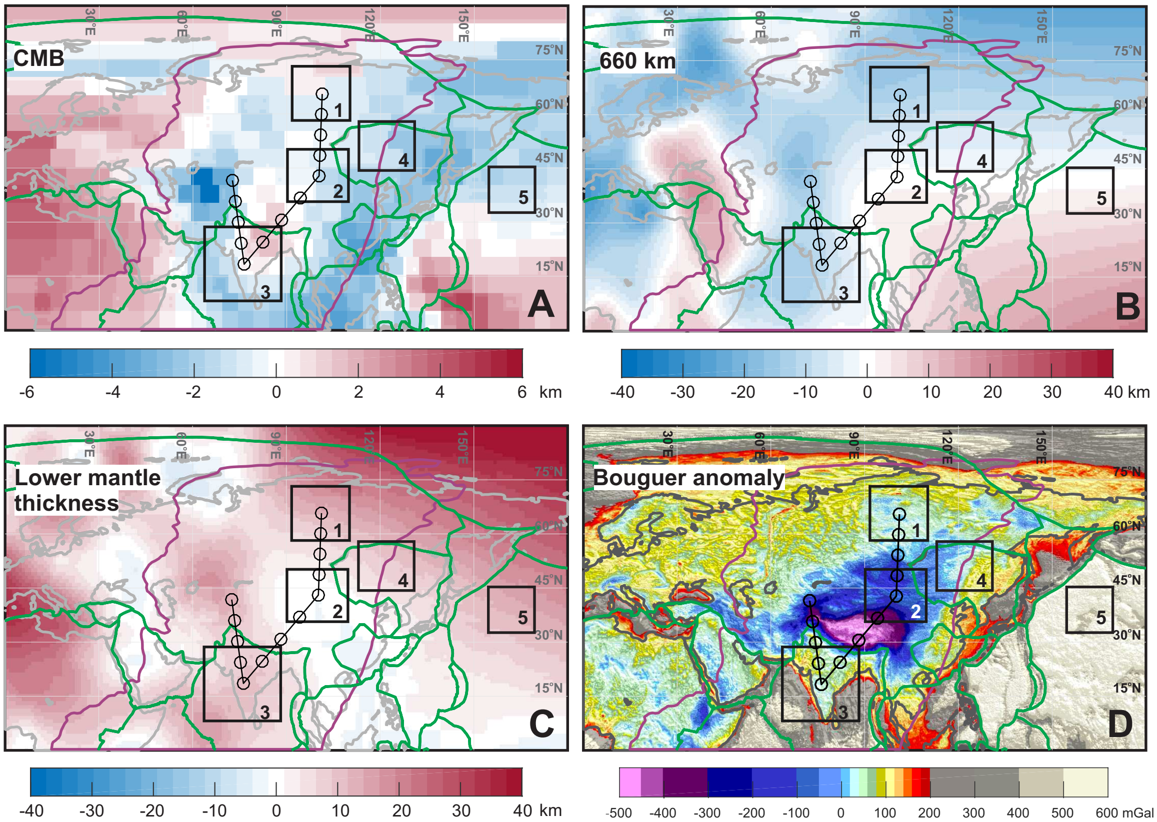

Figure 5.14: Deviations from the average density/viscosity interfaces in the mantle underneath Eurasia. (A) The topography data of the core-mantle boundary (CMB) are from Soldati et al. [2013]. (B) The topography data of the 660 km seismic discontinuities are from Houser et al. [2008]. The average depths for the 660 km discontinuities and the CMB are 655 km [Gu et al., 2012] and 2889 km [Morelli and Dziewonski, 1987], respectively. (C) Thickness of the lower mantle. (D) Bouguer anomaly in Eurasia [Balmino et al., 2012]. The numbered black rectangles 1-3 highlight the areas with increasingly heavy overlap of slabs between 700-2800 km. The black line and circles indicate the profile of interest starting at the center of the rectangle 1. The purple line shows the 0 m isoline encompassing the IEGL [Pavlis et al., 2012]. The green lines delineate the present-day plate boundaries [Bird, 2003].

5.4 Discussion

The results of this study are closely linked with the characteristics of the 660 km discontinuity, which has a negative Clapeyron slope (dP/dT) for the phase change from γ-spinel to perovskite and periclase. So higher temperatures tend to elevate the phase transformation depth (PTD) with lower pressures, while lower temperatures will depress the PTD with higher pressures. The relationship is reversed for the 410 km discontinuity with a positive Clapeyron slope, where olivine is converted to β-spinel. Seismic studies have shown that the depths of the 410 and 660 km discontinuities are anti-correlated in regions dominated by thermal anomalies associated with downgoing slabs (thicker transition zone, TZ) and upwelling plumes (thinner TZ) [Gu et al., 2012]. For two reasons, we focus our investigations on the 660 km rather than the 410 km discontinuity for the dynamic effect on the main density/viscosity boundaries of the upper mantle beneath the IEGL. Firstly, compared with the 410 km discontinuity whose deformation is mainly driven by chemical heterogeneities, the topography of 660 km discontinuity is dominated by temperature anomalies, which means a simpler conversion between seismic velocity anomalies and thermal anomalies because shear-velocity is more sensitive to temperature rather than density variations [Houser et al., 2008]. Secondly, the peak-to-peak amplitudes of the 410 km deformation within the IEGL are mostly smaller than 10 km, which are barely larger than the associated uncertainties averaging 6-8 km [Houser et al., 2008].

As illustrated in Figure 5.14, most parts of the core-mantle boundary (CMB) (based on splitting function inversion to tomography models) inside the 0 m isoline of the IEGL are elevated by 2-4 km except in Tibet and northern India [Soldati et al., 2013]. Below the IEGL, the 660 km discontinuity (based on waveform inversion of SS precursors) is also mostly uplifted with even larger magnitude ($\sim$10 km) except in South China [Houser et al., 2008], which leads to an overall thickened lower mantle below the IEGL. Bouguer anomaly and isostatic anomaly [Balmino et al., 2012] for Eurasia are shown to qualitatively illustrate the variations in the thickness of the continental crust (Figure 5.14D).

To better understand how the geoid is related to the major internal boundaries of the mantle, we select a profile stretching from Siberia through rectangles 1-3 (with increasing degree of slab overlap) to Pamirs (no slabs in the lower mantle according to the model GyPSuM10s) (Figure 5.15). The main observations are summarized as follows. Firstly, the depression of the CMB beneath Tibet-India seems to be caused by the dynamic effect of the downgoing slabs associated with the longstanding subduction of Tethys in the Mesozoic. We would expect a depression for the 660 km topography if it was dynamically maintained [Richards and Hager, 1984]. However, the elevated 660 km discontinuity with relatively higher temperature indicate that the dynamic effects do not dominate near the 660 km discontinuity in the region. Secondly, beneath Siberia, the slabs associated with the subduction of the MOO probably in the Late Paleozoic to Early Mesozoic [Van der Voo et al., 1999], are located close to the CMB. These slabs display no detectable dynamically downward pushing to the underlying CMB, indicating that they might have reached the maximum penetration depths.

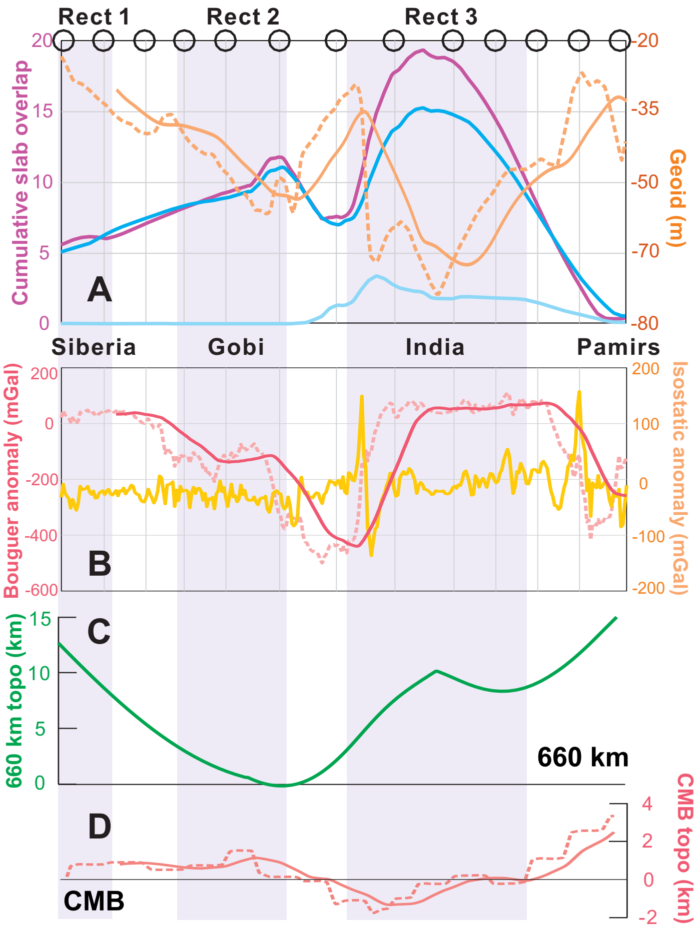

Figure 5.15: Variations in the cumulative slab overlap and the topography of the density/viscosity interfaces in the lower mantle, along the profile stretching from Siberia through Gobi, India to northern Pamirs (Figure 5.14). (A) Lateral variations in the cumulative slab overlap (purple line) and the smoothed geoid anomaly (orange solid line). Dark and light blue lines indicate the slabs at the depths of 1200-2800 km and 700-1200 km according to the shear-velocity model GyPSuM10s [Simmons et al., 2010]. (B) Smoothed Bouguer anomaly (red solid line) and isostatic anomaly (orange solid line) in Eurasia [Balmino et al., 2012]. (C) Topography of the 660 km [Houser et al., 2008]. (D) Smoothed topography of the CMB (pink solid line) [Soldati et al., 2013]. Original data before the low-pass filtration with an running window of 30 are shown in (B) and (D) as the dashed lines.

Based on the robustly strong anti-correlation between the cumulative slab overlap in the lower mantle and the surface geoid undulation (Figures 5.14-5.15), we propose that the negative density contrast between slabs and the ambient lower mantle could be the dominating factor for the mass deficit reflected from the downward geoid undulation in the IEGL. Firstly, there is no simple correlation between the geoid and the bottom of the underlying lithosphere or the thickness of the upper mantle. Secondly, the along-profile variations in the geoid height and the cumulative slab overlap are opposite at the same wavelength. Lastly and most importantly, a mass excess is expected from the volume excess for the lower mantle inside the IEGL. However, the observed geoid trough in India occurs in the region with the heaviest slab overlap, i.e., the biggest slab volume, while the downward geoid undulation get smaller to the region with less volume of slabs such as in Siberia. Similar trend in the slab distribution is seen from other shear-velocity models except S40TRS [Ritsema et al., 2011] (Figures 5.6-5.13). A recent study suggests that light and buoyant mantle upwelling above sinking slabs can cause geoid lows, according to the modelling of global dynamic convection based on the assumption that slabs are denser than the ambient lower mantle [Spasojevic et al., 2010]. However, no broad mantle upwellings especially in middle-east Eurasia have been reported from seismological studies.

All the observations lead us to believe that the mass deficit reflected from the IEGL is more likely to be caused by the positive buoyancy of the sinking slabs rather than the mass anomalies associated with flow-induced boundary deformation in the lower mantle, especially when the dynamic effects on the 660 km discontinuity are less important. This is supported by a recent finding of the density contrast inversion between slabs and the ambient mantle at the bottom of the transition zone where the perovskite forming reaction occurs [Ganguly et al., 2009]. The mass deficit in the area of IEGL, together with the negative correlation between the geoid height and the cumulative slab overlap underneath Eurasia, indicates that this inverted (negative) density contrast continues into the lower mantle. This scenario, if substantiated, would suggest that high-velocity structures in the lower mantle associated with sinking slabs are mainly thermally induced. The sinking of slabs underneath Eurasia is probably maintained by their downgoing momentum, and slabs in the lowermost mantle could therefore have a tendency to rise owing to their positive buoyancy caused by the negative density contrast.

5.5 Conclusions

In this chapter, we find a strong linear correlation of -0.92 between the surface geoid height inside the IEGL and the underlying slab volume at the depth of 1200-2800 km. From the seismically constrained topographies of 660 km and the CMB, a volume excess (mass excess) is indicated for the lower mantle beneath the IEGL. We propose that the localized mass deficit, as reflected from the downward geoid undulations inside the IEGL, could be attributed mainly to the positive buoyancy of the sinking slabs in the lower mantle.

6 Conclusions and future work

6.1 Summary of the main thesis contributions

Throughout my Ph.D. study, I have been devoting my research to exploring some of the under-utilized aspects of paleomagnetic data associated with plate reconstructions. The main target of this thesis is to provide a solution to the longstanding challenge of constraining paleolongitudes from paleomagnetism (see Chapter 1).

We are not the first to use apparent polar wander path (APWP) for absolute plate motion (APM) reconstructions. Smirnov and Tarduno [2010] reconstructed the eruption location of the Siberian Traps at 250 Ma with a similar method. However, reconstructions from their methods are artificially restrained along circle arcs centering on paleomagnetic Euler poles, leading to the resultant paleo-colatitudes incompatible with those determined from paleomagnetism. Moreover, the complex mathematical procedures prevent a wide adoption in the paleomagnetic community. Meanwhile, our attention was drawn by an intriguing method of using mantle structures as reference to constrain paleolongitudes for the eruption sites of deep-sourced large igneous provinces (LIPs) [e.g., Burke and Torsvik, 2004; Torsvik et al., 2008b]. We were interested to implement the methods of Smirnov and Tarduno [2010] to see if comparable eruption sites of these LIPs can be obtained. We were also motivated to extend plate reconstructions beyond the 'memory of the mantle' [van der Meer et al., 2010], because the convecting mantle has been recycled periodically throughout the geologic history. In order to resolve these issues, I started my thesis projects in the summer of 2013 and obtained the following major contributions.

1. A new geometric parametrization algorithm is introduced in Chapter 2 to utilize APWPs to constrain paleo-longitudes for the paleomagnetic-based reconstructions. We propose to parameterize APWP tracks with circle modelling for the derivation of

stage rotation poles and angles. Finite reconstruction parameters can be computed by combining stage rotations and associated paleo-colatitude corrections. Errors in the derived rotation parameters and associated reconstructions are estimated from a bootstrap implementation of the above procedures. Using our proposed apparent polar wander path geometric parameterizations (APWPGP) technique, we reconstruct the drift history of East Gondwana since 130 Ma. Our reconstructions indicate that the paleopositional affinity between India and Australia-East Antarctica broke down at 130-120 Ma, and that Australia and East Antarctica were separated at 60-40 Ma. We compare our reconstructions against those from other APM models, which shows large discrepancies for the reasons discussed in Chapter 1.

2. To provide an easy implementation of our new APM method, Chapter 3 presents a MATLAB-based toolbox PMTec. The main function modules of PMTec include 1) APWP constructions in the form of running average windows and spherical splines and 2) APM calculations from paleomagnetic data. The graphical users interface of PMTec is built on MATLAB considering its powerful mapping toolbox for geospatial data visualization and its popularity in the geoscience community. The computational and graphical performance of PMTec is demonstrated using the published data to provide an overview about its operation procedures. The PMTec package, tutorials and regular updates can be found on the websites: https://sites.google.com/a/ualberta.ca/lei-wu/ and http://www.ualberta.ca/∼vadim/software.htm. PMTec is a freeware for plate tectonic studies and allowed to be redistributed among users.

3. Understanding present-day mantle convection requires an accurate reconstruction of past plate motions, especially those associated with convergent tectonics. However, existing absolute plate motion reconstructions generally require paleo-positional constraints (especially for paleolongitudes) from poorly understood mantle structures. This results in circular reasoning since their interpretations as subducted oceanic lithospheres (or slabs) were based on plate reconstructions in the first place. Chapter 4 presents a new paradigm to quantitatively link surface plate tectonics with mantle downwelling convection, as demonstrated in a case study where the closing of the Mongol-Okhotsk Ocean in the Mesozoic is restored. Our reconstructions quantitatively explain the observed slab morphology underneath Eurasia from seismic imaging.

4. Chapter 5 discloses a very strong anti-correlation of -0.92, with the associated coefficient of determination of 0.84, between the surface geoid anomaly and the slab volume

at the depth of 1200-2800 km underneath Eurasia. Combined with the seismically constrained topographies of the major mantle density/viscoity boundaries, we propose that sinking slabs are less dense than the ambient lower mantle. Future dynamic models of mantle circulation need to account for such thermal effects.

Other than the above main contributions from the thesis, I carried out two additional projects during my Ph.D. program, leading to the following manuscripts that will be and have been submitted for peer review. In the thesis, I only include their abstracts without showing the main texts to avoid distractions.

- **Wu, L.**, Zhang, R., Kravchinsky, V.A., Potter, D.K. Eastward propagation of the deformation in the Tianshan Mountains since 45 Ma. To be submitted.

  Abstract: We performed a paleomagnetic study to the Burqin ([48.0°N, 86.7°E], 44-25 Ma) and Tieersihabahe ([46.7°N, 88.5°E], 25-17 Ma) sections from the northern Junggar basin in northwestern China. The two Cenozoic sections are mainly comprised of mudstones, siltstones and sandstones, and have well-constrained ages from biostratigraphic and magnetostratigraphic evidence. Stepwise thermal demagnetization was applied to a total of 537 samples from the Burqin (178) and Tieersihabahe (359) sections, revealing high-temperature remanence directions with dual polarities from both sections. These remanence directions were suggested to be of the primary origin from the positive results of reversals test. The mean directions after correcting inclination errors from the Burqin and Tieersihabahe sections are $D = -0.6 \pm 6.5°$, $I = 60.7 \pm 8.5°$ (k=16.8, n=59, $A_{95} = 5.4°$, $A_{95min} = 3.3°$, $A_{95max} = 6.3°$) and $D = 5.2 \pm 4.1°$, $I = 61.2 \pm 7.5°$ (k=16.7, n=154, $A_{95} = 3.4°$, $A_{95min} = 2.3°$, $A_{95max} = 3.4°$), leading to two new paleopoles [$227.0°E$, $84.2°N$, $5.4°(dm)$, $4.1°(dp)$, $12.5(K)$] and [$270.8°E, 83.7°N, 8.2°(dm), 6.3°(dp), 12.7(K)$], respectively. The time-varying paleomagnetic-based rotation fields in northwestern China during the last 45 Myr were constructed in 10 Myr's step from published declinations and those from this study. The interpreted temporal variations of localized shear strain suggested eastward propagation of shear deformation in the Tianshan Mountains since 45 Ma.

- **Wu, L.**, Kravchinsky, V.A., Potter, D.K. Apparent polar wander paths of the major China Blocks since the Late Paleozoic: toward reconciling the paleogeography of East Eurasia. Earth-Science Reviews (in revision).

  Abstract: High-quality paleomagnetic poles (i.e. paleo-poles) are essential for quantitative plate reconstructions. However, the current paleomagnetic database of the major China Blocks (i.e. North China Block, South China Block and Tarim Block) since the Late Paleozoic is full of outdated and low-quality data. Here we update this database by recruiting recently published high-fidelity paleo-poles and rejecting low-quality outdated ones. The database includes 288 paleo-poles published between 1980-2014, with 90 new paleo-poles published after 2000. Following the Van der Voo's paleo-poles grading scheme, 75 paleo-poles with quality factor smaller than 4 are rejected. Another 59 paleo-poles are removed during the further quality evaluation, leaving 154 paleo-poles from which we compute the new China apparent polar wander paths (APWPs). The calculations are presented in the form of running means and spherical splines, whose discrepancies are mostly within 5°. During the further quality evaluation, we find inconclusive evidence for the influence of inclination shallowing errors on the clastic paleo-poles in most intervals, which leads us to present the new China APWPs with and without the correction for inclination shallowing errors.

Here we propose that the 'apparent low-paleolatitude anomalies' for the China Blocks with respect to stable Europe could be exaggerated owing to the underestimation of errors of the European reference curves. For plate reconstructions, spline curves with shallowing correction are therefore recommended considering the poor data coverage and such low-paleolatitude anomalies during certain periods.

Together with the global hybrid reconstruction model and up-to-date geological observations, the new China APWPs allow us to re-evaluate the coalescence history of East Eurasia since the Late Paleozoic. Four major tectonic events are confirmed as the results of such a synthetic reconciliation: 1) Tarim had been accreted with the Kazakhstan orocline during the amalgamation of the West Altaids between 265-250 Ma (Middle-Late Permian); 2) the suturation between the North and South China Blocks underwent in a scissor-like pattern probably starting from the Middle Permian and was accomplished no later than 180-160 Ma (Middle Jurassic); 3) the fusion between North China, Tarim and the blocks in between might have been achieved around 160-140 Ma (Late Jurassic to Early Cretaceous); 4) the Mongol-Okhotsk Ocean should have been closed no later than 140-120 Ma (Early Cretaceous).

6.2 Directions for future work

The traditional paleomagnetic reconstructions are semi-quantitatively derived from individual paleo-poles by discretely rotating these poles back to the spin axis (Figure 1.4).

Paleolongitudes are commonly adjusted to match geologic and geophysical observations. Too many unaccounted uncertainties and artifacts exist in such paleomagnetic reconstructions because researchers have the freedom to place the studied plates 'anywhere' along the paleo-parallels (determined from paleo-colatitudes) as long as the reconstructions are 'compatible' with independent constraints. I urge future paleomagnetic reconstructions to be presented in a way such that the continuous apparent polar wandering is actually reflected in plate motions, because the changing coordinates of paleo-poles must indicate that the studied plates had moved if there were not events of true polar wandering. This new paleomagnetic-based reconstruction method should largely advance our understanding of past plate motions, especially those related to convergent tectonics such as the collision between India and Eurasia in the Cenozoic, because locations of sinking slabs in the mantle can be used to evaluate the robustness of the resultant reconstructions. Here I list a few research topics and challenges for future work.

1. To reconstruct the global continental motions in the Mesozoic using our new APWPGP method. The work is crucial because in this geologic interval we have the most complete geologic and geophysical observations (e.g., hotspot tracks, seafloor isochrons and seismic tomography), with which quantitative comparisons and correlations are feasible. Such reconstructions should advance our understanding of the kinematics of the breakup of the supercontinent Pangea and the long-wavelength mantle structures, especially those high-velocity anomalies revealed from seismic imaging. Such results could also be of potential interests for economic geologists who seek to understand large-scale ore-forming processes in an evolving plate configuration [e.g., Zhou et al., 2002]. This proposed work is facilitated by the high-quality APWPs published in the last decade [e.g., Torsvik et al., 2012] and has good chances of success as demonstrated from the self-consistency in the restored APMs and the compatibility with independent observations (see Chapter 2 & 4).

2. To keep updating PMTec on a regular basis for the next few years. Compared with other reconstruction software such as GPlates [Boyden et al., 2011], the current PMTec has disadvantages in interactivity with users and visualization performance. The source code for the three-dimensional projection of spherical data has been completed and will be added in future annual updates. New scripts need to be written to allow interactive plate reconstructions, such as adjusting paleolongitudes and azimuthal orientations of the reconstructed plates. To this end, future effort should focus on better utilizing

rotation trees to connect different plates (Figure 1.7), whereas the current script implementation of reconstruction visualizations in the module ‘PMTec_AniMaker’ is made on a discrete basis.

3. To further explore the relationship between surface plate motions, slab distribution and geoid undulations. For instance, future work should be carried out in other areas such as North America to test if the main conclusion in Chapter 4 that sinking slabs in the lower mantle are buoyant stands globally. There is a spatial deviation between the greatest slab overlap and the geoid minima in the northern Indian Ocean (Figures 5.2-5.3), which indicates that the sinking slabs and boundary undulations in the lower mantle are not the only factors contributing to the local mass deficit. Further research needs to be conducted to explain this observation. Firstly, the geoid responses from the slab-induced mass anomalies and the deformed mantle boundaries need to be quantified. This can be done by evaluating their respective effects on geoid kernels by following the method of Panasyuk et al. [1996]. Secondly, no broad buoyant upwellings in the upper mantle has been reported from geodynamic studies. Are there small-scale mantle upwellings underneath the Indian Ocean? How do they contribute to the local mass anomalies if there are any? Thirdly, a reasonable mechanism of the associated dynamics and mineralogical changes need to be proposed to account for the cold but less dense sinking slabs in the lower mantle.

7

Bibliography

Bibliography

Anderson, D. L. (1982). Hotspots, polar wander, Mesozoic convection and the geoid. *Nature*, 297(5865):391–393.

Anderson, D. L. (2007). *New theory of the Earth.* Cambridge University Press.

Anderson, D. L. and King, S. D. (2014). Driving the Earth machine? *Science*, 346(6214):1184–1185.

Auer, L., Boschi, L., Becker, T., Nissen-Meyer, T., and Giardini, D. (2014). Savani: A variable resolution whole-mantle model of anisotropic shear velocity variations based on multiple data sets. *Journal of Geophysical Research: Solid Earth*, 119(4):3006–3034.

Ball, P., Eagles, G., Ebinger, C., McClay, K., and Totterdell, J. (2013). The spatial and temporal evolution of strain during the separation of Australia and Antarctica. *Geochemistry, Geophysics, Geosystems*, 14(8):2771–2799.

Balmino, G., Vales, N., Bonvalot, S., and Briais, A. (2012). Spherical harmonic modelling to ultra-high degree of Bouguer and isostatic anomalies. *Journal of Geodesy*, 86(7):499–520.

Becker, T. W. and Boschi, L. (2002). A comparison of tomographic and geodynamic mantle models. *Geochemistry, Geophysics, Geosystems*, 3(1):10.129/2001GC000168.

Besse, J. and Courtillot, V. (2002). Apparent and true polar wander and the geometry of the geomagnetic field over the last 200 Myr. *Journal of Geophysical Research: Solid Earth*, 107(B11):EPM 6–1–EPM 6–31.

Bird, P. (2003). An updated digital model of plate boundaries. *Geochemistry, Geophysics, Geosystems*, 4(3).

Boyden, J. A., Müller, R. D., Gurnis, M., Torsvik, T. H., Clark, J. A., Turner, M., Ivey-Law, H., Watson, R. J., and Cannon, J. S. (2011). Next-generation plate-tectonic reconstructions using GPlates. *Geoinformatics: cyberinfrastructure for the solid earth sciences*, pages 95–114.

Bullard, E., Everett, J. E., and Smith, A. G. (1965). The fit of the continents around the Atlantic. *Philosophical Transactions of the Royal Society of London. Series A, Mathematical and Physical Sciences*, 258(1088):41–51.

Burke, K. and Torsvik, T. H. (2004). Derivation of large igneous provinces of the past 200 million years from long-term heterogeneities in the deep mantle. *Earth and Planetary Science Letters*, 227(3):531–538.

Butterworth, N., Talsma, A., Müller, R., Seton, M., Bunge, H.-P., Schuberth, B., Shephard, G., and Heine, C. (2014). Geological, tomographic, kinematic and geodynamic constraints on the dynamics of sinking slabs. *Journal of Geodynamics*, 73:1–13.

Cande, S. C. and Stegman, D. R. (2011). Indian and African plate motions driven by the push force of the Réunion plume head. *Nature*, 475(7354):47–52.

Chang, T. (1987). On the statistical properties of estimated rotations. *Journal of Geophysical Research*, 92:6319–6329.

Chang, T. (1988). Estimating the relative rotation of two tectonic plates from boundary crossings. *Journal of the American Statistical Association*, 83(404):1178–1183.

Chang, T., Stock, J., and Molnar, P. (1990). The rotation group in plate tectonics and the representation of uncertainties of plate reconstructions. *Geophysical journal international*, 101(3):649–661.

Chase, C. G. (1979). Subduction, the geoid, and lower mantle convection. *Nature*, 282:29.

Chase, C. G. and Sprowl, D. R. (1983). The modern geoid and ancient plate boundaries. *Earth and Planetary Science Letters*, 62(3):314–320.

Cocks, L. R. M. and Torsvik, T. H. (2007). Siberia, the wandering northern terrane, and its changing geography through the Palaeozoic. *Earth-Science Reviews*, 82(1–2):29–74.

Cogné, J. (2003). PaleoMac: a Macintosh? application for treating paleomagnetic data and making plate reconstructions. *Geochemistry, Geophysics, Geosystems*, 4(1).

Cogné, J.-P., Besse, J., Chen, Y., and Hankard, F. (2013). A new Late Cretaceous to Present APWP for Asia and its implications for paleomagnetic shallow inclinations in Central Asia and Cenozoic Eurasian plate deformation. *Geophysical Journal International*, 192(3):1000–1024.

Cox, A. and Hart, R. B. (1986). Plate Tectonics: How It Works.

Davies, C. J., Stegman, D. R., and Dumberry, M. (2014). The strength of gravitational core-mantle coupling. *Geophysical Research Letters*, 41(11):3786–3792.

DeMets, C., Gordon, R. G., Argus, D., and Stein, S. (1990). Current plate motions. *Geophysical journal international*, 101(2):425–478.

Doubrovine, P. V., Steinberger, B., and Torsvik, T. H. (2012). Absolute plate motions in a reference frame defined by moving hot spots in the Pacific, Atlantic, and Indian oceans. *Journal of Geophysical Research: Solid Earth*, 117(B9).

Dziewonski, A. M. and Anderson, D. L. (1981). Preliminary reference Earth model. *Physics of the earth and planetary interiors*, 25(4):297–356.

Embleton, B. J., McElhinny, M. W., Ma, X., Zhang, Z., and Li, Z. X. (1996). Permo-Triassic magnetostratigraphy in China: the type section near Taiyuan, Shanxi province, North China. *Geophysical Journal International*, 126(2):382–388.

Evans, M. (1976). Test of the dipolar nature of the geomagnetic field throughout Phanerozoic time.

Finlay, C. C., Olsen, N., and Tøffner-Clausen, L. (2015). DTU candidate field models for IGRF-12 and the CHAOS-5 geomagnetic field model. *Earth, Planets and Space*, 67(1):1–17.

Fisher, N. I., Lewis, T., and Embleton, B. J. (1987). *Statistical analysis of spherical data*. Cambridge University Press.

Fisher, N. I., Lewis, T., and Willcox, M. (1981). Tests of discordancy for samples from Fisher's distribution on the sphere. *Applied Statistiss*, pages 230–237.

Fisher, R. (1958). Statistical Methods for Research Workers 13th edn (Edinburgh: Oliver and Boyd).

Francheteau, J. and Sclater, J. (1969). Paleomagnetism of the southern continents and plate tectonics. *Earth and Planetary Science Letters*, 6(2):93–106.

French, S. and Romanowicz, B. (2014). Whole-mantle radially anisotropic shear velocity structure from spectral-element waveform tomography. *Geophysical Journal International*, 199(3):1303–1327.

French, S. W. and Romanowicz, B. (2015). Broad plumes rooted at the base of the Earth's mantle beneath major hotspots. *Nature*, 525(7567):95–99.

Fukao, Y., Obayashi, M., and Nakakuki, T. (2009). Stagnant slab: a review. *Annual Review of Earth and Planetary Sciences*, 37:19–46.

Gaina, C., Müller, R. D., Brown, B., Ishihara, T., and Ivanov, S. (2007). Breakup and early seafloor spreading between India and Antarctica. *Geophysical Journal International*, 170(1):151–169.

Ganguly, J., Freed, A. M., and Saxena, S. K. (2009). Density profiles of oceanic slabs and surrounding mantle: Integrated thermodynamic and thermal modeling, and implications for the fate of slabs at the 660km discontinuity. *Physics of the Earth and Planetary Interiors*, 172(3):257–267.

Garnero, E. J. and McNamara, A. K. (2008). Structure and dynamics of Earth's lower mantle. *Science*, 320(5876):626–628.

Gordon, R. G., Cox, A., and O'Hare, S. (1984). Paleomagnetic Euler poles and the apparent polar wander and absolute motion of North America since the Carboniferous. *Tectonics*, 3(5):499–537.

Gradstein, F. M., Ogg, J. G., and Schmitz, M. (2012). *The Geologic Time Scale 2012, 2-volume set.* Elsevier.

Gray, N. H., Geiser, P. A., and Geiser, J. R. (1980). On the least-squares fit of small and great circles to spherically projected orientation data. *Journal of the International Association for Mathematical Geology*, 12(3):173–184.

Greff-Lefftz, M. and Besse, J. (2014). Sensitivity experiments on True Polar Wander. *Geochemistry, Geophysics, Geosystems*, 15(12):4599–4616.

Gu, Y. J., Okeler, A., and Schultz, R. (2012). Tracking slabs beneath northwestern Pacific subduction zones. *Earth and Planetary Science Letters*, 331:269–280.

Gubbins, D. and Herrero-Bervera, E. (2007). *Encyclopedia of geomagnetism and paleomagnetism.* Springer Science & Business Media.

Hager, B. and Richards, M. (1989). Long-wavelength variations in Earth's geoid: physical models and dynamical implications. *Philosophical Transactions of the Royal Society of London A: Mathematical, Physical and Engineering Sciences*, 328(1599):309–327.

Hager, B. H. (1984). Subducted slabs and the geoid: Constraints on mantle rheology and flow. *Journal of Geophysical Research: Solid Earth*, 89(B7):6003–6015.

Hager, B. H., Clayton, R. W., Richards, M. A., Comer, R. P., and Dziewonski, A. M. (1985). Lower mantle heterogeneity, dynamic topography and the geoid. *Nature*, 313(6003):541–545.

Hager, B. H. and O'Connell, R. J. (1981). A simple global model of plate dynamics and mantle convection. *Journal of Geophysical Research: Solid Earth*, 86(B6):4843–4867.

Hastings, D. A., Dunbar, P. K., Elphingstone, G. M., Bootz, M., Murakami, H., Maruyama, H., Masaharu, H., Holland, P., Payne, J., Bryant, N. A., Logan, T. L., Muller, J.-P., Schreier, G., and MacDonald, J. S. (1999). The Global Land One-kilometer Base Elevation (GLOBE) Digital Elevation Model (Version 1.0). *National Oceanic and Atmospheric Administration, National Geophysical Data Center, URL: http://www.ngdc.noaa.gov/mgg/topo/globe.html.*

Hellinger, S. (1981). The uncertainties of finite rotations in plate tectonics. *Journal of Geophysical Research: Solid Earth (1978–2012)*, 86(B10):9312–9318.

Houser, C., Masters, G., Flanagan, M., and Shearer, P. (2008). Determination and analysis of long-wavelength transition zone structure using SS precursors. *Geophysical Journal International*, 174(1):178–194.

Huang, B., Shi, R., Wang, Y., and Zhu, R. (2005). Palaeomagnetic investigation on EarlyÍCMiddle Triassic sediments of the North China block: a new Early Triassic palaeopole and its tectonic implications. *Geophysical Journal International*, 160(1):101–113.

Irving, E. (1956). Palaeomagnetic and palaeoclimatological aspects of polar wandering. *Pure and Applied Geophysics*, 33(1):23–41.

Irving, E. (1964). Paleomagnetism and its application to geological and geophysical problems. *Wiley.*

Ishii, M. and Tromp, J. (1999). Normal-mode and free-air gravity constraints on lateral variations in velocity and density of Earth's mantle. *Science*, 285(5431):1231–1236.

Jokat, W., Nogi, Y., and Leinweber, V. (2010). New aeromagnetic data from the western Enderby Basin and consequences for Antarctic-India break-up. *Geophysical Research Letters*, 37(21).

Jupp, P. E. and Kent, J. T. (1987). Fitting Smooth Paths to Speherical Data. *Journal of the Royal Statistical Society. Series C (Applied Statistics)*, 36(1):34–46.

Khramov, A. N. (1987). *Paleomagnetology.* Springer–Verlag, Berlin.

Kravchinsky, V. A., Sorokin, A. A., and Courtillot, V. (2002). Paleomagnetism of Paleozoic and Mesozoic sediments from the southern margin of Mongol-Okhotsk ocean, far eastern Russia. *Journal of Geophysical Research: Solid Earth*, 107(B10).

Lay, T., Hernlund, J., and Buffett, B. A. (2008). Core–mantle boundary heat flow. *Nature Geoscience*, 1(1):25–32.

Li, C., van der Hilst, R. D., Engdahl, E. R., and Burdick, S. (2008). A new global model for P wave speed variations in Earth's mantle. *Geochemistry, Geophysics, Geosystems*, 9(5).

Lithgow-Bertelloni, C. and Silver, P. G. (1998). Dynamic topography, plate driving forces and the African superswell. *Nature*, 395(6699):269–272.

Ma, X., Xing, L., Yang, Z., Xu, S., and Zhang, J. (1993). Palaeomagnetic study since Late Paleozoic in the Ordos Basin. *Chinese Journal of Geophysics*, 36(1):68–79.

Matias, L. M., Olivet, J.-L., Aslanian, D., and Fidalgo, L. (2005). PLACA: a white box for plate reconstruction and best-fit pole determination. *Computers & geosciences*, 31(4):437–452.

Maus, S., Barckhausen, U., Berkenbosch, H., Bournas, N., Brozena, J., Childers, V., Dostaler, F., Fairhead, J., Finn, C., Von Frese, R., et al. (2009). EMAG2: A 2–arc min resolution Earth Magnetic Anomaly Grid compiled from satellite, airborne, and marine magnetic measurements. *Geochemistry, Geophysics, Geosystems*, 10(8).

McElhinny, M., Embleton, B., Ma, X., and Zhang, Z. (1981). Fragmentation of Asia in the Permian. *Nature*, 293:212–216.

McFadden, P. L. and McElhinny, M. W. (1995). Combining groups of paleomagnetic directions or poles. *Geophysical Research Letters*, 22(16):2191–2194.

Meng, Z., Coe, R., and Frost, G. (1989). Paleomagnetic Results From Late Permian Redbeds in Gansu Province, China. *Eos Trans. AGU*, 70:1070.

Metcalfe, I. (2013). Gondwana dispersion and Asian accretion: Tectonic and palaeogeographic evolution of eastern Tethys. *Journal of Asian Earth Sciences*, 66(0):1–33.

Mitchell, R. N., Kilian, T. M., and Evans, D. A. (2012). Supercontinent cycles and the calculation of absolute palaeolongitude in deep time. *Nature*, 482(7384):208–211.

Molnar, P., Boos, W. R., and Battisti, D. S. (2010). Orographic controls on climate and paleoclimate of Asia: thermal and mechanical roles for the Tibetan Plateau. *Annual Review of Earth and Planetary Sciences*, 38(1):77–102.

Morelli, A. and Dziewonski, A. M. (1987). Topography of the core–mantle boundary and lateral homogeneity of the liquid core. *Nature*, 325(6106):678–683.

Morgan, W. J. (1971). Convection plumes in the lower mantle. *Nature*, 230:42–43.

Müller, R. D., Royer, J.-Y., and Lawver, L. A. (1993). Revised plate motions relative to the hotspots from combined Atlantic and Indian Ocean hotspot tracks. *Geology*, 21(3):275–278.

Müller, R. D., Sdrolias, M., Gaina, C., and Roest, W. R. (2008). Age, spreading rates, and spreading asymmetry of the world's ocean crust. *Geochemistry, Geophysics, Geosystems*, 9(4).

Obayashi, M., Sugioka, H., Yoshimitsu, J., and Fukao, Y. (2006). High temperature anomalies oceanward of subducting slabs at the 410-km discontinuity. *Earth and Planetary Science Letters*, 243(1):149–158.

O'Neill, C., Müller, D., and Steinberger, B. (2005). On the uncertainties in hot spot reconstructions and the significance of moving hot spot reference frames. *Geochemistry, Geophysics, Geosystems*, 6(4).

Opdyke, N. and Henry, K. (1969). A test of the dipole hypothesis. *Earth and Planetary Science Letters*, 6(2):139–151.

Panasyuk, S. V., Hager, B. H., and Forte, A. M. (1996). Understanding the effects of mantle compressibility on geoid kernels. *Geophysical Journal International*, 124(1):121–133.

Panet, I., Pajot-Métivier, G., Greff-Lefftz, M., Métivier, L., Diament, M., and Mandea, M. (2014). Mapping the mass distribution of Earth's mantle using satellite-derived gravity gradients. *Nature Geoscience*, 7(2):131–135.

Parsons, B. and Daly, S. (1983). The relationship between surface topography, gravity anomalies, and temperature structure of convection. *Journal of Geophysical Research: Solid Earth*, 88(B2):1129–1144.

Pavlis, N. K., Holmes, S. A., Kenyon, S. C., and Factor, J. K. (2012). The development and evaluation of the Earth Gravitational Model 2008 (EGM2008). *Journal of geophysical research: solid earth*, 117(B4).

Ricard, Y., Richards, M., Lithgow-Bertelloni, C., and Le Stunff, Y. (1993). A geodynamic model of mantle density heterogeneity. *Journal of Geophysical Research: Solid Earth*, 98(B12):21895–21909.

Richards, M. A. and Engebretson, D. C. (1992). Large-scale mantle convection and the history of subduction. *Nature*, 355(6359):437–440.

Richards, M. A. and Hager, B. H. (1984). Geoid anomalies in a dynamic Earth. *Journal of Geophysical Research*, 89(B7):5987–6002.

Ritsema, J., Deuss, A., Van Heijst, H., and Woodhouse, J. (2011). S40RTS: a degree-40 shear-velocity model for the mantle from new Rayleigh wave dispersion, teleseismic traveltime and normal-mode splitting function measurements. *Geophysical Journal International*, 184(3):1223–1236.

Scheidegger, A. E. (1965). On the statistics of the orientation of bedding planes, grain axes, and similar sedimentological data. *US Geological Survey Professional Paper*, 525:164–167.

Schettino, A. (2014). *Quantitative Plate Tectonics: Physics of the Earth-Plate Kinematics-Geodynamics*. Springer.

Schettino, A. and Scotese, C. R. (2005). Apparent polar wander paths for the major continents (200 Ma to the present day): a palaeomagnetic reference frame for global plate tectonic reconstructions. *Geophysical Journal International*, 163(2):727–759.

Schettino, A. and Turco, E. (2009). Breakup of Pangaea and plate kinematics of the central Atlantic and Atlas regions. *Geophysical Journal International*, 178(2):1078–1097.

Seton, M., Müller, R., Zahirovic, S., Gaina, C., Torsvik, T., Shephard, G., Talsma, A., Gurnis, M., Turner, M., Maus, S., et al. (2012). Global continental and ocean basin reconstructions since 200Ma. *Earth-Science Reviews*, 113(3):212–270.

Shephard, G. E., Bunge, H.-P., Schuberth, B. S., Müller, R., Talsma, A., Moder, C., and Landgrebe, T. (2012). Testing absolute plate reference frames and the implications for the generation of geodynamic mantle heterogeneity structure. *Earth and Planetary Science Letters*, 317:204–217.

Shi, R., Huang, B., Zhu, R., and Ren, S. (2004). Paleomagnetic study on the Early Triassic red beds from Jiaocheng, Shanxi Province. *Science in China Series D: Earth Sciences*, 47(2):108–114.

Sigloch, K. and Mihalynuk, M. G. (2013). Intra-oceanic subduction shaped the assembly of Cordilleran North America. *Nature*, 496(7443):50–56.

Simmons, N., Myers, S., Johannesson, G., Matzel, E., and Grand, S. (2015). Evidence for long-lived subduction of an ancient tectonic plate beneath the southern Indian Ocean. *Geophysical Research Letters*, 42.

Simmons, N. A., Forte, A. M., Boschi, L., and Grand, S. P. (2010). GyPSuM: A joint tomographic model of mantle density and seismic wave speeds. *Journal of Geophysical Research: Solid Earth (1978–2012)*, 115(B12).

Simmons, N. A., Myers, S. C., Johannesson, G., and Matzel, E. (2012). LLNL-G3Dv3: Global P wave tomography model for improved regional and teleseismic travel time prediction. *Journal of Geophysical Research: Solid Earth (1978–2012)*, 117(B10).

Simons, M. and Hager, B. H. (1997). Localization of the gravity field and the signature of glacial rebound. *Nature*, 390(6659):500–504.

Smirnov, A. V. and Tarduno, J. A. (2010). Co-location of eruption sites of the Siberian Traps and North Atlantic Igneous Province: Implications for the nature of hotspots and mantle plumes. *Earth and Planetary Science Letters*, 297(3):687–690.

Soldati, G., Koelemeijer, P., Boschi, L., and Deuss, A. (2013). Constraints on core-mantle boundary topography from normal mode splitting. *Geochemistry, Geophysics, Geosystems*, 14(5):1333–1342.

Spasojevic, S., Gurnis, M., and Sutherland, R. (2010). Mantle upwellings above slab graveyards linked to the global geoid lows. *Nature Geoscience*, 3(6):435–438.

Steinberger, B. (2000). Plumes in a convecting mantle: Models and observations for individual hotspots. *Journal of Geophysical Research: Solid Earth*, 105(B5):11127–11152.

Steinberger, B. and Holme, R. (2008). Mantle flow models with core-mantle boundary constraints and chemical heterogeneities in the lowermost mantle. *Journal of Geophysical Research: Solid Earth*, 113(B5).

Steinberger, B., Sutherland, R., and O'connell, R. J. (2004). Prediction of Emperor-Hawaii seamount locations from a revised model of global plate motion and mantle flow. *Nature*, 430(6996):167–173.

Steinberger, B. and Torsvik, T. H. (2008). Absolute plate motions and true polar wander in the absence of hotspot tracks. *Nature*, 452(7187):620–623.

Tan, X., Fang, D., Yuan, Y., Fan, S., and Bao, J. (1991). Paleomagnetic study on red beds, Liujiaogou Formation (TRL) from Taoyuan, Yaoqu, Jixian, Shanxi Province. *Acta Geophysica Sinica*, 34(6):736–743.

Tarduno, J. A. (2007). On the motion of Hawaii and other mantle plumes. *Chemical Geology*, 241(3):234–247.

Tarduno, J. A. and Cottrell, R. D. (1997). Paleomagnetic evidence for motion of the Hawaiian hotspot during formation of the Emperor seamounts. *Earth and Planetary Science Letters*, 153(3):171–180.

Tauxe, L., Banerjee, S., Butler, R., and Van der Voo, R. (2010). Essentials of paleomagnetism. *University of California Press*.

Tomurtogoo, O., Windley, B., Kröner, A., Badarch, G., and Liu, D. (2005). Zircon age and occurrence of the Adaatsag ophiolite and Muron shear zone, central Mongolia: constraints on the evolution of the Mongol–Okhotsk ocean, suture and orogen. *Journal of the Geological Society*, 162(1):125–134.

Torsvik, T. H., der Voo, R. V., Meert, J. G., Mosar, J., and Walderhaug, H. J. (2001). Reconstructions of the continents around the North Atlantic at about the 60th parallel. *Earth and Planetary Science Letters*, 187(1-2):55 – 69.

Torsvik, T. H., der Voo, R. V., Preeden, U., Niocaill, C. M., Steinberger, B., Doubrovine, P. V., van Hinsbergen, D. J., Domeier, M., Gaina, C., Tohver, E., Meert, J. G., McCausland, P. J., and Cocks, L. R. M. (2012). Phanerozoic polar wander, palaeogeography and dynamics. *Earth-Science Reviews*, 114(3–4):325–368.

Torsvik, T. H., Müller, R. D., Van der Voo, R., Steinberger, B., and Gaina, C. (2008a). Global plate motion frames: toward a unified model. *Reviews of Geophysics*, 46(3).

Torsvik, T. H. and Smethurst, M. A. (1999). Plate tectonic modelling: virtual reality with GMAP. *Computers & Geosciences*, 25(4):395–402.

Torsvik, T. H., Steinberger, B., Cocks, L. R. M., and Burke, K. (2008b). Longitude: linking Earth's ancient surface to its deep interior. *Earth and Planetary Science Letters*, 276(3):273–282.

Torsvik, T. H., Steinberger, B., Gurnis, M., and Gaina, C. (2010). Plate tectonics and net lithosphere rotation over the past 150my. *Earth and Planetary Science Letters*, 291(1):106–112.

Torsvik, T. H., van der Voo, R., Doubrovine, P. V., Burke, K., Steinberger, B., Ashwal, L. D., Trønnes, R. G., Webb, S. J., and Bull, A. L. (2014). Deep mantle structure as a reference frame for movements in and on the Earth. *Proceedings of the National Academy of Sciences*, page 201318135.

Trampert, J., Deschamps, F., Resovsky, J., and Yuen, D. (2004). Probabilistic tomography maps chemical heterogeneities throughout the lower mantle. *Science*, 306(5697):853–856.

Turcotte, D. L. and McAdoo, D. (1979). Geoid anomalies and the thickness of the lithospere. *Journal of Geophysical Research: Solid Earth*, 84(B5):2381–2387.

Turcotte, D. L. and Schubert, G. (2014). *Geodynamics.* Cambridge University Press.

van der Hilst, R. D. and Kárason, H. (1999). Compositional heterogeneity in the bottom 1000 kilometers of Earth's mantle: toward a hybrid convection model. *Science*, 283(5409):1885–1888.

van der Meer, D. G., Spakman, W., van Hinsbergen, D. J., Amaru, M. L., and Torsvik, T. H. (2010). Towards absolute plate motions constrained by lower-mantle slab remnants. *Nature Geoscience*, 3(1):36–40.

van der Meer, D. G., Torsvik, T. H., Spakman, W., Van Hinsbergen, D. J., and Amaru, M. L. (2012). Intra-Panthalassa Ocean subduction zones revealed by fossil arcs and mantle structure. *Nature Geoscience*, 5(3):215–219.

Van der Voo, R. (1990). Phanerozoic paleomagnetic poles from Europe and North America and comparisons with continental reconstructions. *Reviews of Geophysics*, 28(2):167–206.

Van der Voo, R., Spakman, W., and Bijwaard, H. (1999). Mesozoic subducted slabs under Siberia. *Nature*, 397(6716):246–249.

Van der Voo, R., Van Hinsbergen, D. J., Domeier, M., Spakman, W., and Torsvik, T. H. (2015). Latest Jurassic–earliest Cretaceous closure of the Mongol–Okhotsk Ocean: a paleomagnetic and seismological–tomographic analysis. In *Late Jurassic Margin of LaurasiaąłA Record of Faulting Accommodating Plate Rotation*, volume 513.

Van der Voo, R., Wu, F., Zhongmin, W., Dongwoo, S., Peacor, D. R., and Qizhong, L. (1993). Paleomagnetism and electron microscopy of the Emeishan Basalts, Yunnan, China. *Tectonophysics*, 221(3):367–379.

Vine, F. J. (1966). Spreading of the ocean floor: new evidence. *Science*, 154(3755):1405–1415.

Vine, F. J. and Matthews, D. H. (1963). Magnetic anomalies over oceanic ridges. *Nature*, 199(4897):947–949.

Wessel, P. and Kroenke, L. (1997). A geometric technique for relocating hotspots and refining absolute plate motions. *Nature*, 387(6631):365–369.

Whittaker, J. M., Williams, S. E., and Müller, R. D. (2013). Revised tectonic evolution of the Eastern Indian Ocean. *Geochemistry, Geophysics, Geosystems*, 14(6):1891–1909.

Williams, S., Flament, N., Müller, R. D., and Butterworth, N. (2015). Absolute plate motions since 130 Ma constrained by subduction zone kinematics. *Earth and Planetary Science Letters*, 418:66–77.

Wu, L. and Kravchinsky, V. A. (2014). Derivation of paleolongitude from the geometric parametrization of apparent polar wander path: Implication for absolute plate motion reconstruction. *Geophysical Research Letters*, 41(13):4503–4511.

Wu, L., Kravchinsky, V. A., and Potter, D. K. (2015). PMTec: A new MATLAB toolbox for absolute plate motion reconstructions from paleomagnetism. *Computers & Geosciences*, 82:139–151.

Xiao, W., Windley, B., Sun, S., Li, J., Huang, B., Han, C., Yuan, C., Sun, M., and Chen, H. (2015). A Tale of Amalgamation of Three Collage Systems in the Permian-Middle Triassic in Central-East Asia: Oroclines, Sutures, and Terminal Accretion. *Annual Review of Earth and Planetary Sciences*, 43(1).

Yang, Z., Ma, X., Besse, J., Courtillot, V., Xing, L., Xu, S., and Zhang, J. (1991). Paleomagnetic results from Triassic sections in the Ordos Basin, North China. *Earth and Planetary Science Letters*, 104(2–4):258–277.

Zhang, S. and Christensen, U. (1993). Some effects of lateral viscosity variations on geoid and surface velocities induced by density anomalies in the mantle. *Geophysical Journal International*, 114(3):531–547.

Zhao, P., Chen, Y., Xu, B., Faure, M., Shi, G., and Choulet, F. (2013). Did the Paleo-Asian Ocean between North China Block and Mongolia Block exist during the late Paleozoic? First paleomagnetic evidence from central-eastern Inner Mongolia, China. *Journal of Geophysical Research: Solid Earth*, 118(5):1873–1894.

Zhao, X. and Coe, R. S. (1989). Tectonic implications of Perm-Triassic paleomagnetic results from north and south China. *Geophysical Monograph Series*, 50:267–283.

Zhao, X., Coe, R. S., Zhou, Y., Wu, H., and Wang, J. (1990). New paleomagnetic results from northern China: collision and suturing with Siberia and Kazakhstan. *Tectonophysics*, 181(1–4):43–81.

Zhou, T., Goldfarb, R. J., and Phillips, N. G. (2002). Tectonics and distribution of gold deposits in China–an overview. *Mineralium Deposita*, 37(3-4):249–282.